Rational Synthesis of Multimetallic Nanocrystals for Plasmonics and Catalysis

A Dissertation
Presented to
The Academic Faculty

By

Jae Wan Ahn

In Partial Fulfillment
Of the Requirement for the Degree
Doctor of Philosophy in the
School of Materials Science and Engineering

Georgia Institute of Technology
December 2019

Rational Synthesis of Multimetallic Nanocrystals

for Plasmonics and Catalysis

Approved by:

Dr. Dong Qin, Advisor
School of Materials Science
and Engineering
Georgia Institute of Technology

Dr. Zhiqun Lin
School of Materials Science
and Engineering
Georgia Institute of Technology

Dr. Meilin Liu
School of Materials Science
and Engineering
Georgia Institute of Technology

Dr. Preet Singh
School of Materials Science
and Engineering
Georgia Institute of Technology

Dr. Joseph Sadighi
School of Chemistry and Biochemistry
Georgia Institute of Technology

Date Approved: October 31, 2019

Dedicated to my dear and beloved family.

ACKNOWLEDGEMENTS

Most prominently, I would like to express my sincere gratitude to my research advisor, Professor Dong Qin, for providing invaluable guidance for my path toward an independent scholar and researcher. She has provided countless thought-provoking advices and abundantly supplied the resources to facilitate effective and impactful research, which I could have in my graduate career otherwise. I would like to acknowledge Professor Meilin Liu, Professor Zhiqun Lin, Professor Joseph Sadighi, and Professor Preet Singh for willing to spend their valuable time to serve on my dissertation committee and provide words of advice and encouragement.

I could not go without recognizing the support from the members of the Qin Lab, for their helpful discussions and assistance in the lab. I would like to specifically thank three Qin lab alumni, Dr. Xiaojun Sun, Dr. Yiren Wu, and Dr. Yun Zhang, for sharing much of their experimental and theoretical knowledge, and being patient even when I approach them with an exorbitant number of questions. I also thank Junki Kim and Daniel Wang for their key roles in the execution of experiments. Furthermore, I thank all the former and current members of the Qin Lab with whom I shared enjoyable and delightful moments throughout the last six years of my time. In addition, I am grateful to Professor Jingyue Liu (Arizona State University) and Dr. Yong Ding for providing the training for various aspects of my high-resolution electron microscopy skills.

Lastly, I could not have reached this point without the unconditional love and support from both my mother, late Ms. Insoon Park, and my father, Dr. Kyeongseop Ahn, especially through the toughest times that our family had to face in the last three years.

I acknowledge that the research presented in this dissertation was made possible by the generous funding from the National Science Foundation (CHE-1412006, CHE-1708300), start-up funds from the Georgia Institute of Technology (GT), and a 3M non-tenured faculty award. Part of my graduate stipend was also funded by the National Science Foundation (CMMI-1634687) and the U.S. Department of Energy. The electron microscope and related characterization works were performed in part at the Institute for Electronics and Nanotechnology at GT, a member of the National Nanotechnology Coordinated Infrastructure (NNCI), which is supported by the National Science Foundation (ECCS-1542174).

TABLE OF CONTENTS

LIST OF TABLES

LIST OF FIGURES

LIST OF SYMBOLS AND ABBREVIATIONS

γ	surface energy
ε_m	relative dielectric constant of the medium
ε_r	real part of dielectric function
ε_i	imaginary part of dielectric function
4-AP	4-aminophenol
A_t	intensity of extinction at time *t*
4-ATP	4-aminothiophenol
1,4-BDT	1,4-benzenedithiol
C_{ext}	extinction cross section
C_s	spherical aberration
CTAC	cetyltrimethylammonium chloride
DDA	discrete dipole approximation
DI	deionized
E_0	electric field component of incident light
EDS	energy dispersive X-ray spectroscopy
EELS	electron energy-loss spectroscopy
EF	enhancement factor
$E_{out}(\omega)$	electromagnetic field of incident excitation at frequency ω
$E_{out}(\omega-\omega_v)$	Stokes-shifted Raman electromagnetic fields

FCC	face-centered cubic
FTIR	Fourier-transform infrared spectroscopy
GOx	glucose oxidase
HAADF	high-angle annular dark-field
$HAsc^-$	ascorbate monoanion
H_2Asc	ascorbic acid
ICP-MS	inductively coupled plasma mass spectrometry
$I_{SERS}(\omega_v)$	surface-enhanced Raman intensity
$I_{NRS}(\omega_v)$	normal Raman intensity
k	wave vector
LSP	localized surface plasmons
LSPR	localized surface plasmon resonance
4-NP	4-nitrophenol
N_{surf}	number of molecules bound to the metal surface
4-NTP	4-nitrothiophenol
N_{vol}	number of molecules in the excitation volume
ORR	oxygen reduction reaction
1,4-PDI	1,4-phenylene diisocyanide
PEMFC	proton exchange membrane fuel cells
PSP	propagating surface plasmons

PVP	poly(vinylpyrrolidone)
Q	quality factor
$R_{deposition}$	rate of deposition
$R_{etching}$	rate of oxidative etching
SAM	self-assembled monolayers
S.D.	standard deviation
SEM	scanning electron microscopy
SERS	surface enhanced Raman scattering/spectroscopy
SHG	second-harmonic generation spectroscopy
SPR	surface plasmon resonance
STEM	scanning transmission electron microscopy
STM	scanning tunneling microscopy
TEM	transmission electron microscopy
trans-DMAB	*trans*-dimercaptoazobenzene
UPD	underpotential deposition
UV-vis	ultraviolet-visible light

SUMMARY

Multimetallic noble-metal nanocrystals have attracted considerable attention owing to their broad structure-property relationship for applications in plasmonics and catalysis. However, it remains a major challenge to rationally synthesize these nanocrystals because most of the reported protocols lack a mechanistic understanding and often involve a trial-and-error approach when optimizing the experimental parameters. This dissertation demonstrates the use of facet-selective etching and deposition as a powerful method for the transformation of colloidal silver nanocrystals into multimetallic nanostructures with intricate properties. In particular, I leverage the metal-coordination ligands to direct the etching and deposition in an orthogonal manner. In the first case study, I transform silver nanocubes into bimetallic concave nanocubes encased by silver-gold alloy frames via selective removal of the silver atoms from side faces while co-depositing silver and gold atoms as an alloy on the edges and corners. I further subject the core-frame nanocubes to galvanic replacement for the fabrication of nanoscale, multimetallic, cage cubes by confining the drilling of silver to the center of each side face. In the second case study, I investigate the roles played by poly(vinylpyrrolidone) and cetyltrimethylammonium chloride in controlling the orthogonal deposition of gold on different facets of silver cuboctahedra for the fabrication of nanoboxes with complementary surface structures. To understand the interaction between the ligands noble-metal and nanocrystals, I develop an *in situ* platform based on surface-enhanced Raman spectroscopy for analyzing the competitive binding of thiol and isocyanide molecules to the surface of silver nanocubes. Collectively, this work offers insights into the rational synthesis of multimetallic nanocrystals for applications in plasmonics and catalysis.

CHAPTER 1. INTRODUCTION

1.1 Noble Metal Nanocrystals and Their Structure-Property Relationship

Noble metals such as silver, gold, platinum, and palladium have long been prized for their rarity, admired for their aesthetic value, and found various uses in some disciplines of science, but their full industrial potential was only realized upon significant advancements in nanotechnology. When their dimensions are reduced to the nanometer regime and form nanocrystals, their properties become significantly different from that of the bulk noble metals, with additional options to further tailor their properties in correlation to their morphology and composition. The ability to manipulate the morphology and composition of nanocrystals for attaining desired functionalities opens possibilities for advanced industrial applications such as optical imaging, sensing, and catalysis.[1-6]

In this work, I focus on two specific functionalities of noble-metal nanocrystals that can be tailored by their morphology and composition for applications in plasmonics and catalysis (Figure 1.1).[7] Firstly, there is a strong interaction between an incident electromagnetic radiation at a resonant wavelength and delocalized electrons in metals such as silver or gold, which leads to a collective electronic oscillation referred to as surface plasmon resonance (SPR), or localized surface plasmon resonance (LSPR) when the oscillations are confined to a nanocrystal.[8] The size dependency becomes important because the resonant wavelength will depend on the geometry of the nanocrystal.[6] LSPR is responsible for the enhancement of electric fields near the nanocrystal surface, especially strongly at “hot spots” such as corners or interparticle junctions,[9] serving as the basis for surface-enhanced Raman scattering (SERS).[10-12] In addition, the effectiveness of metals

Figure 1.1. Selected section of the periodic table highlighting the noble metals used for catalytic (Pd, Pt, Au) and/or plasmonic (Ag, Au) applications.

such as gold or platinum in catalysis applications is significantly improved when they are in their nanocrystal form. As the size of the metal particle decreases, the specific surface-area rapidly increases, resulting in a larger number of atoms available on the surface as a catalyst for participating in reactions to achieve a higher catalytic activity. For example, Pt nanocrystals have been used as effective catalysts for reactions such as the oxygen reduction reaction (ORR) for proton-exchange membrane fuel cells (PEMFC) and carbon monoxide oxidation in catalytic converters.[13-15] In this section, I will elucidate in detail the origin of the plasmonic and catalytic properties of noble metal nanocrystals as well as their explicit dependence on the morphology of the nanocrystals.

1.1.1 Plasmonic Properties of Noble Metal Nanocrystals

1.1.1.1 Localized Surface Plasmon Resonance

Plasmonics is the study of how incident electromagnetic waves interact with collective oscillations of free electrons, or plasmons, typically found in metals. Plasmonic effects provide an alternative way, in addition to using dielectric materials, in which light could be artificially manipulated. There are largely two modes through which plasmonic interactions could manifest.[6] Figure 1.2A shows propagating surface plasmons (PSPs), which are found in metal nanocrystals where one or more dimensions are larger than the

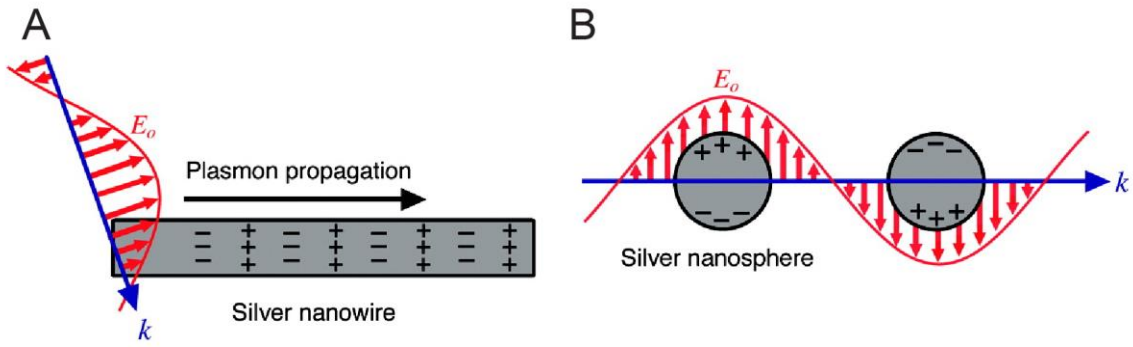

Figure 1.2. Schematic illustration of two plasmon modes when nanocrystals of different morphologies were excited by an incident light with a wave vector of *k* and an electric field of E_0: (A) a silver nanowire having one dimension longer than the wavelength of incoming light; and (B) silver nanospheres having radii much shorter than the wavelength of incoming light. Copyright 2011 American Chemical Society.[6]

wavelength of the incident light. Because the time-varying electric field component of the incident light (E_0) is not uniform across the structure in this case, the electronic oscillation in response to E_0 occurs along the long axis direction of the nanocrystal. PSPs are affected by many factors that complicate the understanding of their nature.[16] On the other hand, Figure 1.2B describes localized surface plasmons (LSPs) which are found in metal nanocrystals with all three dimensions smaller than the wavelength of the incident

electromagnetic waves. The E_0 will exert a Coulombic force on the free conduction electrons to move in the opposite direction, resulting in their collective oscillation over time. When the light at a certain frequency is in resonance with the LSP, the plasmonic oscillation is greatly enhanced, and this phenomenon is known as localized surface plasmon resonance (LSPR).

LSPR can be described by Gustav Mie's solution to the Maxwell equations[17] in the simplest case, which calculates the extinction cross section of a spherical particle, as shown in Equation 1:

$$C_{ext} = \frac{24\pi^2 R^3 \varepsilon_m^{3/2}}{\lambda}\left[\frac{\varepsilon_i}{(\varepsilon_r+2\varepsilon_m)^2+\varepsilon_i^2}\right] \quad \text{(Eq. 1)}$$

where C_{ext} is the extinction cross section, R is the radius of the sphere, and ε_m is the relative dielectric constant of the medium (solvent). ε_r and ε_i correspond to the real and imaginary part of the dielectric function of the material. For metal nanocrystals of more complex geometries, the discrete-dipole approximation (DDA) could be used to more accurately describe their C_{ext}.[18] This approach sections the nanocrystal into a finite number of discrete points, regarding each point as a dipole that can be polarized by incoming light and nearby dipoles, and computing the overall C_{ext} from the polarizations at each point. Examining Equation 1, there are two conditions that must be satisfied to maximize C_{ext}. The first is that ε_r be close to $-2\varepsilon_m$, and the second is that ε_i be close to zero. While most non-plasmonic materials exhibit ε_r values ranging from 1 to 50,[19] good plasmonic metals such as Ag exhibit negative values for ε_r (Figure 1.3A).[20] In addition, while most materials have high ε_i values across the wavelengths in the visible range, metals such as Ag stay close to zero, contributing to C_{ext} (Figure 1.3B). The two conditions are often evaluated simultaneously by a combined parameter called the "quality factor" to describe the

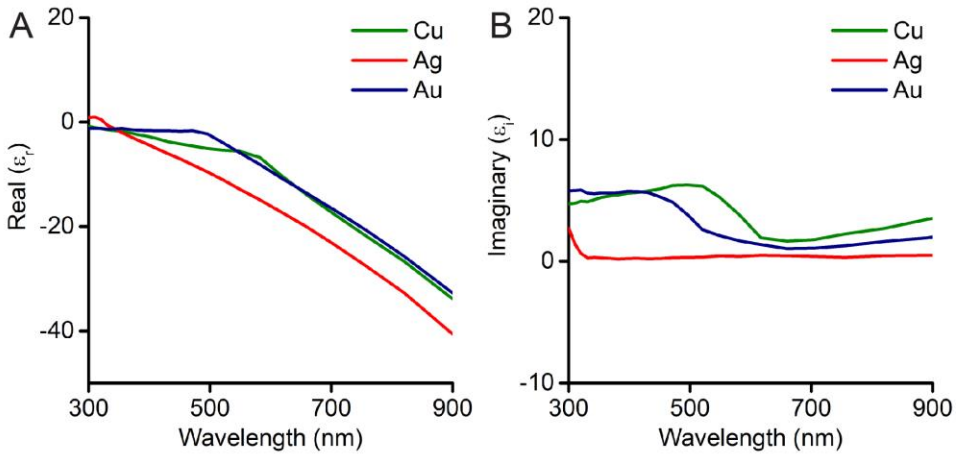

Figure 1.3. Plot of the (A) real and (B) imaginary component of dielectric function ($\varepsilon = \varepsilon_r + i\varepsilon_i$) with respect to the wavelength, comparing the case of Ag, Au, and Cu, respectively. Experimentally measured optical constants were used to compute each component of dielectric function.[20]

plasmonic strength of a given material, as shown in Equation 2. In this equation, w corresponds to the frequency of incident light.

$$Q = \frac{w(d\varepsilon_r/dw)}{2(\varepsilon_i)^2} \qquad \text{(Eq. 2)}$$

Figure 1.4 illustrates the quality factors of various metals as a function of wavelength.[21] In the case of Ag, a high Q-value is maintained throughout all visible wavelengths and even for near-IR and ultraviolet, making it a valuable metal for plasmonic applications. Au and Cu show high Q-values only in low frequency regions, and other noble metals such as Pd or Pt show poor Q-values throughout all wavelengths. Although Li seems to be an efficient plasmonic material, its poor chemical stability renders it impractical.

The resonance conditions for plasmonic nanocrystals will also be affected by the size and shape of the nanocrystals.[19] Figure 1.5, A and B, shows that 40-nm Ag nanospheres dispersed in water exhibit an LSPR peak at around 410 nm, while 40-nm Ag nanocubes show distinct LSPR peaks around 510 nm and another around 450 nm.[22] In addition,

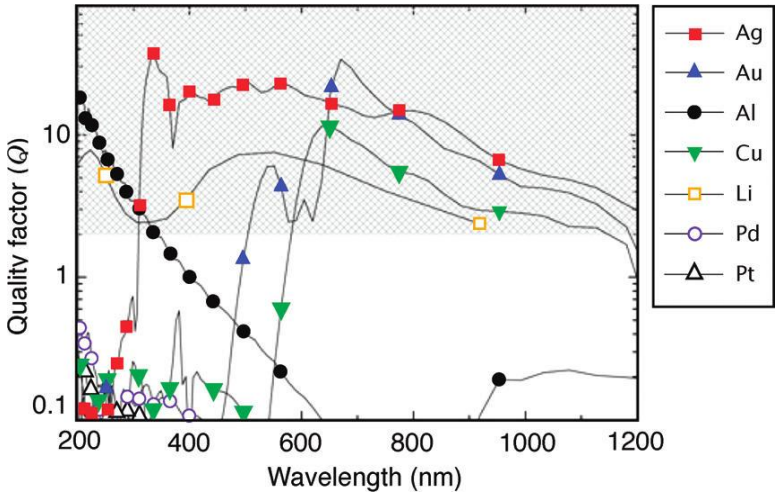

Figure 1.4. Plot of the quality factor (Q) of the LSPR across a metal/air interface for a variety of metals, with respect to the excitation wavelength. Higher Q-value indicates stronger plasmonic resonance for the given wavelength. Q-values falling into the grey region are sufficiently high for plasmonic applications. Copyright 2009 Elsevier.[21]

it has been demonstrated that when the edge lengths of Ag nanocubes are varied from 36 to 172 nm, the main LSPR peak of the Ag nanocubes shifts from 420 to 600 nm.[23] Since plasmonic oscillations are driven by the charge separation that occurs when the incident electric field displaces the cloud of free conduction electrons, it is natural that when plasmonic oscillations occur over longer distances their frequencies will be lower.[24] In fact, charge separation becomes greater when there are sharp features such as corners, where it is suggested that charges will be concentrated.[25] This explains the LSPR behavior of Ag nanocubes in comparison to that of the Ag nanospheres, since the cubic geometry has additional plasmon modes such as the corner-to-corner dipole.[26] Therefore, it is possible to use UV-vis spectrometry to extract information about the size and shape of nanocrystals in a solution, such as for the four nanocrystal geometries shown in Figure 1.5, A-D.[8]

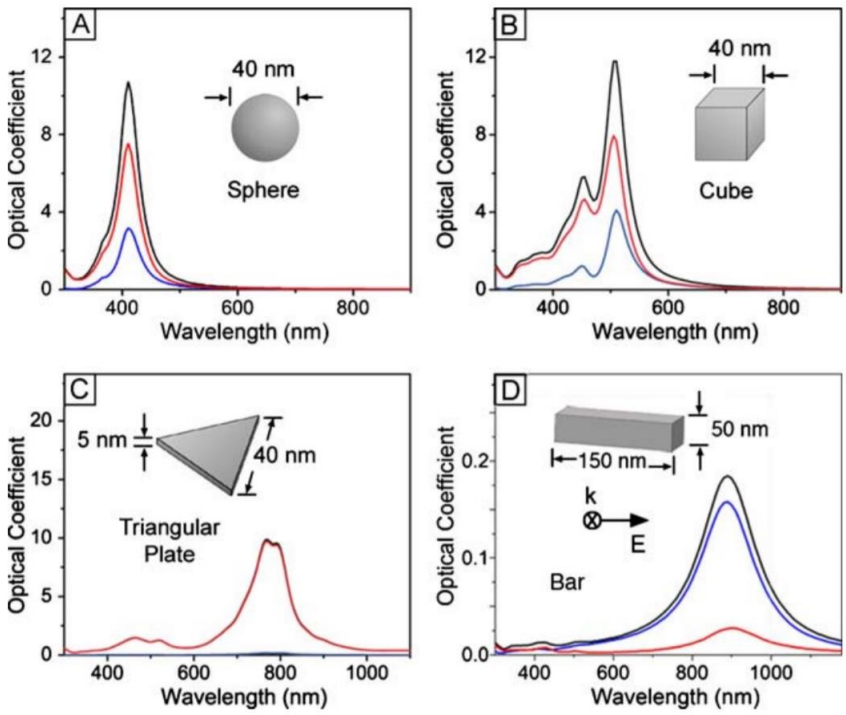

Figure 1.5. Calculated UV-vis spectra of various Ag nanocrystal morphologies, (A) nanosphere, (B) nanocube, (C) triangular nanoplate, and (D) rectangular nanoprism. The Mie theory was used to calculate for the nanosphere, while the other geometries were calculated using the discrete dipole approximation method. The overall extinction is shown in black, the absorption component is shown in red, and the scattering component is shown in blue. Copyright 2006 American Chemical Society.[22]

1.1.1.2 Surface-Enhanced Raman Scattering

At the resonance of the LSPR peak, metal nanocrystals would embrace enhanced electromagnetic fields in some of regions of nanocrystals, leading to the enhanced Raman cross sections of molecules in proximity to the surface. This effect is called surface-enhanced Raman scattering (SERS).[21] Raman scattering signals contain valuable information about a molecule's chemical fingerprint, and with the development of SERS technology, it has been made possible to detect molecules with up to single-molecule sensitivities.[27-29] SERS can be quantified by an enhancement factor (EF), which is described by Equation 3,[30-32] in which $E_{out}(\omega)$ and $E_{out}(\omega - \omega_v)$ stand for the incident

$$\mathrm{EF_{SERS}}(\omega_v) = \frac{|E_{out}(\omega)^2||E_{out}(\omega-\omega_v)^2|}{E_0^4} = \frac{I_{SERS}(\omega_v)/N_{surf}}{I_{NRS}(\omega_v)/N_{vol}} \quad \text{(Eq. 3)}$$

excitation (with frequency ω) and that which results from a Stokes shift (with difference in frequency ω_v) upon Raman scattering, respectively. In practice, the EF is calculated as the ratio between the surface-enhanced Raman intensity ($\mathrm{I_{SERS}}(\omega_v)$) normalized to the number of molecules bound to the nanocrystal surface ($\mathrm{N_{surf}}$) and the unmodified normal Raman intensity ($\mathrm{I_{NRS}}(\omega_v)$) normalized to the number of molecules in the excitation volume ($\mathrm{N_{vol}}$). Improvements could be made to this EF calculation by expressing the two number terms using experimental parameters instead of estimations.[32]

Regions near a nanocrystal surface with an exceptionally high electric field enhancement are referred to as "hot spots" for SERS and they will occur near sharp surface features such as sharp edges and small spaces between particles.[9, 12, 25, 33] Strategies to improve the SERS enhancement will rely on increasing the relative abundance of these hot spots.[9] One way is to use shape-controlled synthesis methods,[22] a detailed discussion for which could be found in Section 1.2.2, to fabricate nanocrystals with sharp, concave surfaces on which many SERS hot spots will be generated.[1, 34-36] The other way is to allow nanocrystals to be slightly aggregated under control, bringing them close enough with each other to form hot spots between nanocrystals.[37, 38] Figure 1.6 shows the calculated electric field enhancements on the surface of a single Ag nanocube upon excitation with an external electric field, and it clearly shows the presence of SERS hot spots along the cubic edges.[33] On the other hand, Figure 1.7 shows a calculation of the SERS hot spot distribution in the region between two Au nanospheres with a 2-nm gap between each particle, for which the electric field enhancements show a significant spatial variation over the surface of the nanoparticle.[39]

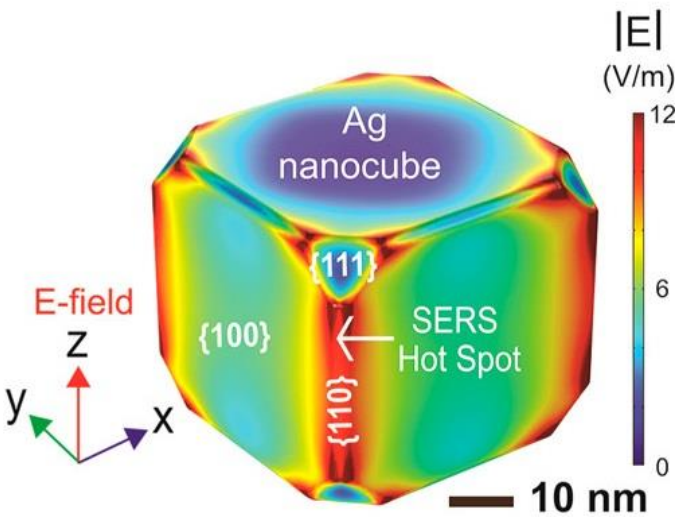

Figure 1.6. Calculated intensity of electric field enhancements on the surface of a slightly truncated 39-nm Ag nanocube at a laser excitation of 532 nm. SERS hot spots are visible at the sharp edges of the nanocube. Copyright 2017 American Chemical Society.[33]

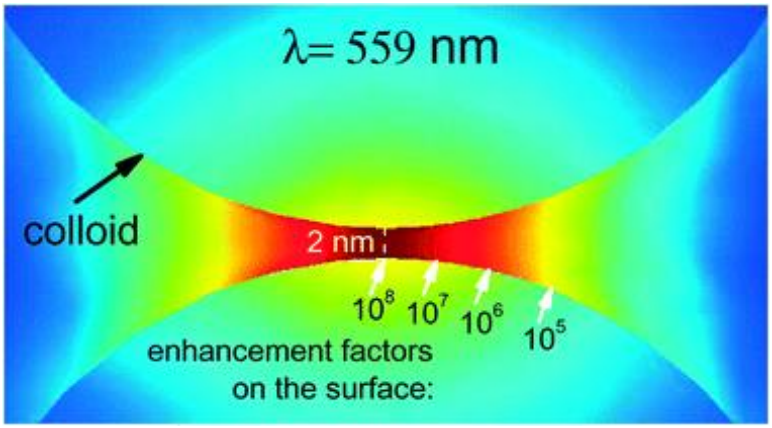

Figure 1.7. Calculated intensity of electric field enhancements (depicted in enhancement factor values) distributed in the region of a 2-nm gap between two Au nanospheres with radii of 30 nm. Copyright 2008 Royal Society of Chemistry.[39]

1.1.2 Catalytic Properties of Noble Metal Nanocrystals

Nanocrystals of noble metals such as Au, Pt, and Pd have shown notable catalytic activities towards various reactions. For example, Au nanocrystals have been used for various catalytic applications such as CO_2 hydrogenation for generating methanol,[40] NO reduction,[41] water-gas shift reaction,[42] H_2O_2 production directly from H_2 and O_2,[43] and other various organic syntheses. Pt nanocrystals have been used for O_2 reduction (ORR),[44, 45] ethanol oxidation reaction,[44] and methanol oxidation reaction.[45] These chemical reactions are especially critical to the design of fuel cells. Pd nanocrystals[46-48], together with Au nanocrystals[49, 50] and Pt nanocrystals,[51, 52] have been widely explored as catalysts for CO oxidation reactions in catalytic converters. In addition, Pd nanocrystals have demonstrated catalytic activity towards many organic syntheses such as the Heck,[53-56] Suzuki,[54, 57-59] Stille,[60, 61], and Sonogashira[54, 62, 63] reactions.

The origin of the catalytic activity of otherwise inert noble metals have been attributed to several different effects,[64] including size-dependent quantum effects,[50, 65] charge transfer,[66-68], and interfacial strain.[69, 70] Especially important is the charge transfer effect, which takes place from a less electronegative atom to a more electronegative atom. Since Ag has a smaller electronegativity value,[71] when Ag is alloyed with catalytic metals, electrons from Ag atoms will migrate to the atoms of Au or Pt, and the greater electron density at the catalytic metals will enhance their catalytic activity compared to their monometallic counterparts. A recent study argues that electrostatic interactions are responsible for catalytic activity in noble-metal nanocrystals such as Au or Pt.[72] Low-coordinated surface atoms have singly occupied s-orbitals that overlap with each other, generating sites of positive electrostatic potential, or σ-holes,[73] that affect the adsorption

affinity of reactant species such as a Lewis base with slightly negative region of (δ^-) lone-pair electrons.

Notably, the nanocrystal morphology also affects the catalytic activity, as it has been observed that the catalytic activities would vary across surfaces of different facets. For example several groups have demonstrated that the catalytic properties of Pd and Pt nanocrystals could be engineered by controlling their shape and thus the types of facets expressed on the surface.[48, 74-76] Moreover, their catalytic activity can be further enhanced by introducing surfaces with high-index facets, which have a greater density of surface atoms with low-coordination numbers.[77-79] It follows that a fine control over the nanocrystal morphology is crucial to achieve a rational design of functional nanocrystals. For example, Pt-based nanocages with hollow cores and porous surfaces allow access to Pt atoms both inside and outside of the nanocrystal, leading to higher mass activities.[80, 81] In addition, bimetallic[13, 14, 62] and trimetallic[68, 82, 83] nanocrystals have been shown to have enhanced catalytic activities, suggesting that chemical composition of nanocrystals must be carefully controlled. and ultimately maximize their performance.

1.1.3 Evaluating the Structures and Properties of Noble Metal Nanocrystals

1.1.3.1 Characterizing the Morphology and Composition of Nanocrystals

As discussed in Sections 1.1.2 and 1.1.3, the morphology and composition of noble-metal nanocrystals is a key factor in tuning their plasmonic and catalytic activities. Therefore, the accurate characterization of nanocrystals is just as important as, if not more than, the synthesis itself. Transmission electron microscopy (TEM) images show the morphology of nanocrystals in a 2D projection. In the bright-field (BF) mode, where a

parallel electron beam illuminates the sample and the transmitted electrons are detected by a camera below the sample, a region of relatively darker contrast indicates a thicker structure or a presence of heavier atoms. One may also quantitatively assess the size of nanocrystals with a mean value and a standard deviation across at least 30 individual nanocrystals. All TEM images shown in each chapter were taken by a Hitachi HT7700 TEM operating at 120 kV. On the other hand, scanning electron microscopy (SEM) images have a large depth of field, directly providing a 3D topological information about the sample. For its operation, a focused electron beam is rasterized across the sample to locally release secondary electrons, which are guided to a detector. Features such as sharp edges, corners, holes, and local depressions can be identified with SEM. A Hitachi SU8230 field emission (FE) SEM operating at a range from 10 to 30 kV was used to collect the SEM images displayed in each chapter. Furthermore, an aberration-corrected scanning transmission electron microscope (STEM) operating in the high-angle annular dark field (HAADF) mode was used to collect atomic-resolution images. In this instrument, a highly focused electron beam is rasterized across the sample, and each atom will scatter the electron beam at a specific angle according to their atomic weight. The scattered beam at each pixel is captured by an annular disk detector below the sample, and a computer software can combine the signals into a full image. Each atom appears as a bright dot, and atoms of heavier elements appear brighter. With HAADF-STEM, one can collect information about the atomic spacing, lattice mismatch, and elemental distribution. Also, as the STEM electron beam interacts with each atom, characteristic X-rays are released from each atom, which can be collected by another detector to perform energy-dispersive X-ray spectroscopy (EDS). EDS provides a spectrum of characteristic X-rays at each pixel,

and a software can map them onto a single image to reveal the spatial distribution of any element on the nanocrystal. In this dissertation, a Hitachi HD2700 HAADF-STEM with C_s-correction operating at 200 kV was used for characterization, equipped with a side EDS detector for elemental analysis. Inductively coupled plasma mass spectrometry (ICP-MS) is a mass analysis technique that involves converting a sample of nanocrystals into plasma, or cations of every metal atoms present in the sample, then using mass spectrometry techniques to differentiate between atoms of dissimilar atomic weights. ICP-MS can provide information about the chemical composition of nanocrystals and the precursor conversion rate. The mass analyses in this dissertation were performed using a PerkinElmer NexION 300Q ICP-MS.

1.1.3.2 Evaluating the Plasmonic and Catalytic Properties of Nanocrystals

The extinction of incoming light due to LSPR at a specific resonance wavelength can be identified by UV-vis spectroscopy. Ag and Au will have the strongest plasmonic response, and therefore these nanocrystals can be effectively characterized through UV-vis spectroscopy.[6] In analyzing a UV-vis spectrum of a solution of plasmonic nanocrystals, there are a number of considerations. First, the Beer-Lambert law elucidates that the extinction coefficient, as indicated by the LSPR peak intensity, is linearly related to the concentration of plasmonic nanocrystals in the solution and to the path length of the sample solution. Second, as discussed in Section 1.1.1, the UV-vis spectra are greatly affected by the nature of the nanocrystals. The number of LSPR peaks and their positions correspond to the different plasmon modes that are present in the nanocrystal due to its shape and size.[8, 19] The broadening of the LSPR peaks are attributed to electron-surface scattering and/or

radiation dampening effects depending on the size, shape, and surface chemistry of nanocrystals.[84, 85] Third, even a small change to the morphology and/or composition of nanocrystals can be detected using UV-vis spectroscopy. Figure 1.8 shows a plot of simulated spectra using Mie theory where if a nanocrystal becomes less spherical and more oblate, the LSPR peak is red-shifted.[19]

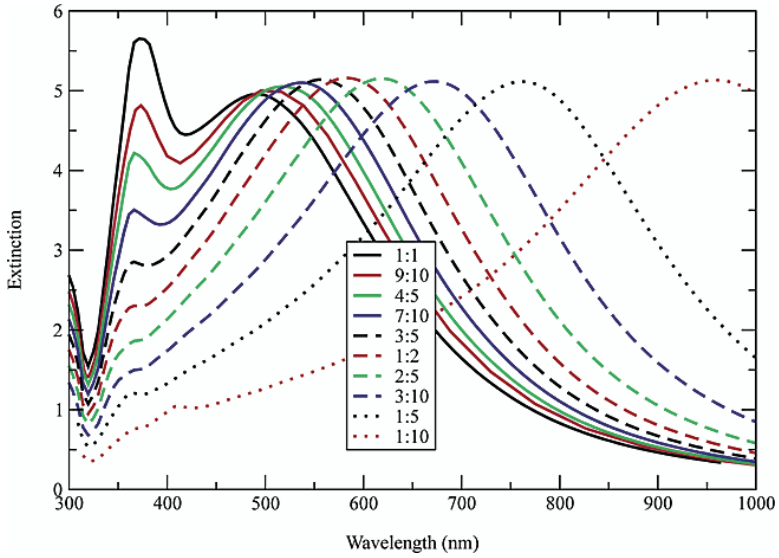

Figure 1.8. Calculation of the extinction spectra for spherical or oblate spheroid plasmonic nanocrystals. All nanocrystals have the same volume as a sphere with radius of 80 nm. The polarization was chosen to be along the major axis of the spheroid, and the extinctions were normalized accordingly. The ratios shown are between the major and minor axes of an oblate spheroid. Copyright 2003 American Chemical Society.[19]

In addition, Figure 1.9 shows a plot of DDA-simulated spectra where the corner truncation of a triangular plate results in the LSPR peak being blue-shifted.[19] In these cases, the distance at which the primary plasmonic resonance occurs affects the plasmonic frequency, leading to a red-shift and a blue-shift, respectively. Overall, UV-vis spectroscopy is useful to quickly monitor experimental progress, and to supplement the

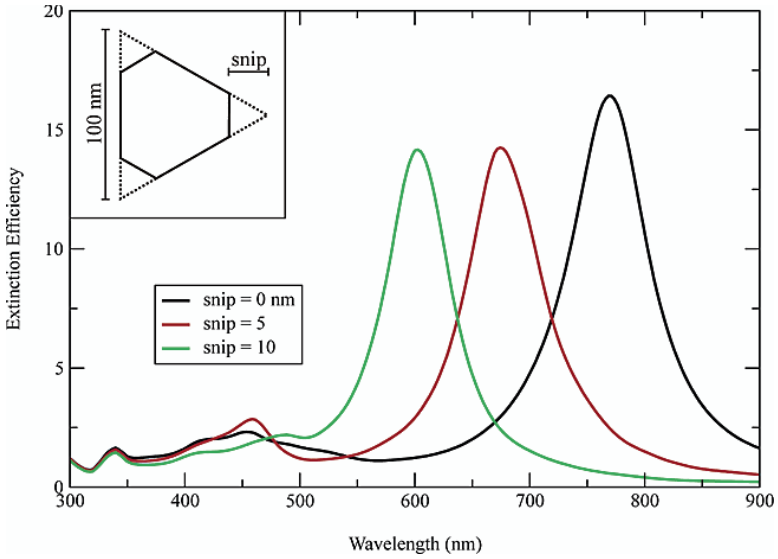

Figure 1.9. Plot of the discrete dipole approximation of the extinction spectra for trigonal prisms with 100 nm edge length and 16 nm thickness having "snips" of 0 (black), 5 (red), or 10 nm (green), respectively. As the length of the snip increases, the resonance peak shifts to lower wavelengths. Copyright 2003 American Chemical Society.[19]

data from other characterization tools discussed in Section 1.1.3.1 to ultimately elucidate the mechanistic details of each syntheses.

The SERS properties can be evaluated in the solution phase by first dispersing solid nanocrystals into a solution of probe molecules, such as 1,4-benzenedithiol (1,4-BDT), for functionalization. Afterwards, excess probe molecules were removed by washing the nanocrystals with DI water, and finally dispersed in a small volume of DI water. A small aliquot was withdrawn for each measurement and placed within a polydimethylsiloxane (PDMS) sample cell, which was then placed in the Renishaw inVia Raman spectrometer. Raman spectra were obtained using either the 532-nm or the 785-nm laser, depending on the nature of the sample. Figure 1.10 shows SERS spectra collected from the aqueous suspensions of either Ag nanocubes (black) or Ag@Ag-Au concave nanocubes (red), functionalized with 1,4-BDT. Compared to the Ag nanocubes, the Ag@Ag-Au concave

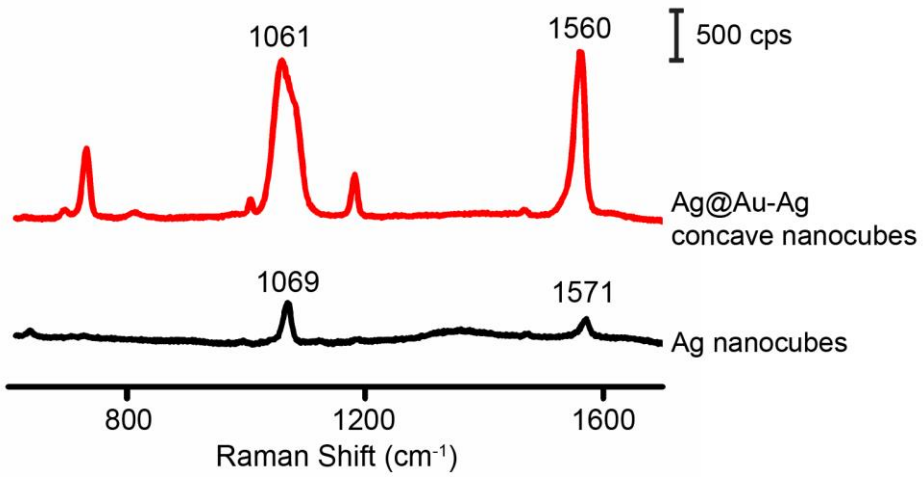

Figure 1.10. SERS spectra of 1,4-benzenedithiol (1,4-BDT) collected from either Ag nanocubes (black) or Ag@Ag-Au concave core-frame nanocubes (red) as the substrate, measured with an excitation wavelength of 785 nm. The Ag@Ag-Au concave nanocubes were prepared with 1.6 mL of 0.1 mM $HAuCl_4$ involved in the synthesis.

nanocubes show significant enhancement in the SERS signal,[86] controlled for the number of particles and the amount of 1,4-BDT involved. Also, upon the transformation from Ag nanocubes to Ag@Ag-Au concave nanocubes, one could observe a red-shift in the major peaks, specifically from 1571 to 1560 cm^{-1} and 1069 to 1061 cm^{-1}.

Catalytic properties of nanocrystals could be evaluated by using a UV-vis spectrophotometer for systems involving molecules with absorptions in the working wavelength range. In particular, one could implement the Au-catalyzed reduction of 4-nitrophenol (4-NP) to 4-aminophenol (4-AP) by $NaBH_4$ as a model reaction. In the presence of $NaBH_4$, the 4-NP would spontaneously transform into the 4-nitrophenolate ion, which exhibits a strong absorption at 400 nm. Upon the addition of $NaBH_4$ in the presence of the catalyst, the NO_2 group of the nitrophenolate ion reduces to NH_2, forming the 4-AP species with a weak absorption around 300 nm and no signal at 400 nm. Therefore, one could track the decrease in the absorbance signal at 400 nm to monitor the progression of

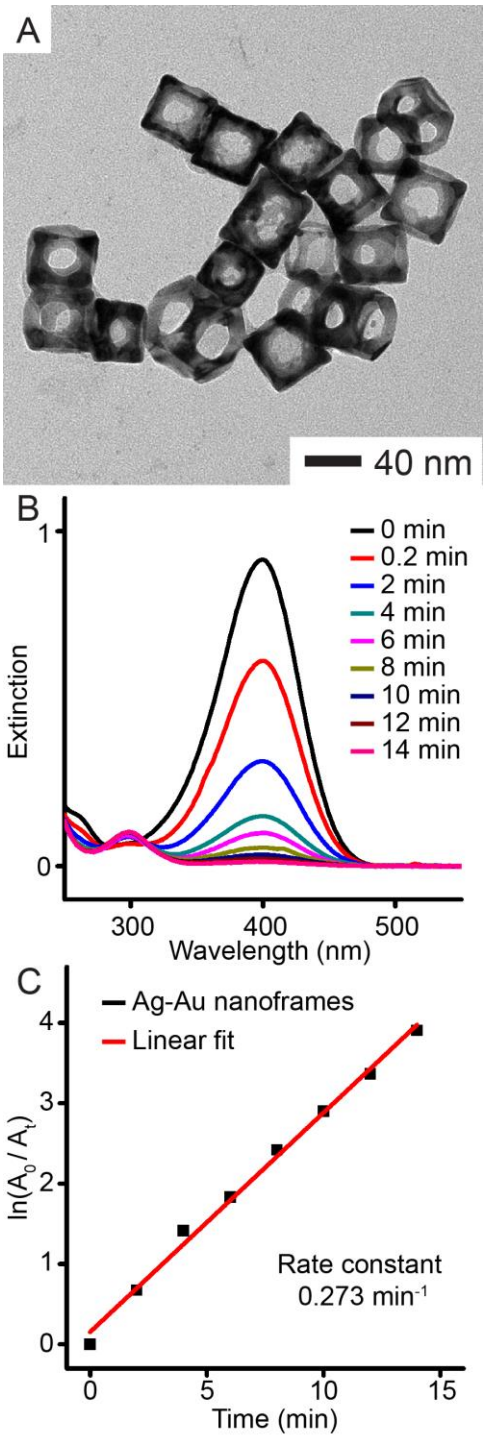

Figure 1.11. (A) TEM image of 10-nm thick Ag-Au nanoframes used as the catalyst for the reduction of 4-NP. (B) UV-vis spectra of 4-NP collected every 2 min after adding the Ag-Au nanoframes and $NaBH_4$ into the solution. (C) Plot of the natural log of extinction values normalized to the original value as a function of time. The linear trendline shows good fitting ($R^2 = 0.994$), and the first-order rate constant was calculated to be 0.273.

the reaction. For example, this setup could be used to evaluate the catalytic property of 10-nm thick Ag-Au nanoframes (Figure 1.11A), derived from the Ag@Ag-Au concave nanocubes (see Chapter 2 for detailed synthesis) upon selective removal of Ag with H_2O_2. Figure 1.11B shows time-dependent UV-vis spectra of the 4-nitrophenolate ion in $NaBH_4$ before (black) and after (color) the addition of the Ag-Au nanoframes. By t=14 min, the UV-vis shows no sign of the 4-nitrophenolate species, indicating the reaction had completed. Figure 1.11C plots the $\ln(A_0/A_t)$ values (computed from the extinction values at 400 nm) as a function of time. The data showed a good linear fit, indicating that the reaction progressed according to first-order kinetics with a rate constant of 0.273 min^{-1}. To draw meaningful conclusions, however, it would be necessary to perform comparative studies with other samples while also controlling for the relative number of particles and/or the specific surface area.

1.2. Rational Synthesis of Noble Metal Nanocrystals

1.2.1 Nucleation and Growth of Metal Nanocrystals

In general, there are two approaches to the fabrication of nanostructures. The first is a "top-down" approach, in which atoms are removed from an initial bulk material until nanometer sizes are reached. While this approach can accurately produce nanocrystals of desired morphologies, the prohibitive cost and slow rate of production discourages its use for industrial settings. The alternative is a "bottom-up" approach, which relies on the self-assembly of atoms into nanometer-sized crystals and has a significant advantage over the top-down approach with respect to cost and time. Most often, a colloidal method is used over a template-assisted method to maximize the throughput. In a typical colloidal

synthesis, a metal precursor of choice is dissolved to yield the metal cations, which are reduced by a reducing agent into zerovalent metal atoms. Through thermodynamic driving forces and an optional kinetic control, metal atoms first cluster to form homogeneous seed particles and subsequently deposit onto them for further growth, eventually generating nanocrystals. Stabilizing molecules are added to enhance the stability of the colloid by preventing nanocrystals from aggregating. The challenge is to accurately manipulate the thermodynamics and kinetics to be able to produce nanocrystals optimized for respective applications.

The two critical stages in the synthesis of nanocrystals that define the morphology of the final product are nucleation and growth. The LaMer model serves as a guide to understanding how the seed particles are generated, or "nucleated," in the absence of any pre-formed nucleation sites.[87, 88] Figure 1.12 shows the model plotting the concentration

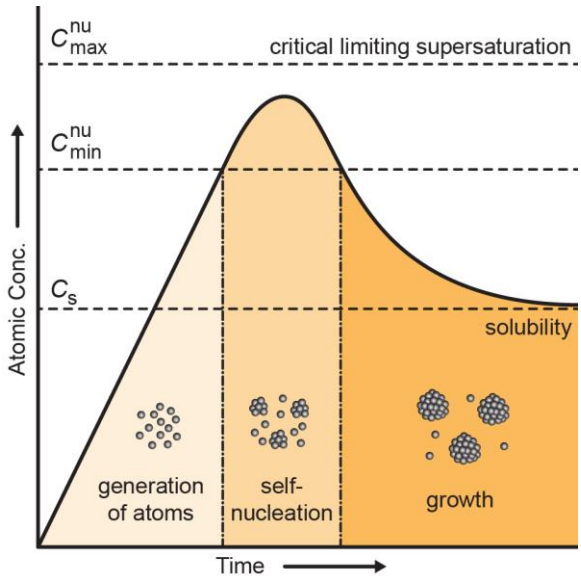

Figure 1.12. LaMer model of nucleation showing the atomic concentration as a function of time, indicating the stages of reaction where atoms are generated, where atoms cluster to form nuclei, and where the nuclei grows into larger nanocrystals. Adapted from Ref 87. Copyright 1950 American Chemical Society.[87]

of single atoms in the solution as a function of time, assuming atoms are continuously produced by reducing the metal precursors. There exists a critical atomic concentration above which single atoms are consumed to cluster into nuclei, and the atomic concentration starts to show negative curvature and an eventual decrease. While any types of nuclei can be formed in this stage, oxidizing agents may be involved in the reaction to selective remove nuclei with prominent defects such as twin boundaries.[89] Afterwards, newly generated metal atoms will be deposited onto the nuclei, or "grow," instead of forming new nuclei themselves, and the LaMer model indicates this behavior as the atomic concentration having equilibrated to a constant value. The growth process is affected by the free energies of each of the surfaces present on a nanocrystal.[90] In fact, for a face-centered cubic (FCC) metal such as Ag, Au, and Pt, the most thermodynamically stable morphology is the Wulff polyhedron, a type of truncated octahedron bounded by a mix of {100} and {111} surfaces as well as some {110} surfaces at the edges, because this morphology minimizes the total surface energy of a bare FCC nanocrystal. When surface energies are modified by using ligands that could bind to the metal surface, the morphology of the final product will be different. The Wulff plot shows that the surface with lower energy will dominate the surface of the final product.[91]

One can think of another scenario for the synthesis of nanocrystals, where previously formed nanocrystals are added into the growth solution as heterogeneous templates, otherwise known as "seed-mediated growth". There are four considerations for a successful seed-mediated growth. First, the equilibrium deposition mode could be a layer-by-layer growth in case of high wettability (Frank-van der Merwe mode), island growth in case of low wettability (Volmer-Weber mode), or a mix of both characters (Stranski-Krastanov

mode), depending on the surface energies and lattice mismatch across the interfaces created between the seed, the deposited metal, and the solvent.[92, 93] While kinetic barriers may hinder the system from reaching equilibrium, increasing the temperature can encourage the surface diffusion of atoms, allowing the system to reach the equilibrium deposition mode. Second, the deposition could either be site-selective or conformal, depending on the surface chemistry of the seed and between the seed and the deposited metal.[93, 94] For conditions where there is small lattice mismatch between the seed and the deposited metal, the seed is more electronegative, and the inter-elemental bond energy is higher than the bond energies of each element, it is observed that the deposition is conformal. Otherwise, the deposition favors sites with higher surface energy and avoids sites bound with capping agents. As such, it becomes important to understand and use different capping agents to appropriately modify the surface energies of the seeds. Third, changing the relative rates of atomic deposition and surface diffusion will affect the final morphology of the product.[93] When the deposition rate is much faster than the diffusion rate, a deposited atom will not have time to relocate to other surfaces on the seed before other atoms are deposited on top of them, resulting in the atoms "piling up" at the initial deposition sites. It follows that the rate at which the precursor is introduced to the solution with respect to the solution temperature becomes critical in determining the morphology of the nanocrystal. Lastly, when the deposited metal has a higher electrochemical potential then that of the seed, the seed could suffer from galvanic corrosion and lose its original morphology as the deposition continues. For example, when depositing Au onto Ag seeds, three Ag atoms will be oxidized for every atom of Au deposited, resulting in an overall loss of mass in the nanocrystals.[95, 96]

1.2.2 Rational Synthesis of Multimetallic Nanocrystals Through Facet-Selective Etching and Deposition

Facet-selective etching and deposition, as determined by the landscape of surface energy, represent two powerful methods for the transformation of noble-metal nanocrystals into nanostructures with complex shapes or morphologies.[97] In general, etching refers to an electrochemical process, in which metal atoms are oxidized by an oxidant and dissolved as cations. When the surface atoms are located on distinctive facets of a nanocrystal, they will exhibit different surface energies and thus differ in reactivity.[98] Generally, the atoms located on the facets with the highest surface energy are the most susceptible to etching, and the surface energies may be modified by using specific ligands. Because the etching rates would be different for each facet, a nanocrystal could be carved into various unique morphologies.[99, 100] On the other hand, pre-formed nanocrystals can be used as seeds for the deposition of metal atoms (same or different element as the seed) through heterogeneous nucleation and growth to transform into larger nanocrystals.[23, 101-104] The deposition of atomic species would preferentially occur on the crystallographic facets with the highest surface energy, leading to a faster rate of growth in the direction perpendicular to these facets, and therefore resulting in the elimination of these facets from the final product which would minimize the total surface energy. Considering that the deposited adatoms can diffuse across the seed nanocrystal surface during the growth process, one can tune the rates of deposition and surface diffusion to tailor the shape of the resultant nanocrystal.[105] Notably, etching can be coupled with deposition to remove atoms from some facets while adding atoms to other facets in an orthogonal manner.[106-109] If the rate of etching is higher than that of deposition, a solid nanocrystal can be transformed into a

hollow, porous and/or frame-like structure. In comparison, when growth prevails over etching, the nanocrystal would become larger and have concaved side faces.

1.2.2.1 Facet-Selective Etching versus Deposition

Yang and co-workers demonstrated that the surface energy landscape could guide the facet-selective etching of Ag octahedral nanocrystals.[99] Figure 1.13A shows a schematic diagram illustrating how a Ag octahedron is transformed into a series of nanocrystals with hollow and branched structures by preferentially etching Ag from {100} facets with a weak etchant. In a typical process, a mixture of NH_4OH and H_2O_2 was introduced into an aqueous solution of poly(vinylpyrrolidone) (PVP) under vigorous stirring at 4 ^oC, followed by the addition of Ag octahedrons in an ethanol suspension. The etching rates along the {111} and {100} directions could be controlled by varying the concentration of the etchant. Figure 1.13B shows SEM image of the Ag octahedra. When the concentration of the etchant was low, Figure 1.13C shows the selective etching of Ag from {111} facets for the generation of nanostructures with hollow side faces. As the concentration of the etchant was increased, Figure 1.13, D and E, indicates the predominant etching from the {100} facets for the formation of eight distinctive arms and then octapods, respectively. Taken together, it is feasible to select an etchant with an optimal etching power to facilitate facet-selective etching for the fabrication of nanocrystals with complex morphologies and tunable plasmon resonances. It has been demonstrated that these etched particles can serve as sensitive SERS substrates for chemical sensing.

On the other hand, Xia and co-workers explored the role of surface energy in directing facet-selective deposition of Ag cubic nanocrystals. In one study, they

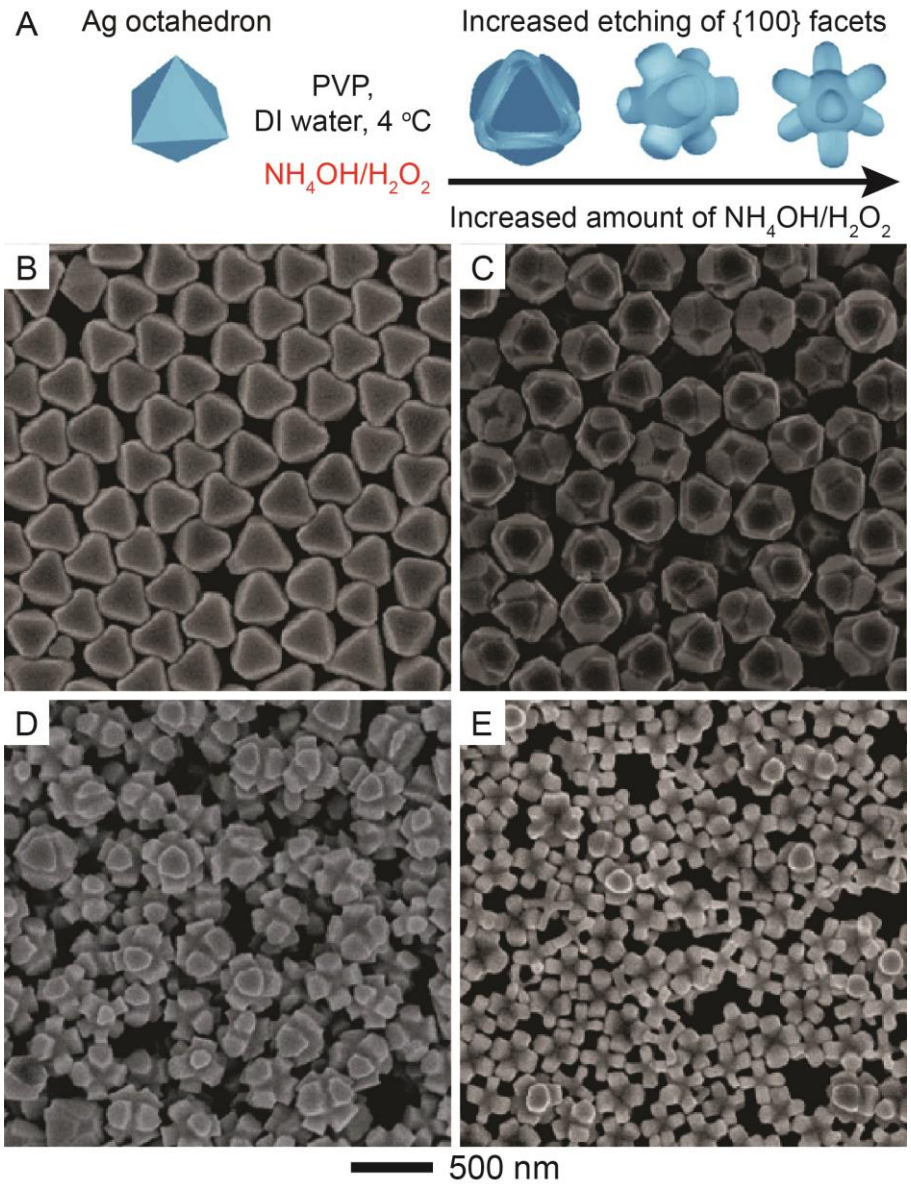

Figure 1.13. (A) Schematic illustration showing the transformation of a Ag octahedron into various types of nanostructures through selective etching of Ag from the {111} and {100} facets. SEM images of (B) Ag octahedrons and (C-E) the resultant nanostructures after etching with an increased amount of NH_4OH/H_2O_2 in the presence of PVP. Copyright 2011 American Chemical Society.[99]

demonstrated that the surface energies of {100} and {111} facets on the surface of Ag nanocubes could be maneuvered by introducing ionic species such as Cu(II) to control the deposition of Ag on different types of facets.[110] Figure 1.14A illustrates the two pathways

proposed to account for the evolution of a Ag nanocube into nanocrystals with different morphologies depending on the absence or presence of $Cu(NO_3)_2$ in the reaction solution. In a typical synthesis, aqueous $AgNO_3$ was titrated into an aqueous suspension of Ag nanocubes with slight truncation at corners and then reduced by ascorbic acid (H_2Asc) under ambient conditions. When $Cu(NO_3)_2$ was absent from the reaction solution, the surface energy of {100} facets was greater than that of {111} facets, $\gamma_{(100)} > \gamma_{(111)}$. As such, the Ag atoms derived from the reduction of $AgNO_3$ by H_2Asc were preferentially deposited on {100} to accelerate their growth along <100> directions for the eventual elimination of these facets on the final products.[111] More interestingly, when H_2Asc was used at a sufficiently high concentration, the deposition rate of Ag atoms would surpass the diffusion rate of Ag adatoms, evolving each {100} facet into a concaved surface.[105] Figure 1.14, B-D, shows SEM images of the products. Alternatively, when $Cu(NO_3)_2$ was present in the reaction system, the Cu(II) ions could selectively cap the {100} facets, reversing the order of the surface energies to $\gamma_{(111)} > \gamma_{(100)}$ and promoting the deposition of Ag on {111} facets. Figure 1.14, E-G, shows SEM images of the resultant concave cubes, octapods, and trisoctahedrons, respectively. When tested as SERS substrates, the concave octahedrons and trisoctahedrons were more active than the conventional Ag octahedrons with a similar size but covered by flat faces.

The facet-selective deposition and etching was also investigated with the use of Ag nanocubes, and it was identified that these two processes could follow the opposite pathways.[112] Figure 1.15A shows a schematic illustration describing the transformation of a Ag nanoplate into a twinned cube and its reverse process that involves etching with H_2O_2 locally produced through enzymatic oxidation of glucose. In the first step, citrate-free Ag

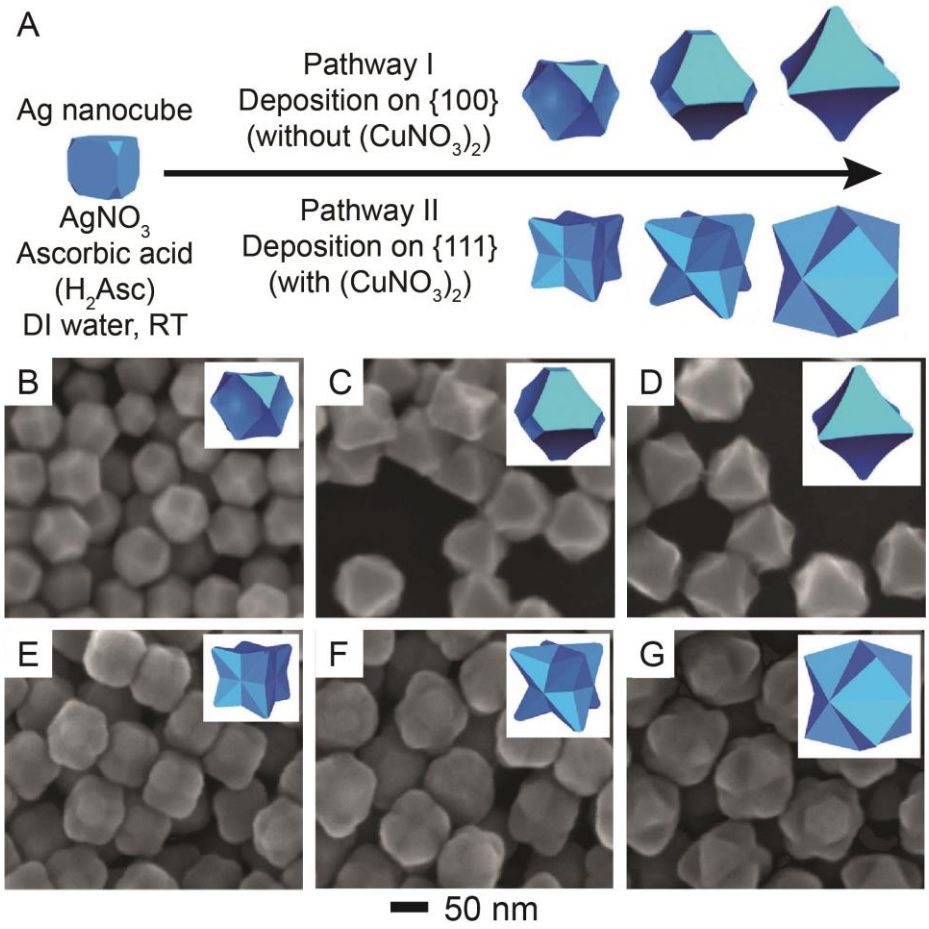

Figure 1.14. (A) Schematic illustration showing the transformation of a Ag nanocube with truncation at corners into a concave octahedron or a trisoctahedron through selective deposition of Ag on the {100} or {111} facets, respectively. SEM images showing the transformation of Ag nanocubes into (B-D) concave octahedrons and (E-G) trisoctahedrons after adding different amounts of aqueous $AgNO_3$ into a mixture of Ag nanocubes and H_2Asc in the absence and presence of $Cu(NO_3)_2$, respectively. The inset shows a model of the corresponding structure. Copyright 2011 Wiley-VCH Verlag GmbH & Co.[110]

nanoplates were synthesized according to published protocol[113] and then re-dispersed in an aqueous solution containing H_2Asc and PVP. When aqueous $HAuCl_4$ was introduced, the $AuCl_4^-$ ions could be reduced by both Ag and H_2Asc for the generation of Au atoms through galvanic replacement and chemical reduction, respectively, followed by their deposition on the Ag nanoplates for the production of Ag-Au nanoframes. On the other hand, the Cl^- ions originating from $AuCl_4^-$ could selectively bind to the {100} facets

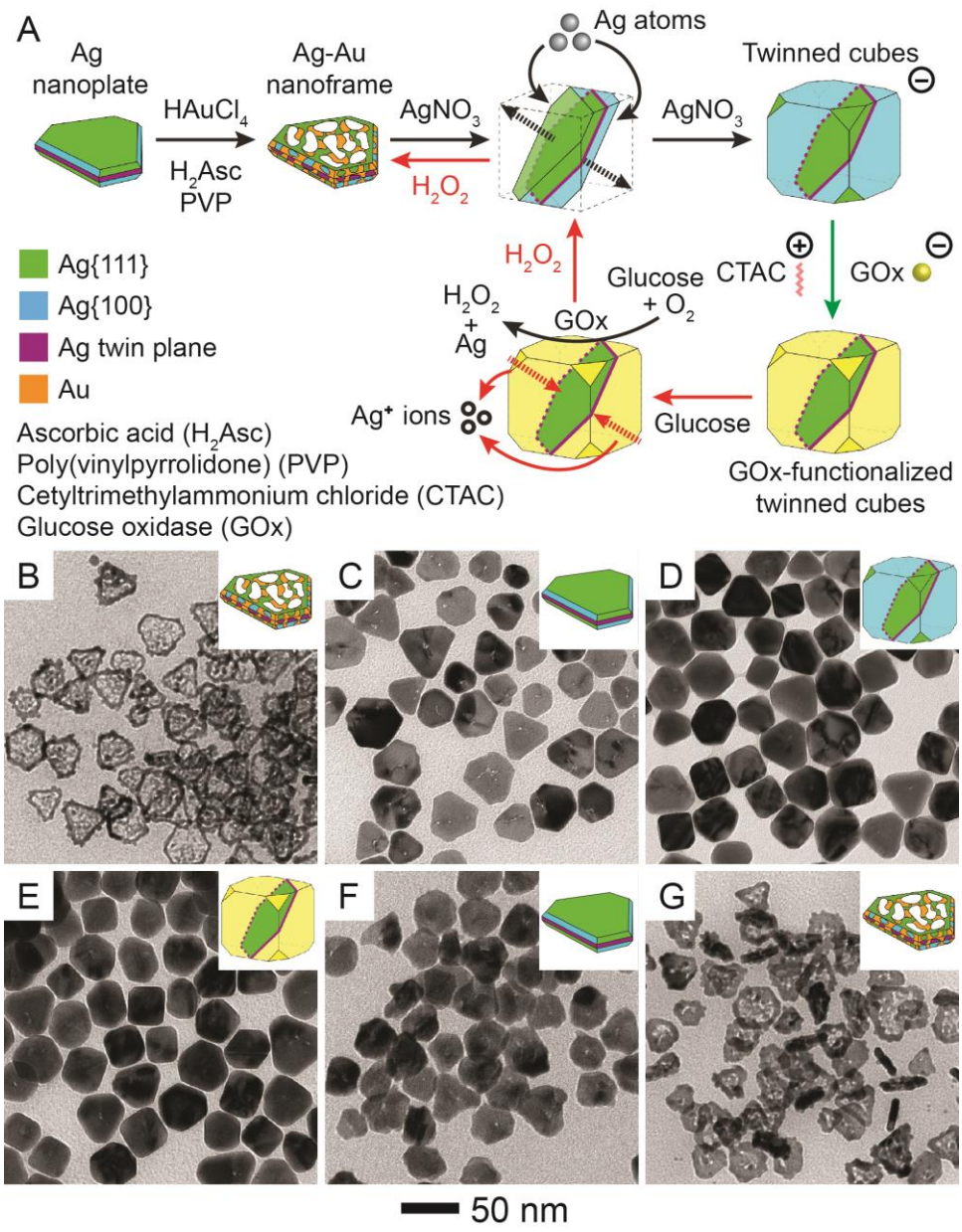

Figure 1.15. (A) Schematic illustration of site-selected growth of a citrate-free Ag nanoplate into a twinned cube, followed by site-selected etching by enzymatic H_2O_2 along the reversed direction of growth. (B-D) TEM images of the products obtained during the growth of Ag nanoplates in an aqueous solution of $HAuCl_4$, H_2Asc, and PVP, followed by the titration of aqueous $AgNO_3$ at volumes of (B) 0 mL, (C) 0.8 mL, and (D) 1.5 mL, respectively. (E-G) TEM images of (E) GOx-functionalized Ag twinned cubes and two samples after adding the glucose solution at (F) 15 min and (G) 60 min, respectively. The inset shows the corresponding model for each nanocrystal. Copyright 2016 American Chemical Society.[112]

(side edges) of the Ag nanoplate to lower the surface energy for attaining $\gamma_{(111)} > \gamma_{(100)}$.[114, 115] Under this circumstance, upon the titration of $AgNO_3$ into the reaction solution, the Cl^- ions, rather than the Au atoms, directed the deposition of Ag atoms derived from the reduction of $AgNO_3$ by H_2Asc onto {111} facets, transforming Ag nanoplates with a hexagonal shape into twinned cubes with truncated corners. Figure 1.15, C and D, shows TEM images of the products that were obtained at different stages of the growth process.

In the second step, the enzymatically derived H_2O_2 could consecutively remove the Ag atoms located at the two high-energy {111} facets parallel to the twinned plane of the Ag twinned cubes through oxidative etching by following a pathway opposite to deposition. In a typical process, the as-obtained Ag twinned cubes were functionalized with cetyltrimethylammonium chloride (CTAC) to change the surface charge from negative to positive, making it possible to adsorb the negatively charged glucose oxidase (GOx). Because GOx can catalyze the oxidation of glucose by O_2 to produce gluconic acid and H_2O_2,[116-118] one can control the amount of glucose involved in the reaction system to produce enzymatic H_2O_2 on the surface of the particles for the etching of Ag atoms with selectivity determined by surface energy. As shown in Figure 1.15E, there was no change to the morphology of the sample before the addition of glucose. Figure 1.15, F and G, shows TEM images of the particles after the introduction of glucose at time points of 15 and 60 min, respectively, indicating the transformation of twinned cubes into nanoplates and then nanoframes in a sequential manner. Altogether, these results confirm that the growth and etching processes essentially share the same mechanism that relies on the relative surface energies of different facets.

In summary, the facet selective etching versus deposition are two independent

processes for the generation of complex nanostructures. It has been demonstrated that both strategies rely on the surface energies of nanocrystal facets to promote either the dissolution of atoms from the original templates or the growth on the nanocrystal seeds, leading to the further increase in the diversity of nanocrystal morphologies for their expanded scope of applications.

1.2.2.2 Coupling Site-Selective Etching with Deposition

Though there have been successes through facet-selective etching or deposition, the combination of these two processes opens up even more new opportunities. For example, Xia reported a method that combined etching with deposition (regrowth) for the transformation of Pd nanocubes of a single size into Pd octahedrons with different edge lengths.[119] A typical experiment was carried out using HCl/O_2 as an oxidative etchant,[120] together with triethylene glycol (Tri-EG) serving as a reducing agent. Because the {100} facets on a Pd nanocube were capped by chemisorbed Br^- ions,[121] Pd atoms were selectively removed from the {111} facets at corner sites during oxidative etching and the resultant Pd(II) ions were then reduced and deposited back onto the nanocube, but preferentially on the {100} facets. By varying the amount of HCl added into the reaction system, it was feasible to control the ratio between the rates for etching and regrowth. At a large amount of HCl, etching was in dominance, resulting in the formation of Pd octahedrons with an edge length about 70% of that of the nanocubes. When HCl was used at a small amount, all the newly formed Pd(II) ions could be reduced and deposited back onto the Pd nanocube. In this case, the resultant Pd octahedron had roughly the same volume as that of the starting nanocube due to the balance between etching and regrowth so that the edge length was

about 130% of that of the nanocube. When the amount of HCl was in between, the resultant Pd octahedrons would take an edge length between these two values. This work not only demonstrates the importance of both etching and regrowth in the formation of metal nanocrystals but also offers a simple method for controlling both the shape and size of metal nanocrystals.

Jin, Yin, and co-workers explored the transformation of solid nanocrystals with well-defined shapes into nanoframes by integrating facet-selective etching with deposition.[122] Figure 1.16A illustrates the mechanism responsible for the generation of an octahedral nanoframe. In a typical synthesis, Pd octahedrons were dispersed in a N,N-dimethylformamide (DMF) solution containing potassium iodide (KI), formaldehyde (HCHO), and PVP. After the reaction vessel was vacuumed and then filled with a certain volume of pure O_2 gas, it was held at 100 ^{o}C for 1 h. In the reaction system, the O_2/I^- pair served as an etchant to remove Pd atoms from the octahedron through oxidative etching while HCHO acted as a reducing agent to reduce the dissolved Pd(II) ions back into Pd atoms for their subsequent re-deposition onto the octahedron. By increasing the concentration of HCHO to increase the reducing power, it was possible to maneuver the rates of oxidative etching and deposition, $R_{etching}$ and $R_{deposition}$, on the faces, edges, and corners of the octahedron, respectively. When $R_{deposition}$ became smaller than $R_{etching}$ on the side faces while it was comparable to $R_{etching}$ along the edges and corners, the removal of Pd atoms would be predominantly located on the side faces but largely suppressed at the edges and corners, leading to the conversion of an octahedron into a Pd octahedral nanoframe. In fact, this concept can be applicable to Pd nanocrystals with different shapes. Figure 1.16, B-E, shows TEM images of the resultant Pd nanoframes that were derived

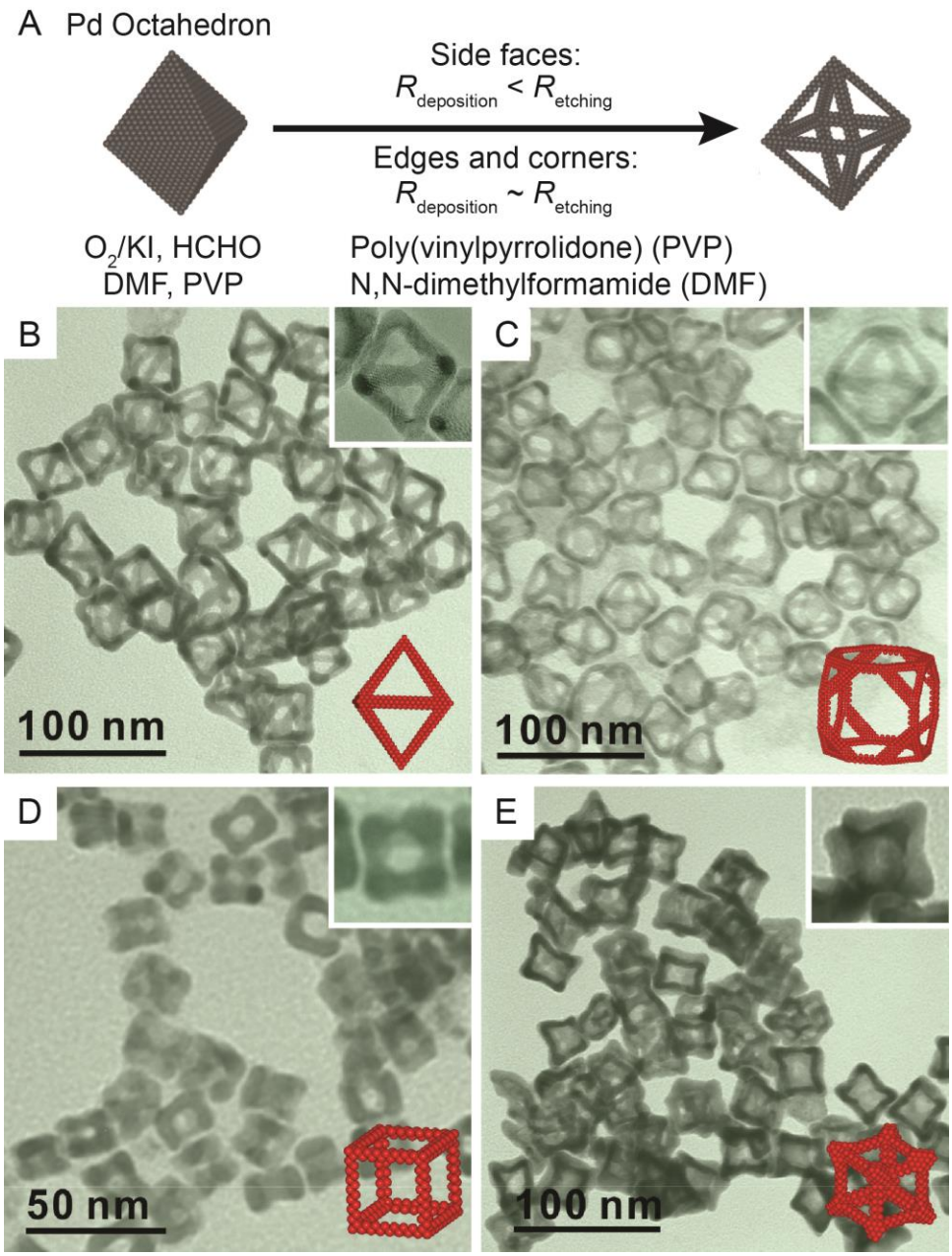

Figure 1.16. (A) Schematic diagram elucidating the transformation of a Pd octahedron into an octahedral nanoframe as a result of comparable deposition and etching rates along the edges and corners of the octahedron and a higher etching rate along the faces. (C-E) TEM images (with a representative model in the inset) of various types of Pd nanoframes derived from (B) octahedra, (C) cuboctahedra, (D) nanocubes, and (E) concave nanocubes, respectively, using the standard protocol. Copyright 2017 American Chemical Society.[122]

from Pd octahedra, cuboctahedra, nanocubes, and concave nanocubes, respectively. In conclusion, coupling site-selective etching with deposition provides an opportunity to transform solid nanocrystals to nanoframes by simply controlling the rates of etching and deposition on different facets of nanocrystal templates. This facile and versatile approach could become the mainstream for the creation of large fraction of atoms on the active sites of nanoframes for applications in catalysis.

1.2.2.3 Integrating Etching with Deposition through Galvanic Replacement

Galvanic replacement offers another opportunity to integrate oxidative etching with deposition for the transformation of solid nanocrystals of various shapes into complex nanostructures.[123-128] It is an electrochemical process for the deposition of metal *A* on the surface of a template made of a more reactive metal *B*. For example, when Ag nanocubes are mixed with a gold precursor such as $HAuCl_4$ in an aqueous solution, Ag will be dissolved (partially or completely) through oxidation while Au atoms derived from the reduction by Ag will be deposited on the surface of the nanocubes, leading to the production of hollow nanostructures comprised of Ag-Au alloys with tunable LSPR peaks in the range of 500 nm to 1200 nm.[25, 129] Likewise, Ag nanocubes could react with Na_2PdCl_4 or K_2PtCl_4 for the generation of Ag-Pd or Ag-Pt bimetallic hollow nanostructures with tunable compositions and interesting catalytic properties.[130-133]

In addition to the fabrication of hollow or porous nanostructures, galvanic replacement has also been explored for the fabrication of bimetallic nanocrystals with a concaved structure. The success relies on the ability to control oxidative etching of atoms from specific facets of nanocrystals while the deposition of another metal would occur on

the other facets in an orthogonal manner. To this end, Xia and co-workers demonstrated the transformation of Pd nanocubes into Pd-Pt concave nanocrystals by leveraging the surface capping of Br^- ions toward the {100} facets of Pd nanocubes.[134] In a typical process, as illustrated in Figure 1.17A, the as-prepared Pd nanocubes are dispersed in an aqueous solution of KBr and PVP, followed by the titration of aqueous H_2PtCl_6 at 90 °C. It was hypothesized that the added Br^- ions would play dual roles in this synthesis. Firstly, Br^- ions would preferentially bind to the {100} facets of the Pd, making these sites more susceptible to dissolution through an oxidation reaction.[121] On the other hand, the Br^- ions would undertake ligand exchange with $PtCl_6^{2-}$ for the formation of $PtBr_6^{2-}$ ions because of the favorable binding constant.[135] Under this circumstance, the Pt atoms derived from the reduction of Pt(IV) by Pd would be deposited on the corners, {111} facets, nanocubes in a fashion orthogonal to etching, leading to the formation of Pd-Pt concave nanocubes. As the replacement reaction continues, the concave nanocubes were further transformed into octapods with concave surfaces. Figure 1.17, B-E, shows TEM images of the products after Pd nanocubes had reacted with a Pt(IV) precursor for different periods of time. In the early stage, Figure 1.17B shows that the cubic morphology was essentially preserved but there was a slight change to the degree of corner truncation due to the oxidative etching enabled by the pair of Cl^-/Br^- ions and dissolved O_2 in the reaction solution.[136, 137] As the reaction progressed, Figure 1.17, C and D, shows that the side faces of the nanocubes became more concaved, suggesting the etching of Pd atoms from the {100} facets. At the end, Figure 1.17E shows the nanostructures after Pd atoms had been extensively removed from the side facets of the nanocubes while the resultant Pt atoms were deposited at the corners. Likewise, the same protocol was also extended to transform Pd octahedra and cuboctahedra into

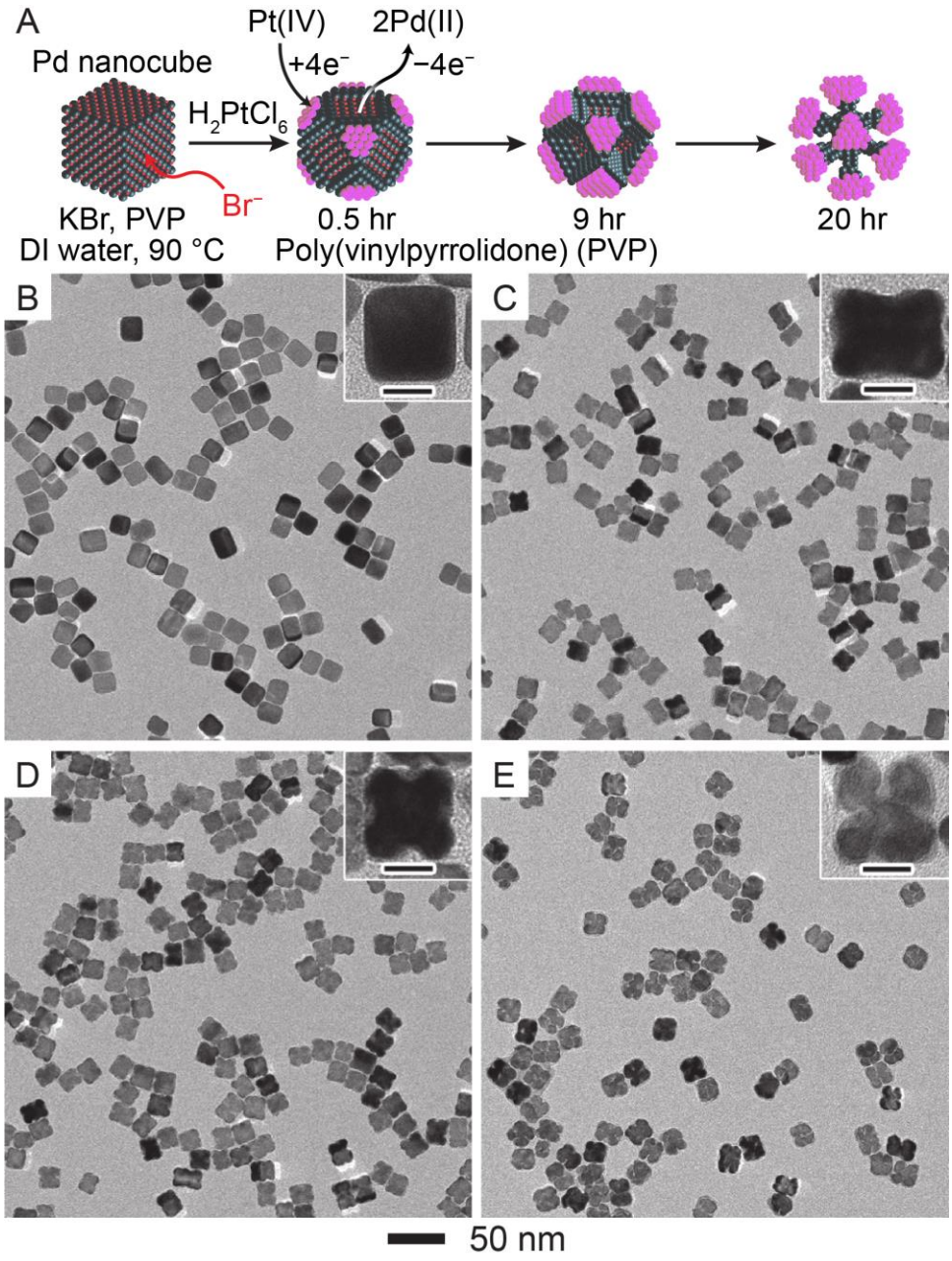

Figure 1.17. (A) Schematic diagram illustrating the transformation of a Pd nanocube into a Pd-Pt concave nanocube and octapod *via* galvanic replacement reaction between Pd atoms and Pt(IV) ions in the presence of Br^- ions to selectively cap the {100} facets. (B-E) TEM images of the resultant Pd-Pt nanocrystals obtained at (B) 0.5, (C) 4, (D) 9, and (E) 20 h, respectively, after the galvanic replacement reaction was initiated. Scale bars in the insets: 10 nm. Copyright 2011 American Chemical Society.[134]

conncave nanostructures by selectively etching Pd atoms from the {100} facets as accompanied by the deposition of Pt on the {111} facets in an orthogonal fashion. The Pd-Pt concave nanocubes with different weight percentages of Pt were also evaluated as electrocatalysts for the oxygen reduction reaction (ORR). Remarkably, the sample with 3.4 wt.% of Pt exhibited a large specific electrochemical surface area of 185.8 m^2/g_{Pt} and its mass activity toward ORR was almost four times as great as that of the commercial Pt/C catalyst. In summary, galvanic replacement reaction allows the integration of oxidative etching with deposition on the individual nanocrystals. It has been demonstrated that the lower surface energy facets could serve as an anode to carve atoms in the form of ions through oxidation while the deposition of metal would proceed in other facets in an orthogonal manner. In turn, galvanic replacement reaction offers a simple approach to produce octapods and concave nanostructures, in addition to its utility to fabricate hollow nanostructures and nanocages.

1.3 Motivation for Research

As evidenced by the above-mentioned case studies throughout this chapter, the past two decades have witnessed remarkable advancements in the shape-controlled synthesis for noble metal nanocrystals for various applications. In particular, template-assisted methods in the solution phase, such as seed-mediated growth, have been demonstrated as a versatile approach to engineer nanocrystals having specific shapes and compositions. Because of the peculiar structure-property relationship of nanomaterials, a meticulous control in the size, shape, and composition of nanocrystals could tailor their properties towards their optimal performance. However, there are several gaps in our collective

understanding of the fundamental principles underlying the different synthesis methods, making it challenging to synergize the different strategies. Part of the difficulty arises from the lack of a specific understanding of the roles of ligands involved in the colloidal syntheses of nanoparticles in achieving the facet-selective deposition and carving on the surfaces of nanocrystals. At the moment, researchers often rely on a trial-and-error approach to optimize the synthetic conditions. As discussed in Section 1.2.3, the galvanic replacement reaction offers a convenient solution that combines both the oxidative etching of the nanocrystal template and the reduction of metal ions followed by the deposition of metal atoms onto the template. The success to the shape-controlled transformation of a nanocrystal template via galvanic replacement relies on the ability to guide and confine the oxidation (dissolution) and/or reduction (deposition) half-reactions to specific sites on the surface of the template. In many cases, people documented that various ligands involved in the reaction solution would selectively interact with specific facets on the surface of the template nanocrystal to inhibit or promote the etching and/or deposition at that location. Unfortunately, it remains elusive to detect the binding of ligands to the surface of nanocrystals in a solution. To this end, it is of importance to develop a technique capable of probing the adsorption of organic molecules on the surface of nanoparticles *in situ*. The understanding of the interaction between ligands and the metal surface would provide additional insights for the development of the rational design and synthesis of complex-shape nanocrystals.

1.4 Scope of Research

The aim of this work is to develop the rational synthesis of noble metal nanocrystals

with a complex morphology and well-defined spatial distribution of elements. Specifically, I develop a methodology to combine the etching and growth processes on a Ag nanocrystal template for the generation of complex nanostructures with concave or hollow morphologies. My strategy relies on the use of two chemical reactions, the galvanic replacement reaction and chemical reduction, to integrate both the facet-selective oxidation (etching) and reduction (growth) reaction in an orthogonal manner. I demonstrate the importance in the use of different ligands to modify the etching and growth rates on various facets of nanocrystals in the reaction solution, and ultimately to control the facet-selective carving and deposition in an orthogonal manner. In this dissertation, I use Ag nanocubes as the building blocks for their transformation into bi- and tri-metallic nanostructures such as the Ag@Ag-Au core-frame nanocubes, the Ag-Au-M (M:Pt, Pd, Au) cage cubes, and the Ag-Au cuboctahedral nanoboxes, with a focus on the discussion of the mechanistic details underlying these transformations. I also develop the SERS-based *in situ* detection of the interactions between Ag and ligands in the solution for elucidating the competitive binding of thiol and isocyanide molecules on the Ag nanocubes.

In Chapter 2, I demonstrate the generation of Ag@Ag-Au concave core-frame nanocubes by titrating aqueous $HAuCl_4$ to an aqueous suspension of Ag nanocubes in the presence of H_2Asc, NaOH, and CTAC at an initial pH of 11.6 under ambient conditions. Completely different from all the previous studies involving PVP, the use of CTAC sends the reaction along an unusual pathway. The mechanism involves the co-deposition of Au and Ag atoms on the edges and corners of the Ag nanocubes while Ag atoms are concomitantly etched away from the side faces. Specifically, the added $HAuCl_4$ remains in the form of $AuCl_4^-$ under an alkaline condition, facilitating the galvanic replacement

reaction with the Ag nanocubes. Because Cl^- ions can selectively bind to the {100} facets of Ag nanocubes, one may argue that the dissolution of Ag atoms occurs from the side faces. The released Ag^+ ions can be retained in the soluble form of $AgCl_2^-$ by complexing with the Cl^- ions. Both the $AuCl_4^-$ and $AgCl_2^-$ are then reduced by $HAsc^-$ to generate Au and Ag atoms, followed by their preferentially co-deposition onto the edges and corners of Ag nanocubes. As the reaction progresses, Ag atoms located at the side faces of the nanocubes are continuously carved by the galvanic reaction while Ag and Au atoms are increasingly deposited on the edges and corners, leading to the generation of Ag@Ag-Au core-frame nanocubes with concave side faces. The concave nanocrystals show much stronger SERS activity at 785 nm excitation, making it feasible to monitor the Au-catalyzed reduction of 4-nitrothiophenol by $NaBH_4$ *in situ*. Furthermore, the concave nanocrystals could be transformed into Ag-Au nanoframes with controllable ridge thicknesses upon the removal of Ag in the core.

In Chapter 3, I develop a general methodology based on galvanic replacement for the fabrication of nanoscale, multi-metallic, cage cubes by drilling through all the side faces of Ag nanocubes. The key to the success is to align the intersected holes by confining the drilling to the center of each side face through the deposition of Ag-Au alloy frames along the corners and edges of Ag nanocubes. A typical fabrication involves the galvanic replacement reaction between Ag and a salt precursor by dispersing the aforementioned Ag@Ag-Au core-frame nanocubes (see Chapter 2) in an aqueous solution of CTAC, followed by the titration of an aqueous solution of the precursor under ambient conditions. At the early stage of reaction, because the Cl^- ions derived from CTAC could bind selectivity toward the Ag(100) surface, the oxidation of Ag is preferentially instigated from

the Ag-dominated regions located at the center of each side face of a nanocube for the creation of a cavity while the resultant metal atoms are deposited on the edges and corners in an orthogonal manner. In the case of H_2PtCl_6 precursor, the galvanic reaction proceeds through the production of one Pt atom at the expense of four Ag atoms. As such, Ag atoms will be carved away from the side faces in the form of Ag(I) ions for the generation of a much smaller number of Pt atoms. Because a thin layer of Ag-Au-Pt alloy tends to be formed on the surface, including the areas around cavities but not inside the cavities, it is possible to achieve continuous removal of Ag towards the center of a core-frame nanocube for its ultimate transformation into a cage cube comprised of a Ag-Au-Pt alloy and characterized by three orthogonal, intersected holes. The same strategy also works for other salt precursors, including Pt(II), Pd(II), and Au(III), but the size of the holes may vary depending on the stoichiometry involved in the galvanic replacement reaction.

In Chapter 4, I report the fabrication of Ag-Au cuboctahedral nanoboxes enclosed by {100} or {111} facets through the orthogonal deposition of Au on two different facets of Ag cuboctahedra. Specifically, one may rely on the use of a ligand such as PVP or CTAC in an aqueous suspension of Ag cuboctahedra containing an ascorbic acid and NaOH at the pH of 11.2, followed by the titration of aqueous $HAuCl_4$. In the case of PVP, the oxidation of Ag would be initiated on the {111} facets through the galvanic replacement reaction between Ag and Au(III) for the deposition of Au the {100} facets of Ag cuboctahedra. Because the dissolved Ag(I) ions would react with NaOH to form Ag_2O on these {111} facets and thus terminate the galvanic reaction, the Au(III) ions would be further reduced by ascorbate monoanion ($HAsc^-$) to produce Au atoms for their continuing deposition on the {100} facets, converting Ag cuboctahedra to $Ag@Au_{\{100\}}$ cuboctahedra and then

cuboctahedral nanoboxes enclosed by the {100} facets after the etching of Ag. In contrast, when the CTAC was involved in the reaction, the oxidation of Ag through galvanic reaction would contiguously progress on the {100} facets as the dissolved Ag(I) ions would react with the excessive amount of Cl^- ions derived from CTAC to produce soluble $AgCl_2^-$ ions rather than Ag_2O. Under this circumstance, the dissolved Ag(I) ions and the Au(III) would be co-reduced by $HAsc^-$ for the generation of Ag and Au atoms, followed by their co-deposition on the {111} facets for the generation of $Ag@Au_{\{111\}}$ concave cuboctahedra and the resultant $Ag\text{-}Au_{\{111\}}$ cuboctahedral nanoboxes enclosed by {111} facets upon the removal of Ag. The as-obtained cuboctahedral nanoboxes exhibit strong optical properties in the infrared region. In particular, the cuboctahedral nanoboxes enclosed by the {111} facets embrace catalytic activities toward the reduction of 4-nitrophenol by $NaBH_4$.

In Chapter 5, I explore the use of *in situ* SERS to investigate the adsorption of different ligands on the surface of colloidal Ag nanocubes. In a typical process, the SERS spectra were collected at different time points from a mixture of Ag nanocubes and a ligand such as 4-nitrothiophenol (4-NTP), 4-aminothiophenol (4-ATP), or 1,4-phenylene diisocyanide (1,4-PDI) at a specific concentration. Time-dependent SERS spectra of 4-NTP indicate that the adsorption could be achieved within 3 min due to the strong binding of thiol to Ag surface. I also recorded the concentration-dependent SERS spectra of 4-NTP, from which I observed a red-shift for all peaks at a concentration of 10^{-7} M relative to the case 10^{-5} M or 10^{-4} M. I argue that such a red-shift could be attributed to the difference in molecular orientation, with the benzene ring oriented parallel to or tilting away from the surface at low and high concentrations, respectively. I confirmed that the adsorption kinetics of 4-ATP on Ag was similar to that of 4-NTP, although the SERS signals from 4-

ATP were much weaker due to the absence of chemical enhancement. Different from the case of thiol, 1,4-PDI would bind to a Ag surface through σ-donation, giving slower adsorption kinetics over a time scale of 60 min. At a concentration of 10^{-5} M and above, I observed both $\nu_{NC(free)}$ and $\nu_{NC(Ag)}$ peaks in the SERS spectra, suggesting that the 1,4-PDI molecules could be oriented with the benzene ring tilting away from the surface. I further evaluated the relative binding strength of the thiol and isocyanide groups toward Ag surface by dispersing Ag nanocubes in an ethanol solution containing both ligands. The SERS signals from 1,4-PDI were not detectable in either case when it was used at the same concentration as 4-NTP or 4-ATP at 10^{-5} M. However, the 1,4-PDI signals became detectable when its concentration was increased by 100 times relative to 4-NTP or 4-ATP. Collectively, these data indicate that the thiols have a much stronger binding to the surface on Ag nanocubes, making it possible to impede or even inhibit the adsorption of isocyanides.

1.5 Notes to Chapter 1

Parts of this chapter are adapted from the article "Transforming Noble-Metal Nanocrystals into Complex Nanostructures through Facet-Selective Etching and Deposition," a minireview published in *ChemNanoMat*,[138] the article "Site-Selective Carving and Co-Deposition: Transformation of Ag Nanocubes into Concave Nanocrystals Encased by Au–Ag Alloy Frames" published in *ACS* Nano,[86] the article "Fabrication of Nanoscale Cage Cubes by Drilling Orthogonal, Intersected Holes through All Six Side Faces of Ag Nanocubes" under revision for publication in *Chemistry of Materials*,[139] the article "Orthogonal Deposition of Au on Different Facets of Ag Cuboctahedra for the

Fabrication of Nanoboxes with Complementary Surfaces" published in *Nanoscale*,[140] and the article "Comparative Study of the Adsorption of Thiol and Isocyanide Molecules on Silver Surface by In Situ Surface-Enhanced Raman Scattering" published in the *Journal of Physical Chemistry C*.[141]

1.6 References

(1) Zhang, H.; Jin, M.; Xia, Y. Noble-Metal Nanocrystals with Concave Surfaces: Synthesis and Applications. *Angew. Chem. Int. Ed.* **2012,** *51*, 7656-7673.

(2) Burda, C.; Chen, X.; Narayanan, R.; El-Sayed, M. A. Chemistry and Properties of Nanocrystals of Different Shapes. *Chem. Rev.* **2005,** *105*, 1025-1102.

(3) Willets, K. A.; Van Duyne, R. P. Localized Surface Plasmon Resonance Spectroscopy and Sensing. *Annu. Rev. Phys. Chem.* **2007,** *58*, 267-297.

(4) Jain, P. K.; Huang, X.; El-Sayed, I. H.; El-Sayed, M. A. Noble Metals on the Nanoscale: Optical and Photothermal Properties and Some Applications in Imaging, Sensing, Biology, and Medicine. *Acc. Chem. Res.* **2008,** *41*, 1578-1586.

(5) Haes, A. J.; Haynes, C. L.; McFarland, A. D.; Schatz, G. C.; Van Duyne, R. P.; Zou, S. Plasmonic Materials for Surface-Enhanced Sensing and Spectroscopy. *MRS Bull.* **2005,** *30*, 368-375.

(6) Rycenga, M.; Cobley, C. M.; Zeng, J.; Li, W.; Moran, C. H.; Zhang, Q.; Qin, D.; Xia, Y. Controlling the Synthesis and Assembly of Silver Nanostructures for Plasmonic Applications. *Chem. Rev.* **2011,** *111*, 3669-3712.

(7) Zhang, Y.; Wu, Y.; Qin, D. Rational Design and Synthesis of Bifunctional Metal Nanocrystals for Probing Catalytic Reactions by Surface-Enhanced Raman Scattering. *J. Mater. Chem. C* **2018,** *6*, 5353-5362.

(8) Cobley, C. M.; Skrabalak, S. E.; Campbell, D. J.; Xia, Y. Shape-Controlled Synthesis of Silver Nanoparticles for Plasmonic and Sensing Applications. *Plasmonics* **2009,** *4*, 171-179.

(9) Shiohara, A.; Wang, Y.; Liz-Marzan, L. M. Recent Approaches Toward Creation of Hot Spots for SERS Detection. *J. Photochem. Photobiol. C: Photochem. Rev.* **2014,** *21*, 2-25.

(10) Albrecht, M. G.; Creighton, J. A. Anomalously Intense Raman Spectra of Pyridine at a Silver Electrode. *J. Am. Chem. Soc.* **1977,** *99*, 5215-5217.

(11) Jeanmaire, D. L.; Van Duyne, R. P. Surface Raman Spectroelectrochemistry: Part I. Heterocyclic, Aromatic, and Aliphatic Amines Adsorbed on the Anodized Silver Electrode. *J. Electroanal. Chem. Interfacial Electrochem.***1977,** *84*, 1-20.

(12) Haynes, C. L.; Van Duyne, R. P. Plasmon-Sampled Surface-Enhanced Raman Excitation Spectroscopy. *J. Phys. Chem. B* **2003,** *107*, 7426-7433.

(13) Peng, Z.; Yang, H. Synthesis and Oxygen Reduction Electrocatalytic Property of Pt-on-Pd Bimetallic Heteronanostructures. *J. Am. Chem. Soc.* **2009,** *131*, 7542-7543.

(14) Zhang, J.; Yang, H.; Fang, J.; Zou, S. Synthesis and Oxygen Reduction Activity of Shape-Controlled Pt_3Ni Nanopolyhedra. *Nano Lett.* **2010,** *10*, 638-644.

(15) Kongkanand, A.; Subramanian, N. P.; Yu, Y.; Liu, Z.; Igarashi, H.; Muller, D. A. Achieving High-Power PEM Fuel Cell Performance with an Ultralow-Pt-Content Core–Shell Catalyst. *ACS Catal.* **2016,** *6*, 1578-1583.

(16) Sanders, A. W.; Routenberg, D. A.; Wiley, B. J.; Xia, Y.; Dufresne, E. R.; Reed, M. A. Observation of Plasmon Propagation, Redirection, and Fan-Out in Silver Nanowires. *Nano Lett.* **2006,** *6*, 1822-1826.

(17) Mie, G. Beiträge zur Optik trüber Medien, speziell kolloidaler Metallösungen. *Ann. Phys. (Berl.)* **1908,** *330*, 377-445.

(18) Draine, B. T.; Flatau, P. J. Discrete-Dipole Approximation for Scattering Calculations. *J. Opt. Soc. Am. A* **1994,** *11*, 1491-1499.

(19) Kelly, K. L.; Coronado, E.; Zhao, L. L.; Schatz, G. C. The Optical Properties of Metal Nanoparticles: the Influence of Size, Shape, and Dielectric Environment. *J. Phys. Chem. B* **2003**, *107*, 668-677.

(20) Johnson, P. B.; Christy, R. W. Optical Constants of the Noble Metals. *Phys. Rev. B* **1972,** *6*, 4370-4379.

(21) Le Ru, E.; Etchegoin, P., *Principles of Surface-Enhanced Raman Spectroscopy: and Related Plasmonic Effects*. Elsevier: 2008.

(22) Wiley, B. J.; Im, S. H.; Li, Z.-Y.; McLellan, J.; Siekkinen, A.; Xia, Y., Maneuvering the Surface Plasmon Resonance of Silver Nanostructures through Shape-Controlled Synthesis. *J. Phys. Chem. B* **2006**, *110*, 15666-15675.

(23) Cobley, C. M.; Rycenga, M.; Zhou, F.; Li, Z.-Y.; Xia, Y. Controlled Etching as a Route to High Quality Silver Nanospheres for Optical Studies. *J. Phys. Chem. C* **2009,** *113*, 16975-16982.

(24) Tao, A. R.; Habas, S.; Yang, P. Shape Control of Colloidal Metal Nanocrystals. *Small* **2008,** *4*, 310-325.

(25) Kottmann, J. P.; Martin, O. J. F.; Smith, D. R.; Schultz, S. Plasmon Resonances of Silver Nanowires with a Nonregular Cross Section. *Phys. Rev. B* **2001,** *64*, 235402.

(26) Fuchs, R. Theory of the Optical Properties of Ionic Crystal Cubes. *Phys. Rev. B* **1975,** *11*, 1732.

(27) Dieringer, J. A.; Lettan, R. B.; Scheidt, K. A.; Van Duyne, R. P. A Frequency Domain Existence Proof of Single-Molecule Surface-Enhanced Raman

Spectroscopy. *J. Am. Chem. Soc.* **2007,** *129*, 16249-16256.

(28) Kneipp, J.; Kneipp, H.; Kneipp, K., SERS—a single-molecule and nanoscale tool for bioanalytics. *Chem. Soc. Rev.* **2008,** *37* (5), 1052-1060.

(29) Blackie, E. J.; Ru, E. C. L.; Etchegoin, P. G. Single-Molecule Surface-Enhanced Raman Spectroscopy of Nonresonant Molecules. *J. Am. Chem. Soc.* **2009,** *131*, 14466-14472.

(30) Van Duyne, R. P. Laser Excitation of Raman Scattering from Adsorbed Molecules on Electrode Surfaces. *Chemical and Biochemical Applications of Lasers.* Academic Press: 1979.

(31) McFarland, A. D.; Young, M. A.; Dieringer, J. A.; Van Duyne, R. P. Wavelength-Scanned Surface-Enhanced Raman Excitation Spectroscopy. *J. Phys. Chem. B* **2005,** *109*, 11279-11285.

(32) Le Ru, E.; Blackie, E.; Meyer, M.; Etchegoin, P. G. Surface Enhanced Raman Scattering Enhancement Factors: a Comprehensive Study. *J. Phys. Chem. C* **2007,** *111*, 13794-13803.

(33) Zhang, Y.; Liu, J.; Ahn, J.; Xiao, T.-H.; Li, Z.-Y.; Qin, D. Observing the Overgrowth of a Second Metal on Silver Cubic Seeds in Solution by Surface-Enhanced Raman Scattering. *ACS Nano* **2017,** *11*, 5080-5086.

(34) Rycenga, M.; Langille, M. R.; Personick, M. L.; Ozel, T.; Mirkin, C. A. Chemically Isolating Hot Spots on Concave Nanocubes. *Nano Lett.* **2012,** *12*, 6218-6222.

(35) Hong, J. W.; Lee, S.-U.; Lee, Y. W.; Han, S. W. Hexoctahedral Au Nanocrystals with High-Index Facets and their Optical and Surface-Enhanced Raman Scattering Properties. *J. Am. Chem. Soc.* **2012,** *134*, 4565-4568.

(36) Zhang, J.; Winget, S. A.; Wu, Y.; Su, D.; Sun, X.; Xie, Z.-X.; Qin, D. Ag@Au Concave Cuboctahedra: A Unique Probe for Monitoring Au-Catalyzed Reduction and Oxidation Reactions by Surface-Enhanced Raman Spectroscopy. *ACS Nano* **2016,** *10*, 2607-2616.

(37) Braun, G.; Pavel, I.; Morrill, A. R.; Seferos, D. S.; Bazan, G. C.; Reich, N. O.; Moskovits, M. Chemically Patterned Microspheres for Controlled Nanoparticle Assembly in the Construction of SERS Hot Spots. *J. Am. Chem. Soc.* **2007,** *129*, 7760-7761.

(38) Bell, S. E.; McCourt, M. R. SERS Enhancement by Aggregated Au colloids: Effect of Particle Size. *Phys. Chem. Chem. Phys.* **2009,** *11*, 7455-7462.

(39) Etchegoin, P. G.; Le Ru, E. C. A Perspective on Single Molecule SERS: Current Status and Future Challenges. *Phys Chem. Chem. Phys.* **2008,** *10*, 6079-7089.

(40) Sakurai, H.; Haruta, M. Synergism in Methanol Synthesis from Carbon Dioxide over Gold Catalysts Supported on Metal Oxides. *Catal. Today* **1996,** *29*, 361-365.

(41) Ueda, A.; Oshima, T.; Haruta, M. Reduction of Nitrogen Monoxide with Propene

in the Presence of Oxygen and Moisture over Gold Supported on Metal Oxides. *Appl. Catal. B Environ.* **1997,** *12*, 81-93.

(42) Andreeva, D.; Tabakova, T.; Idakiev, V.; Christov, P.; Giovanoli, R. Au/α-Fe_2O_3 Catalyst for Water–Gas Shift Reaction Prepared by Deposition–Precipitation. *Appl. Catal. A* **1998,** *169*, 9-14.

(43) Okumura, M.; Kitagawa, Y.; Yamagcuhi, K.; Akita, T.; Tsubota, S.; Haruta, M. Direct Production of Hydrogen Peroxide from H_2 and O_2 over Highly Dispersed Au Catalysts. *Chem. Lett.* **2003,** *32*, 822-823.

(44) Tan, L.; Li, L.; Peng, Y.; Guo, L. Synthesis of Au@Pt Bimetallic Nanoparticles with Concave Au Nanocuboids as Seeds and their Enhanced Electrocatalytic Properties in the Ethanol Oxidation Reaction. *Nanotechnology* **2015,** *26*, 505401.

(45) Wang, S.; Jiang, S. P.; Wang, X.; Guo, J. Enhanced Electrochemical Activity of Pt Nanowire Network Electrocatalysts for Methanol Oxidation Reaction of Fuel Cells. *Electrochim. Acta* **2011,** *56*, 1563-1569.

(46) Stuve, E.; Madix, R.; Brundle, C. CO Oxidation on Pd (100): a Study of the Coadsorption of Oxygen and Carbon Monoxide. *Surf. Sci.* **1984,** *146*, 155-178.

(47) Bekyarova, E.; Fornasiero, P.; Kašpar, J.; Graziani, M. CO Oxidation on Pd/CeO_2–ZrO_2 Catalysts. *Catal. Today* **1998,** *45*, 179-183.

(48) Zhang, C.; Hu, P. CO Oxidation on Pd (100) and Pd (111): A Comparative Study of Reaction Pathways and Reactivity at Low and Medium Coverages. *J. Am. Chem. Soc.* **2001,** *123*, 1166-1172.

(49) Haruta, M.; Kobayashi, T.; Sano, H.; Yamada, N. Novel Gold Catalysts for the Oxidation of Carbon Monoxide at a Temperature Far Below 0 C. *Chem. Lett.* **1987,** *16*, 405-408.

(50) Valden, M.; Lai, X.; Goodman, D. W. Onset of Catalytic Activity of Gold Clusters on Titania with the Appearance of Nonmetallic Properties. *Science* **1998,** *281*, 1647-1650.

(51) Mergler, Y.; Van Aalst, A.; Van Delft, J.; Nieuwenhuys, B. CO Oxidation over Promoted Pt Catalysts. *Appl. Catal. B Environ.* **1996,** *10*, 245-261.

(52) Manasilp, A.; Gulari, E. Selective CO Oxidation over Pt/Alumina Catalysts for Fuel Cell Applications. *Appl. Catal. B Environ.* **2002,** *37*, 17-25.

(53) Amatore, C.; Jutand, A. Anionic Pd(0) and Pd(II) Intermediates in Palladium-Catalyzed Heck and Cross-Coupling Reactions. *Acc. Chem. Res.* **2000,** *33*, 314-321.

(54) Stevens, P. D.; Li, G.; Fan, J.; Yen, M.; Gao, Y. Recycling of Homogeneous Pd Catalysts Using Superparamagnetic Nanoparticles as Novel Soluble Supports for Suzuki, Heck, and Sonogashira Cross-Coupling Reactions. *Chem. Comm.* **2005,** 4435-4437.

(55) Zhou, X.; Luo, J.; Liu, J.; Peng, S.; Deng, G.-J. Pd-Catalyzed Desulfitative Heck

Coupling with Dioxygen as the Terminal Oxidant. *Org. Lett.* **2011,** *13*, 1432-1435.

(56) Yu, L.; Huang, Y.; Wei, Z.; Ding, Y.; Su, C.; Xu, Q. Heck Reactions Catalyzed by Ultrasmall and Uniform Pd Nanoparticles Supported on Polyaniline. *J. Org. Chem.* **2015,** *80*, 8677-8683.

(57) Narayanan, R.; El-Sayed, M. A. Effect of Catalysis on the Stability of Metallic Nanoparticles: Suzuki Reaction Catalyzed by PVP-Palladium Nanoparticles. *J. Am. Chem. Soc.* **2003,** *125*, 8340-8347.

(58) Chen, Y.-H.; Hung, H.-H.; Huang, M. H. Seed-Mediated Synthesis of Palladium Nanorods and Branched Nanocrystals and their Use as Recyclable Suzuki Coupling Reaction Catalysts. *J. Am. Chem. Soc.* **2009,** *131*, 9114-9121.

(59) Li, Y.; Fan, X.; Qi, J.; Ji, J.; Wang, S.; Zhang, G.; Zhang, F. Palladium Nanoparticle-Graphene Hybrids as Active Catalysts for the Suzuki Reaction. *Nano Res.* **2010,** *3*, 429-437.

(60) Garcia-Martinez, J. C.; Lezutekong, R.; Crooks, R. M. Dendrimer-Encapsulated Pd Nanoparticles as Aqueous, Room-Temperature Catalysts for the Stille Reaction. *J. Am. Chem. Soc.* **2005,** *127*, 5097-5103.

(61) Pacardo, D. B.; Sethi, M.; Jones, S. E.; Naik, R. R.; Knecht, M. R. Biomimetic Synthesis of Pd Nanocatalysts for the Stille Coupling Reaction. *ACS Nano* **2009,** *3*, 1288-1296.

(62) Sonogashira, K. Development of Pd–Cu Catalyzed Cross-Coupling of Terminal Acetylenes with sp^2-Carbon Halides. *J. Organomet. Chem.* **2002,** *653*, 46-49.

(63) Doucet, H.; Hierso, J. C. Palladium-Based Catalytic Systems for the Synthesis of Conjugated Enynes by Sonogashira Reactions and Related Alkynylations. *Angew. Chem. Ind. Ed.* **2007,** *46*, 834-871.

(64) Hvolbæk, B.; Janssens, T. V.; Clausen, B. S.; Falsig, H.; Christensen, C. H.; Nørskov, J. K. Catalytic Activity of Au Nanoparticles. *Nano Today* **2007,** *2*, 14-18.

(65) Lai, X.; Clair, T. S.; Valden, M.; Goodman, D. Scanning Tunneling Microscopy Studies of Metal Clusters Supported on TiO_2 (110): Morphology and Electronic Structure. *Prog. Surf. Sci.* **1998,** *59*, 25-52.

(66) Sanchez, A.; Abbet, S.; Heiz, U.; Schneider, W.-D.; Häkkinen, H.; Barnett, R.; Landman, U. When Gold is Not Noble: Nanoscale Gold Catalysts. *J. Phys. Chem. A* **1999,** *103*, 9573-9578.

(67) van Bokhoven, J. A.; Louis, C.; Miller, J. T.; Tromp, M.; Safonova, O. V.; Glatzel, P. Activation of Oxygen on Gold/Alumina Catalysts: In Situ High-Energy-Resolution Fluorescence and Time-Resolved X-ray Spectroscopy. *Angew. Chem. Ind. Ed.* **2006,** *118*, 4767-4770.

(68) Zhang, H.; Okumura, M.; Toshima, N. Stable Dispersions of PVP-Protected Au/Pt/Ag Trimetallic Nanoparticles as Highly Active Colloidal Catalysts for Aerobic Glucose Oxidation. *J. Phys. Chem. C* **2011,** *115*, 14883-14891.

(69) Mavrikakis, M.; Stoltze, P.; Nørskov, J. K. Making Gold Less Noble. *Catal. Lett.* **2000,** *64*, 101-106.

(70) Zhang, S.; Zhang, X.; Jiang, G.; Zhu, H.; Guo, S.; Su, D.; Lu, G.; Sun, S. Tuning Nanoparticle Structure and Surface Strain for Catalysis Optimization. *J. Am. Chem. Soc.* **2014,** *136*, 7734-7739.

(71) Rumble, J. R.; Rumble, J., *CRC Handbook of Chemistry and Physics, 98th Edition*. CRC Press LLC: 2017.

(72) Stenlid, J. H.; Brinck, T. Extending the σ-Hole Concept to Metals: An Electrostatic Interpretation of the Effects of Nanostructure in Gold and Platinum Catalysis. *J. Am. Chem. Soc.* **2017,** *139*, 11012-11015.

(73) Wang, H.; Wang, W.; Jin, W. J. σ-hole Bond vs π-hole Bond: a Comparison Based on Halogen Bond. *Chem. Rev.* **2016,** *116*, 5072-5104.

(74) Mostafa, S.; Behafarid, F.; Croy, J. R.; Ono, L. K.; Li, L.; Yang, J. C.; Frenkel, A. I.; Cuenya, B. R. Shape-Dependent Catalytic Properties of Pt Nanoparticles. *J. Am. Chem. Soc.* **2010,** *132*, 15714-15719.

(75) Yin, A.-X.; Min, X.-Q.; Zhang, Y.-W.; Yan, C.-H. Shape-Selective Synthesis and Facet-Dependent Enhanced Electrocatalytic Activity and Durability of Monodisperse Sub-10 nm Pt−Pd Tetrahedrons and Cubes. *J. Am. Chem. Soc.* **2011,** *133*, 3816-3819.

(76) Wang, R.; He, H.; Liu, L.-C.; Dai, H.-X.; Zhao, Z. Shape-Dependent Catalytic Activity of Palladium Nanocrystals for the Oxidation of Carbon Monoxide. *Catal. Sci. Technol.* **2012,** *2*, 575-580.

(77) Quan, Z.; Wang, Y.; Fang, J. High-Index Faceted Noble Metal Nanocrystals. *Acc. Chem. Res.* **2013,** *46*, 191-202.

(78) Collins, G.; Schmidt, M.; O'Dwyer, C.; McGlacken, G.; Holmes, J. D. Enhanced Catalytic Activity of High-Index Faceted Palladium Nanoparticles in Suzuki–Miyaura Coupling Due to Efficient Leaching Mechanism. *ACS Catal.* **2014,** *4*, 3105-3111.

(79) Tian, N.; Zhou, Z.-Y.; Sun, S.-G.; Ding, Y.; Wang, Z. L. Synthesis of Tetrahexahedral Platinum Nanocrystals with High-Index Facets and High Electro-Oxidation Activity. *Science* **2007,** *316*, 732-735.

(80) Zhang, L.; Roling, L. T.; Wang, X.; Vara, M.; Chi, M.; Liu, J.; Choi, S.-I.; Park, J.; Herron, J. A.; Xie, Z. Platinum-Based Nanocages with Subnanometer-Thick Walls and Well-Defined, Controllable Facets. *Science* **2015,** *349*, 412-416.

(81) He, D. S.; He, D.; Wang, J.; Lin, Y.; Yin, P.; Hong, X.; Wu, Y.; Li, Y. Ultrathin Icosahedral Pt-Enriched Nanocage with Excellent Oxygen Reduction Reaction Activity. *J. Am. Chem. Soc* **2016,** *138*, 1494-1497.

(82) Toshima, N.; Ito, R.; Matsushita, T.; Shiraishi, Y. Trimetallic Nanoparticles Having a Au-Core Structure. *Catal. Today* **2007,** *122*, 239-244.

(83) Jiao, C.; Huang, Z.; Wang, X.; Zhang, H.; Lu, L.; Zhang, S. Synthesis of Ni/Au/Co Trimetallic Nanoparticles and Their Catalytic Activity for Hydrogen Generation from Alkaline Sodium Borohydride Aqueous Solution. *RSC Adv.* **2015,** *5*, 34364-34371.

(84) Link, S.; El-Sayed, M. A., Spectral Properties and Relaxation Dynamics of Surface Plasmon Electronic Oscillations in Gold and Silver Nanodots and Nanorods. *J. Phys. Chem. B* **1999**, *103*, 8410-8426.

(85) Hu, M.; Novo, C.; Funston, A.; Wang, H.; Staleva, H.; Zou, S.; Mulvaney, P.; Xia, Y.; Hartland, G. V. Dark-Field Microscopy Studies of Single Metal Nanoparticles: Understanding the Factors that Influence the Linewidth of the Localized Surface Plasmon Resonance. *J. Mater. Chem.* **2008,** *18*, 1949-1960.

(86) Ahn, J.; Wang, D.; Ding, Y.; Zhang, J.; Qin, D. Site-Selective Carving and Co-Deposition: Transformation of Ag Nanocubes into Concave Nanocrystals Encased by Au-Ag Alloy Frames. *ACS Nano* **2017**.

(87) LaMer, V. K.; Dinegar, R. H. Theory, Production and Mechanism of Formation of Monodispersed Hydrosols. *J. Am. Chem. Soc.* **1950,** *72*, 4847-4854.

(88) LaMer, V. K. Nucleation in Phase Transitions. *Ind. Eng. Chem.* **1952,** *44*, 1270-1277.

(89) Im, S. H.; Lee, Y. T.; Wiley, B.; Xia, Y. Large-Scale Synthesis of Silver Nanocubes: the Role of HCl in Promoting Cube Perfection and Monodispersity. *Angew. Chem. Int. Ed.* **2005,** *117*, 2192-2195.

(90) Xia, Y.; Xia, X.; Peng, H.-C. Shape-Controlled Synthesis of Colloidal Metal Nanocrystals: Thermodynamic Versus Kinetic Products. *J. Am. Chem. Soc* **2015,** *137*, 7947-7966.

(91) Pimpinelli, A.; Villain, J., *Physics of Crystal Growth*. Cambridge University Press Cambridge: 1998; Vol. 53.

(92) Bauer, E.; van der Merwe, J. H. Structure and Growth of Crystalline Superlattices: From Monolayer to Superlattice. *Phys. Rev. B* **1986,** *33*, 3657.

(93) Xia, Y.; Gilroy, K. D.; Peng, H. C.; Xia, X. Seed-Mediated Growth of Colloidal Metal Nanocrystals. *Angew. Chem. Ind. Ed.* **2017,** *56*, 60-95.

(94) Habas, S. E.; Lee, H.; Radmilovic, V.; Somorjai, G. A.; Yang, P. Shaping Binary Metal Nanocrystals through Epitaxial Seeded Growth. *Nat. Mater.* **2007,** *6*, 692-697.

(95) Sun, Y.; Mayers, B. T.; Xia, Y. Template-Engaged Replacement Reaction: a One-Step Approach to the Large-Scale Synthesis of Metal Nanostructures with Hollow Interiors. *Nano Letters* **2002,** *2*, 481-485.

(96) Yang, Y.; Zhang, Q.; Fu, Z.-W.; Qin, D. Transformation of Ag Nanocubes into Ag–Au Hollow Nanostructures with Enriched Ag Contents to Improve SERS Activity and Chemical Stability. *ACS Appl. Mater. Interfaces* **2014,** *6*, 3750-3757.

(97) Zhang, H.; Jin, M.; Xia, Y. Noble-Metal Nanocrystals with Concave Surfaces: Synthesis and Applications. *Angew. Chem. Ind. Ed.* **2012,** *51*, 7656-7673.

(98) Wang, Z. L.; Ahmad, T. S.; El-Sayed, M. A. Steps, Ledges and Kinks on the Surfaces of Platinum Nanoparticles of Different Shapes. *Surf. Sci.* **1997,** *380*, 302-310.

(99) Mulvihill, M. J.; Ling, X. Y.; Henzie, J.; Yang, P. Anisotropic Etching of Silver Nanoparticles for Plasmonic Structures Capable of Single-Particle SERS. *J. Am. Chem. Soc.* **2010,** *132*, 268-274.

(100) Wang, Z.; Yang, G.; Zhang, Z.; Jin, M.; Yin, Y. Selectivity on Etching: Creation of High-Energy Facets on Copper Nanocrystals for CO2 Electrochemical Reduction. *ACS Nano* **2016,** *10*, 4559-4564.

(101) Jana, N. R.; Gearheart, L.; Murphy, C. J. Seeding Growth for Size Control of 5−40 nm Diameter Gold Nanoparticles. *Langmuir* **2001,** *17*, 6782-6786.

(102) Nikoobakht, B.; El-Sayed, M. A. Preparation and Growth Mechanism of Gold Nanorods (NRs) Using Seed-Mediated Growth Method. *Chem. Mater.* **2003,** *15*, 1957-1962.

(103) Xia, Y.; Gilroy, K. D.; Peng, H.-C.; Xia, X. Seed-Mediated Growth of Colloidal Metal Nanocrystals. *Angew. Chem. Ind. Ed.* **2017,** *56*, 60-95.

(104) Gilroy, K. D.; Yang, X.; Xie, S.; Zhao, M.; Qin, D.; Xia, Y. Shape-Controlled Synthesis of Colloidal Metal Nanocrystals by Replicating the Surface Atomic Structure on the Seed. *Adv. Mater.* **2018,** *30*, 1706312.

(105) Xia, X.; Xie, S.; Liu, M.; Peng, H.-C.; Lu, N.; Wang, J.; Kim, M. J.; Xia, Y. On the Role of Surface Diffusion in Determining the Shape or Morphology of Noble-Metal Nanocrystals. *Proc. Natl. Acad. Sci. U.S.A.* **2013,** *110*, 6669-6673.

(106) Zhang, J.; Langille, M. R.; Personick, M. L.; Zhang, K.; Li, S.; Mirkin, C. A. Concave Cubic Gold Nanocrystals with High-Index Facets. *J. Am. Chem. Soc.* **2010,** *132*, 14012-14014.

(107) Villarreal, E.; Li, G. G.; Wang, H. Carving Growing Nanocrystals: Coupling Seed-Mediated Growth with Oxidative Etching. *Nanoscale* **2018,** *10*, 18457-18462.

(108) Sun, X.; Yang, Y.; Zhang, Z.; Qin, D. Mechanistic Roles of Hydroxide in Controlling the Deposition of Gold on Colloidal Silver Nanocrystals. *Chem. Mater.* **2017,** *29*, 4014-4021.

(109) Zhang, Y.; Ahn, J.; Liu, J.; Qin, D. Syntheses, Plasmonic Properties, and Catalytic Applications of Ag–Rh Core-Frame Nanocubes and Rh Nanoboxes with Highly Porous Walls. *Chem. Mater.* **2018,** *30*, 2151-2159.

(110) Xia, X.; Zeng, J.; McDearmon, B.; Zheng, Y.; Li, Q.; Xia, Y. Silver Nanocrystals with Concave Surfaces and Their Optical and Surface-Enhanced Raman Scattering Properties. *Angew. Chem. Ind. Ed.* **2011,** *50*, 12542-12546.

(111) Xia, Y.; Xiong, Y.; Lim, B.; Skrabalak, S. E. Cover Picture: Shape-Controlled Synthesis of Metal Nanocrystals: Simple Chemistry Meets Complex Physics? *Angew. Chem. Ind. Ed.* **2009,** *48*, 60-103.

(112) Wang, C.-W.; Sun, X.; Chang, H.-T.; Qin, D. Generation of Enzymatic Hydrogen Peroxide to Accelerate the Etching of Silver Nanocrystals with Selectivity. *Chem. Mater.* **2016,** *28*, 7519-7527.

(113) Zhang, Q.; Yang, Y.; Li, J.; Iurilli, R.; Xie, S.; Qin, D. Citrate-Free Synthesis of Silver Nanoplates and the Mechanistic Study. *ACS Appl. Mater. Interfaces* **2013,** *5*, 6333-6345.

(114) Gómez-Graña, S.; Goris, B.; Altantzis, T.; Fernández-López, C.; Carbó-Argibay, E.; Guerrero-Martínez, A.; Almora-Barrios, N.; López, N.; Pastoriza-Santos, I.; Pérez-Juste, J.; Bals, S.; Van Tendeloo, G.; Liz-Marzán, L. M. Au@Ag Nanoparticles: Halides Stabilize {100} Facets. *J. Phys. Chem. Lett.* **2013,** *4*, 2209-2216.

(115) Kim, M. H.; Kwak, S. K.; Im, S. H.; Lee, J.-B.; Choi, K.-Y.; Byun, D.-J. Maneuvering the Growth of Silver Nanoplates: Use of Halide Ions to Promote Vertical Growth. *J. Mater. Chem. C* **2014,** *2*, 6165-6170.

(116) Wilson, R.; Turner, A. P. F. Glucose Oxidase: an Ideal Enzyme. *Biosens. Bioelectron.* **1992,** *7*, 165-185.

(117) He, H.; Xu, X.; Wu, H.; Jin, Y. Enzymatic Plasmonic Engineering of Ag/Au Bimetallic Nanoshells and Their Use for Sensitive Optical Glucose Sensing. *Adv. Mater.* **2012,** *24*, 1736-1740.

(118) He, H.; Xu, X.; Wu, H.; Zhai, Y.; Jin, Y. In Situ Nanoplasmonic Probing of Enzymatic Activity of Monolayer-Confined Glucose Oxidase on Colloidal Nanoparticles. *Anal. Chem.* **2013,** *85*, 4546-4553.

(119) Liu, M.; Zheng, Y.; Zhang, L.; Guo, L.; Xia, Y. Transformation of Pd Nanocubes into Octahedra with Controlled Sizes by Maneuvering the Rates of Etching and Regrowth. *J. Am. Chem. Soc.* **2013,** *135*, 11752-11755.

(120) Zheng, Y.; Zeng, J.; Ruditskiy, A.; Liu, M.; Xia, Y. Oxidative Etching and Its Role in Manipulating the Nucleation and Growth of Noble-Metal Nanocrystals. *Chem. Mater.* **2014,** *26*, 22-33.

(121) Peng, H.-C.; Xie, S.; Park, J.; Xia, X.; Xia, Y. Quantitative Analysis of the Coverage Density of Br– Ions on Pd{100} Facets and Its Role in Controlling the Shape of Pd Nanocrystals. *J. Am. Chem. Soc.* **2013,** *135*, 3780-3783.

(122) Wang, Z.; Wang, H.; Zhang, Z.; Yang, G.; He, T.; Yin, Y.; Jin, M. Synthesis of Pd Nanoframes by Excavating Solid Nanocrystals for Enhanced Catalytic Properties. *ACS Nano* **2017,** *11*, 163-170.

(123) Chen, J.; McLellan, J. M.; Siekkinen, A.; Xiong, Y.; Li, Z.-Y.; Xia, Y. Facile Synthesis of Gold−Silver Nanocages with Controllable Pores on the Surface. *J. Am. Chem. Soc.* **2006,** *128*, 14776-14777.

(124) Cobley, C. M.; Xia, Y. Engineering the Properties of Metal Nanostructures via Galvanic Replacement Reactions. *Mater. Sci. Eng. R Rep.* **2010,** *70*, 44-62.

(125) Cobley, C. M.; Zhang, Q.; Song, W.; Xia, Y. The Role of Surface Nonuniformity in Controlling the Initiation of a Galvanic Replacement Reaction. *Chem. Asian J.* **2011,** *6*, 1479-1484.

(126) Lu, X.; Tuan, H.-Y.; Chen, J.; Li, Z.-Y.; Korgel, B. A.; Xia, Y. Mechanistic Studies on the Galvanic Replacement Reaction between Multiply Twinned Particles of Ag and HAuCl4 in an Organic Medium. *J. Am. Chem. Soc.* **2007,** *129*, 1733-1742.

(127) Xia, X.; Wang, Y.; Ruditskiy, A.; Xia, Y. 25th Anniversary Article: Galvanic Replacement: A Simple and Versatile Route to Hollow Nanostructures with Tunable and Well-Controlled Properties. *Adv. Mater.* **2013,** *25*, 6313-6333.

(128) Wu, Y.; Cai, S.; Wang, D.; He, W.; Li, Y. Syntheses of Water-Soluble Octahedral, Truncated Octahedral, and Cubic Pt–Ni Nanocrystals and Their Structure–Activity Study in Model Hydrogenation Reactions. *J. Am. Chem. Soc.* **2012,** *134*, 8975-8981.

(129) Chen, J.; Wiley, B.; Li, Z.-Y.; Campbell, D.; Saeki, F.; Cang, H.; Au, L.; Lee, J.; Li, X.; Xia, Y. Gold Nanocages: Engineering Their Structure for Biomedical Applications. *Adv. Mater.* **2005,** *17*, 2255-2261.

(130) Chen, J.; Wiley, B.; McLellan, J.; Xiong, Y.; Li, Z.-Y.; Xia, Y. Optical Properties of Pd−Ag and Pt−Ag Nanoboxes Synthesized via Galvanic Replacement Reactions. *Nano Lett.* **2005,** *5*, 2058-2062.

(131) Hong, J. W.; Kang, S. W.; Choi, B.-S.; Kim, D.; Lee, S. B.; Han, S. W. Controlled Synthesis of Pd–Pt Alloy Hollow Nanostructures with Enhanced Catalytic Activities for Oxygen Reduction. *ACS Nano* **2012,** *6*, 2410-2419.

(132) Zhang, W.; Yang, J.; Lu, X. Tailoring Galvanic Replacement Reaction for the Preparation of Pt/Ag Bimetallic Hollow Nanostructures with Controlled Number of Voids. *ACS Nano* **2012,** *6*, 7397-7405.

(133) Jing, H.; Wang, H. Structural Evolution of Ag–Pd Bimetallic Nanoparticles through Controlled Galvanic Replacement: Effects of Mild Reducing Agents. *Chem. Mater.* **2015,** *27*, 2172-2180.

(134) Zhang, H.; Jin, M.; Wang, J.; Li, W.; Camargo, P. H. C.; Kim, M. J.; Yang, D.; Xie, Z.; Xia, Y. Synthesis of Pd−Pt Bimetallic Nanocrystals with a Concave Structure through a Bromide-Induced Galvanic Replacement Reaction. *J. Am. Chem. Soc.* **2011,** *133*, 6078-6089.

(135) Srivastava, S. C.; Newman, L. Mixed Ligand Complexes of Palladium (II) with Chloride and Bromide. *Inorg. Chem.* **1966,** *5*, 1506-1510.

(136) Seo, D.; Yoo, C. I.; Chung, I. S.; Park, S. M.; Ryu, S.; Song, H. Shape Adjustment between Multiply Twinned and Single-Crystalline Polyhedral Gold Nanocrystals: Decahedra, Icosahedra, and Truncated Tetrahedra. *J. Phys. Chem. C* **2008,** *112*, 2469-2475.

(137) Xiong, Y.; Cai, H.; Wiley, B. J.; Wang, J.; Kim, M. J.; Xia, Y. Synthesis and Mechanistic Study of Palladium Nanobars and Nanorods. *J. Am. Chem. Soc.* **2007,** *129*, 3665-3675.

(138) Ahn, J.; Zhang, L.; Qin, D. Transforming Noble-Metal Nanocrystals into Complex Nanostructures through Facet-Selective Etching and Deposition. *ChemNanoMat* **2019**. DOI: 10.1002/cnma.201900378.

(139) Ahn, J.; Qin, D. Fabrication of Nanoscale Cage Cubes by Drilling Orthogonal, Intersected Holes through All Six Side Faces of Ag Nanocubes. *Chem. Mater.*, in press (under revision).

(140) Ahn, J.*; Kim, J.*; Qin, D. Orthogonal Deposition of Au on Different Facets of Ag Cuboctahedra for the Fabrication of Nanoboxes with Complementary Surfaces. *Nanoscale* **2019**, DOI: 10.1039/C9NR08420G. (*Equal contribution.)

(141) Ahn, J.; Shi, S.; Vannatter, B.; Qin, D. Comparative Study of the Adsorption of Thiol and Isocyanide Molecules on a Silver Surface by in Situ Surface-Enhanced Raman Scattering. *J. Phys. Chem. C* **2019**, *123*, 21571-21580.

CHAPTER 2. SITE-SELECTIVE CARVING AND CO-DEPOSITION: TRANSFORMATION OF AG NANOCUBES INTO CONCAVE NANOCRYSTALS ENCASED BY AU–AG ALLOY FRAMES

2.1 Introduction

As discussed in Chapter 1, noble metal nanocrystals with concave surface features are attractive for a range of applications in catalysis,[1,2] optical sensing,[3,4] and plasmonics.[5,6] Specifically, the high-index facets associated with a concave surface can be employed to enhance the catalytic activity by increasing the density of surface atoms with low-coordination numbers. The sharp features formed among or between concave faces can also lead to significant enhancement in local electric field, promoting their use as probes for surface-enhanced Raman scattering (SERS).[6-8]

There are two documented strategies for the synthesis of concave nanocrystals. The first one involves the use of an oxidative etchant to carve atoms from a specific set of facets on the nanocrystals for the creation of concave structures. Among those, Yang *et. al.* demonstrated the fabrication of Ag concave nanocrystals by controlling the etching of Ag octahedra with a mixture of NH_4OH and H_2O_2.[9] Xia *et. al.* reported the transformation of Pd nanocubes into Pd@Pt-Pd concave nanocubes by controlling the galvanic replacement reaction between Pd nanocubes and a Pt(II) precursor under the assistance of Br^- ions.[10] The second strategy relies on the selective deposition of atoms derived from a metal precursor at certain sites on the surface of a nanocrystal under the mediation of surface capping. To this end, Mirkin *et. al.* demonstrated the fabrication of Au concave nanocubes and convex tetrahexahedra by varying the type of anions such as Cl^- and Br^- involved in

the reaction.[11] Xia *et. al.* reported the synthesis of Pt and Pd concave nanocubes by employing Br^- as a capping agent toward the {100} facets and thus slowing down the growth rate at these sites.[12,13] Xia *et. al.* also demonstrated the deposition of Ag on Ag nanocubes for the generation of Ag concave nanocrystals by introducing Cu^{2+} ions into the solution to mediate the growth rates along different directions.[14] Huang *et. al.* demonstrated the synthesis of Pd@Au concave nanocubes by introducing Ag^+ ions into the reaction solution under a reducing environment.[15] Most recently, Personick *et. al.* reported the use of I^- ions to manipulate the growth of Pd on Au nanocrystals for the production of Au@Pd nanocrystals with a mix of concave and convex surfaces.[16]

Although the aforementioned approaches have been successfully implemented for the fabrication of nanocrystals with concave structures on the surface, few of these studies have explored the possibility to combine these two approaches together. I argue that the synergy of carving and deposition will offer some immediate advantages, including the ability to fabricate metal nanocrystals with more significant concaveness on the surface and the flexibility to manipulate the elemental compositions in addition to the spatial distributions of different elements. In this Chapter, I demonstrate the synthesis of Ag nanocubes with concave side faces and Ag-Au alloy frames, namely Ag@Ag-Au concave nanocrystals, by simply titrating $HAuCl_4$ solution into an aqueous suspension of Ag nanocubes in the presence of cetyltrimethylammonium chloride (CTAC), ascorbic acid (H_2Asc), NaOH, and at an initial pH of 11.6. Completely different from the prior work involving poly(vinylpyrrolidone) (PVP),[17,18] the use of CTAC sends the reaction along an unusual pathway. Equivalent to PVP, CTAC can serve as a colloidal stabilizer to prevent the nanoparticles from aggregation in a colloidal suspension. However, the Cl^- ions

dissociated from CTAC can affect both the speciation of the Au(III) precursor and the reduction/deposition pathway. Different from the PVP case, in the presence of Cl^- ions at a sufficient concentration, the added $HAuCl_4$ would be neutralized only by NaOH to form $AuCl_4^-$ species without further transformation into $AuCl(OH)_3^-$ and $Au(OH)_4^-$ species under an alkaline condition,[19] making it easier to initiate the galvanic reaction with Ag. Because the Cl^- ions have binding selectivity toward the Ag(100) surface,[20] I argue that the dissolution of Ag atoms would occur on the side faces of Ag nanocubes. The released Ag^+ can be quickly converted to $AgCl_2^-$ by complexing with the Cl^- ions,[21] ruling out the formation of AgOH and then Ag_2O patches as it was observed in the case of PVP.[22] Under an alkaline condition, H_2Asc should be neutralized into ascorbic monoanion ($HAsc^-$),[23] a strong reducing agent, that can quickly reduce both $AuCl_4^-$ and $AgCl_2^-$ to Au and Ag atoms, respectively. When the side faces are dominated by the galvanic replacement reaction, the co-deposition of Au and Ag atoms should occur on the edges and corners of the nanocubes. As Ag atoms are continuously etched away from the side faces and more Au and Ag are co-deposited on the edges and corners, the concavities on the side faces of the nanocubes are increasingly deepened toward the formation of Ag@Ag-Au concave nanocrystals. Such bimetallic nanocrystals embrace both the SERS activity arising from the original Ag cores and the catalytic capability through the introduction of Au to the surface, making them practical for monitoring Au-catalyzed reaction on the surface by *in situ* SERS. When the Ag cores are etched away selectively, the concave nanocrystals are transformed into Ag-Au alloy nanoframes with controllable ridge thicknesses. This study clearly demonstrates the feasibility to engineer the structures of bimetallic nanocrystals by manipulating the site selectivity of both etching and deposition through the introduction of a simple additive

such as Cl^- ions.

2.2 Experimental Section

Chemicals. Ethylene glycol (EG) was purchased from J.T. Baker. Sodium hydrosulfide hydrate ($NaSH \cdot xH_2O$), aqueous hydrochloric acid (HCl, 37 wt.%), poly(vinylpyrrolidone) (PVP) with an average molecular weight of 29000 or 55000 (PVP-29k or PVP-55k), silver trifluoroacetate (CF_3COOAg, ≥99.99% trace metal basis), aqueous cetyltrimethylammonium chloride solution (CTAC, 25 wt.%), and L-ascorbic acid (H_2Asc, 99%), gold(III) chloride trihydrate ($HAuCl_4 \cdot 3H_2O$, ≥99.9% trace metal basis), aqueous hydrogen peroxide (H_2O_2, 30 wt.%), sodium tetrachloropalladate(II) (Na_2PdCl_4, ≥99.99% trace metal basis), thiourea (99.0+%), were acquired from Sigma-Aldrich (St. Louis, MO). Acetone (HPLC grade, 99.5+%) and sodium hydroxide (NaOH, 98%) were obtained from Alfa Aesar. All chemicals were used as received. All aqueous solutions were prepared using deionized (DI) water with a resistivity of 18.2 MΩ·cm at room temperature.

Synthesis of the Ag Nanocubes. I prepared the Ag nanocubes with an average edge length of 40.5±2.8 nm using the polyol method developed by Xia and co-workers.[24] The as-obtained Ag nanocubes were washed with acetone and water once each and then dispersed in water for further use.

Synthesis of the Ag@Ag-Au Nanocrystals. In a typical synthesis, 2 mL of aqueous CTAC (0.1 M) was added into a glass vial, followed by the addition of 0.5 mL of aqueous H_2Asc (0.1 M) and 0.5 mL of aqueous NaOH (0.2 M) under magnetic stirring. Immediately after the introduction of 25 μL of the aqueous suspension of Ag nanocubes (with a final concentration of about 2.6×10^{11} particles/mL), aqueous $HAuCl_4$ (0.1 mM) was titrated into

the solution at a rate of 0.02 mL/min using a syringe pump under ambient conditions. As soon as the titration was completed, the solid sample was collected by centrifugation at 6000 rpm for 11 min, washed with water twice, and re-dispersed in water for future use.

Etching of Ag Cores from the Ag@Ag-Au Nanocrystals. In a typical process, the as-prepared nanocrystals were dispersed in 0.1 mL of water, followed by the addition of 0.9 mL of aqueous H_2O_2 (3 wt.%) solution. The suspension was left at room temperature for 5 h and then centrifuged at 12000 rpm for 15 min to collect the products. The particles were washed once with water and re-dispersed in water for further use.

SERS Monitoring of the Reduction of 4-NTP on the Ag@Ag-Au Nanocrystals. I first collected the as-prepared nanocrystals by centrifugation and had them dispersed in 0.1 mL of water. I then functionalized their surfaces with 4-NTP molecules by dispersing them in 0.9 mL of an ethanol-based 4-NTP solution (10^{-5} M). After incubation at room temperature for 2 h, I collected the 4-NTP-functionalized nanocrystals by centrifugation and washed with water prior to characterization. I took 0.2 mL of the suspension of 4-NTP-functionalized nanocrystals and mixed it with 0.2 mL of aqueous $NaBH_4$ (1 mg/mL) to start the reaction at room temperature. I sampled an aliquot of 20 μL from the reaction solution every several minutes and placed it in a polydimethylsiloxane (PDMS) sample cell to collect the SERS spectrum for monitoring the progress of the reaction. I used a Renishaw inVia Raman spectrometer (Wotton-under-Edge, UK) coupled with a Leica optical microscope (Leica Camera, Wetzlar, Germany) to collect the Raman spectra using 100× objective. I used an excitation wavelength of 785 nm in conjunction with a grating of 1200 lines/mm, and a maximum (100%) power of 100 mW. 10% of the maximum laser power was used to collect the Raman spectra from Ag@Au concave core-frame nanocubes

as substrate, while 100% was used in the case of Ag nanocubes as substrate.

Instrumentation and Characterization. The samples were washed and collected using an Eppendorf 5430 centrifuge (Eppendorf North America, Hauppauge, NY). The pH values were measured using a FiveEasy pH Meter (Mettler Toledo, Columbus, OH). The UV-vis spectra were collected using the Cary 60 spectrophotometer (Agilent Technologies, Santa Clara, CA). The Ag and Au contents in the nanocrystals were quantified using a NexION 300Q ICP-MS (PerkinElmer, Waltham, MA). Transmission electron microscopy (TEM) images were captured on a Hitachi HT7700 microscope (Tokyo, Japan) operated at 120 kV. Scanning electron microscopy (SEM) images were taken using a Hitachi SU8230 field-emission microscope. High-angle annular dark field scanning electron microscopy (HAADF-STEM) images were recorded on a Hitachi HD2700 C_s-corrected microscope operated at 200 kV. The EDS detector on the HD2700 was used to generate an elemental mapping of the nanocrystals.

2.3 Results and Discussion

2.3.1 Synthesis and Characterization of Ag@Ag-Au Concave Nanocrystals

In a typical process, I followed an established protocol to prepare Ag nanocubes with an average edge length of 40.5±2.8 nm (Figure 2.1).[24] I then dispersed the nanocubes in an aqueous solution containing H_2Asc, NaOH, and CTAC at an initial pH of 11.6, followed by the titration of 0.1 mM aqueous $HAuCl_4$ using a syringe pump under ambient conditions. Because the reaction solution was made alkaline by adding NaOH, essentially all the H_2Asc should be neutralized to generate $HAsc^-$, a much stronger reductant than H_2Asc.[23] Likewise, the titrated $HAuCl_4$ should be quickly neutralized by OH^- to form $AuCl_4^-$, which then

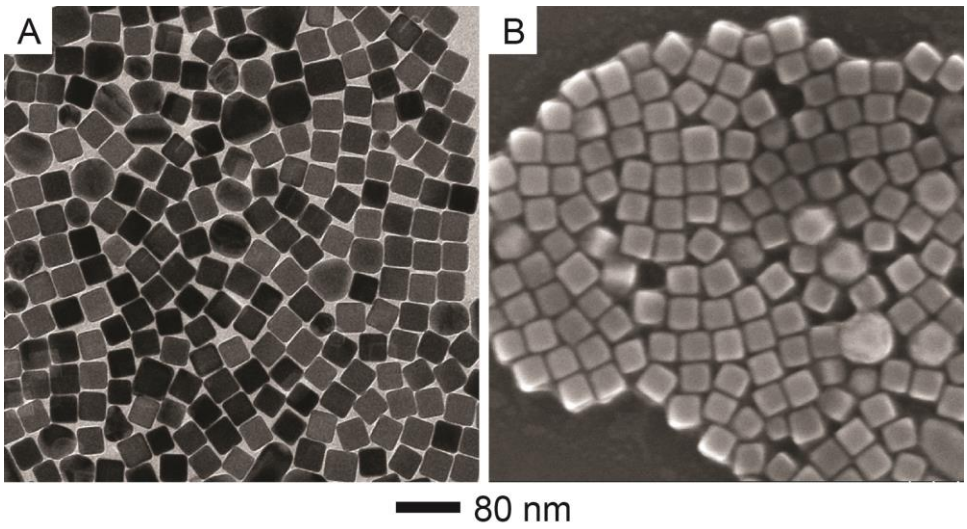

Figure 2.1. (A) TEM and (B) SEM image of Ag nanocubes with an average edge length of 40.5±2.8 nm.

potentially underwent ligand exchange with OH^- to produce $AuCl(OH)_3^-$ and $Au(OH)_4^-$, both of which have lower reduction potentials than $AuCl_4^-$.[19] However, the CTAC was supposed to dissociate into cetyltrimethylammonium (CTA^+) and chloride (Cl^-) ions in the reaction medium.[25] At an adequate concentration, I argue that the Cl^- ions should be able to keep the titrated Au(III) precursor in the form of $AuCl_4^-$ and thus maintain a relatively high reduction potential to support the galvanic replacement with the Ag nanocubes. To validate my hypothesis, I performed two sets of experiments by titrating 0.1 mM $HAuCl_4$ into the aqueous suspension of Ag nanocubes in absence or presence of NaOH. When NaOH was not involved in the reaction at an initial pH of 3.2, Figure 2.2A shows the UV-vis spectra of the Ag nanocubes before and after reacting with different volumes of H_2AuCl_4. It was found that the major LSPR peak of Ag nanocubes was shifted from 433 to 468, 503, 499, and 523 nm at 0.2, 0.4, 0.6, and 0.8 mL, respectively, together with a continuing decrease in the peak intensity. Figure 2.2B shows TEM image of the as-obtained sample prepared at a titration volume of 0.8 mL, in which voids were clearly identified.

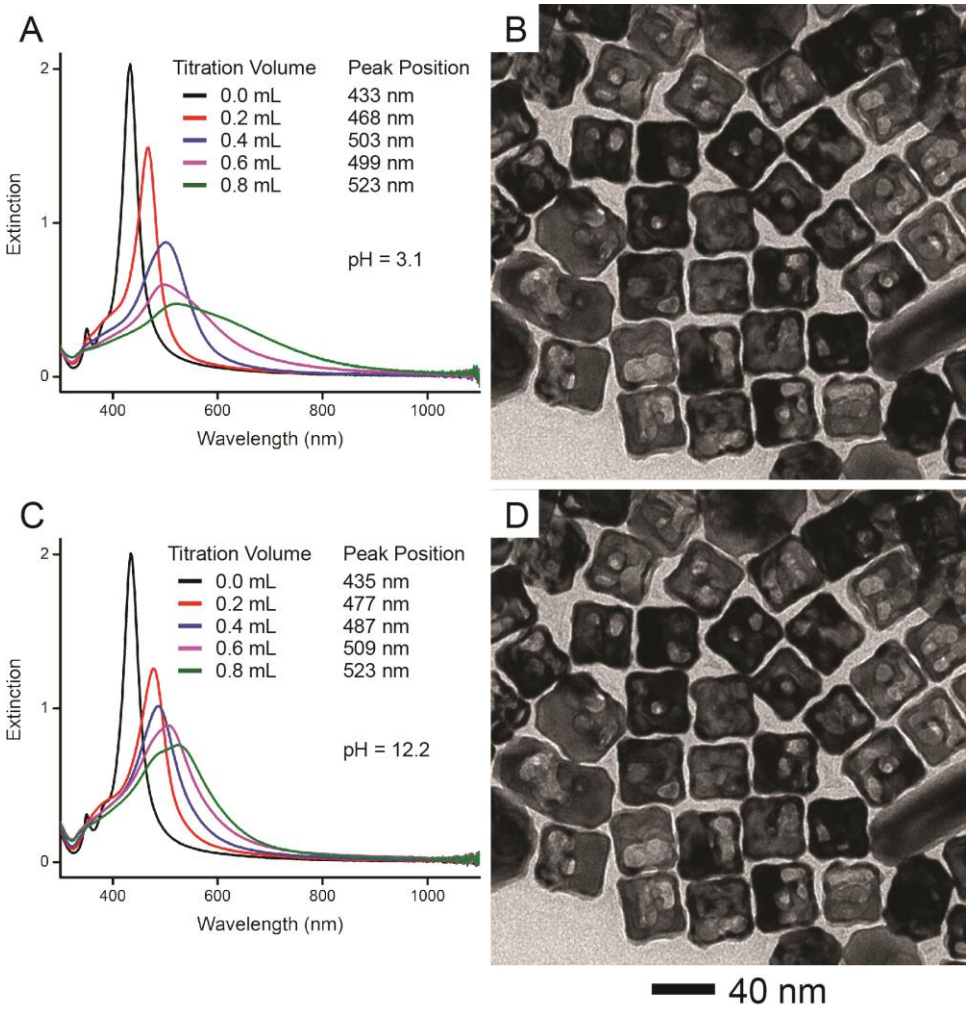

Figure 2.2. (A) UV-vis spectra of Ag nanocubes before and after reacting with different volumes of 0.1 mM aqueous $HAuCl_4$ in the presence CTAC at an initial pH of 3.2. (B) TEM image of the sample prepared with 0.8 mL of aqueous $HAuCl_4$ in the presence of CTAC. (C) UV-vis spectra of Ag nanocubes before and after reacting with different volumes of 0.1 mM aqueous $HAuCl_4$ in the presence CTAC and NaOH at an initial pH of 12.2. (D) TEM image of the sample prepared with 0.8 mL of aqueous $HAuCl_4$ in presence of CTAC and NaOH.

These results indicate the involvement of galvanic replacement reaction between Ag nanocubes and $HAuCl_4$ in the absence of NaOH. When the initial pH of reaction solution was adjusted to 12.2 by adding NaOH, Figure 2.2C shows the corresponding UV-vis spectra of the Ag nanocubes at different titration volumes. Similar to the trend shown in Figure 2.2A, the major LSPR peak of the Ag nanocubes was shifted from 435 to 477, 548,

509, and 523 nm at 0.2, 0.4, 0.6, and 0.8 mL, respectively, together with some decrease in the peak intensity. Again, as shown in Figure 2.2D, I observed the formation of hollow interiors from the sample prepared at a titration volume of 0.8 mL. This observation is completely different from that of the previous report in the case of PVP when all other reaction parameters kept the same.[18] In the case of PVP under an alkaline condition, the galvanic replacement reaction between the Ag nanocubes and the added $HAuCl_4$ only occurred to a very minor extent. Taken together, under an alkaline condition, I believe that the added $HAuCl_4$ was only neutralized by NaOH to generate $AuCl_4^-$ with no further ligand exchange with OH^-, enabling its galvanic replacement reaction with Ag under an alkaline condition. The resultant Ag^+ ions remained in the soluble form of $AgCl_2^-$ by complexing with Cl^- ions.[21] Both the $AuCl_4^-$ and $AgCl_2^-$ in the reaction solution could be reduced by $HAsc^-$ to generate Ag and Au atoms for their co-deposition onto the Ag nanocubes.

Figure 2.3, A-F, shows SEM and TEM images of the products obtained after adding different volumes of aqueous $HAuCl_4$. To help identify the Au deposition pathway, I used aqueous H_2O_2 to dissolve the Ag cores while leaving the deposited Ag-Au alloy intact. Figure 2.3, G-I, shows TEM images of the resultant structures. At a titration volume of 0.2 mL, Figure 2.3, A and D, shows nanoparticles with a similar morphology to that of the original Ag nanocubes, together with slightly sharpened corners. After the removal of Ag cores, Figure 2.3G shows the formation of broken nanoframes. In this case, the amount of Au atoms derived from the Au(III) precursor was insufficient to form continuous, robust structures on all the edges of the Ag nanocubes, leading to the formation of broken nanoframes. This result suggests that the initial deposition of Au selectively occurred on the edges, or the {110} facets, of Ag nanocubes, consistent with previous findings.[26-28]

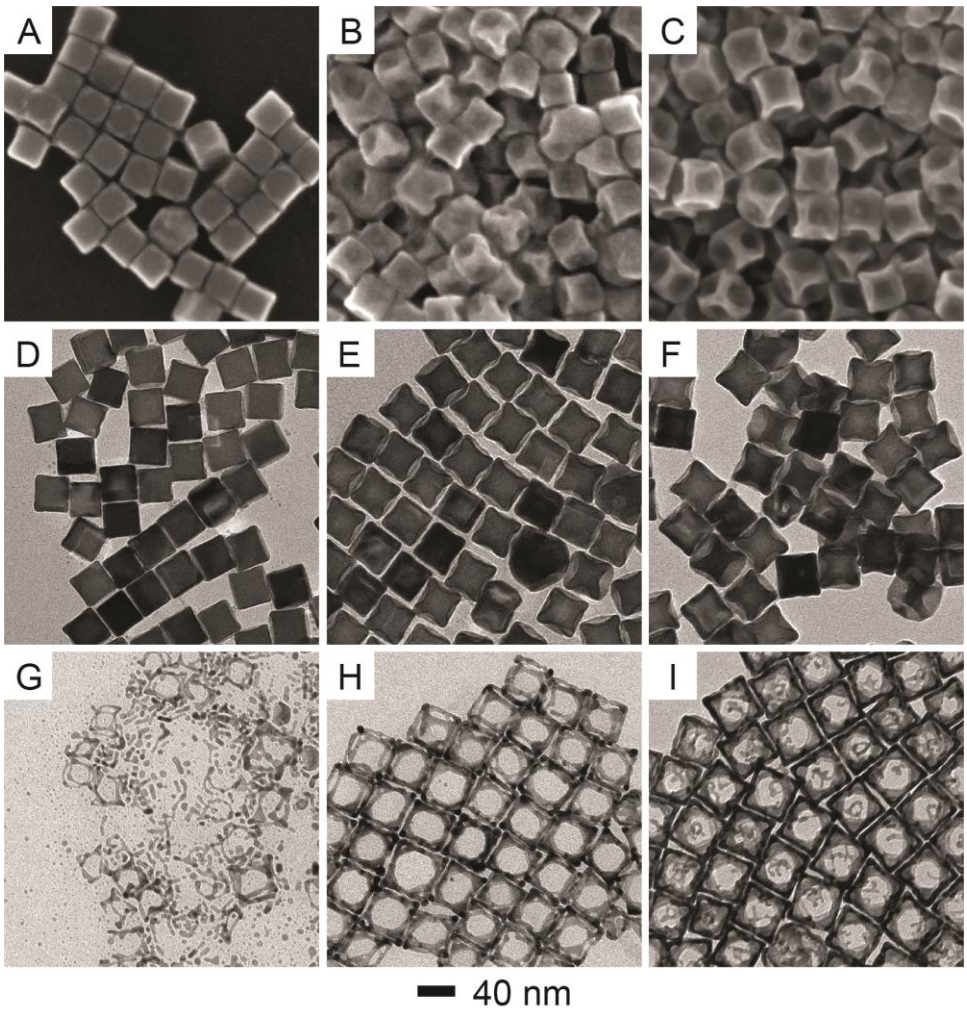

Figure 2.3. (A-C) SEM and (D-F) TEM images of the Ag@Ag-Au concave nanocrystals. The samples were prepared by titrating different volumes of 0.1 mM aqueous $HAuCl_4$ into a suspension of Ag nanocubes in the presence of H_2Asc, NaOH, and CTAC at an initial pH of 11.6: (A, D) 0.2, (B, E) 0.8, and (C, F) 1.6 mL, respectively. (G-I) TEM images of the resultant structures after etching of the samples in (D-F) with aqueous H_2O_2. Scale bars in the insets: 40 nm.

When the titration volume was increased to 0.8 mL, Figure 2.3, B and E, shows the generation of nanocrystals with visibly concave side faces at the sites of {100} facets on the original Ag nanocubes. After the selective etching of Ag cores, Figure 2.3H confirms the transformation of the concave nanocrystals into cubic nanoframes as most of the Au atoms were deposited on the edges and then corners of the Ag nanocubes. As the titration volume was further increased to 1.6 mL, Figure 2.3, C and F, confirms the formation of

cubic nanocrystals with more significantly concave side faces. After the removal of Ag cores, Figure 2.3I shows the creation of nanoframes made of ridges thicker than the sample shown in Figure 2.3H while some Au atoms could also be found at the {100} facets. This observation suggests that some Au atoms could migrate from edges and corners to side faces through surface diffusion when a considerable amount of Au atoms are deposited on the nanocubes.[29]

I used aberration-corrected high-angle annular dark-field scanning TEM (HAADF-STEM) to examine the detailed structure and morphology of the as-obtained particles. I also performed energy dispersive X-ray spectroscopy (EDS) mapping on an individual particle to resolve the distributions of constituent elements. Figure 2.4A shows a HAADF-STEM image taken from an individual particle prepared using 0.8 mL of aqueous $HAuCl_4$, with the particle oriented along the ⟨001⟩ zone axis. I clearly observed the formation of concave side faces. Figure 2.4, B-D, shows the spatial distributions of Ag, Au, and Cl for the same nanocrystal shown in Figure 2.4A. I noticed that the distribution of Ag was confined to a solid square with no inclusion of hollow interior and no extrusion from the corner sites while Au was largely deposited around the nanocube. These results suggest that there was a limited galvanic replacement reaction between the Au(III) species and the Ag nanocubes while the Au atoms derived from the reduction by both Ag and $HAsc^-$ were preferentially deposited onto the edges and corners of the Ag nanocubes. The presence of Cl^- on the entire surface validates the selective capping of CTAC toward the {100} facets on the Ag nanocubes.

To further confirm the deposition pathway for Au, I also used aqueous H_2O_2 to remove Ag for the sample prepared with 0.8 mL of aqueous $HAuCl_4$ and then characterized

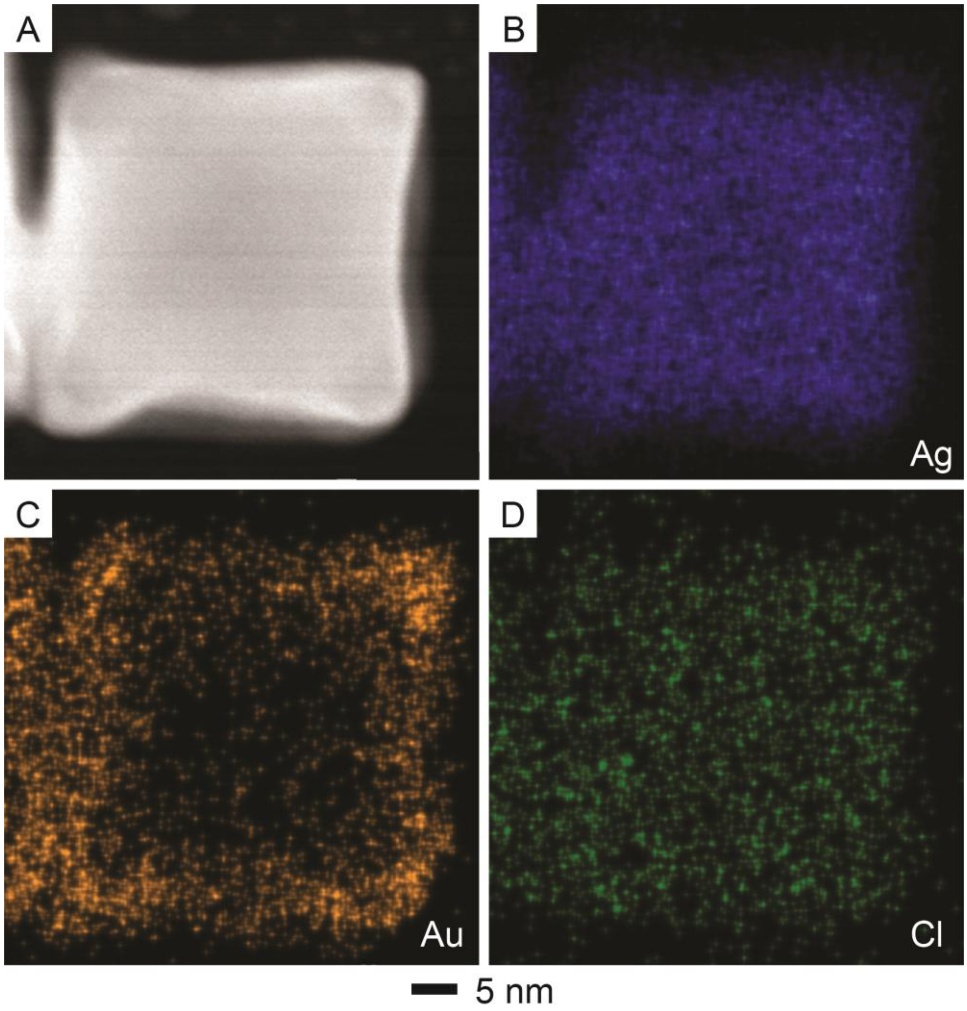

Figure 2.4. (A) HAADF-STEM image recorded from one of the Ag@Ag-Au concave nanocrystals prepared with the titration volume of 0.8 mL of $HAuCl_4$ (see Figure 2.3E) when it was orientated along the <001> zone axis. (B-D) EDS mapping of the same concave nanocube (blue: Ag; orange: Au; green: Cl).

the resultant nanostructures. Figure 2.5A shows an SEM image of the resultant nanoframes. Figure 2.5B gives a HAADF-STEM image of an individual nanoframe. The sharp bright contrast at the corners signifies local abundance of Au. Figure 2.5, C and D, shows the distributions of Ag and Au in the nanoframe. Again, I confirm the presence of Au on the edges and corners of the nanoframe. Because a small amount of Ag was observed at the corner sites after etching, I argue that the Ag atoms were included in the structure as a Ag-Au alloy, making it possible for them to survive the etching process. This result suggests

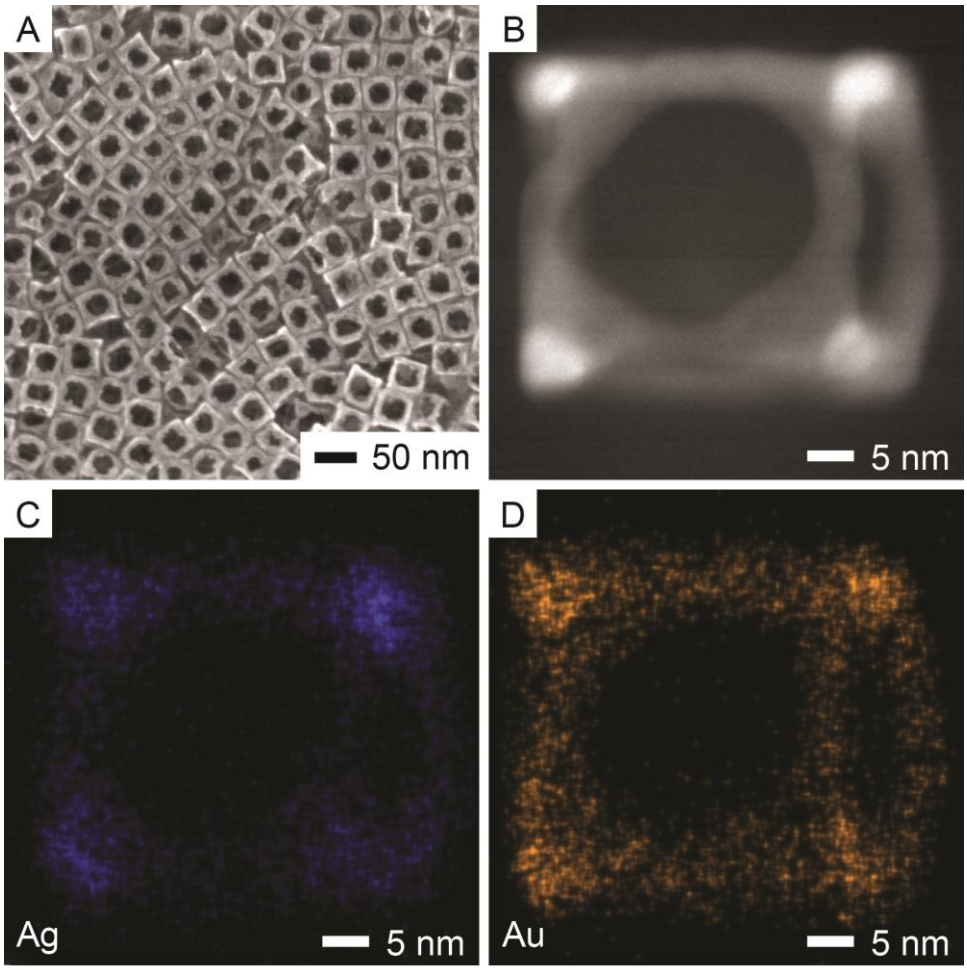

Figure 2.5. (A) SEM image of the nanoframes shown in Figure 2.3F. (B) HAADF-STEM image taken from one of the nanoframes shown in A when it was orientated at orientated along the <001> zone axis. (C, D) EDS mapping of a Ag-Au nanoframe (blue: Ag; orange: Au).

that some Ag^+ ions were released from the {100} facets due to the galvanic replacement reaction with $AuCl_4^-$. These Ag^+ ions, likely in the form of $AgCl_2^-$ complex due to the presence of Cl^- ions at a relatively high concentration, could be reduced by $HAsc^-$ to produce Ag atoms, followed by their co-deposition with the Au atoms on the edges and corners of the Ag nanocubes.

I also performed HAADF-STEM and EDS analyses on one of the nanocrystals prepared with a larger titration volume of aqueous $HAuCl_4$ at 1.6 mL. Figure 2.6A shows

a HAADF-STEM image when the particle was oriented along the ⟨001⟩ zone axis. Evidently, I observed the regions with a darker contrast on the side faces and in the center, indicating the loss of Ag from the side faces and thus formation of cavities at these sites. Figure 2.6B reveals the atoms that were located in the concave region. Based on the atom arrangement, I measured the lattice constant of the nanocrystal to be 0.404 nm, which is close to the lattice constant of Ag.[30] This result indicates that there was no lattice distortion in the concave region. The distribution of Ag in Figure 2.6C is consistent with the contrast pattern shown in Figure 2.6A. Figure 2.6D confirms the deposition of Au mainly on the {110} and {111} facets of the Ag nanocube, with a limited amount on the {100} facets. This data directly supports my TEM observation of the resultant nanostructures after the removal of Ag from the core (see Figure 2.3I). Taken together, it is clear that Ag atoms were oxidized and dissolved from the {100} facets of Ag nanocubes *via* galvanic replacement with $AuCl_4^-$ and the released Ag^+ ions subsequently complexed with the Cl^- ions to generate $AgCl_2^-$ until it was co-reduced with $AuCl_4^-$ by $HAsc^-$ for the generation of Ag and Au atoms.

To validate my hypothesis that the Ag atoms dissolved from the {100} facets of the Ag nanocubes were deposited back onto the edges and corners of nanocubes with Au atoms, I used inductively coupled plasma mass spectrometry (ICP-MS) to measure the contents of Ag and Au in the as-prepared samples when Ag nanocubes were reacted with different volumes of 0.1 mM $HAuCl_4$. In a typical process, I collected both solids and supernatants after centrifugation to separately determine their Ag and Au contents by ICP-MS analysis. Figure 2.7A shows that the amount of Ag in the solid samples did not change from the initial value of 184 μg as the titration volume of 0.1 mM $HAuCl_4$ was increased

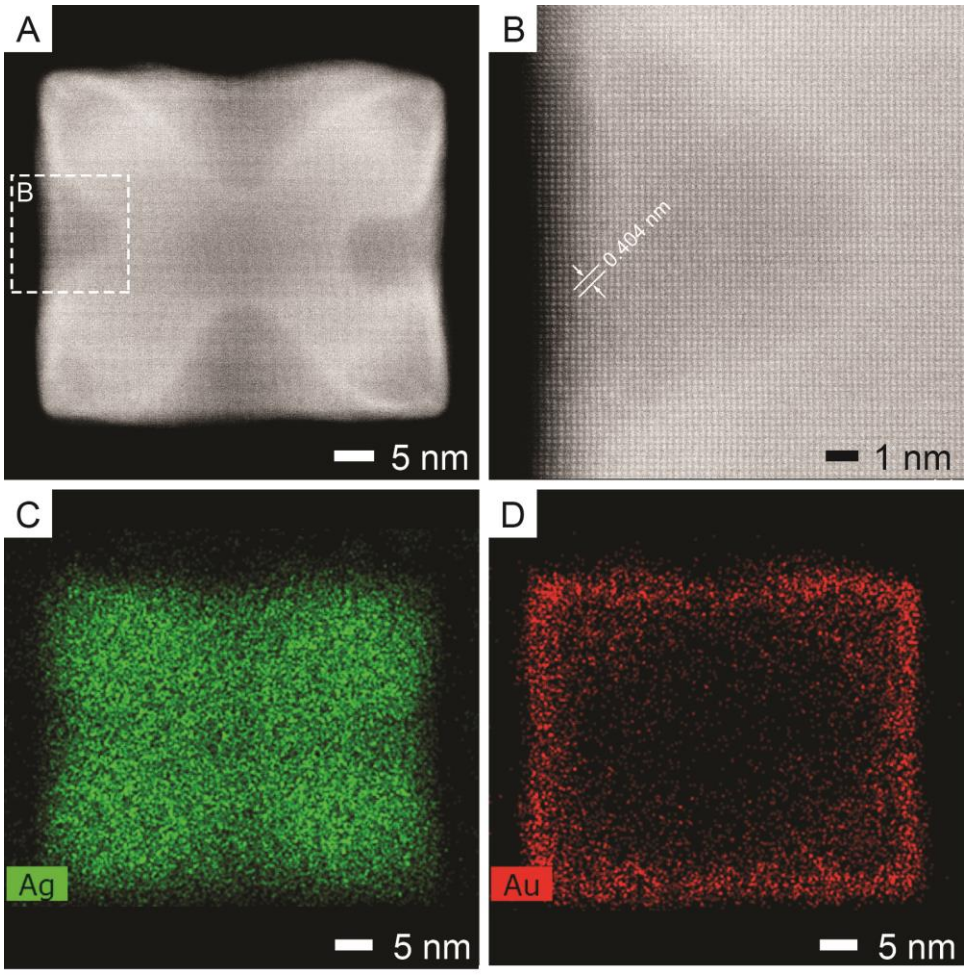

Figure 2.6. (A, B) HAADF-STEM images taken from one of the Ag@Ag-Au concave nanocrystal prepared with the titration of 1.6 mL of $HAuCl_4$ (see Figure 2.3F) when it was orientated along the <001> zone axis. (C, D) EDS mapping of the concave nanocrystal (green: Ag; red: Au).

up to 1.6 mL. The Ag content in the supernatant was less than 0.1% of that in the solid at all the titration volumes, suggesting no loss of Ag from nanocubes during the titration process. This result supports my argument that the Ag atoms oxidized from the side faces of Ag nanocubes were reduced by $HAsc^-$ to generate Ag atoms for their re-deposition onto the edges and corners of the nanocubes, increasing the concaveness on the {100} facets of the nanocubes. In comparison, Figure 2.7B indicates that the amount of Au in the solid samples linearly increased from 8.7 to 31.7 μg as the titration volume of $HAuCl_4$ was

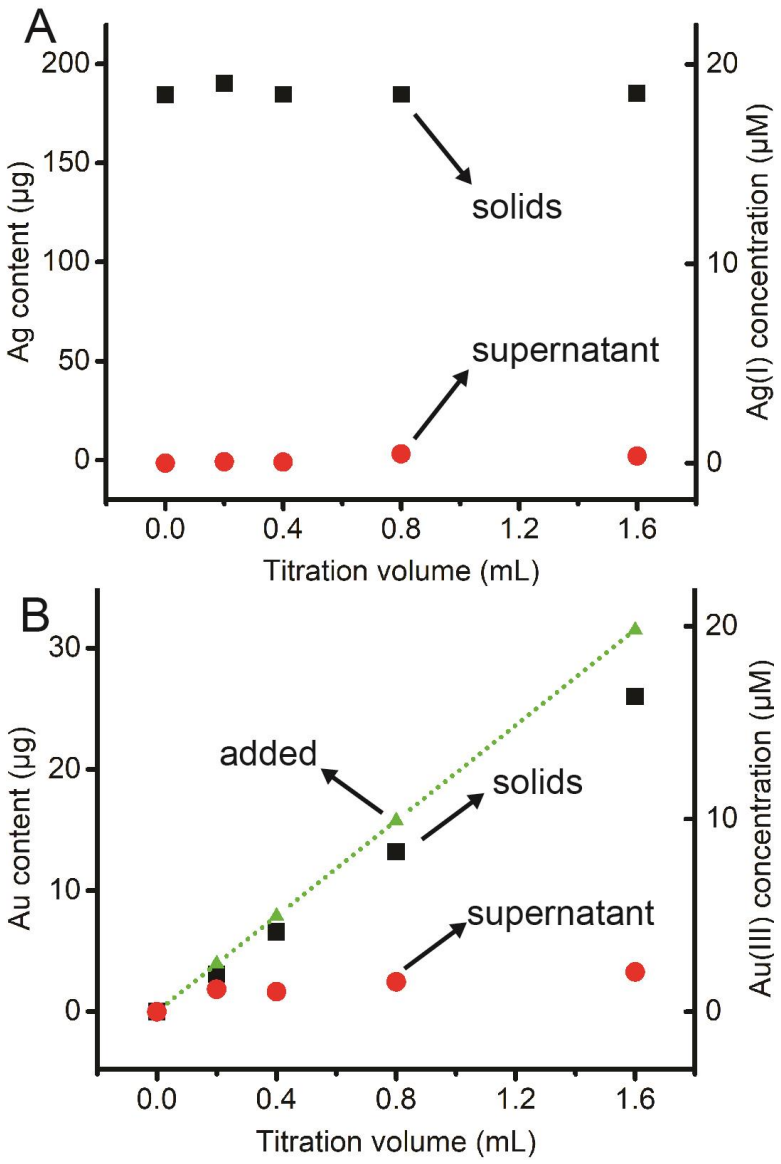

Figure 2.7. ICP-MS data of (A) Ag and (B) Au for the corresponding products (solids and supernatant) prepared by titrating aqueous $HAuCl_4$ into an aqueous suspension of Ag nanocubes in the presence of H_2Asc, NaOH, and CTAC at an initial pH of 11.6. The data points marked as "added" represent the amount of Au calculated by assuming complete reduction for the added $HAuCl_4$, followed by the deposition of Au atoms onto the Ag nanocubes.

increased from 0.2 to 1.6 mL. It was found that the Au content in the supernatant was also below the detection limit in the course of titration. By assuming that the added $AuCl_4^-$ precursor was completely reduced to Au atoms by chemical reduction with $HAsc^-$ and

through galvanic replacement with Ag nanocubes, and then deposited onto the Ag nanocubes, I calculated the amount of Au in the solids at different titration volumes (see solid line in Figure 2.7B), which are close to the experimental values. These results confirm that the added $AuCl_4^-$ was completely reduced into Au atoms, followed by their deposition onto the Ag nanocubes.

In addition to the characterization of the as-prepared products by electron microscopy, I used UV-vis spectroscopy to monitor the transformation of Ag nanocubes into Ag@Ag-Au nanocrystals by analyzing the localized surface plasmon resonance (LSPR) properties of the Ag nanocubes before and after reacting with aqueous $HAuCl_4$ in the presence of H_2Asc, NaOH, and CTAC at an initial pH of 11.6. As the titration volume was increased, Figure 2.8 shows that the major LSPR peak of the Ag nanocubes was constantly red-shifted from 435 to 455, 473, 499, and 530 nm at titration volumes of 0.2, 0.4, 0.8, and 1.6 mL, respectively. Additionally, the intensity of the major LSPR peak showed an initial decrease and then increase during the titration process. The red-shift of the LSPR peak could be attributed to the emergence of cavities on the side faces of the nanocrystals.[7] The initial decrease in peak intensity could be accounted by considering the dissolution of Ag atoms from the side faces and the deposition of Au on the edges and corners because Au has a weaker LSPR response in the visible region relative to Ag.[5] The subsequent increase in peak intensity could be ascribed to the reduction of the release Ag^+ ions for their co-deposition of the Au atoms.

To elucidate the explicit roles played by NaOH in transforming Ag nanocubes into the Ag@Ag-Au concave nanocrystals, I also recorded UV-vis spectra from Ag nanocubes before and after reacting with different volumes of 0.1 mM aqueous $HAuCl_4$ in the

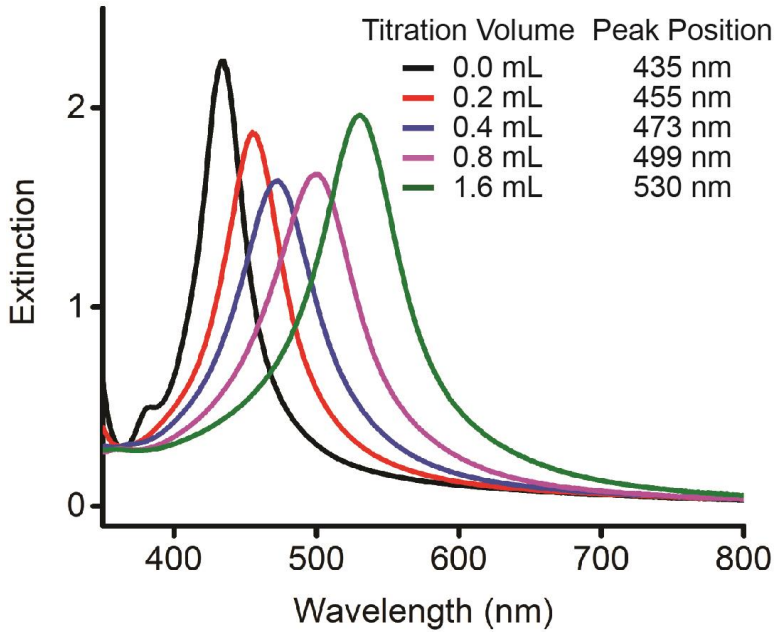

Figure 2.8. UV-vis spectra of Ag nanocubes before and after reacting with different volumes of 0.1 mM aqueous $HAuCl_4$ in the presence of H_2Asc, NaOH, and CTAC at an initial pH of 11.6.

presence of H_2Asc and CTAC but in the absence of NaOH at an initial pH of 2.8. Figure 2.9A shows the red-shift in LSPR peak position for the Ag nanocubes, together with broadening in peak width and a decrease in peak intensity. Figure 2.9B shows TEM image of the product obtained with a titration volume of 0.8 mL, from which I observed the transformation of Ag nanocubes into hollow nanocubes with slightly concave side faces. These results support my argument on the involvement of galvanic replacement reaction between Ag nanocubes and the Au(III) species in the presence of CTAC regardless of the initial pH. However, under an alkaline condition, NaOH would neutralize H_2Asc to $HAsc^-$, making the chemical reduction faster. Ultimately, the balance between galvanic reaction and chemical reduction would enable the generation of Ag concave nanocubes framed with a Ag-Au alloy at the corners and edges, different from the products in the absence of NaOH, or under an acid condition, when hollow interiors were created in the Ag nanocubes.

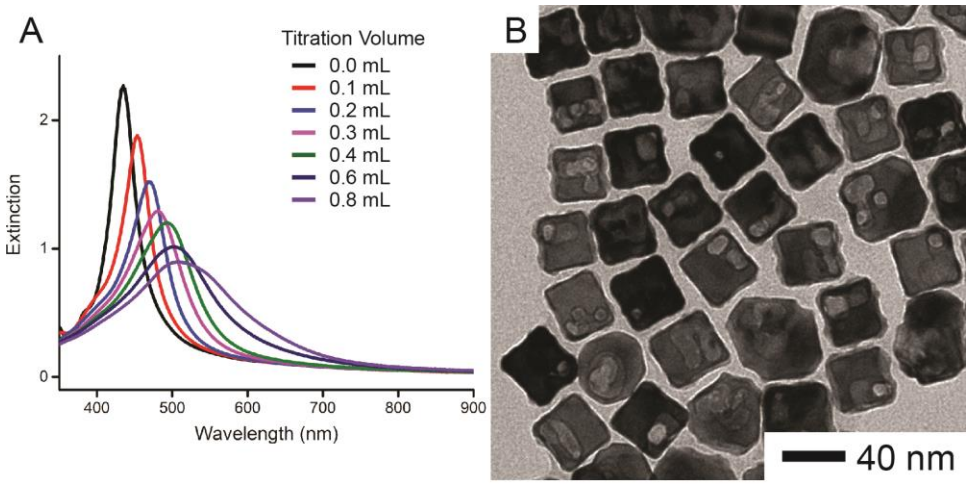

Figure 2.9. (A) UV-vis spectra of Ag nanocubes before and after reacting with different volumes of 0.1 mM aqueous $HAuCl_4$ in the presence of H_2Asc and CTAC at an initial pH of 2.8. (B) TEM image of the sample prepared with 0.8 mL of aqueous $HAuCl_4$.

2.3.2 Proposed Mechanism for Site-Selective Carving and Co-Deposition

Based on the experimental results shown in Figures 2.1-2.9, I propose a mechanism to account for the transformation of Ag nanocubes into Ag@Ag-Au concave nanocrystals in an aqueous phase in the presence of H_2Asc, NaOH, and CTAC at an initial pH of 11.6 (Figure 2.10, left panel). Because the Cl^- ions derived from CTAC can selectively bind to the side faces, that is, {100} facets, on Ag nanocubes, I argue that these sites will be preferentially activated toward oxidation.[19] Upon the titration of aqueous $HAuCl_4$, the {100} facets can act as an anode for the initiation of a galvanic the soluble form of $AgCl_2^-$ by complexing with Cl^- ions. Meanwhile, both the $AgCl_2^-$ and the Au(III) species can be reduced by $HAsc^-$ for the generation of Ag and Au atoms, followed by their deposition on the Ag nanocubes. Because the side faces are involved in the galvanic replacement reaction, I believe that the co-deposition of Au and Ag atoms is automatically directed and confined to the edges and corners. At a low titration volume of $HAuCl_4$, the site-selective deposition of Au and Ag atoms on the edges and corners is mainly responsible for the formation of

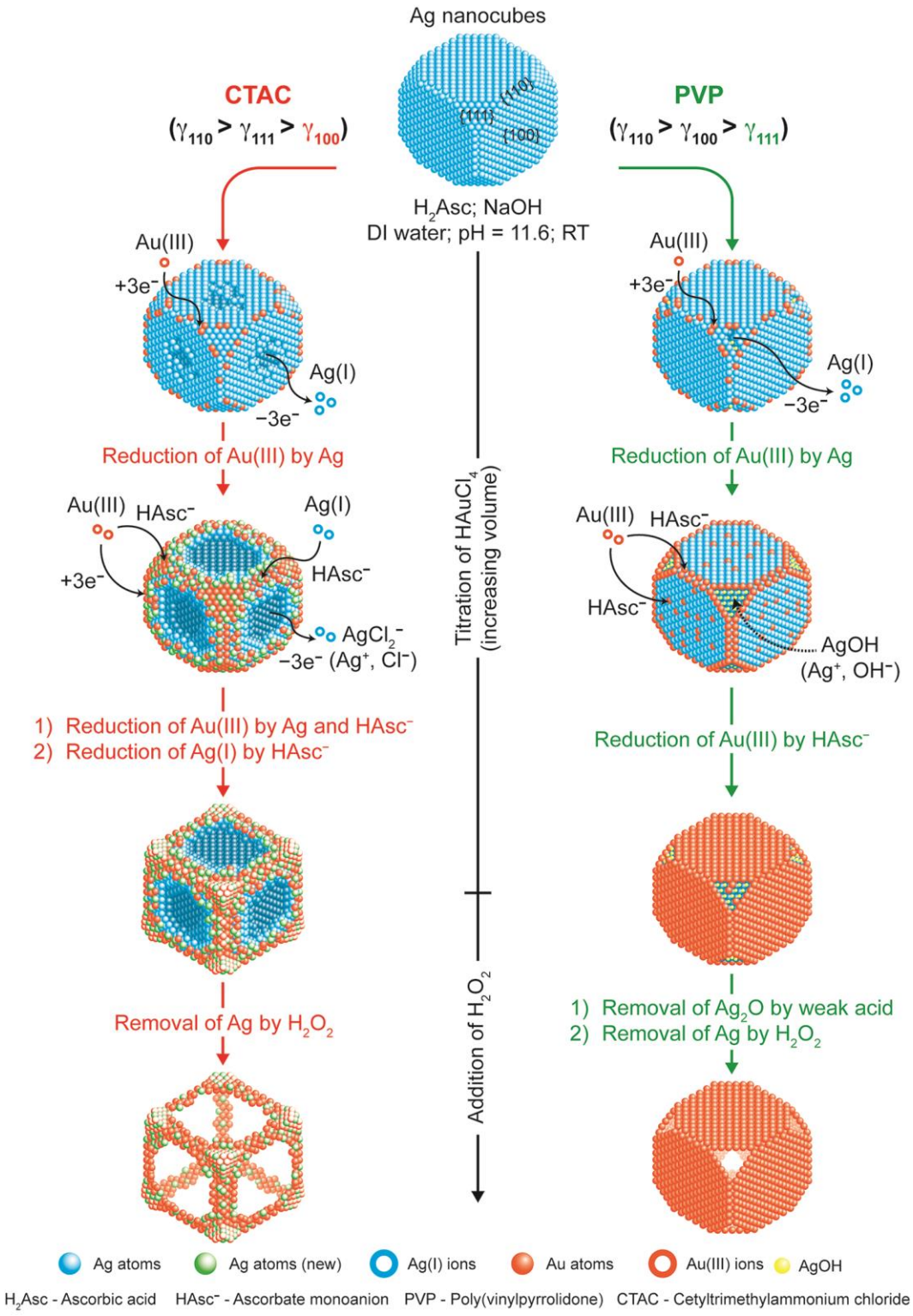

Figure 2.10. Schematic illustration describing the proposed mechanisms for the deposition of Au onto Ag nanocubes by titrating $HAuCl_4$ into an aqueous suspension of Ag nanocubes in the presence of H_2Asc, NaOH, and CTAC (left) or PVP (right) at an initial pH of 11.6. replacement reaction between Ag and $AuCl_4^-$ species. The released Ag^+ ions should stay in

slightly concave side faces when the carving on the side faces of nanocubes is limited. As more $HAuCl_4$ is titrated into the system, the Ag atoms are increasingly carved away from the side faces, leading to the formation of Ag@Ag-Au nanocrystals with more concaved side faces. Upon etching of pure Ag in the core with H_2O_2, the Ag@Ag-Au concave nanocrystals are transformed into Ag-Au nanoframes.

It is important to acknowledge that the deposition of Au on Ag nanocubes in the presence of CTAC is completely different from my previously published work in which PVP was used as the colloidal stabilizer while all other experimental conditions were kept essentially the same (Figure 2.10, right panel).[18] In the case of PVP, the galvanic replacement reaction is initiated from the corner sites, the {111} facets, rather than the side faces due to the lack of insufficient Cl^- ions originating from the titrated $AuCl_4^-$ precursor to activate the {100} facets. The galvanic replacement is also quickly terminated due to the formation of AgOH and then Ag_2O patches at the corner sites. The formation of $AuCl(OH)_3^-$ and $Au(OH)_4^-$ through ligand exchange between $AuCl_4^-$ and OH^- also helps terminate the galvanic reaction by increasing the reduction potential of the Au(III) precursor. As a result, the titrated Au(III) precursor is mainly reduced by $HAsc^-$ to generate Au atoms, for their sequential deposition onto the edges and then side faces, leading to the transformation of Ag nanocubes into Ag@Au core-shell nanocubes. After the treatment with a weak acid to remove the Ag_2O and then etching of Ag cores with H_2O_2, the core-shell nanocubes are converted into Au-based nanoboxes with well-defined openings at the corners.[22]

Collectively, CTAC at a sufficiently high concentration plays a number of roles in the transformation of Ag nanocubes into Ag@Ag-Au concave nanocrystals in an aqueous

system. Firstly, the CTAC-derived Cl^- ions would support the Au(III) species in the $AuCl_4^-$ format even under an alkaline condition, enabling the galvanic replacement reaction with the Ag nanocubes. Secondly, Cl^- ions can selectively bind to the {100} facets of Ag nanocubes, initiating the dissolution of Ag atoms from the side faces for the deposition of Au atoms on the edges and corners. Thirdly, the released Ag^+ ions from side faces of nanocubes can be retained in the soluble form of $AgCl_2^-$ by complexing with the Cl^- ions, and $AgCl_2^-$ can be reduced back to Ag atoms for their co-deposition with the Au atoms on the edges and corners of nanocubes.

2.3.3 Evaluating the Integrated SERS and Catalytic Properties of Ag@Ag-Au Concave Nanocrystals

I evaluated the SERS activity of Ag@Ag-Au concave nanocrystals by benchmarking against Ag nanocubes. With excitation at 785 nm, Figure 2.11 shows the SERS spectra collected from 4-nitrothiophenol (4-NTP) adsorbed on the Ag nanocubes and Ag@Ag-Au concave nanocrystals prepared with 1.6 mL of 0.1 mM aqueous $HAuCl_4$ (see Figure 2.3C). The SERS peak at 1574 cm^{-1} was increased 10 times for the concave nanocrystals (at 10% of laser power) relative to that of Ag nanocubes (at 100% laser power). I further demonstrated the use of these Ag@Ag-Au concave nanocrystals as a SERS probe for monitoring the reduction of 4-NTP by $NaBH_4$ *in situ* (Figure 2.12). In a typical measurement, I functionalized the concave nanocrystals with 4-NTP and then collected the SERS spectra at different time intervals with the laser excitation wavelength at 785 nm. At t=0 min, I observed the characteristic peaks of 4-NTP at 1111 cm^{-1} (C-N stretching mode, ν_{CN}), 1349 cm^{-1} (O-N-O stretching mode, ν_{NO2}), and 1574 cm^{-1} (C-C stretching mode, ν_{CC}),

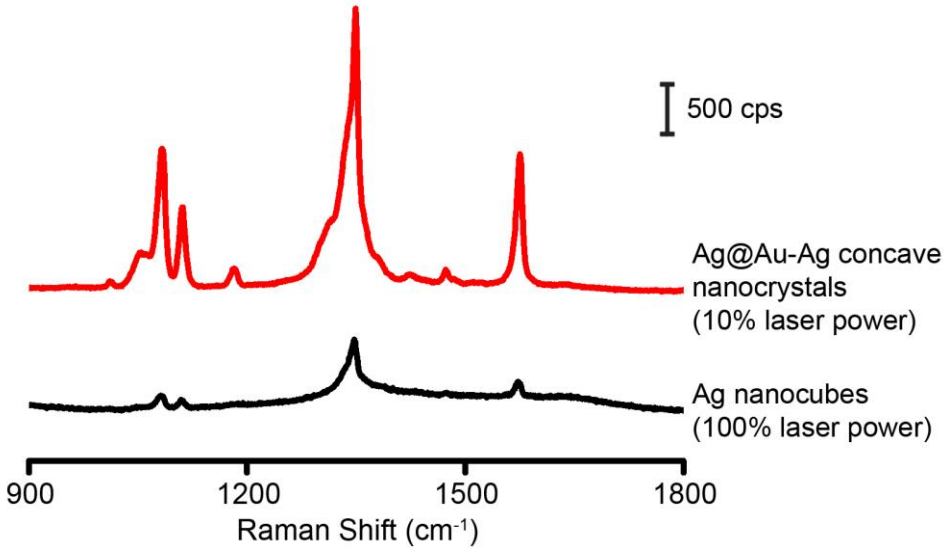

Figure 2.11. SERS spectra of 4-nitrothiophenol (4-NTP) collected from either Ag nanocubes (black) or Ag@Au concave core-frame nanocubes (red) as the substrate, under the same experimental conditions except for the difference in laser power.

respectively. The peak at 1083 cm^{-1} can be assigned to the C-S stretching mode (ν_{CS}). At *t*=4 min, the three bands of 4-NTP remained essentially unchanged except that the ν_{NO2} band was slightly shifted from 1349 to 1336 cm^{-1}. At the same time, I began to resolve the characteristic peak of 4-ATP at 1593 cm^{-1} (C-C stretching mode, ν_{CC}), together with three new peaks associated with *trans*-dimercaptoazobenzene (*trans*-DMAB) at 1141 cm^{-1} (C-N stretching mode, ν_{CN}, and C-H bending mode, β_{CH}), 1390 cm^{-1} (C-N stretching mode, ν_{CN}, and N=N stretching mode, ν_{NN}), and 1432 cm^{-1} (N=N stretching mode, ν_{NN}, and C-H bending mode, β_{CH}), respectively.[31] As the reaction progressed to 12 and then 43 min, I observed the decrease in the peak intensities of three vibration bands for 4-NTP while the peak intensities of the bands associated with 4-ATP and *trans*-DMAB were increased. This data suggests the reduction of 4-NTP to 4-ATP by $NaBH_4$ via the intermediate *trans*-DMAB. At the reaction time of 57 min and beyond up to 103 min, the three peaks in the SERS spectra were assigned to 4-ATP, indicating the completion of reaction.

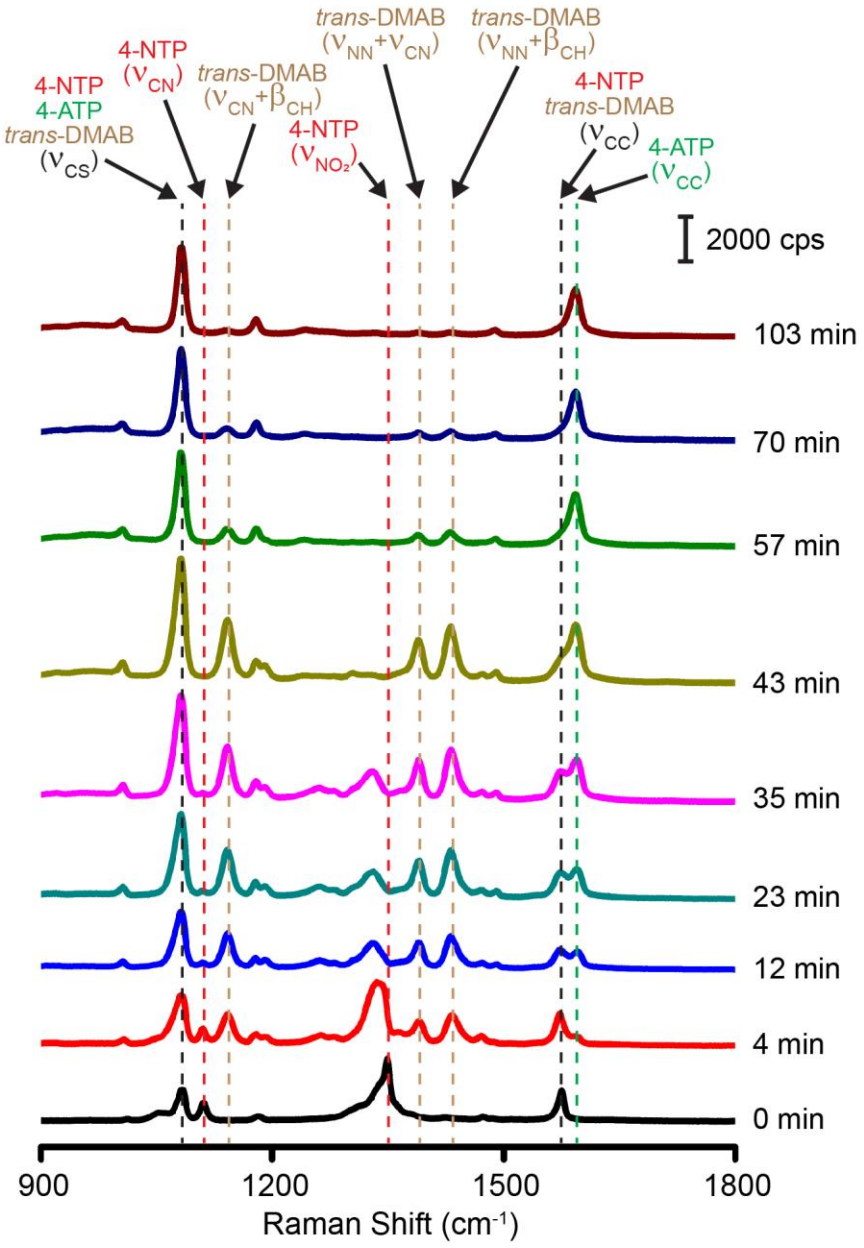

Figure 2.12. Time-dependent SERS spectra collected during the reduction of 4-NTP by $NaBH_4$ at an excitation wavelength of 785 nm. The reaction was catalyzed by the Ag@Ag-Au concave nanocrystals prepared with the titration of 1.6 mL of 0.1 mL $HAuCl_4$. The spectrum labelled "0 min" is reproduced from the red curve in Figure 2.11.

2.4 Conclusions

In summary, I have demonstrated the generation of Ag@Ag-Au concave nanocrystals by titrating aqueous $HAuCl_4$ to an aqueous suspension of Ag nanocubes in the presence of H_2Asc, NaOH, and CTAC at an initial pH of 11.6 under ambient conditions. Completely different from all the previous studies involving PVP, the use of CTAC sends the reaction along an unusual pathway. The mechanism involves the co-deposition of Au and Ag atoms on the edges and corners of the Ag nanocubes while Ag atoms are concomitantly etched away from the side faces. Specifically, the added $HAuCl_4$ remains in the form of $AuCl_4^-$ under an alkaline condition, facilitating the galvanic replacement reaction with the Ag nanocubes. Because Cl^- ions can selectively bind to the {100} facets of Ag nanocubes, I argue that the dissolution of Ag atoms occurs from the side faces. The released Ag^+ ions can be retained in the soluble form of $AgCl_2^-$ by complexing with the Cl^- ions. Both the $AuCl_4^-$ and $AgCl_2^-$ are then reduced by $HAsc^-$ to generate Au and Ag atoms, followed by their preferentially co-deposition onto the edges and corners of Ag nanocubes. As the reaction progresses, Ag atoms located at the side faces of the nanocubes are continuously carved by the galvanic reaction while Ag and Au atoms are increasingly deposited on the edges and corners, leading to the generation of Ag@Ag-Au nanocrystals with concave side faces. The concave nanocrystals show much stronger SERS activity at 785 nm excitation, making it feasible to monitor the Au-catalyzed reduction of 4-nitrothiophenol by $NaBH_4$ *in situ*. The concave nanocrystals could be transformed into Ag-Au nanoframes with controllable ridge thicknesses upon the removal of Ag in the core.

2.5 Notes to Chapter 2

This chapter was adapted from the article "Site-Selective Carving and Co-Deposition: Transformation of Ag Nanocubes into Concave Nanocrystals Encased by Au–Ag Alloy Frames" published in *ACS* Nano.[32]

2.6 References

(1) Zhang, H.; Jin, M.; Xia, Y. Noble-Metal Nanocrystals with Concave Surfaces: Synthesis and Applications. *Angew. Chem., Int. Ed.* **2012**, *51*, 7656−7673.

(2) Burda, C.; Chen, X.; Narayanan, R.; El-Sayed, M. A. Chemistry and Properties of Nanocrystals of Different Shapes. *Chem. Rev.* **2005**, *105*, 1025−1102.

(3) Willets, K. A.; Van Duyne, R. P. Localized Surface Plasmon Resonance Spectroscopy and Sensing. *Annu. Rev. Phys. Chem.* **2007**, *58*, 267−297.

(4) Jain, P. K.; Huang, X.; El-Sayed, I. H.; El-Sayed, M. A. Noble Metals on the Nanoscale: Optical and Photothermal Properties and Some Applications in Imaging, Sensing, Biology, and Medicine. *Acc. Chem. Res.* **2008**, *41*, 1578−1586.

(5) Haes, A. J.; Haynes, C. L.; McFarland, A. D.; Schatz, G. C.; Van Duyne, R. P.; Zou, S. Plasmonic Materials for Surface-Enhanced Sensing and Spectroscopy. *MRS Bull.* **2005**, *30*, 368−375.

(6) Rycenga, M.; Cobley, C. M.; Zeng, J.; Li, W.; Moran, C. H.; Zhang, Q.; Qin, D.; Xia, Y. Controlling the Synthesis and Assembly of Silver Nanostructures for Plasmonic Applications. *Chem. Rev.* **2011**, *111*, 3669−3712.

(7) Xia, X.; Zeng, J.; McDearmon, B.; Zheng, Y.; Li, Q.; Xia, Y. Silver Nanocrystals with Concave Surfaces and Their Optical and Surface-Enhanced Raman Scattering Properties. *Angew. Chem., Int. Ed.* **2011**, *50*, 12542−12546.

(8) Rycenga, M.; Langille, M. R.; Personick, M. L.; Ozel, T.; Mirkin, C. A. Chemically Isolating Hot Spots on Concave Nanocubes. *Nano Lett.* **2012**, *12*, 6218−6222.

(9) Mulvihill, M. J.; Ling, X. Y.; Henzie, J.; Yang, P. Anisotropic Etching of Silver Nanoparticles for Plasmonic Structures Capable of Single-Particle SERS. *J. Am. Chem. Soc.* **2010**, *132*, 268–274.

(10) Zhang, H.; Jin, M.; Wang, J.; Li, W.; Camargo, P. H. C.; Kim, M. J.; Yang, D.; Xie, Z.; Xia, Y. Synthesis of Pd−Pt Bimetallic Nanocrystals with a Concave Structure through a Bromide-Induced Galvanic Replacement Reaction. *J. Am. Chem. Soc.* **2011**, *133*, 6078–6089.

(11) Zhang, J.; Langille, M. R.; Personick, M. L.; Zhang, K.; Li, S.; Mirkin, C. A. Concave Cubic Gold Nanocrystals with High-Index Facets. *J. Am. Chem. Soc.*

2010, *132*, 14012–14014.

(12) Jiang, B.; Xu, L.; Chen, W.; Zou, C.; Yang, Y.; Fu, Y.; Huang, S. Ag^{+}-Assisted heterogeneous growth of concave Pd@Au nanocubes for surface enhanced Raman scattering (SERS). *Nano Res.* **2017**, *10*, 3509–3521.

(13) Yu, T.; Kim, D. Y.; Zhang, H.; Xia, Y. Platinum Concave Nanocubes with High-Index Facets and Their Enhanced Activity for Oxygen Reduction Reaction. *Angew. Chem., Int. Ed.* **2011**, *123*, 2825–2829.

(14) Jin, M.; Zhang, H.; Xie, Z.; Xia, Y. Palladium Concave Nanocubes with High-Index Facets and Their Enhanced Catalytic Properties. *Angew. Chem., Int. Ed.* **2011**, *123*, 7996–8000.

(15) Xia, X.; Zeng, J.; Mcdearmon, B.; Zheng, Y.; Li, Q.; Xia, Y. Silver Nanocrystals with Concave Surfaces and Their Optical and Surface-Enhanced Raman Scattering Properties. *Angew. Chem., Int. Ed.* **2011**, *123*, 12750–12754.

(16) King, M. E.; Personick, M. L. Bimetallic Nanoparticles: Bimetallic Nanoparticles with Exotic Facet Structures via Iodide-Assisted Reduction of Palladium. *Part. Part. Syst. Charact.* **2017**, *34*, 1600422.

(17) Yang, Y.; Liu, J.; Fu, Z.-W.; Qin, D. Galvanic Replacement-Free Deposition of Au on Ag for Core–Shell Nanocubes with Enhanced Chemical Stability and SERS Activity. *J. Am. Chem. Soc.* **2014**, *136*, 8153–8156.

(18) Sun, X.; Yang, Y.; Zhang, Z.; and Qin, D. Mechanistic Roles of Hydroxide in Controlling the Deposition of Gold on Colloidal Silver Nanocrystals. *Chem. Mater.* 2017, 27, 4014–4027.

(19) Wang, S.; Qian, K.; Bi, X.; Huang, W. Influence of Speciation of Aqueous $HAuCl_4$ on the Synthesis, Structure, and Property of Au Colloids. *J. Phys. Chem. C* **2009**, *113*, 6505−6510.

(20) Zhou, S.; Li, J.; Gilroy, K. D.; Tao, J.; Zhu, C.; Yang, X.; Sun, X.; Xia, Y. Facile Synthesis of Silver Nanocubes with Sharp Corners and Edges in an Aqueous Solution. *ACS Nano* **2016**, *10*, 9861–9870.

(21) Du, J.; Chen, Z.; Chen, C.; Meyer, T. J. A Half-Reaction Alternative to Water Oxidation: Chloride Oxidation to Chlorine Catalyzed by Silver Ion. *J. Am. Chem. Soc.* **2015**, *137*, 3193–3196.

(22) Sun, X.; Kim, J.; Gilroy, K. D.; Liu, J.; König, T. A. F.; Qin, D. Gold-Based Cubic Nanoboxes with Well-Defined Openings at the Corners and Ultrathin Walls Less Than Two Nanometers Thick. *ACS Nano* **2016**, *10*, 8019–8025.

(23) Du, J.; Cullen, J. J.; Buettner, G. R. Ascorbic Acid: Chemistry, Biology, and the Treatment of Cancer. *Biochim. Biophys. Acta, Rev. Cancer* **2012**, *1826*, 443−457.

(24) Skrabalak, S. E.; Au, L.; Li, X.; Xia, Y. Facile Synthesis of Ag Nanocubes and Au Nanocages. *Nature Protocols* **2007**, *2*, 2182–2190.

(25) Wang, Z.; Larson, R. G. Molecular Dynamics Simulations of Thread like Cetyltrimethylammonium Choride Micllle: Effects of Sodium Choloride and Sodium Salicylate Salts. *J. Phys. Chem. B* **2009**, *113*, 13697–13710.

(26) Yang, Y.; Zhang, Q.; Fu, Z.-W.; Qin, D. Transformation of Ag Nanocubes into Ag–Au Hollow Nanostructures with Enriched Ag Contents to Improve SERS Activity and Chemical Stability. *ACS Appl. Mater. Interfaces* **2014**, *6*, 3750–3757.

(27) Sun, X.; Qin, D. Co-titration of $AgNO_3$ and $HAuCl_4$: A New Route to the Synthesis of Ag@Ag-Au Core-Frame Nanocubes with Enhanced Plasmonic and Catalytic Properties. *J. Mater. Chem. C* **2015**, *3*, 11833–11841.

(28) Wu, Y.; Sun, X.; Yang, Y.; Li, J.; Zhang, Y.; Qin, D. Enriching Silver Nanocrystals with a Second Noble Metal. *Acc. Chem. Res.* **2017**, *50*, 1774–1784.

(29) Xia, X.; Xie, S.; Liu, M.; Peng, H.-C.; Lu, N.; Wang, J.; Kim, M. J.; Xia, Y. On the Role of Surface Diffusion in Determining the Shape or Morphology of Noble-Metal Nanocrystals. *Proc. Natl. Acad. Sci.* **2013**, *110*, 6669–6673.

(30) Physical Constants of Organic Compounds. In *CRC Handbook of Chemistry and Physics*, 98th ed.; Rumble, J. R., Ed.; CRC Press: Boca Raton, FL, 2015.

(31) Huang, Y.-F.; Wu, D.-Y.; Zhu, H.-P.; Zhao, L.-B.; Liu, G.-K.; Ren, B.; Tian, Z.-Q. Surface-Enhanced Raman Spectroscopic Study of p-Aminothiophenol. *Phys. Chem. Chem. Phys.* **2012**, *14*, 8485-8497.

(32) Ahn, J.; Wang, D.; Ding, Y.; Zhang, J.; Qin, D. Site-Selective Carving and Co-Deposition: Transformation of Ag Nanocubes into Concave Nanocrystals Encased by Au-Ag Alloy Frames. *ACS Nano* **2018**, *12*, 298–307.

CHAPTER 3. FABRICATION OF NANOSCALE CAGE CUBES BY DRILLING ORTHOGONAL, INTERSECTED HOLES THROUGH ALL SIX SIDE FACES OF AG NANOCUBES

3.1 Introduction

As discussed in the previous chapters, the galvanic replacement reaction offers a facile method for transform solid mono- or bimetallic nanocrystals of various shapes into hollow and/or porous metallic nanostructures having well-controlled morphologies and compositions for a range of applications in biomedicine,[1-3] catalysis,[4-6] optical sensing,[7, 8] and surface-enhanced Raman scattering (SERS).[9-12] For example, Ag nanocubes were reacted with a Au(I) or Au(III) precursor in an aqueous solution for the production of Ag-Au nanoboxes and nanocages with tunable optical properties.[13,14] Similar approaches have been successfully applied to the generation of hollow and/porous nanostructures made of Ag-Pt,[15] Ag-Pd,[16] and Pd-Pt;[17] and some of these nanostructures were further explored for catalytic applications. When combined with the Kirkendall effect, galvanic replacement has also been employed to convert Ag nanocubes into double-walled nanoboxes with different exterior and interior compositions.[18,19]

In recent years, many groups have explored the spatial separation of the galvanic replacement reaction on a nanoscale surface for the fabrication of nanostructures with increasingly complex morphologies and compositions. To this end, Xia and coworkers observed the oxidation of Ag could be initiated from the {111} facets or corner sites of truncated Ag nanocubes when they were reacted with a Au(III) precursor in the presence of poly(vinylpyrrolidone) (PVP).[13] They also reported the fabrication of Pd-Pt concave nanocubes through the galvanic replacement reaction between Pd nanocubes and a Pt(IV)

precursor.[20] It was shown that the Br^- ions in the reaction solution could selectively bind to and activate the {100} facets on Pd nanocubes, leading to the oxidation of Pd from the {100} facets or side faces for the deposition of Pt on the {111} facets or corners in an orthogonal manner. Liz-Marzan and coworkers reported a detailed analysis of the structural evolution of Ag nanocubes when they were reacted with $HAuCl_4$ in an organic solvent, together with the use of Cl^- ions.[21] Using electron tomography, they were able to capture the generation of a small pinhole on the side faces of nanocubes at the early stage of a synthesis, confirming that the oxidation of Ag was also initiated from the side faces due to the selective binding of Cl^- ions to the {100} facets.[22, 23] As the reaction progressed, they revealed that the oxidation of Ag atoms was continued from the center of each side face for the generation of gradually enlarged holes while the resultant Au atoms were deposited on the other regions of a nanocube, leading to the generation of octahedral nanocages made of Ag-Au alloys. Furthermore, recent studies have demonstrated the site selectivity of the galvanic replacement reaction between Ag nanocubes and a Au(III) or Pd(II) precursor in the presence of Cl^- ions, during which Ag oxidation occurred at the {100} facets of nanocubes for the deposition of Au or Pd atoms on the {110} and {111} facets and thus the formation of Ag@Ag-Au or Ag-Pd concave nanocubes.[24, 25]

In addition to these studies involving the use of monometallic nanocrystals as templates with surface inhomogeneity associated with faceting and/or capping, bimetallic systems with spatially controlled distributions of elements were also explored in recent years.[26,27] In one study, Skrabalak and coworkers used Ag-Pd dimers with a Janus structure as templates to react with various Au(III) precursors having different reduction potentials in the presence of PVP.[26] They demonstrated that the replacement of Ag was more rapidly

than Pd, leading to the creation of Ag vacancies as the Au atoms were deposited on the Ag surface. Because some of the Ag vacancies would diffuse into Pd to generate a Ag-Pd alloy, the subsequent oxidation of Ag by the Au(III) precursor would progress on both Ag and Pd surfaces for the generation of Au-based alloys on both Ag and Pd regions.[28] Wang and co-workers leveraged the use of atomically intermixed $AuCu_3$ and AuCu bimetallic nanoparticles as the sacrificial templates to react with a Au(III) precursor in an aqueous solution.[27] They established that the compositional stoichiometry and structural ordering of the Au-Cu nanoparticles played two important roles in controlling the galvanic replacement reaction for the production of complex nanostructures through an interplay of dealloying,[29-31] Kirkendall diffusion,[18,32] and Ostwald ripening.[33,34]

Despite the success in transforming mono- and bimetallic nanocrystals into hollow and/or porous nanostructures through galvanic replacement reactions, it remains a challenge to spatially confine the oxidation (dissolution) and reduction (deposition) reactions to different sites on the surface of a sacrificial template. In this chapter, I report a systematic study of the galvanic replacement reactions between various types of precursors and Ag@Ag-Au concave core-frame nanocubes, a newly developed template with well-defined spatial distributions for Ag and Au on the surface (as discussed in Chapter 2)[24]. The replacement reactions were conducted by titrating the precursor into an aqueous suspension of the core-frame nanocubes under ambient conditions and in the presence of cetyltrimethylammonium chloride (CTAC). In an orthogonal manner, the oxidation of Ag was initiated and continued from all the side faces dominated by Ag atoms while the resultant metal atoms (*e.g.*, Pt, Pd, or Au) were concurrently deposited along the edges enriched by Au atoms. By controlling the reaction stoichiometry involved, the core-frame

nanocubes were transformed into cage cubes with different compositions and hole sizes. For example, with the use of a Pt(IV) precursor such as H_2PtCl_6, Ag oxidation was initiated from the Ag-dominated regions located at the center of each side face, creating a cavity on each side face of the nanocube. Concomitantly, the Pt atoms derived from the reduction by Ag were deposited on the edges for the generation of a Ag@Ag-Au-Pt concave nanocube. As the reaction progressed, Ag oxidation was continued in the Ag-dominated region located on each side face rather than those regions where the Ag atoms had formed alloys with Au and/or Pt due to the difference in reduction potentials. Because one Pt atom would be produced at the expense of four Ag atoms during the replacement reaction, it was possible to carve away all Ag atoms from the side faces toward the center in a well-aligned, orthogonal manner. As a result, the Ag@Ag-Au-Pt concave nanocubes were transformed into nanoscale cage cubes made of a Ag-Au-Pt alloy. The same approach also works for other precursors, including Pt(II), Pd(II), and Au(III), albeit the size and exact location of the hole might vary due to the differences in stoichiometry and reduction potential.

3.2 Experimental Section

Chemicals. Ethylene glycol (EG) was ordered from J.T. Baker. Sodium hydrosulfide hydrate ($NaSH{\cdot}xH_2O$), aqueous hydrochloric acid (HCl, 37 wt.%), poly(vinylpyrrolidone) (PVP) with an average molecular weight of 55000 (PVP-55k), silver trifluoroacetate (CF_3COOAg, ≥99.99% trace metal basis), gold(III) chloride trihydrate ($HAuCl_4{\cdot}3H_2O$, ≥99.9% trace metal basis), chloroplatinic acid hexahydrate ($H_2PtCl_6{\cdot}6H_2O$, ACS reagent, ≥37.50% Pt basis), iron(III) nitrate nonahydrate ($Fe(NO_3)_3{\cdot}9H_2O$), potassium tetrachloroplatinate(II) (K_2PtCl_4, ≥99.9% trace metal basis), sodium tetrachloropalladate(II)

(Na_2PdCl_4, ≥99.99% trace metal basis), aqueous cetyltrimethylammonium chloride solution (CTAC, 25 wt.%), and L-ascorbic acid (H_2Asc, 99%) were acquired from Sigma-Aldrich (St. Louis, MO). Sodium hydroxide (NaOH, 98%) and acetone (HPLC grade, 99.5+%) were obtained from Alfa Aesar. All chemicals were used as received. All aqueous solutions were prepared using deionized (DI) water with a resistivity of 18.2 MΩ·cm at room temperature.

Synthesis of Ag Nanocubes. I synthesized Ag nanocubes with an average edge length of 40.5 ± 2.8 nm by following the published protocol.[35] After washing the Ag nanocubes with acetone and water, once each, I re-dispersed them in water for storage.

Synthesis of Ag@Ag-Au Core-frame Nanocubes. In a standard protocol, the reaction solution was prepared by mixing 2 mL of aqueous CTAC (0.1 M), 0.5 mL of aqueous H_2Asc (0.1 M), and 0.5 mL of aqueous NaOH (0.2 M) under magnetic stirring at 1150 rpm. Next, I added 23 μL of the aqueous suspension of Ag nanocubes into the reaction solution to attain a final particle concentration around 2.6×10^{11} particles/mL, followed by the titration of 0.4 mL or 0.8 mL of aqueous $HAuCl_4$ (0.1 mM) using a syringe pump at a rate of 0.02 mL/min to prepare Ag@Ag-Au concave core-frame nanocubes, namely Ag@Ag-Au-4 and Ag@Ag-Au-8 nanocubes. After the titration was completed, I collected all the nanoparticles at 7200 rpm for 11 min, removed the supernatant, and re-dispersed them in 100 μL of water.

Synthesis of the Ag@Ag-Au-Pt Concave Nanocubes and Ag-Au-Pt Cage Cubes. In a standard protocol, I added 100 μL of the as-prepared Ag@Ag-Au-4 or Ag@Ag-Au-8 nanocubes into a reaction solution containing 2 mL of aqueous CTAC (0.1 M) and 1 mL of water under magnetic stirring at 1150 rpm. Next, I titrated different volumes of aqueous

H_2PtCl_6 (0.2 mM) using a syringe pump at a rate of 0.02 mL/min. After the desired volume had been reached, I left the reaction solution under magnetic stirring for about 30 min before the solid products were collected by centrifugation at 7200 rpm for 11 min. I washed the solid products with water twice before they were re-dispersed in 1 mL of water for further use. The same protocol was also applied to other types of precursors, including K_2PtCl_4, Na_2PdCl_4, $HAuCl_4$, as well as $Fe(NO_3)_3$. In these cases, the concentrations and volumes are specified in the figure captions. In particular, $HAuCl_4$ was added at a very slow titration rate of 0.0025 mL/min.

Instrumentation and Characterization. The particles were collected using an Eppendorf 5430 centrifuge (Eppendorf North America, Hauppauge, NY). The UV-vis spectra were recorded using a Cary 60 spectrophotometer (Agilent Technologies, Santa Clara, CA). The metal contents were determined using a inductively-coupled plasma mass spectrometer (ICP-MS, NexION 300Q, PerkinElmer, Waltham, MA). Transmission electron microscopy (TEM) images were captured on a Hitachi HT7700 microscope (Tokyo, Japan) operated at 120 kV. Scanning electron microscopy (SEM) images were captured on a Hitachi SU8230 FE-SEM (Tokyo, Japan) operated at 20 kV. High-angle annular dark field scanning electron microscopy (HAADF-STEM) images were recorded on a Hitachi HD2700 C_s-corrected microscope operated at 200 kV. The energy-dispersive X-ray spectroscopy (EDS) detector on the HD2700 was used to generate an elemental mapping of the nanocrystals.

3.3 Results and Discussion

I followed my published protocol outlined in Chapter 2 to synthesize the Ag@Ag-Au core-frame nanocubes that were comprised of a Ag core and a Ag-Au alloy frame.[24] Specifically, I titrated 0.4 mL and 0.8 mL of aqueous $HAuCl_4$, respectively, into an aqueous suspension of Ag nanocubes in the presence of H_2Asc, NaOH, and CTAC to generate two types of core-frame nanocubes, namely Ag@Ag-Au-4 and Ag@Ag-Au-8. They embraced different amounts of Ag in the core and different thicknesses for the Ag-Au frame, in addition to different degrees of concaveness on their side faces. I then used the core-frame nanocubes as sacrificial templates to react with a salt precursor such as H_2PtCl_6 in the presence of CTAC. Finally, I analyzed the products using electron microscopy and UV-vis spectroscopy to examine both the structural and compositional changes during the course of galvanic reaction.

3.3.1 Proposed Mechanism for the Confined Drilling on the Side Faces of Ag Nanocubes Based on the Galvanic Replacement Reaction

Figure 3.1 shows a plausible pathway for the gradual transformation of a Ag@Ag-Au core-frame nanocube into a Ag@Ag-Au-Pt concave nanocube and then a Ag-Au-Pt cage cube through a galvanic replacement reaction. In the first step, Ag oxidation would preferentially start from the Ag-dominated regions located in the center of each side face to create a cavity while the resultant Pt atoms are deposited on the edges and corners of the nanocube, leading to the generation of a Ag@Ag-Au-Pt concave nanocube. As the galvanic reaction is continued, holes are continuously drilled in all side faces in an orthogonal but well-aligned manner while Pt atoms are concurrently deposited on the edges and corners

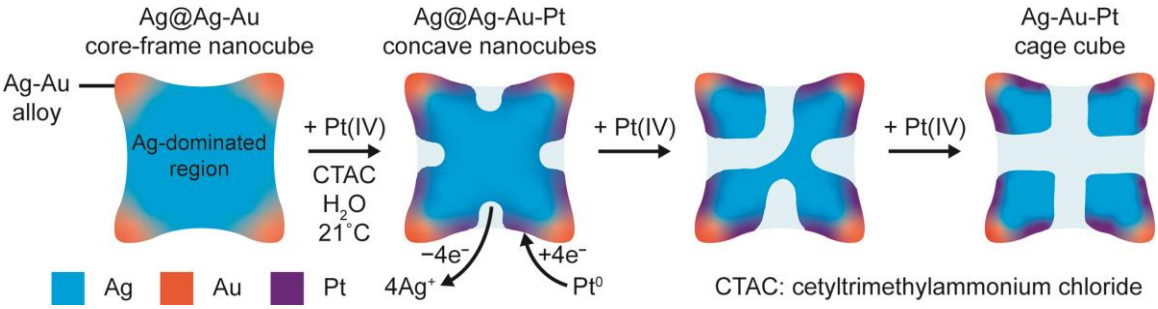

Figure 3.1. Schematic diagram illustrating the structural evolution of a Ag@Ag-Au core-frame nanocube into a Ag@Ag-Au-Pt concave cube and a Ag-Au-Pt cage cube through a galvanic replacement reaction.

followed by inter-diffusion and alloying with Ag and Au atoms. Once a thin layer of Ag-Au-Pt alloy is formed on the surface, including the areas around but not inside the cavities, Ag oxidation can be confined to the center of each side face, making it possible to continuously remove all Ag in the core for the generation of a Ag-Au-Pt cage cube. There are some differences between the cases of Ag@Ag-Au-4 and Ag@Ag-Au-8 core-frame nanocubes. For example, in the latter case, the concaveness of the side faces is increased so it becomes much easier to drill through the core even in the early stage of a synthesis. On the other hand, the greater coverage of Au on the side faces of the core-frame nanocube will significantly reduce the area of the Ag-dominated region for a better confinement of Ag oxidation to the center of each side face, leading to the generation of cage cubes containing smaller through holes.

3.3.2 Synthesis and Characterization of Ag-Au-Pt Cage Cubes

In the first set of experiments, I examined the structural and compositional evolution of Ag@Ag-Au-4 nanocubes after they had reacted with different volumes of H_2PtCl_6 in the presence of CTAC by transmission electron microscopy (TEM). Figure 3.2A shows a TEM

image of the initial core-frame nanocubes, indicating slight concaveness on their side faces. At 0.1 mL of H_2PtCl_6, Figure 3.2B shows their transformation into more concaved nanostructures, primarily due to the preferential oxidation of Ag atoms by Pt(IV) precursor from the center of each side face. At 0.4 mL of H_2PtCl_6, Figure 3.2C shows a mixture of nanocubes with different numbers of holes drilled in their side faces. This result suggests

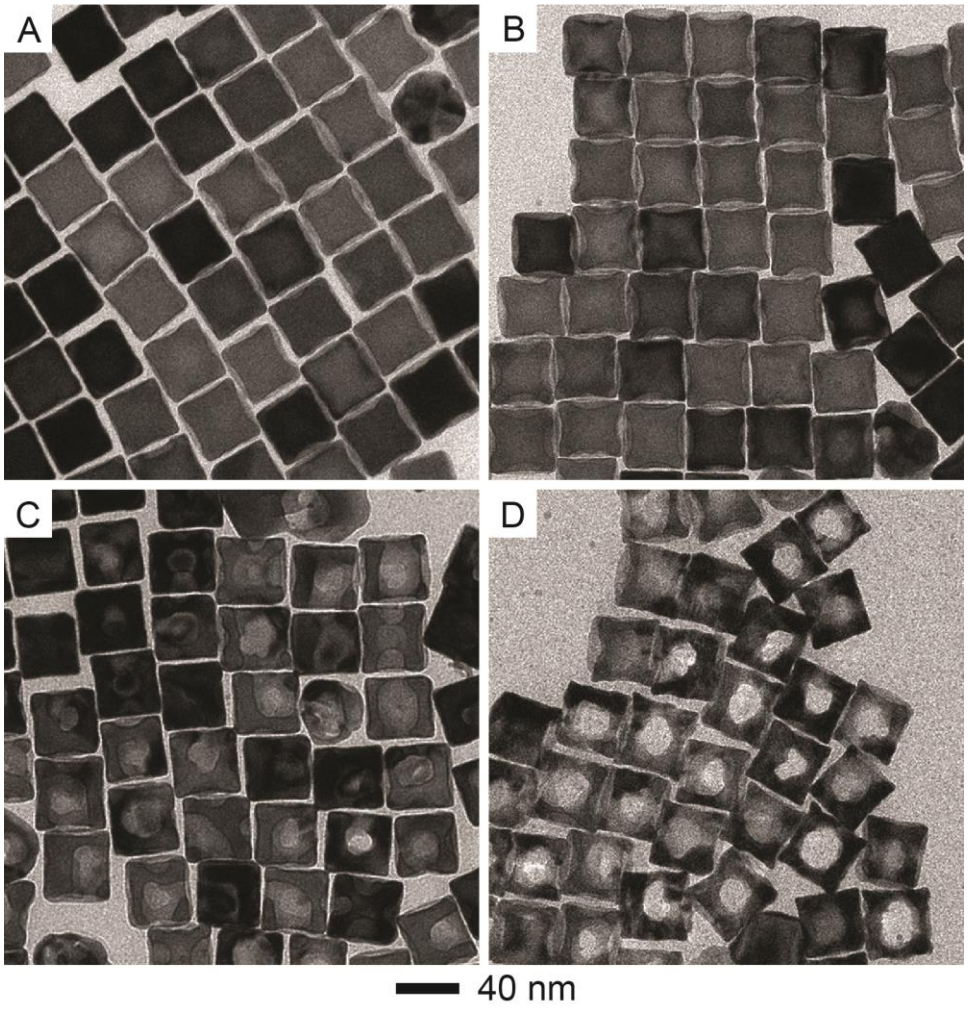

Figure 3.2. TEM images of (A) the Ag@Ag-Au-4 core-frame nanocubes prepared by reacting 0.4 mL of 0.1 mM aqueous $HAuCl_4$ with Ag nanocubes and (B-D) the solid products obtained by further titrating different volumes of aqueous H_2PtCl_6 (0.2 mM) into the suspension in the presence of CTAC. The titration volumes were (B) 0.1, (C) 0.4, and (D) 1.2 mL, respectively.

that the oxidation rates of different side faces likely differed from each other due to the variations in terms of surface defect and coverage density of capping agent such as Cl^- ions derived from CTAC. When the titration volume was increased to 1.2 mL, Figure 3.2D indicates that the product was consisted of cage cubes with orthogonal, well-aligned through holes, confirming that Ag oxidation was more or less confined to the center of each side face.

To gain a better understanding of the onset of Ag oxidation on the side faces of Ag@Ag-Au core-frame nanocubes, I used scanning electron microscopy (SEM) and aberration-corrected high-angle annular dark-field scanning TEM (HAADF-STEM) to characterize the sample prepared with the addition of 0.1 mL of H_2PtCl_6 (*i.e.*, the same shown in Figure 3.2B). Figure 3.3A shows SEM image of the sample, in which the cavities on the side faces could be easily identified. Figure 3.3B shows a HAADF-STEM image collected from one nanocube that was orientated along the <001> zone axis, confirming the presence of concaveness on the side faces. I also performed energy-dispersive X-ray spectroscopy (EDS) mapping on the same particle to resolve the spatial distributions of Ag, Au, Pt, and Cl elements. As shown in Figure 3.3, C-F, Ag followed the contour of the particle while both Au and Pt were largely confined to the edges and corners only. The signal of Pt was rather weak when compared with those of Ag and Au due to the limited amount of the deposited Pt. The Cl signal followed the trend of the Ag signal, suggesting that the CTAC-derived Cl^- ions could selectively bind to the Ag{100} facets, consistent with other findings.[22, 23] I also characterized the same particle by EDS line scanning analysis to better understand the spatial distributions of Ag, Au, and Pt elements. As shown in Figure 3.3G, the line profile of Ag shows a dip in the center of the particle, confirming

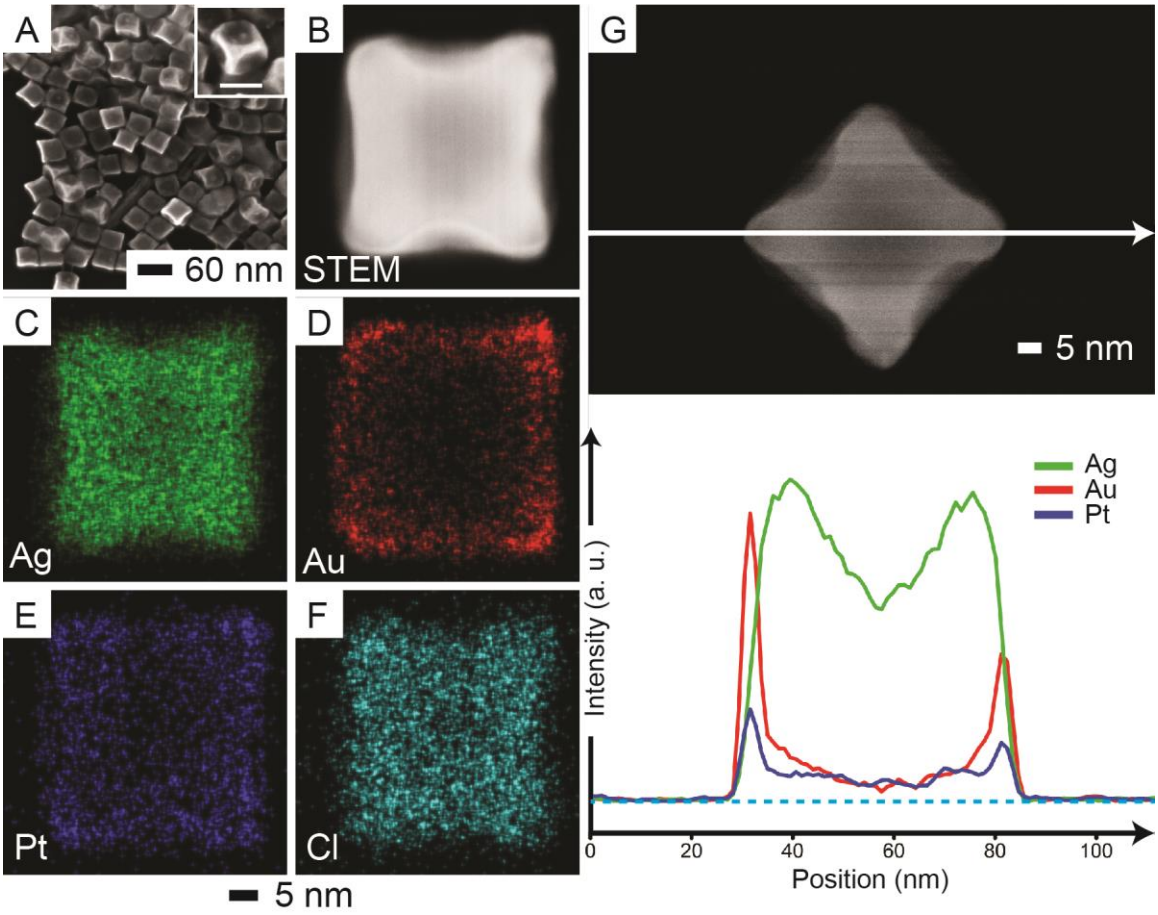

Figure 3.3. (A) SEM image of the Ag@Ag-Au-Pt concave nanocubes as shown in Figure 3.2B (inset scale bar is 40 nm) and (B) HAADF-STEM image of a single concave nanocube. (C-F) EDS mapping of the particle in (B), showing the signals from (C) Ag, (D) Au, (E) Pt, and (F) Cl, respectively. (G) HAADF-STEM image of the particle in (B) but with the raster angle rotated by 45 degrees and the corresponding EDS line-scan profiles of Ag, Au, and Pt, respectively.

the concaveness on the side face. On the other hand, the line profiles of Au and Pt indicate that both Au and Pt atoms were concentrated on the edges and corners of the particle, leaving the side faces still dominated by Ag. Because Au cannot react with Pt(IV), I argue that the Au signal should reflect the original Au distribution on the surface of the Ag@Ag-Au-4 nanocube, consistent with previous findings.[24] Altogether, I believe that the galvanic replacement reaction was initiated through the oxidation of Ag from the Ag-dominated regions located at the center of each side face due to the selective binding of Cl^- ions to

Ag{100} facets for the deposition of Pt on the edges and corners in an orthogonal manner for the generation of Ag@Ag-Au-Pt concave nanocubes. Based on the inductively-coupled plasma mass spectrometry (ICP-MS) analysis, these trimetallic concave nanocubes had an elemental composition of $Ag_{86}Au_{12}Pt_2$.

In the second set of experiments, I replaced the Ag@Ag-Au-4 nanocubes with Ag@Ag-Au-8 nanocubes to increase the thickness of the frames while keeping all other experimental conditions unchanged. Figure 3.4A shows SEM of the Ag@Ag-Au-8 nanocubes, confirming more concaved side faces when compared with those Ag@Ag-Au-4 nanocubes (see Figure 3.2A). With the addition of 0.1 mL of H_2PtCl_6, Figure 3.4B indicates the formation of small holes localized at the center of each side face, which was completely different from the product obtained by reacting the Ag@Ag-Au-4 nanocubes with the same amount of H_2PtCl_6 (see Figure 3.2B). As the reaction progressed to 0.4 mL of H_2PtCl_6, Figure 3.4C shows the formation of holes on most of the side faces in a non-uniform manner, consistent with my previous observation (see Figure 3.2C). At 1.2 mL, Figure 3.4D indicates the formation of cage cubes containing orthogonal, well-aligned through holes.

I further investigated the detailed structure and composition of the nanoframes shown in Figure 3.4D. Figure 3.5, A and B, shows SEM image of the sample and the HAADF-STEM image of one nanoframe that was orientated along the <001> zone axis, respectively, confirming the highly open structure. Figure 3.5, C-F, shows the spatial distributions of Ag, Au, Pt, and Cl, respectively, in the nanoframe. Again, the Ag signal overlapped with the profile of the particle while the Au signal was predominantly distributed at the edges and corners of the particle. On the other hand, both the Pt and Cl signals were distributed across

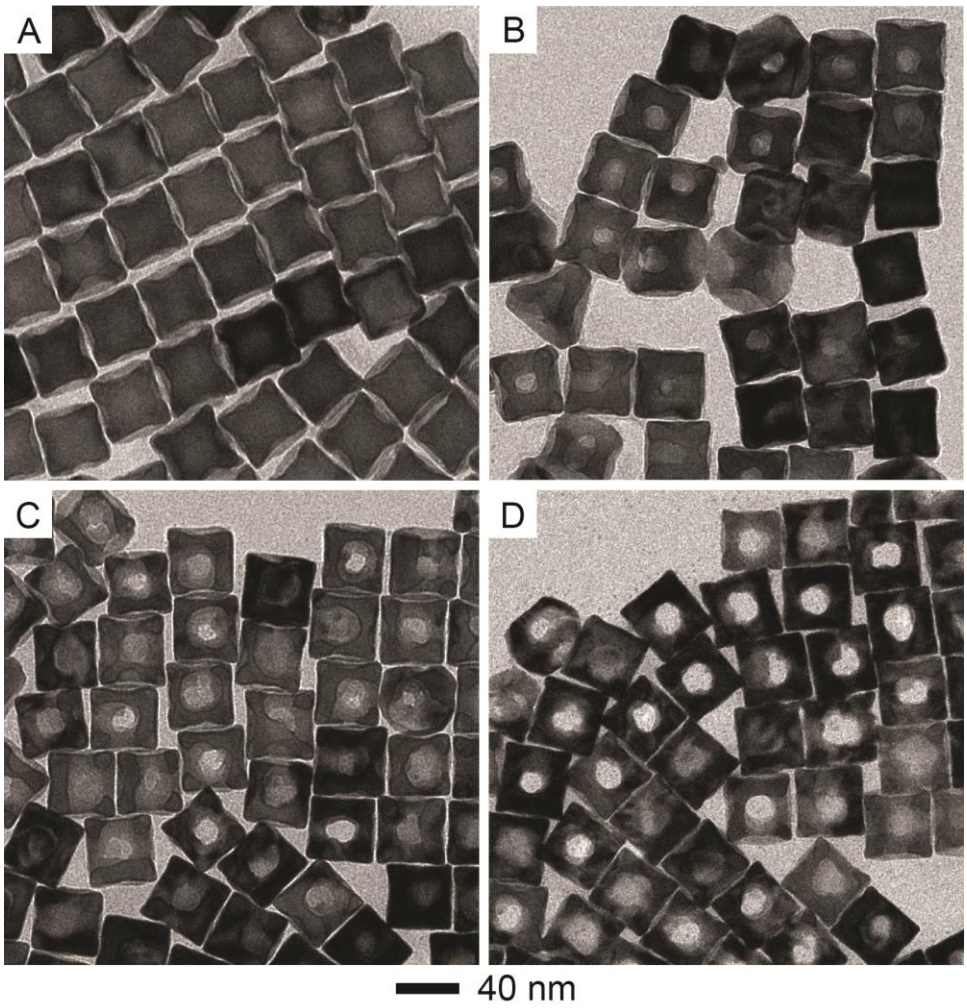

Figure 3.4. TEM images of (A) the Ag@Ag-Au-8 core-frame nanocubes prepared by reacting 0.8 mL of aqueous $HAuCl_4$ (0.1 mM) with Ag nanocubes, and (B-D) the products obtained by titrating different volumes of aqueous H_2PtCl_6 (0.2 mM) into the as-obtained suspension of Ag@Ag-Au-8 nanocubes in the presence of CTAC. The titration volumes were (B) 0.1, (C) 0.4, and (D) 1.2 mL, respectively.

the entire surface of the particle. Figure 3.5G shows the corresponding EDS line profiles of Ag, Au, and Pt, respectively. It was found that the Au signal was mostly distributed on the edges and corners with an extension toward the center of the particle, supporting my argument that more Au was deposited on the side faces of the Ag@Ag-Au-8 nanocubes than the Ag@Ag-Au-4 nanocubes. On the other hand, the Ag signal was rather weak due to the significant loss of Ag at this point of the reaction. The Pt line profile overlapped with

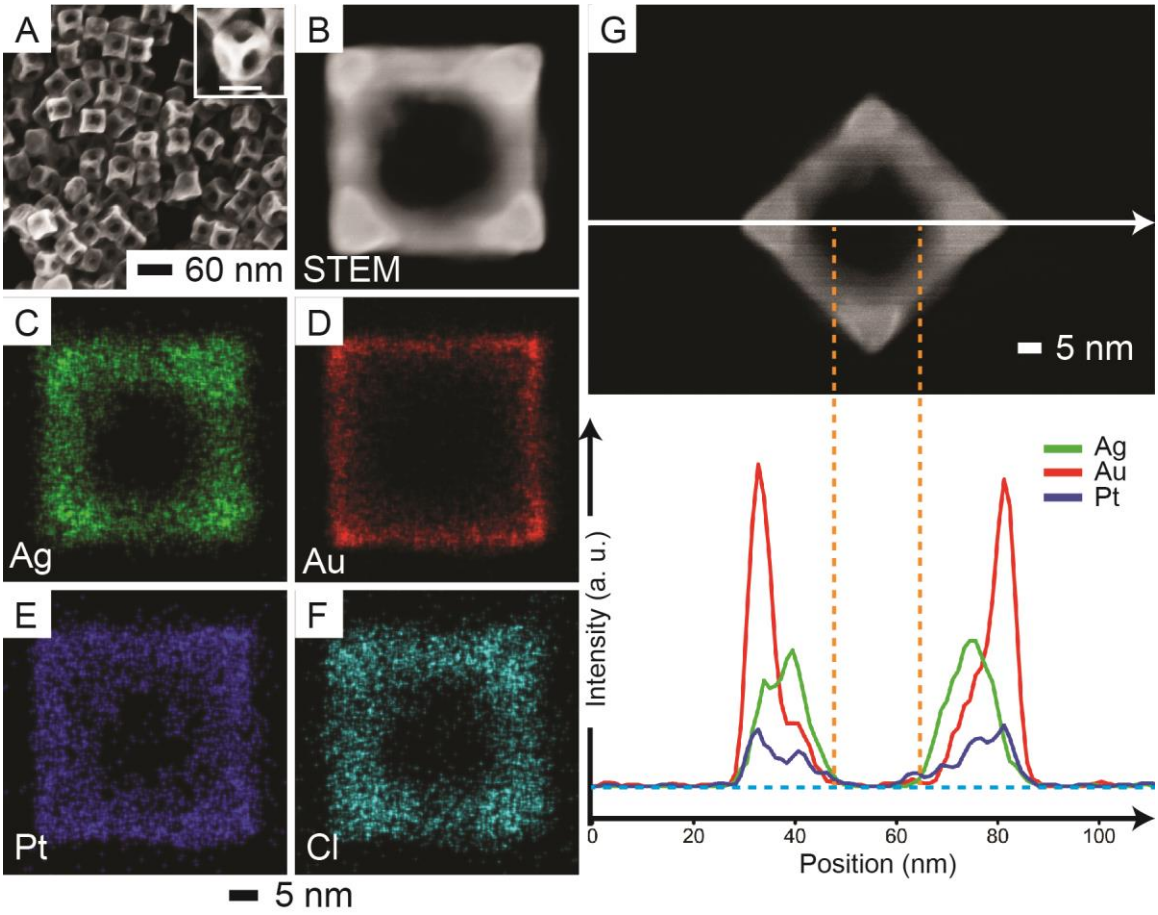

Figure 3.5. (A) SEM image of the Ag-Au-Pt cage cubes as shown in Figure 3.4D (inset scale bar is 40 nm) and (B) HAADF-STEM image of a single cage cube. (C-F) EDS mapping of the particle in (A), showing the signals from (C) Ag, (D) Au, (E) Pt, and (F) Cl, respectively. (G) HAADF-STEM image of the same particle in (A) but with the raster angle rotated by 45 degrees and the corresponding EDS line-scan profiles of Ag, Au, and Pt, respectively.

the Au line profile, suggesting the deposition of Pt on the Au-enriched regions on the particle during the galvanic reaction. There was a thin layer Pt around the holes, together with Au and Ag, making the alloy regions less reactive toward Ag oxidation from these areas. As marked by two orange dotted lines, there was essential very little signals for Ag, Au, and Pt inside the hole, indicating the Ag drilling process indeed penetrated through the entire thickness of the particle. The diameter of the hole was estimated to be around 25 nm. The ICP-MS data gave a composition of $Ag_{73}Au_{23}Pt_4$ for the trimetallic cage cubes.

Our TEM results demonstrate that both Ag@Ag-Au-4 and Ag@Ag-Au-8 nanocubes could be transformed into cage cubes made of Ag-Au-Pt alloy through a galvanic replacement reaction. I further used UV-vis spectroscopy to follow the reaction in an attempt to reveal the subtle differences arising from the difference in Au distribution on the surface of the Ag@Ag-Au nanocubes because the localized surface plasmon resonance (LSPR) properties of Ag-Au alloy nanocrystals are extremely sensitive to the change from solid to hollow nanostructures.[36, 37] Figure 3.6A shows UV-vis spectra of the Ag@Ag-Au-4 nanocubes before and after reacting with 0.1, 0.4, and 1.2 mL of H_2PtCl_6, respectively. It was found that the major LSPR peak of the Ag@Ag-Au-4 nanocubes was located at 471 nm, together with a narrow bandwidth. After reacting with 0.1 mL of H_2PtCl_6, the peak was red-shifted to 492 nm, with a slight decrease in peak intensity and a little broadening in peak width, attributing to the concave morphology of nanocrystals. At 0.4 mL, the LSPR peak was further red-shifted to 541 nm, together with a drastic decrease in peak intensity and a significant broadening in peak width, due to the emergence of cavities on the side faces of the nanocubes. At 1.2 mL, the LSPR peak became extremely weak and broad, with the peak position shifted to 813 nm, corresponding to the formation of Ag-Au-Pt cage cubes.

In comparison, Figure 3.6B shows UV-vis spectra of Ag@Ag-Au-8 nanocubes before and after reacting with 0.1, 0.4, 1.2 mL of H_2PtCl_6, respectively. The nanocubes exhibited a major peak at 490 nm because of more concaveness on the side faces. At 0.1 mL of H_2PtCl_6, the LSPR peak was red-shifted to 517 nm, together with an increase in peak width and a decrease in peak intensity. These LSPR characteristics would be attributed to the formation of cavities, consistent with the TEM results (see Figure 3.4B). As the volume of H_2PtCl_6 was increased to 0.4 mL and 1.2 mL, I noticed that the peak was continuously red-

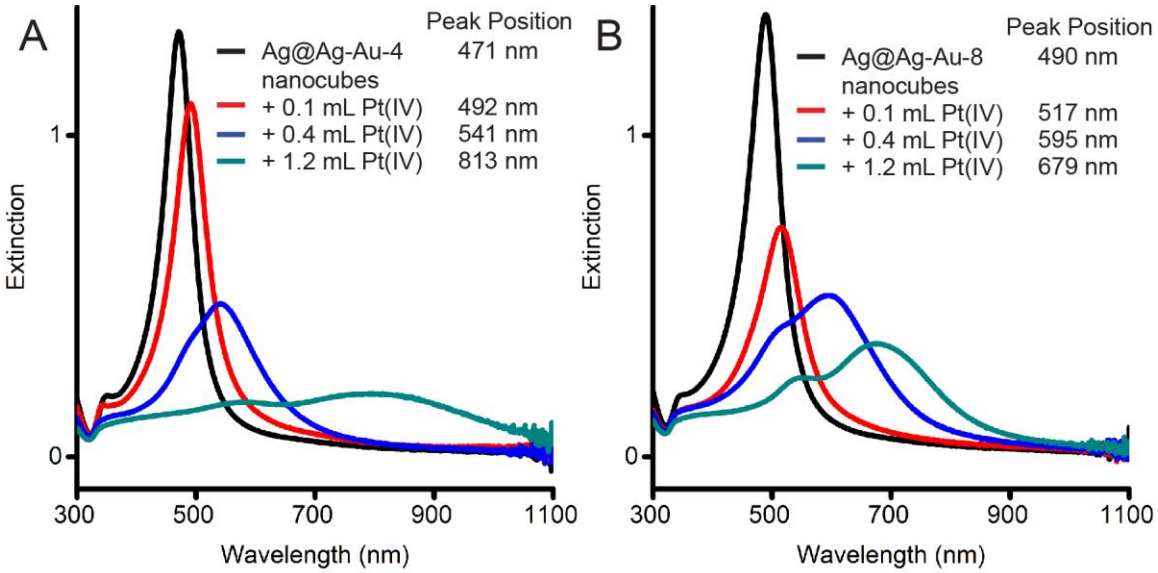

Figure 3.6. (A) UV-vis spectra of the Ag@Ag-Au-4 nanocubes before and after reacting with different volumes of aqueous H_2PtCl_6 (0.2 mM). (B) UV-vis spectra of the Ag@Ag-Au-8 nanocubes before and after reacting with different volumes of aqueous H_2PtCl_6 (0.2 mM).

shifted to 595 and 679 nm, respectively, together with a shoulder peak at 500 nm. These results indicate that the two final products would consist of two populations, consistent with the TEM images (see Figure 3.4, C and D). It is worth mentioning that, after reacting the Ag@Ag-Au-8 nanocubes with 1.2 mL H_2PtCl_6, the major peak position was located at 679 nm, while the peak was positioned at 813 nm after reacting the Ag@Ag-Au-4 nanocubes with the same amount of H_2PtCl_6. Although there is little difference in the TEM images shown in Figures, 3.2D and 3.4D, my UV-vis data suggest that the holes were better confined to the center of the cubes derived from the Ag@Ag-Au-8 nanocubes than those derived from Ag@Ag-Au-4. Taken together, I believe that the amount of Ag located in the core of the Ag@Ag-Au core-frame nanocubes, together with the distribution of Au on the surface of a cubic template, could direct the galvanic replacement reaction to produce either Ag@Ag-Au-Pt concave nanocubes or Ag-Au-Pt cage cubes, respectively.

I also argue that the drilling of Ag could become efficient by complementing Ag oxidative etching at the center of each side face of a nanocube with the deposition of Pt atoms onto the edges and corners in an orthogonal manner. To support my hypothesis, I performed another set of experiments by replacing H_2PtCl_6 with $Fe(NO_3)_3$ in the standard protocol while leaving other parameters unchanged. Different from the galvanic replacement reaction with Pt(IV) during which one Pt would be produced at the expense of four Ag atoms for its deposition on the template, the reaction with $Fe(NO_3)_3$ would produce one Fe(II) ion at the expense of one Ag and thus leave this ion in the reaction solution. Figure 3.7A shows the UV-vis spectra of the Ag@Ag-Au-8 nanocubes before and after reacting with 0.2, 0.4, 1.2, and 2.8 mL of 0.2 mM $Fe(NO_3)_3$, respectively. I noticed that the major LSPR peak of the Ag@Ag-Au-8 nanocubes was only shifted from 490 nm to 503 nm at the end of titration process, which is completely different from results obtained from the use of 0.2 mM H_2PtCl_6 (see Figure 3.5B). Figure 3.7B shows the TEM image of the final product with some cavities on the surface of the concave nanocubes, indicating that the etching of Ag was rather slow. In order to increase the etching rate, I increased the concentration of $Fe(NO_3)_3$ from 0.2 to 0.8 mM. Under this condition, Figure 3.7C shows that the major LSPR peak of the Ag@Ag-Au-8 nanocubes was shifted from 490 to 494, 513, 534, and 540 nm at the titration volume of 0.4, 1.2, 2.8, and 4.0 mL, respectively. Although Figure 3.7D shows the formation of small holes localized at the center of nanocubes in the sample prepared by 4.0 mL of $Fe(NO_3)_3$ (0.8 mM), this morphology is still very different from the cage cube nanostructures produced from the reaction of Ag@Ag-Au-8 nanocubes with 1.2 mL of H_2PtCl_6 (0.2 mM) (see Figure 3.3C). Altogether, I conclude that it would be difficult to use $Fe(NO_3)_3$ to remove Ag uniformly from the Ag-

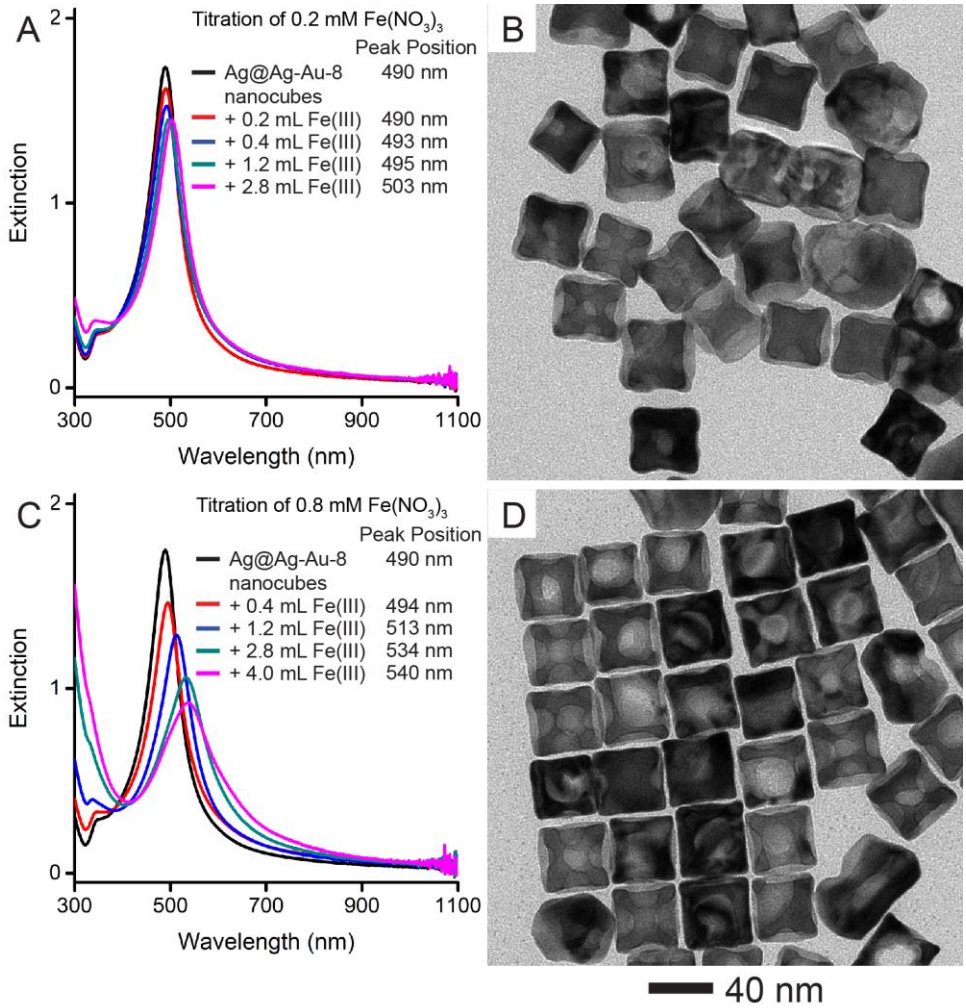

Figure 3.7. (A) UV-vis spectra of the Ag@Ag-Au-8 nanocubes before and after reacting with different volumes of aqueous $Fe(NO_3)_3$ (0.2 mM). (B) TEM image of the sample prepared by reacting 2.8 mL of aqueous $Fe(NO_3)_3$ (0.2 mM) with Ag@Ag-Au-8 nanocubes. (C) UV-vis spectra of the Ag@Ag-Au-8 nanocubes before and after reacting with different volumes of aqueous $Fe(NO_3)_3$ (0.8 mM). (D) TEM image the sample prepared by reacting 4.0 mL of aqueous $Fe(NO_3)_3$ (0.8 mM) with the Ag@Ag-Au-8 nanocubes.

dominated regions of Ag@Ag-Au nanocubes for the generation of cage cube nanostructures through galvanic replacement reaction. Part of the challenges arises from the delocalized carving of Ag across the entire surface of Ag@Ag-Au nanocubes during the reaction, suggesting that the deposition of a third metal such as Pt on the template could help confining the oxidative etching of Ag at the center more effectively.

3.3.3 Synthesis of Ag-Au-M Cage Cubes

I further extended the same strategy to the production of cage cubes with holes in different sizes by reacting the Ag@Ag-Au-8 nanocubes with other types of salt precursors, including K_2PtCl_4, Na_2PdCl_4, and $HAuCl_4$. In these experiments, I followed the standard protocol except for the replacement of H_2PtCl_6 with another precursor. It is worth acknowledging that the reaction between the Ag@Ag-Au-8 nanocubes and H_2PtCl_6 was rather slow. For example, with the titration of 1.2 mL H_2PtCl_6 (0.2 mM), my ICP-MS analysis indicated that 71% of the Pt(IV) would remain in the reaction solution at the time point of 30 min. Figure 3.8A gives UV-vis spectra of the sample before and after the reaction had progressed for 240 min. It was found that the LSPR peak of the Ag@Ag-Au nanocubes was further red-shifted to 736 nm when compared with the peak located at 679 nm (Figure 3.6B). Figure 3.8B shows a TEM image of the product, implying the transformation of the Ag@Ag-Au nanocubes into nanocages. In comparison, the reaction

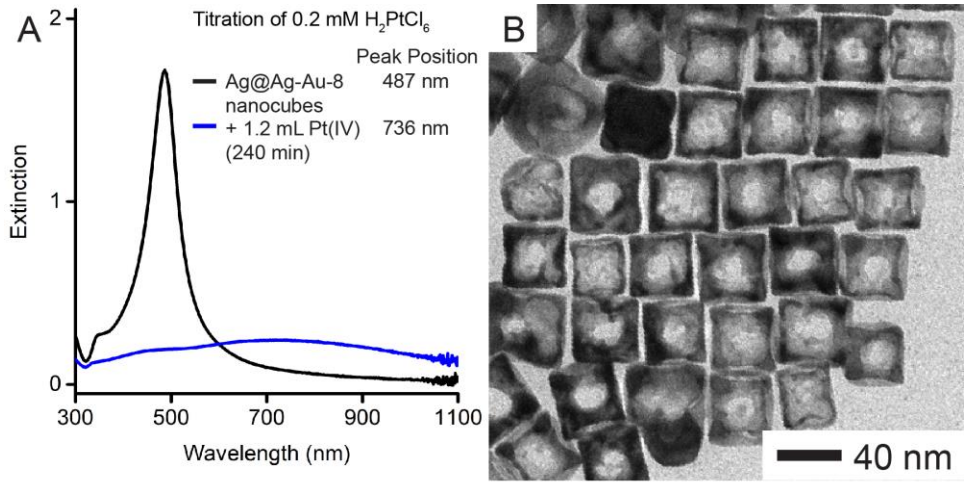

Figure 3.8. (A) UV-vis spectra of Ag@Ag-Au-8 nanocubes before and after reacting with 1.2 mL H_2PtCl_6 (0.2 mM) at the reaction time point of 240 min. (B) TEM image of the product.

between the Ag@Ag-Au-8 nanocubes with other precursors would complete within 30 min because the UV-vis spectra showed almost no change beyond this time point. Under this circumstance, I titrated smaller volumes of the new precursors into the reaction solution.

Figure 3.9A shows UV-vis spectra of Ag@Ag-Au-8 nanocubes before and after reacting with 0.2 mL K_2PtCl_4 (0.2 mM), from which I observed the red-shift of the major LSPR peak from 490 to 515 nm. Figure 3.9B gives a TEM image of the product that includes some cage cubes with relatively small holes in the center. Because one Pt atom was generated at the expense of two Ag atoms during the galvanic replacement between Ag and Pt(II) precursor, I argue that the carving of Ag would become less efficient, leading to the formation of smaller holes. When the titration volume was increased from 0.2 to 0.4 mL, I noticed that the major LSPR peak was shifted from 490 to 511 nm (Figure 3.10A), similar to the trend shown in Figure 3.8A. As shown by the TEM image in Figure 3.10B, Ag was also removed from regions other than the center for the formation of pits on the side faces of a nanocube. Different from H_2PtCl_6, K_2PtCl_4 could react with Ag in the Ag-Pt alloy region through galvanic replacement reaction, making it more difficult to confine the drilling of Ag to the center of each side face.

When I replaced the Pt(II) with a Pd(II) precursor such as Na_2PdCl_4, Figure 3.9C shows UV-vis spectra of the Ag@Ag-Au-8 nanocubes before and after reacting with 0.2 mL Na_2PdCl_4 (0.2 mM), indicating more significant red-shift of the major LSPR peak from 489 to 574 nm. Figure 3.9D shows a TEM image of the product, revealing the generation of cage cubes with holes larger than those derived from K_2PtCl_4. Such a change could be attributed to the difference in reduction potential between these two precursors. As the titration volume was increased to 0.4 mL, the LSPR peak was further shifted to 628 nm

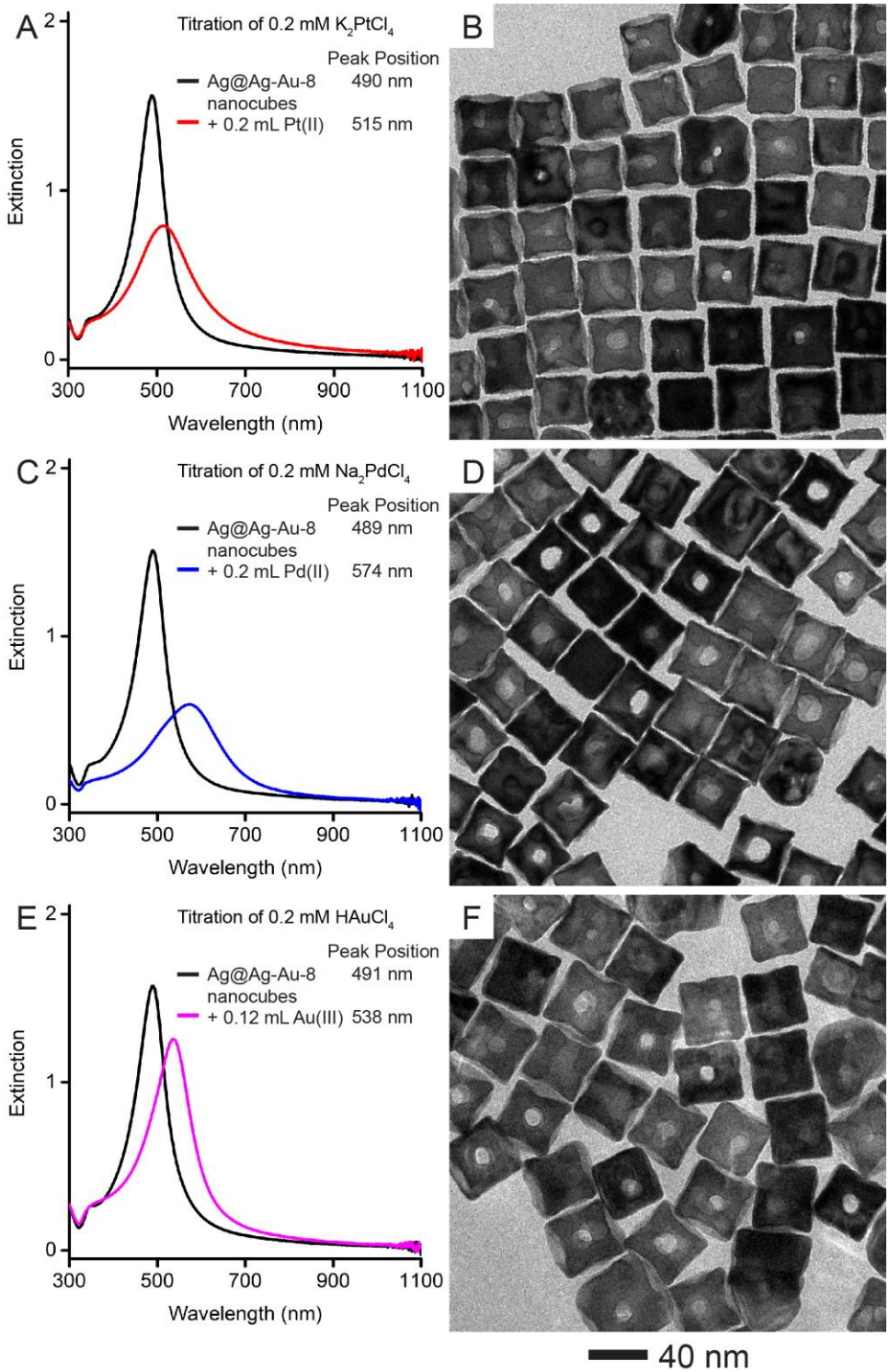

Figure 3.9. (A) UV-vis spectra of the Ag@Ag-Au-8 nanocubes before and after reacting with 0.2 mL of aqueous K_2PtCl_4 (0.2 mM). (B) TEM image of the product. (C) UV-vis spectra of the Ag@Ag-Au-8 nanocubes before and after reacting with 0.2 mL of aqueous Na_2PdCl_4 (0.2 mM). (D) TEM image of the product. (E) UV-vis spectra of the Ag@Ag-Au-8 nanocubes before and after reacting with 0.12 mL of aqueous $HAuCl_4$ (0.2 mM). (F) TEM image of the product.

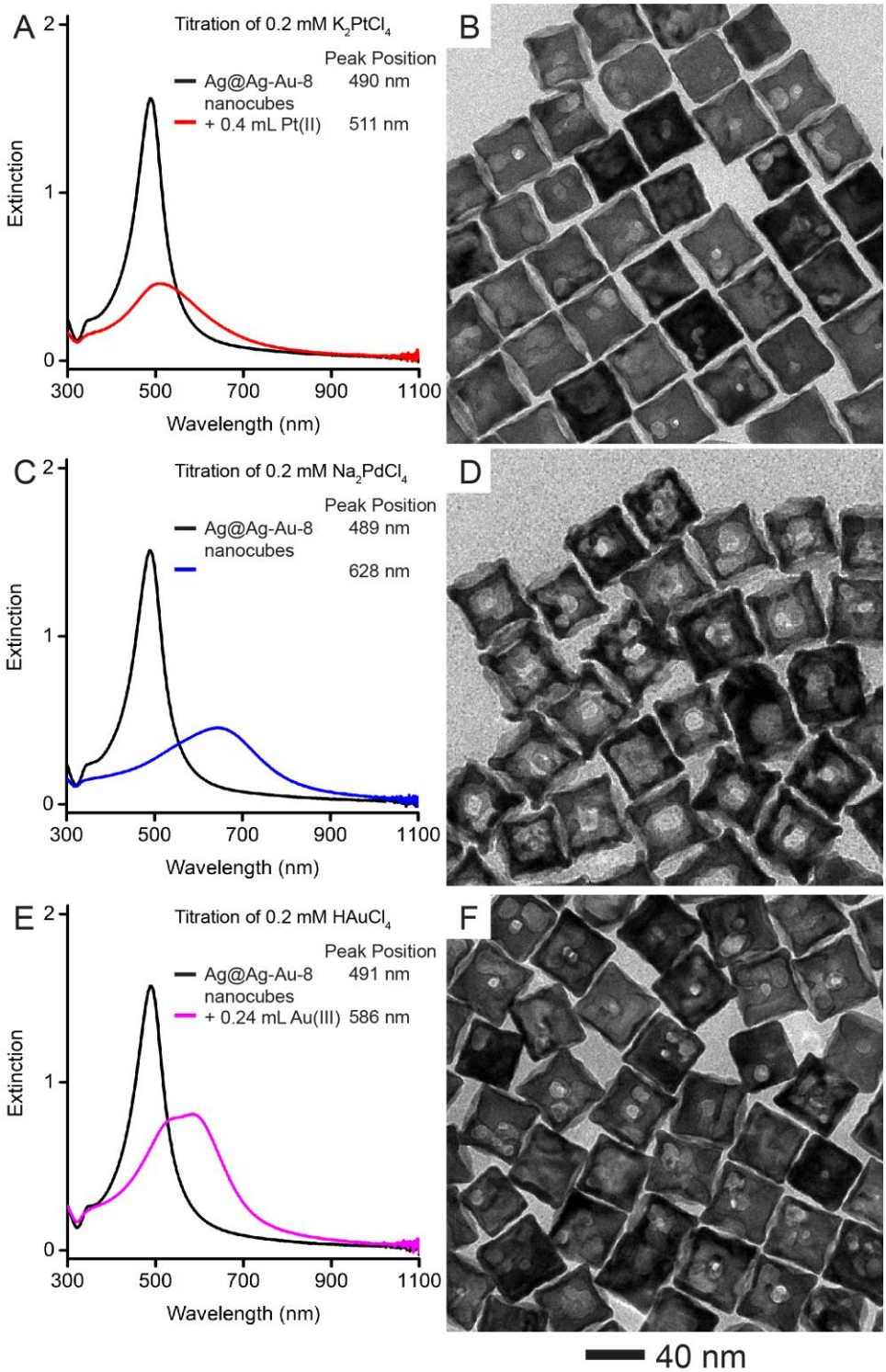

Figure 3.10. (A) UV-vis spectra of Ag@Ag-Au-8 nanocubes before and after reacting with 0.4 mL K_2PtCl_4 (0.2 mM). (B) TEM image of the product. (C) UV-vis spectra of the Ag@Ag-Au-8 nanocubes before and after reacting with 0.4 mL of aqueous Na_2PdCl_4 (0.2 mM). (D) TEM image of the product. (E) UV-vis spectra of the Ag@Ag-Au-8 nanocubes before and after reacting with 0.24 mL of aqueous $HAuCl_4$ (0.2 mM). (F) TEM image of the product.

(Figure 3.10C). The TEM image in Figure 3.10D indicates the formation of nanoframes with rough edges. I also conducted an experiment with $HAuCl_4$ for the generation of bi-metallic cage cubes. Because Au(III) is very easy to be reduced and the galvanic replacement reaction would produce one Au at the expenses of three Ag atoms, I used a smaller titration volumes and a slower titration rate. Figure 3.9E shows UV-vis spectra of the Ag@Ag-Au-8 nanocubes before and after reacting with 0.12 mL $HAuCl_4$ (0.2 mM). It was found that the LSPR peak was changed from 491 to 538 nm. Based on the TEM image in Figure 3.9F, cage cubes were also obtained. As the titration volume was increased to 0.24 mL, the LSPR peak was further shifted to 586 nm (Figure 3.10E). The TEM image in Figure 3.10F indicates the formation of pits on the side faces of a nanocube. Similar to the case of Pt(II), Au also inter-diffuse with Ag for the formation of a Ag-Au alloy. Taken together, my results suggest that it is possible to tailor the experimental conditions such as the concentration of the precursor and the titration rate to optimize the galvanic replacement reaction or the generation of cage cubes. The size of holes would strongly depend on the stoichiometry involved, as well as the reduction potential of the precursor.

3.4 Conclusions

In summary, I developed a facile route to the generation of multi-metallic cage cubes by drilling through all the side faces of Ag nanocubes. This success relies on the use of Ag@Ag-Au core-frame nanocubes with Ag in the core and Ag-Au alloy frames along the corners and edges of a nanocube to confine the drilling of Ag to the center of each side face, and ultimately to align the intersected holes with the center of the nanocube. In a typical protocol, I dispersed Ag@Ag-Au core-frame nanocubes in an aqueous solution containing

CTAC, followed by the titration of an aqueous solution of a salt precursor such as H_2PtCl_6, K_2PtCl_4, Na_2PdCl_4, or $HAuCl_4$ under ambient conditions. Depending on the stoichiometry and reduction potential of the salt precursor, a simple galvanic replacement reaction between the Ag@Ag-Au nanocubes and the precursor could produce multi-metallic cage cubes with holes of different sizes. At the early stage of a synthesis, because the Cl^- ions derived from CTAC could bind selectivity toward the Ag(100) surface, the oxidation of Ag would preferentially started from the Ag-dominated regions located at the center of each side face of a nanocube for the creation of a cavity while the resultant metal atoms are deposited on the edges and corners in an orthogonal manner. As the Ag atoms are removed from the side faces in the form of Ag(I) ions for the generation of other metals followed by their deposition on the edges and corners of nanocubes, I could achieve the continuous carving of Ag atoms from the center of a core-frame nanocube for its ultimate transformation into a cage cube enclosed by a Ag-Au-Pt, Ag-Au-Pd, or Ag-Au alloy, together with three orthogonal, intersected holes.

3.5 Notes to Chapter 3

This chapter was adapted from the manuscript "Fabrication of Nanoscale Cage Cubes by Drilling Orthogonal, Intersected Holes through All Six Side Faces of Ag Nanocubes," under revision for publication in *Chemistry of Materials*.[38]

3.6 References

(1) Rosi, N. L.; Mirkin, C. A. Nanostructures in Biodiagnostics. *Chem. Rev.* **2005,** *105*, 1547-1562.

(2) Huang, X.; El-Sayed, I. H.; Qian, W.; El-Sayed, M. A. Cancer Cell Imaging and Photothermal Therapy in the Near-Infrared Region by Using Gold Nanorods. *J. Am.*

Chem. Soc. **2006,** *128*, 2115-2120.

(3) Xia, Y.; Li, W.; Cobley, C. M.; Chen, J.; Xia, X.; Zhang, Q.; Yang, M.; Cho, E. C.; Brown, P. K. Gold Nanocages: From Synthesis to Theranostic Applications. *Acc. Chem. Res.* **2011,** *44*, 914-924.

(4) Kim, S.-W.; Kim, M.; Lee, W. Y.; Hyeon, T. Fabrication of Hollow Palladium Spheres and Their Successful Application to the Recyclable Heterogeneous Catalyst for Suzuki Coupling Reactions. *J. Am. Chem. Soc.* **2002,** *124*, 7642-7643.

(5) Zeng, J.; Zhang, Q.; Chen, J.; Xia, Y. A Comparison Study of the Catalytic Properties of Au-Based Nanocages, Nanoboxes, and Nanoparticles. *Nano Lett.* **2010,** *10*, 30-35.

(6) Mahmoud, M. A.; Narayanan, R.; El-Sayed, M. A. Enhancing Colloidal Metallic Nanocatalysis: Sharp Edges and Corners for Solid Nanoparticles and Cage Effect for Hollow Ones. *Acc. Chem. Res.* **2013,** *46*, 1795-1805.

(7) Mahmoud, M. A.; El-Sayed, M. A. Gold Nanoframes: Very High Surface Plasmon Fields and Excellent Near-Infrared Sensors. *J. Am. Chem. Soc.* **2010,** *132*, 12704-12710.

(8) Pérez-Juste, J.; Pastoriza-Santos, I.; Liz-Marzán, L. M.; Mulvaney, P. Gold nanorods: Synthesis, characterization and applications. *Coord. Chem. Rev.* **2005,** *249*, 1870-1901.

(9) Xie, H.-N.; Larmour, I. A.; Smith, W. E.; Faulds, K.; Graham, D. Surface-Enhanced Raman Scattering Investigation of Hollow Gold Nanospheres. *J. Phys. Chem. C* **2012,** *116*, 8338-8342.

(10) Yang, Y.; Zhang, Q.; Fu, Z.-W.; Qin, D. Transformation of Ag Nanocubes into Ag–Au Hollow Nanostructures with Enriched Ag Contents to Improve SERS Activity and Chemical Stability. *ACS Appl. Mater. Interfaces* **2014,** *6*, 3750-3757.

(11) Schlücker, S. Surface-Enhanced Raman Spectroscopy: Concepts and Chemical Applications. *Angew. Chem. Int. Ed.* **2014,** *53*, 4756-4795.

(12) Liu, K.; Bai, Y.; Zhang, L.; Yang, Z.; Fan, Q.; Zheng, H.; Yin, Y.; Gao, C. Porous Au–Ag Nanospheres with High-Density and Highly Accessible Hotspots for SERS Analysis. *Nano Lett.* **2016,** *16*, 3675-3681.

(13) Chen, J.; McLellan, J. M.; Siekkinen, A.; Xiong, Y.; Li, Z.-Y.; Xia, Y. Facile Synthesis of Gold−Silver Nanocages with Controllable Pores on the Surface. *J. Am. Chem. Soc.* **2006,** *128*, 14776-14777.

(14) Sun, Y.; Mayers, B.; Xia, Y. Metal Nanostructures with Hollow Interiors. *Adv. Mater.* **2003,** *15*, 641-646.

(15) Zhang, W.; Yang, J.; Lu, X. Tailoring Galvanic Replacement Reaction for the Preparation of Pt/Ag Bimetallic Hollow Nanostructures with Controlled Number of Voids. *ACS Nano* **2012,** *6*, 7397-7405.

(16) Sutter, E.; Jungjohann, K.; Bliznakov, S.; Courty, A.; Maisonhaute, E.; Tenney, S.; Sutter, P. In situ liquid-cell electron microscopy of silver–palladium galvanic replacement reactions on silver nanoparticles. *Nat. Commun.* **2014,** *5*, 4946.

(17) Hong, J. W.; Kang, S. W.; Choi, B.-S.; Kim, D.; Lee, S. B.; Han, S. W. Controlled Synthesis of Pd–Pt Alloy Hollow Nanostructures with Enhanced Catalytic Activities for Oxygen Reduction. *ACS Nano* **2012,** *6*, 2410-2419.

(18) González, E.; Arbiol, J.; Puntes, V. F. Carving at the Nanoscale: Sequential Galvanic Exchange and Kirkendall Growth at Room Temperature. *Science* **2011,** *334*, 1377-1380.

(19) Ruditskiy, A.; Xia, Y. The Science and Art of Carving Metal Nanocrystals. *ACS Nano* **2017**, *11*, 23-27.

(20) Zhang, H.; Jin, M.; Wang, J.; Li, W.; Camargo, P. H. C.; Kim, M. J.; Yang, D.; Xie, Z.; Xia, Y. Synthesis of Pd−Pt Bimetallic Nanocrystals with a Concave Structure through a Bromide-Induced Galvanic Replacement Reaction. *J. Am. Chem. Soc.* **2011,** *133*, 6078-6089.

(21) Goris, B.; Polavarapu, L.; Bals, S.; Van Tendeloo, G.; Liz-Marzán, L. M., Monitoring Galvanic Replacement Through Three-Dimensional Morphological and Chemical Mapping. *Nano Lett.* **2014,** *14*, 3220-3226.

(22) Zhang, J.; Liu, J.; Xie, Z.-X.; Qin, D. HAuCl4: A Dual Agent for Studying the Chloride-Assisted Vertical Growth of Citrate-Free Ag Nanoplates with Au Serving as a Marker. *Langmuir* **2014,** *30*, 15520-15530.

(23) Zhou, S.; Li, J.; Gilroy, K. D.; Tao, J.; Zhu, C.; Yang, X.; Sun, X.; Xia, Y. Facile Synthesis of Silver Nanocubes with Sharp Corners and Edges in an Aqueous Solution. *ACS Nano* **2016,** *10*, 9861-9870.

(24) Ahn, J.; Wang, D.; Ding, Y.; Zhang, J.; Qin, D. Site-Selective Carving and Co-Deposition: Transformation of Ag Nanocubes into Concave Nanocrystals Encased by Au–Ag Alloy Frames. *ACS Nano* **2018,** *12*, 298-307.

(25) Luo, Z.; Ahn, J.; Qin, D. Fabrication of Ag–Pd concave nanocrystals through facet-selective oxidation of Ag atoms. *Nanoscale* **2019**.

(26) Chen, A. N.; McClain, S. M.; House, S. D.; Yang, J. C.; Skrabalak, S. E. Mechanistic Study of Galvanic Replacement of Chemically Heterogeneous Templates. *Chem. Mater.* **2019,** *31*, 1344-1351.

(27) Li, G. G.; Sun, M.; Villarreal, E.; Pandey, S.; Phillpot, S. R.; Wang, H. Galvanic Replacement-Driven Transformations of Atomically Intermixed Bimetallic Colloidal Nanocrystals: Effects of Compositional Stoichiometry and Structural Ordering. *Langmuir* **2018,** *34*, 4340-4350.

(28) Lutz, P. S.; Bae, I.-T.; Maye, M. M. Heterostructured Au/Pd–M (M = Au, Pd, Pt) nanoparticles with compartmentalized composition, morphology, and electrocatalytic activity. *Nanoscale* **2015,** *7*, 15748-15756.

(29) Williams, D. E.; Newman, R. C.; Song, Q.; Kelly, R. G. Passivity breakdown and pitting corrosion of binary alloys. *Nature* **1991,** *350*, 216-219.

(30) Erlebacher, J.; Aziz, M. J.; Karma, A.; Dimitrov, N.; Sieradzki, K. Evolution of nanoporosity in dealloying. *Nature* **2001,** *410*, 450-453.

(31) Li, X.; Chen, Q.; McCue, I.; Snyder, J.; Crozier, P.; Erlebacher, J.; Sieradzki, K. Dealloying of Noble-Metal Alloy Nanoparticles. *Nano Lett.* **2014,** *14*, 2569-2577.

(32) Nakajima, H. The discovery and acceptance of the Kirkendall Effect: The result of a short research career. *JOM* **1997,** *49*, 15-19.

(33) Viswanatha, R.; Sarma, D. D. *Growth of Nanocrystals in Solution*. 2007.

(34) Zhang, Z.; Wang, Z.; He, S.; Wang, C.; Jin, M.; Yin, Y. Redox reaction induced Ostwald ripening for size- and shape-focusing of palladium nanocrystals. *Chem. Sci.* **2015,** *6*, 5197-5203.

(35) Skrabalak, S. E.; Au, L.; Li, X.; Xia, Y. Facile synthesis of Ag nanocubes and Au nanocages. *Nat. Protoc.* **2007,** *2*, 2182-2190.

(36) Kelly, K. L.; Coronado, E.; Zhao, L. L.; Schatz, G. C. The Optical Properties of Metal Nanoparticles: The Influence of Size, Shape, and Dielectric Environment. *J. Phys. Chem. B* **2003,** *107*, 668-677.

(37) Tao, A. R.; Habas, S.; Yang, P. Shape Control of Colloidal Metal Nanocrystals. *Small* **2008,** *4*, 310-325.

(38) Ahn, J.; Qin, D. Fabrication of Nanoscale Cage Cubes by Drilling Orthogonal, Intersected Holes through All Six Side Faces of Ag Nanocubes. *Chem. Mater.*, in press (under revision).

CHAPTER 4. ORTHOGONAL DEPOSITION OF AU ON DIFFERENT FACETS OF AG CUBOCTAHEDRA FOR THE FABRICATION OF NANOBOXES WITH COMPLEMENTARY SURFACES

4.1 Introduction

As it has been extensively discussed in previous chapters that the morphology of noble metal nanocrystals (such as concave or hollow features) serves as a key parameter in determining their properties, it is also very important to consider the particular roles played by the different facets present on the surface of noble metal nanocrystals for their applications in plasmonics and catalysis,[1-4] In particular, it is well-established that the distinctive activity and selectivity of metal nanocrystals in catalytic reactions explicitly depend on the arrangment of atoms situated on the outermost layer of different facets.[5-8] In the past, there has been a growing effort in the rational design and synthesis of metal nanocrystals with well-defined facets. Among those, seed-mediated growth of metal nanocrystals has shown remarkable success in offering a fine control over the geometry of the products by directly depositing the atoms on the facets of preformed seeds.[9-11] It is well known that the introduction of ligands into the growth solution could facilitate their selective chemisorption on different types of facets due to the differences in the binding affinity,[12] making it possible to manuever the growth rates on different facets and thus control the relative surface areas of different facets on the final products.[13, 14] For example, Xia and co-workers demonstrated the transfomration of Ag nanocubes into cuboctahedra by introducing citrate in a reaction solution to bind on the {111} facets of Ag nanocubes.[15] It was found that the Ag atoms would be preferentially deposited on the {100} facets to

accelerate their growth along <100> directions, leading to the evolution of a cube into a cuboctahedron. Another study reported the reversible transformation between Ag nanoplates and Ag twinned cubes, elucidating the role of Cl^- ions in deterring the deposition and etching of Ag atoms along the <100> direction and allowing the deposition and etching along the <111> direction.[16, 17] Recently, Mirkin and co-workers demonstrated the generation of Au octahedra with hollow features by stabilizing the {111} facets of Au concave cubes through the underpotential deposition (UPD) of Ag^+ ions,[18] during which the growth of Au occured almost exclusively on the corners of the cubic seeds. On the other hand, many groups have demonstrated the generation of bimeallic core-frame and core-shell nanocrystals by selectively depositing the metal on the small areas of edges and the entire surfaces of preformed nanocrystal seeds with the involvement of different ligands in the reaction solutions.[19-25] Despite remarkable success, the previous studies involve the use of nanocrystal seeds, such as cubes, plates, and octahedra, with a single type of facets on their surfaces.

In this Chapter, I document the facet-selected, orthogonal deposition of Au on Ag cuboctahedra enclosed by a mix of {100} and {111} facets at a ratio of about 1:1.7 in terms of surface area. In a typical synthesis, I dispersed Ag cuboctahedra in an aqueous solution containing ascobic acid (H_2Asc), NaOH, poly(vinylpyrrolidone) (PVP) or cetyltrimethylammonium chloride (CTAC). This success relies on the use of PVP or CTAC to instigate the Ag oxidation on the {111} or {100} facets, respectively, making it possible to control the deposition pathways for Au atoms on the {100} or {111} facets in the orthongal manner for the generation of Ag@$Au_{\{100\}}$ cuboctahdra or Ag@Ag-$Au_{\{111\}}$ concave cuboctahedra. When the Ag in the core is subjected to removal by etching, I

demonstrate the transformation of solids into Ag-Au$_{\{100\}}$ or Ag-Au$_{\{111\}}$ cuboctahedral nanoboxes with complementary surfaces.

4.2 Experimental Section

Chemicals. Ethylene glycol (EG) was purchased from J. T. Baker. Silver trifluoroacetate (CF_3COOAg, 98%), gold(III) chloride trihydrate ($HAuCl_4 \cdot 3H_2O$, 99.9+%), sodium hydrosulfide hydrate ($NaHS \cdot xH_2O$), poly(vinylpyrrolidone) (PVP) with an average molecular weight of 29,000 (PVP–29) or 55,000 (PVP–55), aqueous hydrochloric acid (HCl, 37 wt. %), acetone (99.5+%), L-ascorbic acid (H_2Asc, 99%), sodium citrate tribasic dihydrate (citrate, 99.0+%), silver nitrate ($AgNO_3$, 99.0+%), aqueous cetyltrimethylammonium chloride solution (CTAC, 25 wt.%), and aqueous hydrogen peroxide (H_2O_2, 30wt.%), 4-nitrophenol (4-NP), and sodium borohydride ($NaBH_4$, 99.99%) were purchased from Sigma-Aldrich. Sodium hydroxide (NaOH, 98%) and acetone (HPLC grade, 99.5+%) were obtained from Alfa Aesar. All chemicals were used as received. All the aqueous solutions were prepared using DI water with a resistivity of 18.2 MΩ·cm at 25 °C.

Synthesis of Ag nanocubes. I followed the protocol reported by Xia and co-workers for the synthesis of Ag nanocubes with an average edge length of 38.1 ± 2.0 nm.[26] The as-obtained Ag nanocubes were washed with acetone and DI water twice and then dispersed in water for further use.

Synthesis of Ag cuboctahedra. I used the as-obtained Ag nanocubes as seeds to grow Ag cuboctahedra.[15] In a typical process, 34 μL of the aqueous suspension of Ag nanocubes (approximately 7.10×10^{10} particles per mL) was injected into an aqueous

solution in a 23-mL glass vial containing 5 mL of PVP-55 (2 mg/mL), 100 μL of H_2Asc (0.1 M), and 50 μL of citrate (20 mM) l under magnetic stirring at room temperature. Next, I used a syringe pump to titrate 1.5 mL of aqueous $AgNO_3$ (1 mM) into the reaction solution at a rate of 5 mL/h. Upon the completion of titration, the mixture was centrifuged at 1000 rpm for 10 min to precipitate out the larger random particles before the supernatant was centrifuged at 8000 rpm for 10 min to collect the solids. Finally, the as-prepared nanocrystals were washed with water twice before they were re-dispersed to 100 μL of water for further use. The Ag cuboctahedra had an average edge length of 47.2 ± 2.2 nm.

Synthesis of Ag@Au$_{\{100\}}$ cuboctahedra. In a typical process, 2 mL of aqueous PVP-29 (1 mM) was placed in a 23-mL glass vial, followed by the addition of 0.5 mL of aqueous H_2Asc (0.1 M), 0.5 mL of aqueous NaOH (0.2 M), and 30 μL of an aqueous suspension of the Ag cuboctahedra (approximately 4.23×10^{10} particles per mL) under magnetic stirring at room temperature. Next, I introduced 0.4 mL of aqueous $HAuCl_4$ (0.1 mM) into the reaction solution using a syringe pump at an injection rate of 1 mL/min. After the completion of titration, the reaction solution was left undisturbed for 5 min before I collected the solid products by centrifugation at 6300 rpm for 10 min and then washed with water three times prior to characterization.

Synthesis of Ag-Au$_{\{100\}}$ cuboctahedral nanoboxes. I mixed 50 μL of the as-prepared Ag@Au$_{\{100\}}$ cuboctahedra with 50 μL of aqueous NaCl (10 mM), followed by the addition of 0.7 mL of PVP-29 (1 mM) and 0.3 mL of H_2Asc (0.1 M) at room temperature. After 20 min of treatment, I collected the particles by centrifugation at 5000 rpm for 15 min, washed with water once, and then introduced the particles into 1 mL of 3% aqueous H_2O_2 at room temperature. After 3 h, the hollow particles were collected by

centrifugation at 13000 rpm for 10 min, washed with water twice, and then re-dispersed in 50 μL of water for both characterization and evaluation of catalytic properties.

Synthesis of Ag@Ag-Au$_{\{111\}}$ concave cuboctahedra. In a typical process, I placed 2 mL of aqueous CTAC (0.1 M) to a 23-mL glass vial, followed by the addition of 0.5 mL of aqueous H_2Asc (0.1 M), 0.5 mL of aqueous NaOH (0.2 M), and 30 μL of an aqueous suspension of the Ag cuboctahedra (approximately 4.23×10^{10} particles per mL) under magnetic stirring at room temperature. Next, I titrated 0.8 mL of aqueous $HAuCl_4$ (0.1 mM) into the reaction solution using a syringe pump at a rate of 0.02 mL/min. Immediately after the titration, I collected the particles by centrifugation at 4800 rpm for 11 min and washed with water once for characterization and further use.

Synthesis of Ag-Au$_{\{111\}}$ cuboctahedral nanoboxes. I dispersed 50 μL of the as-prepared Ag@Au$_{\{111\}}$ cuboctahedra in 1 mL of 3% aqueous H_2O_2 for etching at room temperature. After 3 h of etching, I collected the particles by centrifugation at 13000 rpm for 10 min, washed with water twice, and then re-dispersed them in 50 μL of water for the characterization and evaluation of catalytic properties.

Catalytic characterization of Ag-Au$_{\{100\}}$ and Ag-Au$_{\{111\}}$ nanoboxes. In a typical experiment, 2 mL of aqueous 4-NP (0.2 mM), 5 mL of water, and 1 mL of aqueous $NaBH_4$ (10 mg/mL, freshly prepared, ice cold) were added into a 23-mL glass vial under magnetic stirring. After the introduction of the nanoboxes (~10^{11} particles), I monitored the reaction as a function of time by withdrawing 0.5 mL of the reaction solution to collect the UV-vis spectrum at each time point.

Instrumentation and characterization. The UV-vis spectra were collected using a Cary 50 spectrometer (Agilent Technologies, Santa Clara, CA). The UV-vis-NIR spectra

were collected using a LAMDA 750 (PerkinElmer, Waltham, MA). The nanoparticles in an aqueous suspension were collected using a conventional centrifuge (Eppendorf 5430). The pH values of aqueous solutions were measured using a FE20 FiveEasy pH meter (Mettler Toledo, Columbus, OH). The quantitative measurement of Ag and Au contents in the nanocrystals was performed using an inductively coupled plasma mass spectrometer (NexION 300Q ICP-MS, PerkinElmer, Waltham, MA). Transmission electron microscopy (TEM) images were captured using Hitachi HT7700 (Tokyo, Japan) operated at 120 kV. Scanning electron microscopy (SEM) images were captured with the Hitachi SU8230 FE-SEM (Tokyo, Japan) operated at 15-20 kV. High-angle annular dark field scanning electron microscopy and elemental mapping images were captured using the Hitachi HD2700 C_s-corrected STEM (Tokyo, Japan) operated at 200 kV.

4.3 Results and Discussion

4.3.1 Orthogonal Deposition Controlled by PVP or CTAC

Figure 4.1 illustrates two proposed pathways responsible for the orthogonal deposition of Au on the {100} or {111} facets, respectively, of a Ag cuboctahedron for the generation of a Ag-$Au_{\{100\}}$ or a Ag-$Au_{\{111\}}$ cuboctahedral nanobox. In a typical synthesis, I dispersed Ag cuboctahedra in an aqueous mixture containing H_2Asc, NaOH (at an initial pH of 11.2), and either PVP or CTAC, followed by the titration of aqueous $HAuCl_4$ using a syringe pump at room temperature. Under an alkaline condition, H_2Asc would be neutralized into ascorbic monoanion ($HAsc^-$),[27] a true reducing agent. Based on our previous study,[28] we argue that the Ag atoms on the {111} facets would be initially oxidized by Au(III) to generate a small amount of Au atoms for their immediate deposition

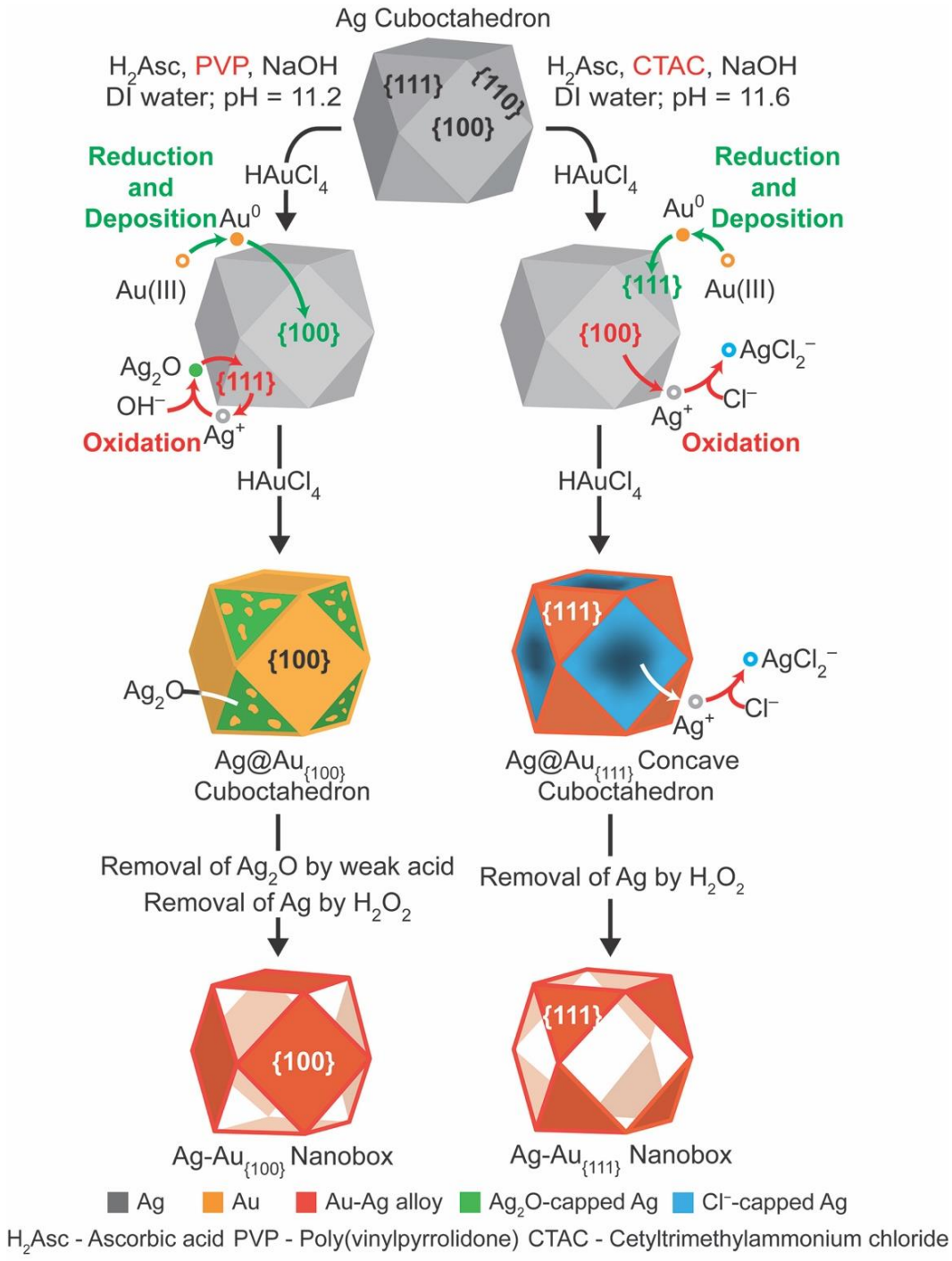

Figure 4.1. Schematic diagram that illustrates the two orthogonal pathways for the deposition of Au on Ag cuboctahedra in the presence of PVP and CTAC, respectively, followed by the removal of Ag to produce cuboctahedral nanoboxes with complementary facets.

on the {100} facets (or the edges). With the involvement of NaOH in the solution, the resultant Ag(I) ions would react with OH^- for the formation of Ag_2O on the {111} facets, prohibiting the underlying Ag from further reacting with Au(III) ions. From this time point, the Au(III) ions would be reduced by $HAsc^-$ to produce more Au atoms for this subsequent deposition onto the {100} facets conformally.[29] Likely, some of the newly deposited Au atoms could migrate to the Ag_2O passivated {111} faets through surface diffusion.[30] At the end, a Ag cuboctahedron is transformed into a $Ag@Au_{\{100\}}$ cuboctahedron with the inclusion of some Au atoms on the Ag_2O regions at the {111} facets. Because Ag_2O layer can be dissolved in a weak acid,[31] we treated the as-obtained products with H2Asc and then etched the Ag from the core with aqueous H_2O_2, leading to the conversion of the Ag@Au{100} cuboctahedron into a Ag-Au{100} cuboctahedral nanobox encased by {100} facets. It is worth noting that some NaCl was added during the weak acid treatment to increase the solubility of Ag_2O for an efficient dissolution of the Ag_2O layer.[32]

In comparison, when the PVP in the reaction solution is replaced by CTAC, the Cl^- ions derived from CTAC could strongly interact with the {100} facets, as reported by others.[33] In this case, the oxidation of Ag by Au(III) would be initiated on the {100} facets, which is orthogonal to what is involved in the PVP-based synthesis.[34] Additionally, the dissolved Ag(I) ions would form soluble $AgCl_2^-$ ions rather than react with OH^- to produce Ag_2O, due to the excessive amount of the Cl^- ions invovled in the reaction soluton.[35] As a consequence, both the $AgCl_2^-$ and Au(III) ions would be co-reduced by $HAsc^-$ into Ag and Au atoms, respectively, for their co-deposition onto the Ag cuboctahedra. Because the {100} facets are involved in the oxidation of Ag, I argue that the co-deposition of Au and Ag atoms would be mainly confined to the {111} facets. As $HAuCl_4$ is titrated into the reaction

solution, more and more Ag atoms would be carved away from the {100} facets, leading to the generation of a Ag@Ag-$Au_{\{111\}}$ concave cuboctahedron. After the etching of Ag from the core with aqueous H_2O_2, Ag-$Au_{\{111\}}$ cuboctahedral nanoboxes covered by {111} facets will be obtained.

4.3.2 Deposition of Au on {100} Facets with the Involvement of PVP

In a typical synthesis, I first produced the Ag nanocubes with an average edge length of 38.1 ± 2.0 nm (Figure 4.2A).[26] The as-obtained Ag nanocubes were then used as seeds to generate Ag cuboctahedra with an average edge length of 47.2 ± 2.2 nm (Figure 4.2B).[15] In one set of study, I dispersed the Ag cuboctadedra in an aqueous solution containing H_2Asc, NaOH, and PVP, followed by the titration of aqueous $HAuCl_4$ (0.1 mM) at an initial pH of 11.2. Figure 4.3A shows a transmission electron microscope (TEM) image of the

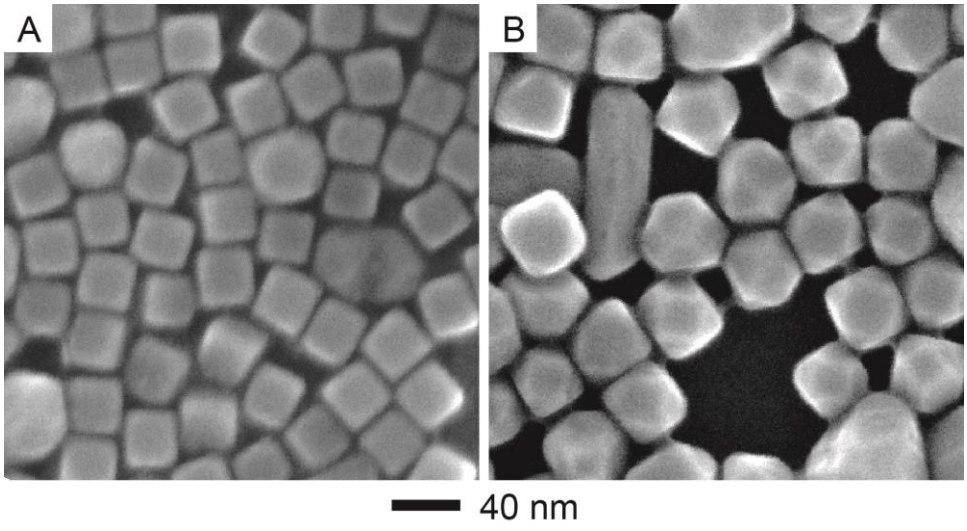

Figure 4.2. SEM images of (A) Ag nanocubes with an average edge length of 38.1 ± 2.0 nm and (B) Ag cuboctahedra with an average edge length of an average edge length of 47.2 ± 2.2 nm.

product prepared by adding 0.4 mL of $HAuCl_4$. Figure 4.3B shows an aberration-corrected high-angle annular dark-field scanning TEM (HAADF-STEM) image of a single cuboctahedron taken from the sample in Figure 4.3A. When aligned along the <001> zone axis, I could easily resolve the distinctive contrast between the bright region at the center and the darker regions at the four corners, which correspond to the {100} and the {111} facets of the cuboctahedron, respectively. Because the heavier Au atoms (which contribute to the mass contrast) were located on the {100} facets that are parallel with the zone axis, I observed brigher contrast at the four edges. I also performed energy dispersive X-ray spectroscopy (EDS) mapping on the same cuboctahedron to confirm the spatial distribution of each element. Figure 4.3, C and D, shows the elemental mapping of Ag and Au, respectively. I noticed that more signals from Ag were distributed at the center face than at the four corners, consistent with the thickness contrast of a cuboctahedron along the <001> zone axis. On the other hand, the signals from Au were mainly localized to the center face and the four edges but not at the four corners. The Au distribution coincides with the presence of four edges that appear brighter on the HAADF-STEM image in Figure 4.3B, confirming the deposition of onto the {100} and {110} surfaces. Unfortunately, we were not able to characterize the Ag_2O layer underneath the Au by STEM and EDS. Figure 4.3, E and F, shows the TEM and SEM images of the final nanoboxes, from which I clearly observed the formation of {100} facets. Because all facets are well connected in a nanobox, I argue that Au deposition would also occur on the {110} facets of the Ag cuboctahedra, serving as the vertices of cuboctahedral nanoboxes. Using inductively coupled plasma mass spectroscopy (ICP-MS), I determined that the Ag-$Au_{\{100\}}$ nanoboxes were made of a Ag-Au alloy with a composition of $Ag_{64}Au_{36}$.

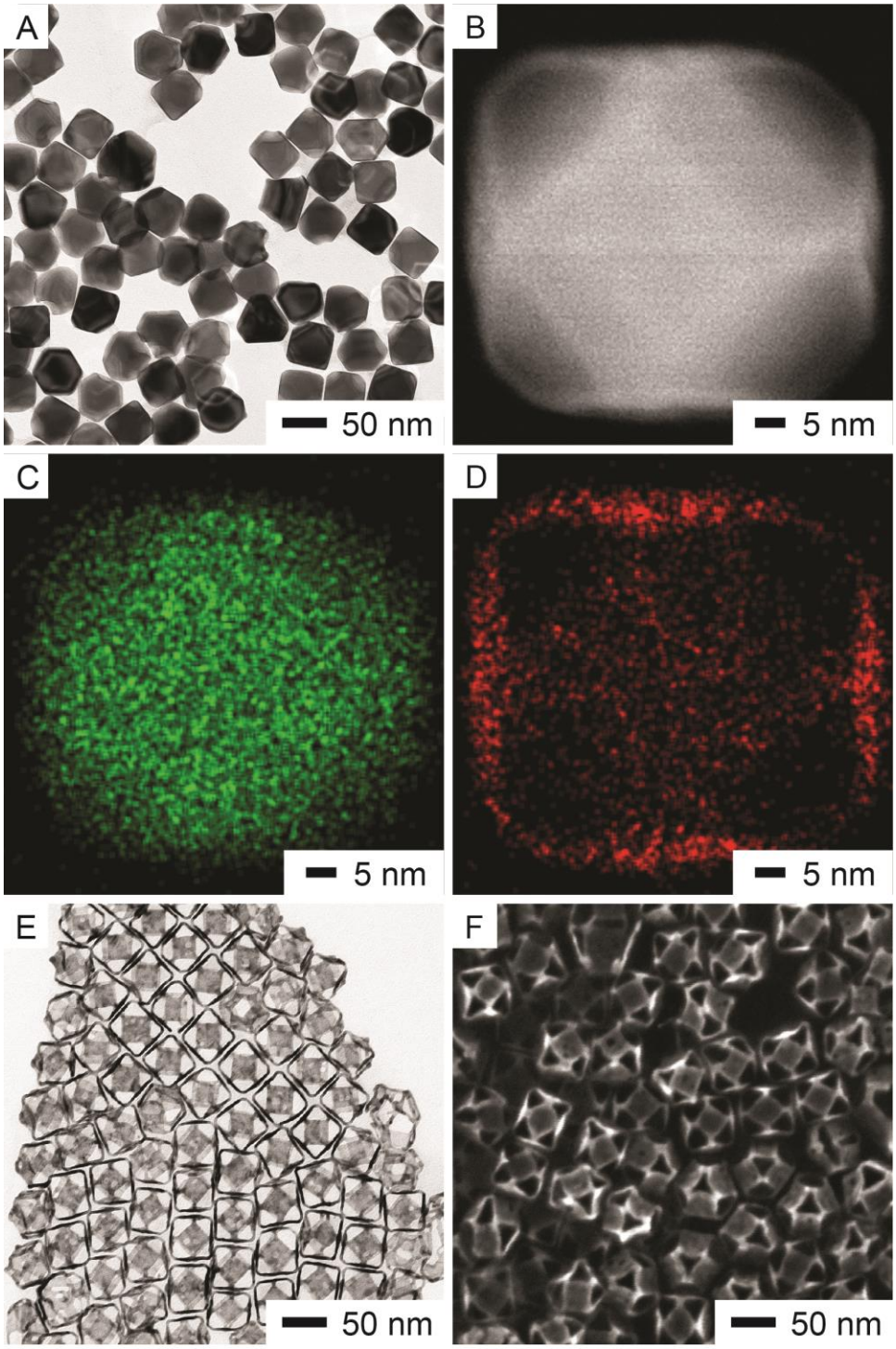

Figure 4.3. (A) TEM image of the as-prepared Ag@Au$_{\{100\}}$ cuboctahedra. (B) HAADF-STEM image of one nanocrystal that was orientated along the <001> zone axis. (C, D) EDS mapping of the same nanocrystal (green: Ag; red: Au). (E) TEM and (F) SEM images of the resultant Ag-Au$_{\{100\}}$ cuboctahedral nanoboxes after the removal of Ag.

4.3.3 Deposition of Au on {111} Facets with the Involvement of CTAC

By replacing the PVP with CTAC while keeping all other parameters the same, Figure 4.4A shows a TEM image of the products obtained after the titration of 0.8 mL of $HAuCl_4$. Figure 4.4B shows a HAADF-STEM image of one nanoparticle taken from the sample in Figure 4.4A. The particle was oriented along the <001> zone axis, confirming the concave features on the {100} facets of the cuboctahedron due to the removal of Ag from these facets. As shown in Figure 4.4, C and D, the EDS elemental mapping of Ag and Au of the same nanoparticle indicates that the Ag signals were more intense in the center region within the concave perimeter while the Au signals were located at the edges, especially more so toward the four corners, suggesting the predominant deposition of Au on the {111} facets with very few on the {100} facets. Figure 4.5A shows a HAADF-STEM image of another nanoparticle oriented along the <111> zone axis, showing a brighter contrast at the {111} facet due to the thickness contrast. In addition, the three {100} surfaces situated at 120° angles from each other show a darker contrast, revealing their concavity. As shown by the EDS mapping in Figure 4.5B, the Ag signals are more intense at the center, generally following the contrast distribution in Figure 4.5A. Figure 4.5C shows that the Au signals are somewhat localized at the edges, which reflects the presence of Au atoms on the {111} facets. Away from the edges, the Au signals seem to be spread out across the particle because of the contribution of Au signals from the three {100} facets at the bottom of the cuboctahedron. After the etching of Ag from the core with aqueous H_2O_2, Figure 4.4, E and F, shows TEM and SEM images of the resultant nanoboxes enclosed by {111} facets, respectively, indicating that the {100} facets of concave cuboctadera would be covered by small amount of Au. The ICP-MS measurement indicates that the Ag-$Au_{\{111\}}$ nanoboxes

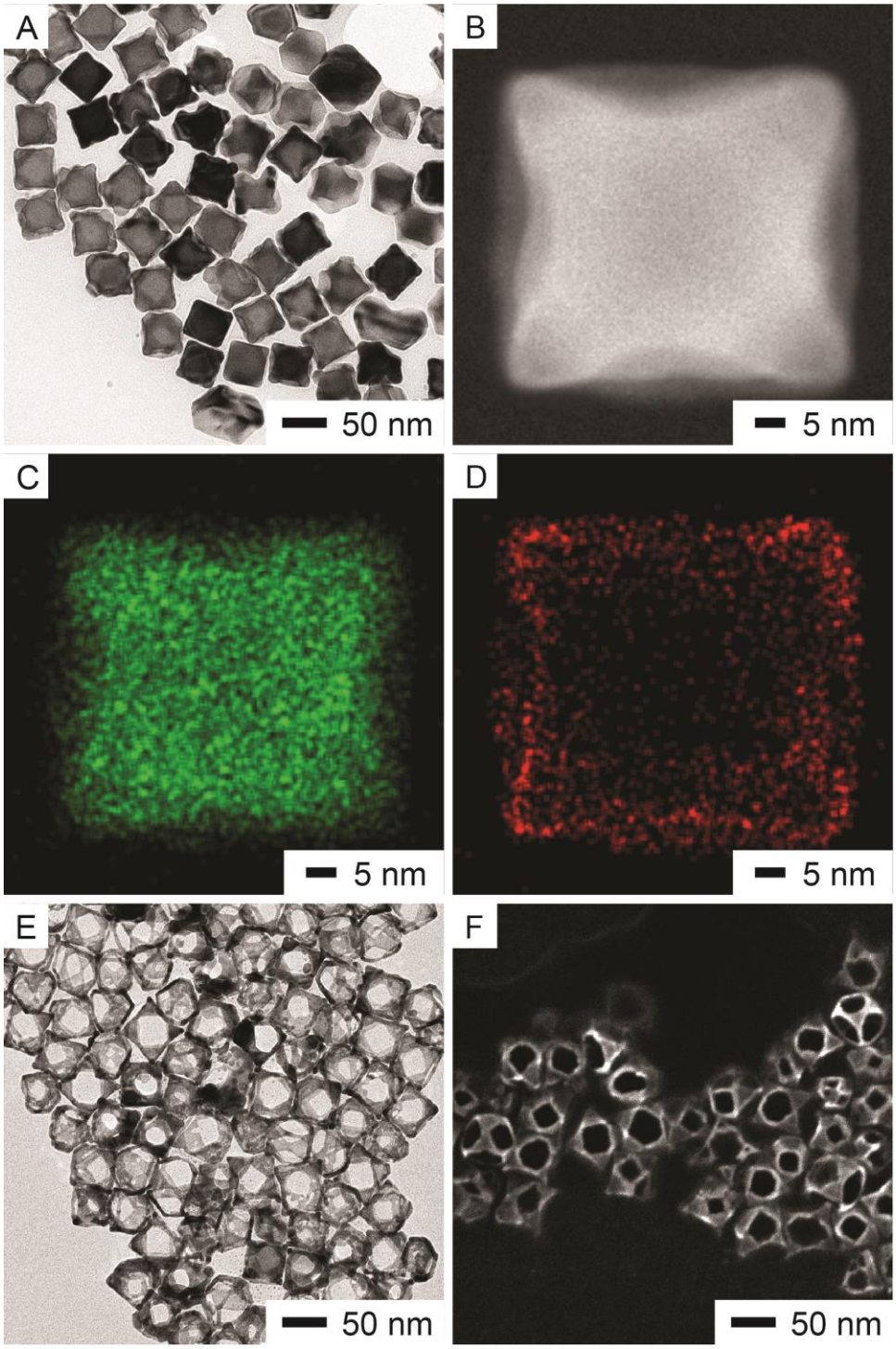

Figure 4.4. (A) TEM image of the as-prepared Ag@Ag-Au$_{\{111\}}$ concave cuboctahedra. (B) HAADF-STEM image of one nanocrystal that was orientated along the <001> zone axis. (C, D) EDS mapping of the same nanocrystal (green: Ag; red: Au). (E) TEM and (F) SEM images of the resultant Ag-Au$_{\{111\}}$ cuboctahedral nanoboxes after the etching of Ag.

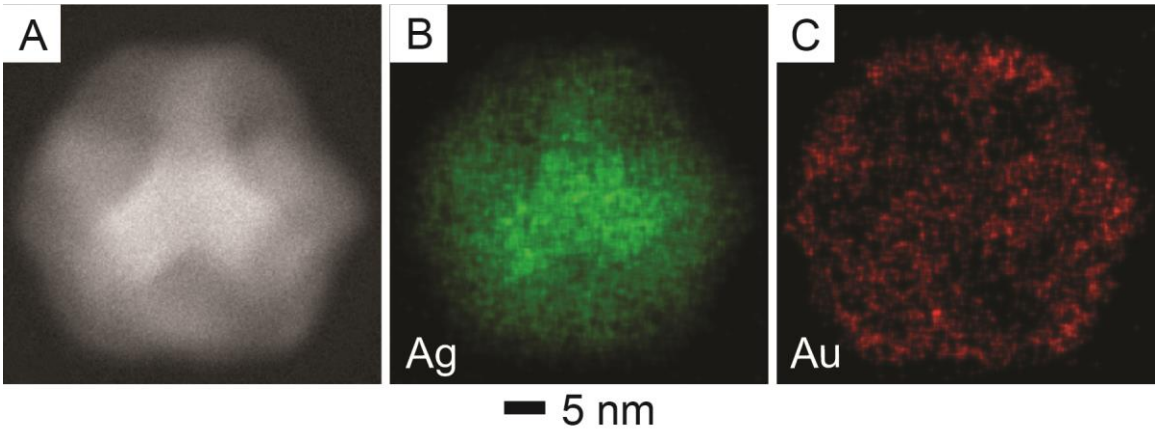

Figure 4.5. (A) HAADF-STEM image of one Ag@Ag-Au$_{\{111\}}$ concave cuboctahedron that was orientated along the <111> zone axis. (B, C) the EDS mapping of the same concave cuboctahedron (green: Ag; red: Au).

were made of of $Ag_{77}Au_{23}$. Interestingly, the composition of Au for these nanoboxes prepared with 0.8 mL of $HAuCl_4$ was lower than that in the Ag-Au$_{\{100\}}$ nanoboxes (with a composition of $Ag_{64}Au_{36}$) prepared with 0.4 mL of $HAuCl_4$ in the presence of PVP. I suspect that part of this difference arises from the co-deposition of both Ag and Au atoms on the {111} facets of the cuboctahedra during the synthesis involving CTAC.

4.3.4 Evaluating the Optical and Catalytic Properties of Ag@Au Cuboctahedra and Ag-Au Cuboctahedral Nanoboxes

We also used UV-vis-NIR spectroscopy to characterize the optical properties of the resultant cuboctahedral nanoboxes. When Ag@Au$_{\{100\}}$ cuboctahedra were transformed into Ag-Au$_{\{100\}}$ nanoboxes, Figure 4.6A shows that the localized surface plasmon resonance (LSPR) peak was red-shifted from 463 nm to 1290 nm, together with the emergence of three other peaks at 845, 925, and 1140 nm. In comparison, Figure 4.6B shows that the major LSPR peak of Ag@Ag-Au$_{\{111\}}$ concave cuboctahedra was located at 499 nm, which is further red-shifted from that of the Ag@Au$_{\{100\}}$ cuboctahedra located at

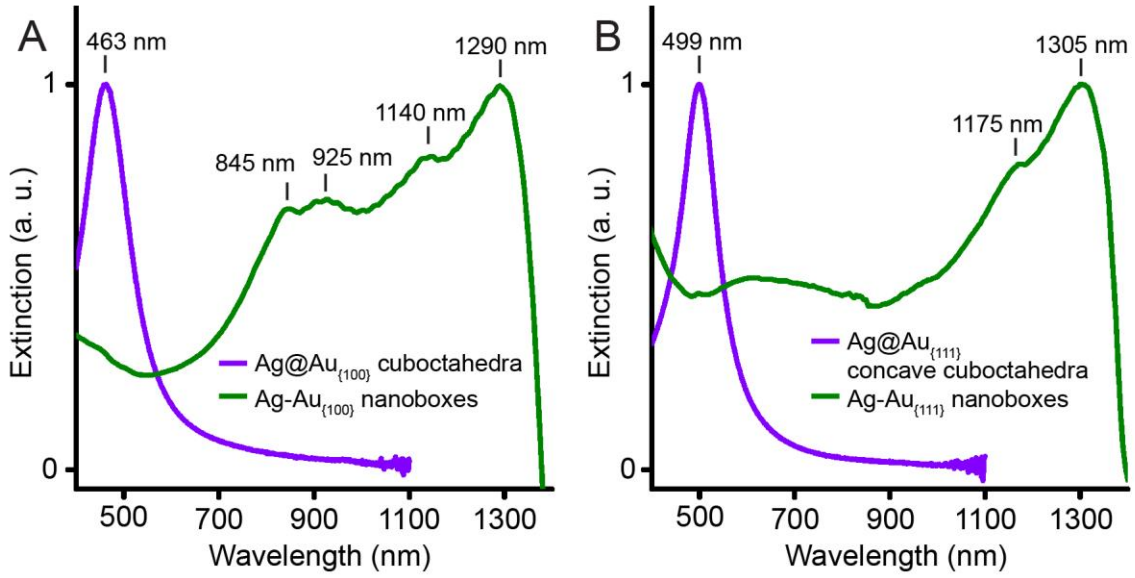

Figure 4.6. (A) UV-vis spectra of the Ag@Au$_{\{100\}}$ cuboctahedra and corresponding Ag-Au$_{\{100\}}$ nanoboxes. (B) UV-vis spectra of the Ag@Ag-Au$_{\{111\}}$ concave cuboctahedra and corresponding Ag-Au$_{\{111\}}$ nanoboxes. Each spectrum was normalized to its maximum intensity.

463 nm due to the surface concavity. When they were transformed into Ag-Au$_{\{111\}}$ nanoboxes, the LSPR peak was shifted to 1305 nm with another peak appeared at 1175 nm. I could attribute the main LSPR peak of both types of nanoboxes (1295 and 1305 nm, respectively for Ag-Au$_{\{100\}}$ and Ag-Au$_{\{111\}}$) to the electric dipole mode, which has a strong correlation with the dimensions of the nanobox.[36] Unfortunately, it remains extremely challenging to measure the thickness of these nanoboxes while the composition can only be obtained by ICP-MS measurements. As such, we cannot perform the discrete dipole approximation (DDA) calculation to make assignments for specific plasmonic modes. Compared to the cubic Au nanoboxes with LSPR peak located at 1080 nm,[28] the LSPR peaks of these two types of Ag-Au cuboctahedral nanoboxes were further shifted to the infrared region.

I evaluated the catalytic activity of the cuboctahedral nanoboxes using a model

reaction based on the reduction of 4-nitrophenol (4-NP) to 4-aminophenol (4-AP) by $NaBH_4$.[37] After the introduction of $NaBH_4$, I recorded the UV-vis spectra of 4-NP at different reaction time points (Figure 4.7, A and C). By following the intensity of the absorption peak at 400 nm, I plotted the $\ln(A_t/A_o)$ as a function of reaction time (Figure 4.7, B and D). In both cases, the reduction reaction exhibited first-order kinetics, from which I obtained the rate constant through curve fitting. The rate constants of Ag-$Au_{\{100\}}$ and Ag-$Au_{\{111\}}$ cuboctahedral nanoboxes were 0.005 min^{-1} and 0.213 min^{-1}, respectively,

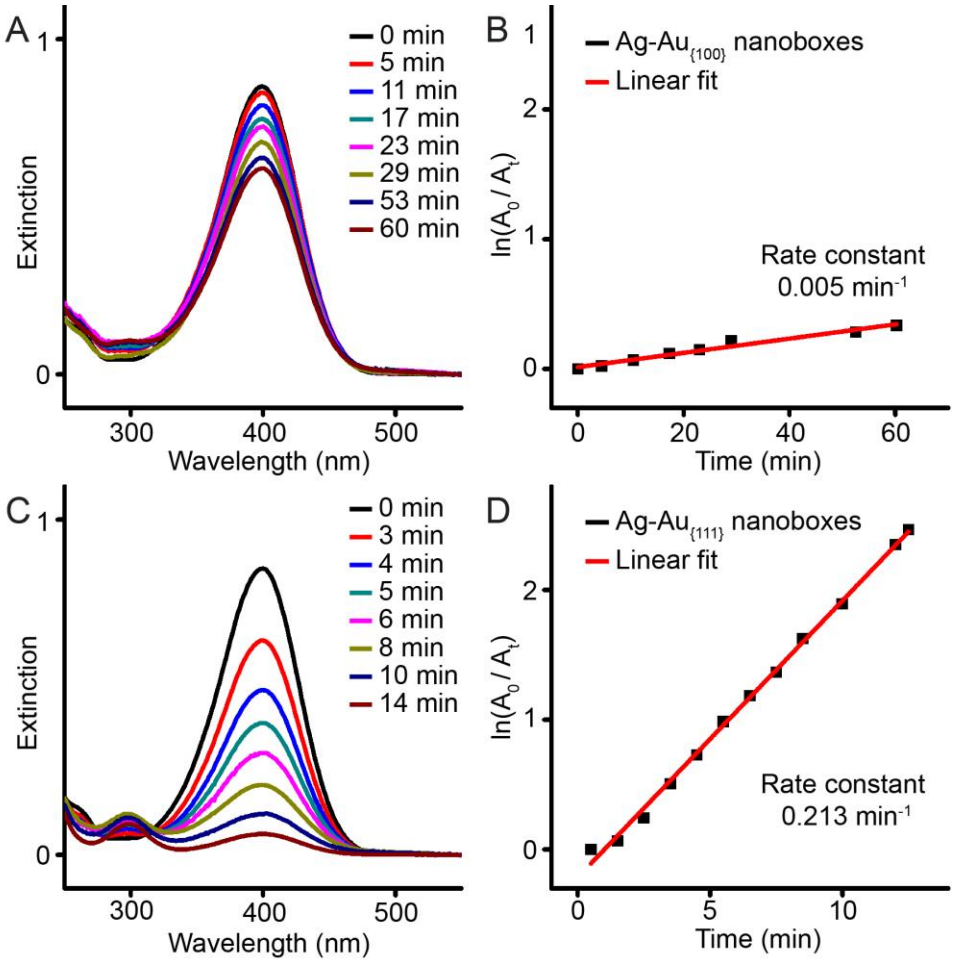

Figure 4.7. (A, C) UV-vis spectra recorded at different time points for the reduction of 4-NP by $NaBH_4$ at room temperature, when the Ag-$Au_{\{100\}}$ and Ag-$Au_{\{111\}}$ nanoboxes were used as the catalysts, respectively. (B, D) Plots of $\ln(A_0/A_t)$ as a function of time for the peaks located at 400 nm in (A) and (C), respectively

indicating distinctive catalytic activities toward this reduction reaction. I believe there are several factors that could contribute to this significant difference. Based on my ICP-MS measurements, both Ag-Au$_{\{100\}}$ and Ag-Au$_{\{111\}}$ cuboctahedral nanoboxes were made of Ag-Au alloy with a composition of $Ag_{64}Au_{36}$ and $Ag_{77}Au_{23}$, respectively. As many groups argue that Au is a more effective catalyst for the reduction of 4-NP compared to Ag,[38-43] it is possible that the difference arises from the fact that the Ag-Au$_{\{111\}}$ cuboctahedral nanoboxes may embrace Au-dominated outermost surfaces while the Ag-Au$_{\{100\}}$ cuboctahedral nanoboxes could consist of Ag-dominated surfaces. However, it is indeed extremely difficult to characterize the composition of the outermost surfaces to fully support this argument. On the other hand, I believe that the use of PVP or CTAC in the original synthesis of these nanoboxes could contribute to the different arrangement of atoms on the {100} or {111} facets of cuboctahedra, respectively, leading to their distinct catalytic activities. Finally, it is also possible that the dissolved oxygen species in reaction solution could attribute to the different induction time of 4-NP reduction because Ag atoms could leach out into the solution as Ag ions and thus affect the catalytic performance.[44, 45]

4.4 Conclusions

We have demonstrated the transformation of Ag cuboctahedra into Ag-Au cuboctahedral nanoboxes with complementary facets by including either poly(vinylpyrrolidone) (PVP) or cetyltrimethylammonium chloride (CTAC) to a reaction solution containing Ag cuboctahedra, H_2Asc, and NaOH at the pH around 11, followed by the titration of aqueous $HAuCl_4$. When the PVP was involved, the oxidation of Ag would be initiated on the on the {111} facets for the deposition of Au on the {100} facets in the orthogonal manner, transforming Ag cuboctahedra into Ag@Au$_{\{100\}}$ cuboctahedra and then

cuboctahedral nanoboxes enclosed by the {100} facets after the etching of Ag by H_2O_2. In comparison, when the CTAC was added to the reaction solution, the oxidation of Ag would continuously progress on the {100} facets for the generation of concavities. Concomitantly, the dissolved Ag(I) ions and the Au(III) would be co-reduced by chemical reduction for the generation of Ag and Au atoms, followed by their co-deposition on the {111} facets for the generation of Ag@$Au_{\{111\}}$ concave cuboctahedra and the resultant Ag-$Au_{\{111\}}$ cuboctahedral nanoboxes enclosed by {111} facets after the removal of Ag. Both types of cuboctahedral nanoboxes embrace strong LSPR properties in the infrared region. On the other hand, cuboctahedral nanoboxes enclosed by the {111} facets exhibit catalytic activities toward the reduction of 4-NP by $NaBH_4$.

4.5 Notes to Chapter 4

This chapter was adapted from the article "Orthogonal Deposition of Au on Different Facets of Ag Cuboctahedra for the Fabrication of Nanoboxes with Complementary Surfaces" published in *Nanoscale*.[46]

4.6 References

(1) Rycenga, M.; Cobley, C. M.; Zeng, J.; Li, W.; Moran, C. H.; Zhang. Q.; Qin, D.; Xia, Y. Controlling the Synthesis and Assembly of Silver Nanostructures for Plasmonic Applications. *Chem. Rev.* **2011**, *111*, 3669-3712.

(2) Orendorff, C. J.; Sau, T. K.; Murphy, C. J.; Shape-Dependent Plasmon-Resonant Gold Nanoparticles. *Small* **2006**, *2*, 636-639.

(3) Tian, N.; Zhou, Z.-Y.; Sun, S.-G.; Ding, Y.; Wang, Z. L. Synthesis of Tetrahexahedral Platinum Nanocrystals with High-Index Facets and High Electro-Oxidation Activity. *Science* **2007**, *316*, 732-735.

(4) Tao, A. R.; Habas, S.; Yang, P.; Shape Control of Colloidal Metal Nanocrystals. *Small* **2008**, *4*, 310-325.

(5) Huang, M. H.; Lin, P.-H. Shape-Controlled Synthesis of Polyhedral Nanocrystals and Their Facet-Dependent Properties. *Adv. Func. Mater.* **2012**, *22*, 14-24.

(6) Chiu, C.-Y.; Chung, P.-J.; Lao, K.-U.; Liao, C.-W.; Huang, M. H.; Facet-Dependent Catalytic Activity of Gold Nanocubes, Octahedra, and Rhombic Dodecahedra toward 4-Nitroaniline Reduction. *J. Phys. Chem. C* **2012**, *116*, 23757-23763.

(7) Xie, S.; Choi, S.-I.; Xia, X.; Xia, Y. Catalysis on Faceted Noble-Metal Nanocrystals: Both Shape and Size Matter. *Curr. Opin. Chem. Eng.* **2013**, *2*, 142-150.

(8) Zhang, Q.; Wang, H. Facet-Dependent Catalytic Activities of Au Nanoparticles Enclosed by High-Index Facets. *ACS Catal.* **2014**, *4*, 4027-4033.

(9) Xia, Y.; Gilroy, K. D.; Peng, H.-C.; Xia, X. Seed-Mediated Growth of Colloidal Metal Nanocrystals. *Angew. Chem. Int. Ed.* **2017**, *56*, 60-95.

(10) Niu, W.; Zhang, L.; Xu, G. Seed-Mediated Growth of Noble Metal Nanocrystals: Crystal Growth and Shape Control. *Nanoscale* **2013**, *5*, 3172-3181.

(11) Wu, Y.; Sun, X.; Yang, Y.; Li, J.; Zhang, Y.; Qin, D. Enriching Silver Nanocrystals with a Second Noble Metal. *Acc. Chem. Res.* **2017**, *50*, 1774-1784.

(12) Adamson, A. W.; Gast, A. P. *Physical Chemistry of Surfaces*. Interscience New York, 1967.

(13) Nikoobakht, B.; El-Sayed, M. A.; Preparation and Growth Mechanism of Gold Nanorods (NRs) Using Seed-Mediated Growth Method. *Chem. Mater.* **2003**, *15*, 1957-1962.

(14) Habas, S. E.; Lee, H.; Radmilovic, V.; Somorjai, G. A.; Yang, P. Shaping Binary Metal Nanocrystals through Epitaxial Seeded Growth. *Nat. Mater.* **2007**, *6*, 692.

(15) Wang, Y; Wan, D.; Xie, S.; Xia, X.; Huang, C. Z.; Xia, Y. Synthesis of Silver Octahedra with Controlled Sizes and Optical Properties via Seed-Mediated Growth. *ACS Nano* **2013**, *7*, 4586-4594.

(16) Zhang, J.; Liu, J.; Xie, Z.-X.; Qin, D. $HAuCl_4$: A Dual Agent for Studying the Chloride-Assisted Vertical Growth of Citrate-Free Ag Nanoplates with Au Serving as a Marker. *Langmuir* **2014**, *30*, 15520-15530.

(17) Wang, C.-W.; Sun, X.; Chang. H.-T.; Qin, D. Generation of Enzymatic Hydrogen Peroxide to Accelerate the Etching of Silver Nanocrystals with Selectivity. *Chem. Mater.* **2016**, *28*, 7519-7527.

(18) Langille, M. R.; Personick, M. L.; Zhang, J.; Mirkin, C. A. Bottom-Up Synthesis of Gold Octahedra with Tailorable Hollow Features. *J. Am. Chem. Soc.* **2011**, *133*, 10414-10417.

(19) Kim, D.; Lee, Y. W.; Lee, S. B.; Han, S. W. Convex Polyhedral Au@Pd Core–Shell Nanocrystals with High-Index Facets. *Angew. Chem. Int. Ed.* **2012**, *51*, 159-163.

(20) Xie, S.; Lu, N.; Xie, Z.; Wang, J.; Kim, M. J.; Xia, Y. Synthesis of Pd-Rh Core–Frame Concave Nanocubes and Their Conversion to Rh Cubic Nanoframes by

Selective Etching of the Pd Cores. *Angew. Chem. Int. Ed.* **2012**, *51*, 10266-10270.

(21) Weiner, R. G.; Kunz, M. R.; Skrabalak, S. E. Seeding a New Kind of Garden: Synthesis of Architecturally Defined Multimetallic Nanostructures by Seed-Mediated Co-Reduction. *Acc. Chem. Res.* **2015**, *48*, 2688-2695.

(22) Li, J.; Sun, X.; Qin, D. Ag-Enriched Ag-Pd Bimetallic Nanoframes and Their Catalytic Properties. *ChemNanoMat* **2016**, *2*, 494-499.

(23) Satyavolu, N. S. R.; Tan, L. H.; Lu, Y. DNA-Mediated Morphological Control of Pd–Au Bimetallic Nanoparticles. *J. Am. Chem. Soc.* **2016**, *138*, 16542-16548.

(24) Zhang, L.; Xie, Z.; Gong, J. Shape-Controlled Synthesis of Au-Pd Bimetallic Nanocrystals for Catalytic Applications. *Chem. Soc. Rev.* **2016**, *45*, 3916-3934.

(25) Sun, X.; Li, D.; Ding, Y.; Zhu, W.; Guo, S.; Wang, Z. L.; Sun, S. Core/Shell Au/CuPt Nanoparticles and Their Dual Electrocatalysis for Both Reduction and Oxidation Reactions. *J. Am. Chem. Soc.* **2014**, *136*, 5745-5749.

(26) Zhang, Q.; Li, W.; Wen, L.-P.; Chen, J.; Xia, Y. Facile Synthesis of Ag Nanocubes of 30 to 70 nm in Edge Length with CF_3COOAg as a Precursor. *Chem. Eur. J.* **2010**, *16*, 10234-10239.

(27) Du, J.; Cullen, J. J.; Buettner, G. R. Ascorbic Acid: Chemistry, Biology and the Treatment of Cancer. *Biochim. Biophys. Acta – Rev. Cancer* **2012**, *1826*, 443-457.

(28) Sun, X.; Kim, J.; Gilroy, K. D.; Liu, J.; König, T. A. F.; Qin, D. Gold-Based Cubic Nanoboxes with Well-Defined Openings at the Corners and Ultrathin Walls Less Than Two Nanometers Thick. *ACS Nano* **2016**, *10*, 8019-8025.

(29) Yang, Y.; Liu, J.; Fu, Z.-W.; Qin, D. Galvanic Replacement-Free Deposition of Au on Ag for Core–Shell Nanocubes with Enhanced Chemical Stability and SERS Activity. *J. Am. Chem. Soc.* **2014**, *136*, 8153-8156.

(30) Xia, X.; Xie, S.; Liu, M.; Peng, H.-C.; Lu, N.; Wang, J.; Kim, M. J.; Xia, Y. On the Role of Surface Diffusion in Determining the Shape or Morphology of Noble-Metal Nanocrystals. *Proc. Natl. Acad. Sci. U.S.A.* **2013**, *110*, 6669-6673.

(31) Johnston, H. L.; Cuta, F.; Garrett, A. B. The Solubility of Silver Oxide in Water, in Alkali and in Alkaline Salt Solutions. The Amphoteric Character of Silver Hydroxide. *J. Am. Chem. Soc.* **1933**, *55*, 2311-2325.

(32) Li, X.; Lenhart, J. J.; Walker, H. W. Aggregation Kinetics and Dissolution of Coated Silver Nanoparticles. *Langmuir* **2011**, *28*, 1095-1104.

(33) Zhou, S.; Li, J.; Gilroy, K. D.; Tao, J.; Zhu, C.; Yang, X.; Sun, X.; Xia, Y. Facile Synthesis of Silver Nanocubes with Sharp Corners and Edges in an Aqueous Solution. *ACS Nano* **2016**, *10*, 9861-9870.

(34) Ahn, J.; Wang, D.; Ding, Y.; Zhang, J.; Qin, D. Site-Selective Carvings and Co-Deposition: Transformation of Ag Nanocubes into Concave Nanocrystals Encased

by Au-Ag Alloy Frames. *ACS Nano* **2018**, *12*, 298-307.

(35) Du, J.; Chen, Z.; Chen, C.; Meyer, T. J. A Half-Reaction Alternative to Water Oxidation: Chloride Oxidation to Chlorine Catalyzed by Silver Ion. *J. Am. Chem. Soc.* **2015**, *137*, 3193-3196.

(36) Schwartzberg, A. M.; Olson, T. Y.; Talley, C. E.; Zhang, J. Z. Synthesis, Characterization, and Tunable Optical Properties of Hollow Gold Nanospheres. *J. Phys. Chem. B* **2006**, *110*, 19935-19944.

(37) Pradhan, N.; Pal, A.; Pal, T. Catalytic Reduction of Aromatic Nitro Compounds by Coinage Metal Nanoparticles. *Langmuir* **2001**, *17*, 1800-1802.

(38) Xu, P.; Kang, L.; Mack, N. H.; Schanze, K. S.; Han, X.; Wang, H.-L. Mechanistic Understanding of Surface Plasmon Assisted Catalysis on a Single Particle: Cyclic Redox of 4-Aminothiophenol. *Sci. Rep.* **2013**, *3*, 2997.

(39) Li, J.; Liu, J.; Yang, Y.; Qin, D. Bifunctional Ag@Pd-Ag Nanocubes for Highly Sensitive Monitoring of Catalytic Reactions by Surface-Enhanced Raman Spectroscopy. *J. Am. Chem. Soc.* **2015**, *137*, 7039-7042.

(40) Zhao, P.; Feng, X.; Huang, D.; Yang, G.; Astruc, D. Basic Concepts and Recent Advances in Nitrophenol Reduction by Gold- and Other Transition Metal Nanoparticles. *Coord. Chem. Rev.* **2015**, *287*, 114-136.

(41) Shin, Y.; Dohnalkova, A.; Lin, Y. Preparation of Homogeneous Gold-Silver Alloy Nanoparticles Using the Apoferritin Cavity as a Nanoreactor. *J. Phys. Chem. C* **2010**, *114*, 5985-5989.

(42) Sun, L; Lv, P.; Li, H.; Wang, F.; Su, W.; Zhang, L. One-Step Synthesis of Au-Ag Alloy Nanoparticles Using Soluble Starch and Their Photocatalytic Performance for 4-Nitrophenol Degradation. *J. Mater. Sci.* **2018**, *53*, 15895-15906.

(43) Sun, L.; Yin, Y.; Wang, F.; Su, W.; Zhang, L. Facile One-Pot Green Synthesis of Au-Ag Alloy Nanoparticles Using Sucrose and Their Composition-Dependent Photocatalytic Activity for The Reduction of 4-Nitrophenol. *Dalton Trans.* **2018**, *47*, 4315-4324.

(44) Menumerov, E.; Hughes, R. A.; Neretina, S. One-Step Catalytic Reduction of 4-Nitrophenol through the Direct Injection of Metal Salts into Oxygen-Depleted Reactants. *Catal. Sci. Technol.* **2017**, *7*, 1460-1464.

(45) Menumerov, E.; Hughes, R. A.; Golze, S. D.; Neal, R. D.; Demille, T. B.; Campanaro, J. C.; Kotesky, K. C.; Rouvimov, S.; Neretina, S. Identifying the True Catalyst in the Reduction of 4-Nitrophenol: A Case Study Showing the Effect of Leaching and Oxidative Etching Using Ag Catalysts. *ACS Catal.* **2018**, *8*, 8879-8888.

(46) Ahn, J.*; Kim, J.*; Qin, D. Orthogonal Deposition of Au on Different Facets of Ag Cuboctahedra for the Fabrication of Nanoboxes with Complementary Surfaces. *Nanoscale* **2019**, DOI: 10.1039/C9NR08420G. (*Equal contribution.)

CHAPTER 5. COMPARATIVE STUDY OF THE ADSORPTION OF THIOL AND ISOCYANIDE MOLECULES ON SILVER SURFACE BY IN SITU SURFACE-ENHANCED RAMAN SCATTERING

5.1 Introduction

As demonstrated by the various synthesis methods described in Chapters 2-4, it is evident that surface ligands play a significant role in controlling the site-selective etching and growth on the nanocrystal template for engineering nanocrystals with complex shapes. The surface of metal nanoparticles is prone to the adsorption of organic molecules because the adsorbates can reduce the interfacial energy between the metal and its surrounding medium.[1] If the organic molecules have a functional group with strong affinity toward the metal atom, they tend to spontaneously arrange themselves into a self-assembled monolayer (SAM),[2] presenting a robust method for engineering the interfacial properties.[3-6] Although there are extensive reports on the formation of thiol-based SAMs on Au nanoparticles,[2,7-10] it remains challenging to characterize the surface adsorption process in gathering information such as coverage density, conformation of the adsorbed ligands, and the relative binding strengths of different ligands. To this end, it is of importance to develop a technique capable of probing the adsorption of organic molecules on the surface of nanoparticles *in situ*. Such a technique would also find immediate use in areas such as surface science and heterogeneous catalysis.

There are a number of documented techniques for characterizing the adsorption of organic molecules on a solid surface. As a direct method, scanning tunneling microscopy (STM) has been used extensively to visualize the SAM on a metal thin film by obtaining topological information with resolution down to the molecular level.[11,12] Recent reports

suggested that STM could analyze mixed-ligand SAMs on Au nanoparticles with sufficient sensitivity to distinguish between the regions comprised of different types of thiol molecules.[13,14] Unfortunately, STM measurements demand a high-vacuum environment,[15] making it impractical to gather information from a solution-phase system. Additionally, it is difficult to extract configuration of organic molecules on a solid surface from the STM data. In comparison, other indirect methods can reveal the structural details of the adsorbed molecules by leveraging molecular vibrations. Among them, Fourier-transform infrared spectroscopy (FTIR) is well known for its ability to reveal the molecular fingerprints about the adsorbates. For example, Murray *et al.* demonstrated the use of FTIR to evaluate the conformations of alkanethiol molecules adsorbed on Au nanoparticles as a function of particle size and under different conditions (*e.g.*, solid state *vs.* solution phase).[16,17] They discovered that alkanethiols would show less ordered packing on smaller particles or for the nanoparticles dispersed in nonpolar solvents. Based on the non-linear optical responses from the surface of nanoparticles,[18,19] second-harmonic generation (SHG) spectroscopy serves as a sensitive technique to create the adsorption isotherm,[20] determine the adsorption energy and coverage density,[21] and investigate the exchange of different ligands on the surface of Au nanoparticles.[22] However, SHG inherits a number of intrinsic problems, including bulk-phase interference, sensitivity restriction, limited range of wavenumbers, and inability to detect vibrational modes parallel to the interfacial plane as a result of surface-selection rules.

Surface-enhanced Raman scattering (SERS) offers a powerful tool for analyzing molecular adsorption on the surface of a plasmonically-active metal such as Au or Ag in liquid phase and under ambient conditions. SERS shares several attributes with electron

energy loss spectroscopy (EELS), including the excellent sensitivity toward low wavenumbers and the ability to detect most adsorbate through their vibrational modes. In the 1990s, Weaver and others used SERS to study the interface between an aqueous phase and an electrocatalytic material that includes a roughened noble-metal electrode or an electrode decorated with nanoparticles of 1-2 nm in size.[23-27] They argued about the feasibility to monitor molecular transformations on a catalytic surface by following the vibrational fingerprints of catalytically relevant molecules, such as ethylene, methanol, and carbon monoxide, as a function of electrode potential.[23-25] In recent years, SERS has been implemented to probe chemical reactions *in situ* on nanoparticles consisting of a plasmonic metal such as Au or Ag and a catalytic metal such a Pd or Pt.[28-30] Most recently, it was further demonstrated the utility of SERS in probing the heterogeneous nucleation and growth of Pd or Pt on Ag nanocubes in solution with the introduction of an isocyanide probe.[31,32] Despite these prior reports, SERS has not been fully explored for monitoring the adsorption of an organic ligand onto the surface of metal nanocrystals *in situ* in a solution phase.[33-35]

Herein, I demonstrate the use of SERS as a platform technique to investigate the competitive adsorption of thiol and isocyanide molecules on the surface of Ag nanocubes. As illustrated in Figure 5.1, I selected three different ligands, 4-nitrothiophenol (4-NTP), 4-aminothiophenol (4-ATP), and 1,4-phenylene diisocyanide (1,4-PDI), to investigate their (competitive) adsorption on the surface of Ag nanocubes. It is well-known that both 4-NTP and 4-ATP can chemisorb onto Ag *via* the establishment of a Ag-thiolate linkage.[36,37] Since $–NO_2$ and $–NH_2$ are an electron acceptor and a donor, respectively, 4-NTP and 4-ATP have been used to study the role of charge transfer in affecting the SERS activities of Ag

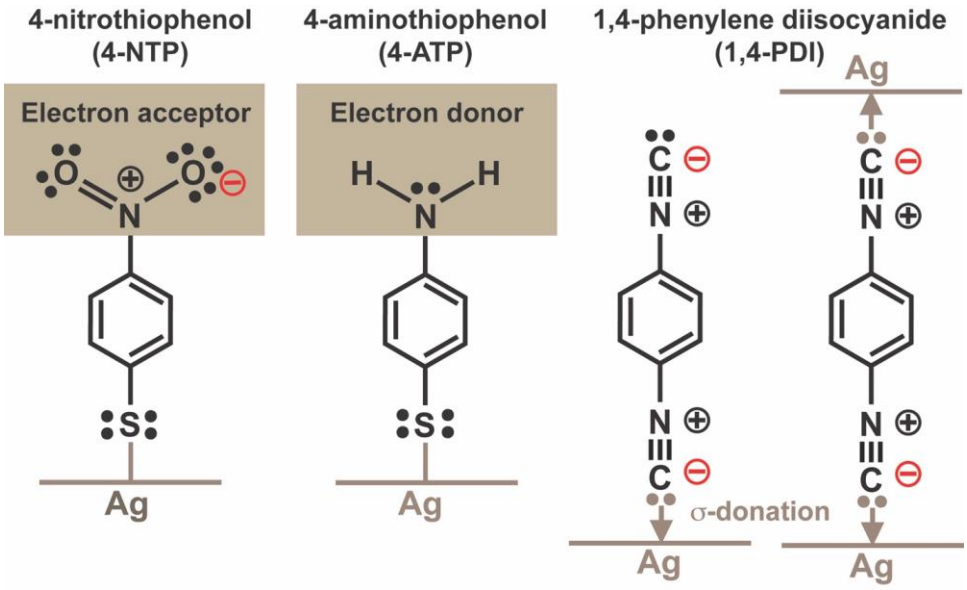

Figure 5.1. Molecular structures of the ligands and schematic illustrations showing how these ligand molecules bind to the surface of Ag nanocubes.

nanoparticles.[38,39] A number of groups have also investigated the production of an azo-compound from 4-NTP or 4-ATP on the surface of Ag or Au nanoparticles using SERS.[39-41] Different from thiol molecules whose vibrational modes exhibit essentially no dependence on the type of metal on the surface, the binding of the isocyanide group (–NC) to a transition metal is similar to that of carbon monoxide, making the stretching frequency of the NC bond (ν_{NC}) sensitive to the interaction between the –NC group and the metal.[42-45] The carbon is assumed to bind to Ag through σ-donation, by which the lone-pair electrons are donated from the anti-bonding σ* orbital of the –NC group to the Ag metal atoms. It is anticipated that there are two possible configurations of 1,4-PDI on the surface of Ag nanocubes. The first configuration involves the binding of one –NC group to Ag in a standing geometry with respect to the surface while leaving the other –NC group free.[46] The second one reflects the binding of both –NC groups to the Ag surface. Because the $\nu_{NC(Ag)}$ and $\nu_{NC(free)}$ peaks have distinctive Raman shifts, it is feasible to characterize the

configuration of 1,4-PDI on the surface of Ag by SERS. It is worth acknowledging that isocyanides have received attention in the molecular electronics community due to the lower barrier to electron transfer at the isocyanide-metal junction than that at the thiol-metal junction.[47,48] It has been argued that 1,4-PDI could serve as a molecular linker to bridge two metal electrodes through the two –NC groups and π-conjugated benzene ring to achieve efficient electron transfer.[48]

Specifically, in this Chapter, I present a systematic study of the adsorption of 4-NTP, 4-ATP, and 1,4-PDI on the surface of colloidal Ag nanocubes suspended in ethanol by *in situ* SERS. In a typical process, I disperse the acid-treated Ag nanocubes in an ethanol solution containing either 4-NTP, 4-ATP, or 1,4-PDI, followed by the collection of SERS spectra at different time points. Because the SERS hot spots are located on the edges of Ag nanocubes, I actually monitored the adsorption of thiol or isocyanide on the edges. By varying the concentration of each solution, there are some subtle differences in the vibrational peaks from the SERS spectra, suggesting that the configurations of molecules on the Ag surface likely change when the surface coverage of ligand molecules was altered. More interestingly, I further evaluate competitive adsorption of thiol and isocyanide by dispersing Ag nanocubes in an ethanol solution containing both thiol (4-NTP or 4-ATP) and 1,4-PDI. These results confirm the preference of thiol over isocyanide in adsorbing onto Ag surface when these two ligands are presented in comparable concentrations.

5.2 Experimental Section

Chemicals. Ethylene glycol (EG) was purchased from J. T. Baker (Avantor Performance Materials, LLC, Center Valley, PA). Silver trifluoroacetate (CF_3COOAg,

≥99.99%), sodium hydrosulfide hydrate ($NaHS \cdot xH_2O$), poly(vinylpyrrolidone) (PVP) with an average molecular weight of 29,000 (PVP-29), aqueous hydrochloric acid (HCl, 37 wt.%), L-ascorbic acid (H_2Asc, 99%), ethyl alcohol (ethanol, ≥99.5%), 1,4-phenylene diisocyanide (1,4-PDI, 97%), 4-nitrothiophenol (4-NTP, 80%), 4-aminothiophenol (4-ATP, 97%), gold(III) chloride trihydrate ($HAuCl_4 \cdot 3H_2O$, ≥99.9% trace metal basis), chloroplatinic acid hexahydrate ($H_2PtCl_6 \cdot 6H_2O$, ACS reagent, ≥37.50% Pt basis), and sodium borohydride ($NaBH_4$, 99.99%) were ordered from Sigma-Aldrich (St. Louis, MO). Sodium hydroxide (NaOH, 98%) and acetone (HPLC grade, 99.5+%) were obtained from Alfa Aesar. All chemicals were used as received. All aqueous solutions were prepared using deionized (DI) water with a resistivity of 18.2 MΩ·cm at room temperature.

Synthesis of Ag Nanocubes. I followed a published protocol involving polyol reduction to synthesize the Ag nanocubes.[49] The as-prepared Ag nanocubes were washed once with acetone, followed by three times with water, and then dispersed in water for storage and future use. The stock suspension of Ag nanocubes contained 1.2×10^{13} particles per mL.

Acid Treatment of Ag Nanocubes. In a standard protocol, I mixed 0.5 mL of aqueous H_2Asc (0.1 M) and 2 mL of aqueous PVP-29 (1 mM) in 0.5 mL of water in a 23-mL glass vial under magnetic stirring at 650 RPM. Next, I injected 25 μL of Ag nanocubes to the acidic solution to attain approximately 3.0×10^{11} particles. The mixture was magnetically stirred under ambient conditions for 2 h. Afterwards, the solution was divided and transferred into three centrifuge tubes, followed by their centrifugation at 5500 RPM for 15 min. After the removal of the supernatant, the solids were used without further modification for the SERS experiments. For TEM characterization, the solids were washed

with ethanol twice and drop-casted onto a TEM grid.

Monitoring the Adsorption of 4-NTP, 4-ATP, or 1,4-PDI on Ag Nanocubes by SERS. In a standard protocol, I first recorded a Raman spectrum from the ligand, such as 4-NTP, 4-ATP, or 1,4-PDI in ethanol solution at the concentration of 10^{-5} M, as a reference. Next, I mixed the ligand solution with the Ag nanocubes, followed by vigorous shaking to disperse the nanocubes. Finally, I withdrew aliquots from each sample at 3, 15, 30, 45 and 60 min for SERS measurements. For the experiments involving different concentrations of ligand, I followed the standard protocol except that the ligand solution was changed to either 10^{-4} M or 10^{-7} M.

Monitoring the Competitive Adsorption of 1,4-PDI and 4-NTP, as well as 1,4-PDI and 4-ATP, on Ag Nanocubes by SERS. In a typical experiment, I mixed two ligand solutions (4-NTP and 1,4-PDI, or 4-ATP and 1,4-PDI), each at a doubled concentration (that is, 2×10^{-3}, 2×10^{-5}, or 2×10^{-7} M) relative to the standard protocol, in equal volumes. As a result, the final mixture would preserve the concentrations of each ligand relative to the single-ligand experiments. I then followed the standard protocol except that the mixture was used as the ligand solution.

SERS Measurements. I performed the SERS measurements using a Renishaw inVia Raman spectrometer (Wotton-under-Edge, UK) coupled with a Leica optical microscope (Leica Camera, Wetzlar, Germany). In a typical measurement, I transferred an aliquot of 20 μL from the sample into a transparent polydimethylsiloxane (PDMS) cell, covered the cell with a thin cover glass, and placed the cell on the sample stage of microscope. After I used the *static* mode for collecting consecutive Raman spectra every second to confirm that the Raman signal was relatively stable (variation is within 100 counts), I recorded the

Raman spectrum in the *extended* mode, using the excitation wavelength of 532 nm, 100× objective, 10% of the laser power (maximum power of 50 mW), and 10 s collection time.

Quantitative Analysis of Raman Data. I used Renishaw's WiRE 5.1 software to calculate the area under the peaks of the characteristic Raman bands present in the SERS spectra at each time point in the experiment, specifically the ν_{CC} band of 4-NTP and the $\nu_{NC(Ag)}$ band of 1,4-PDI. For each data point, I performed the analysis according to the following procedure. In the first step, I loaded the raw data into the software and then centered the viewing window around the peak of interest (1520-1620 cm^{-1} for the ν_{CC} band, and 2000-2300 cm^{-1} for the ν_{NC} band). In the second step, based on the curve-fitting function in the software, I attempted to fit the data using a single Gaussian—Lorentzian peak (50% of each character). The software optimized the curve fit model to minimize the sum of the squared deviations of the fitting from the experimental data, updating the information such as the peak center, peak width, peak height, and the shape (proportion of the Gaussian character). If I cannot fit the band, I would add a second peak and performed the optimization again to better capture the peak area of this band. Finally, I took the sum of the peak areas of all curves used in this fitting to obtain the total area under the peak.

Instrumentation and Characterization. The nanoparticles were collected using an Eppendorf 5430 centrifuge (Eppendorf North America, Hauppauge, NY). The pH values were measured using a FiveEasy pH Meter (Mettler Toledo, Columbus, OH). The UV-vis spectra were collected using the Cary 60 spectrophotometer (Agilent Technologies, Santa Clara, CA). Transmission electron microscopy (TEM) images were captured on a Hitachi HT7700 microscope (Tokyo, Japan) operated at 120 kV.

5.3 Results and Discussion

5.3.1 Preparation of Acid-Treated Ag Nanocubes

We first prepared Ag nanocubes by following the protocol published by Xia and coworkers.[49] To remove any oxides on the surface, I dispersed the Ag nanocubes in an acidic solution (pH=3.1) containing H_2Asc and PVP under magnetic stirring for 120 min. Figure 5.2 shows TEM images of the samples before and after acid treatment, indicating no significant changes to the morphology of nanocubes. After collecting the ethanol solution containing the ligand molecules, followed by withdrawing aliquots from each sample at various time points for SERS measurements. In this study, I assume that the primary contribution to SERS signals would come from molecules adsorbed on the edges of individual Ag nanocubes where hot spots are located, rather than from those situated in the inter-particle junctions.[31] To validate my hypothesis, I recorded UV-vis spectra from the Ag nanocubes dispersed in the acid solution and the acid-treated nanocubes re-dispersed in the ethanol solution. As shown in Figure 5.3, there was essentially no change to the UV-vis spectra, confirming the absence of aggregation for the acid-treated Ag nanocubes re-dispersed in the ethanol solution. It is also worth mentioning that I could use the Raman peak of ethanol at 879 cm^{-1} as an internal reference to calibrate the Raman system. As confirmed by the spectra in Figure 5.4, this band remained at essentially the same position before and after the introduction of Ag nanocubes.

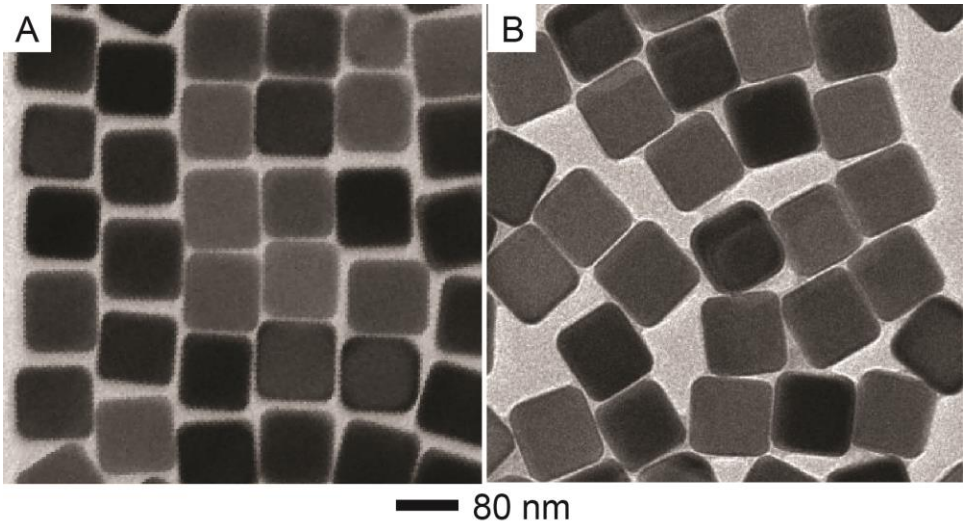

Figure 5.2. TEM images of (A) the as-synthesized Ag nanocubes and (B) the acid-treated Ag nanocubes.

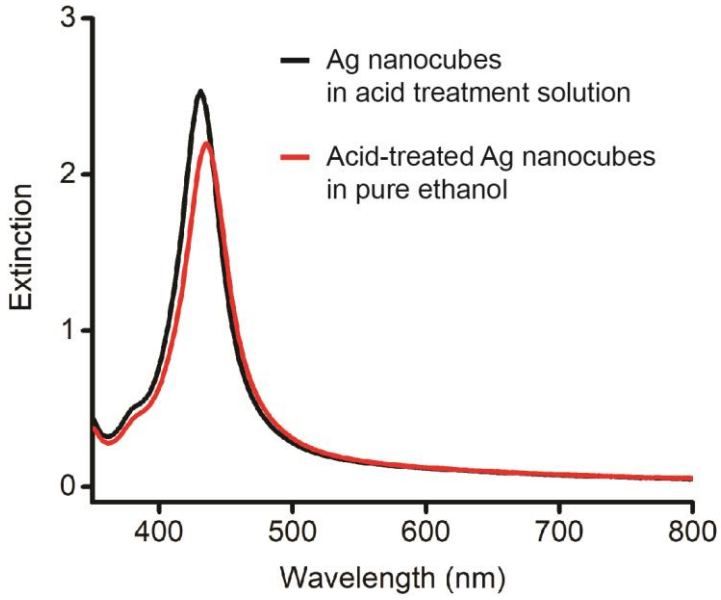

Figure 5.3. UV-vis spectra of Ag nanocubes dispersed in an acid treatment solution (black curve) and the acid-treated Ag nanocubes re-dispersed in pure ethanol (red curve).

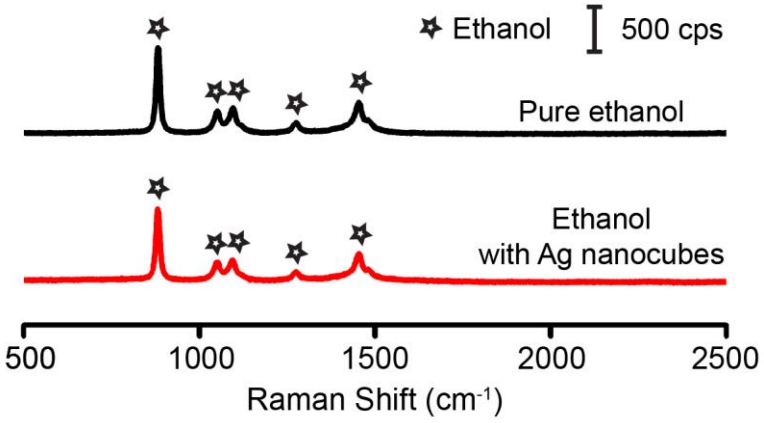

Figure 5.4. Raman spectra recorded from pure ethanol (black) and ethanol containing as-prepared Ag nanocubes (red).

5.3.2 Monitoring the Adsorption of Thiol Molecules on the Surface of Ag Nanocubes by In Situ SERS

We initially studied the interaction of thiols with Ag nanocubes by employing 4-NTP as the ligand. Figure 5.5A shows Raman spectra collected from a 4-NTP solution (10^{-5} M) in ethanol before and after adding the acid-treated Ag nanocubes. Based on my back-of-the-envelope calculation, it is reasonable to assume that the 4-NTP molecules at this concentration would be able to form a full coverage on the Ag nanocubes. In the absence of Ag nanocubes, the Raman spectrum only shows the peaks associated with ethanol. At *t*=3 min after the introduction of nanocubes, the characteristic peaks of 4-NTP appeared at 1083 (C−S stretching, ν_{CS}), 1336, 1347 (NO_2 stretching, ν_{NO2}), and 1572 cm^{-1} (C−C stretching, ν_{CC}). The frequencies and intensities of these peaks did not change over a period up to *t*=60 min. nanocubes into 10^{-5} M 4-NTP ethanol solution, suggesting that the SERS signal remains stable during the collection time of 10 s. It is worth mentioning that I calibrated the Raman spectrometer using Si(100) as a reference every time before we

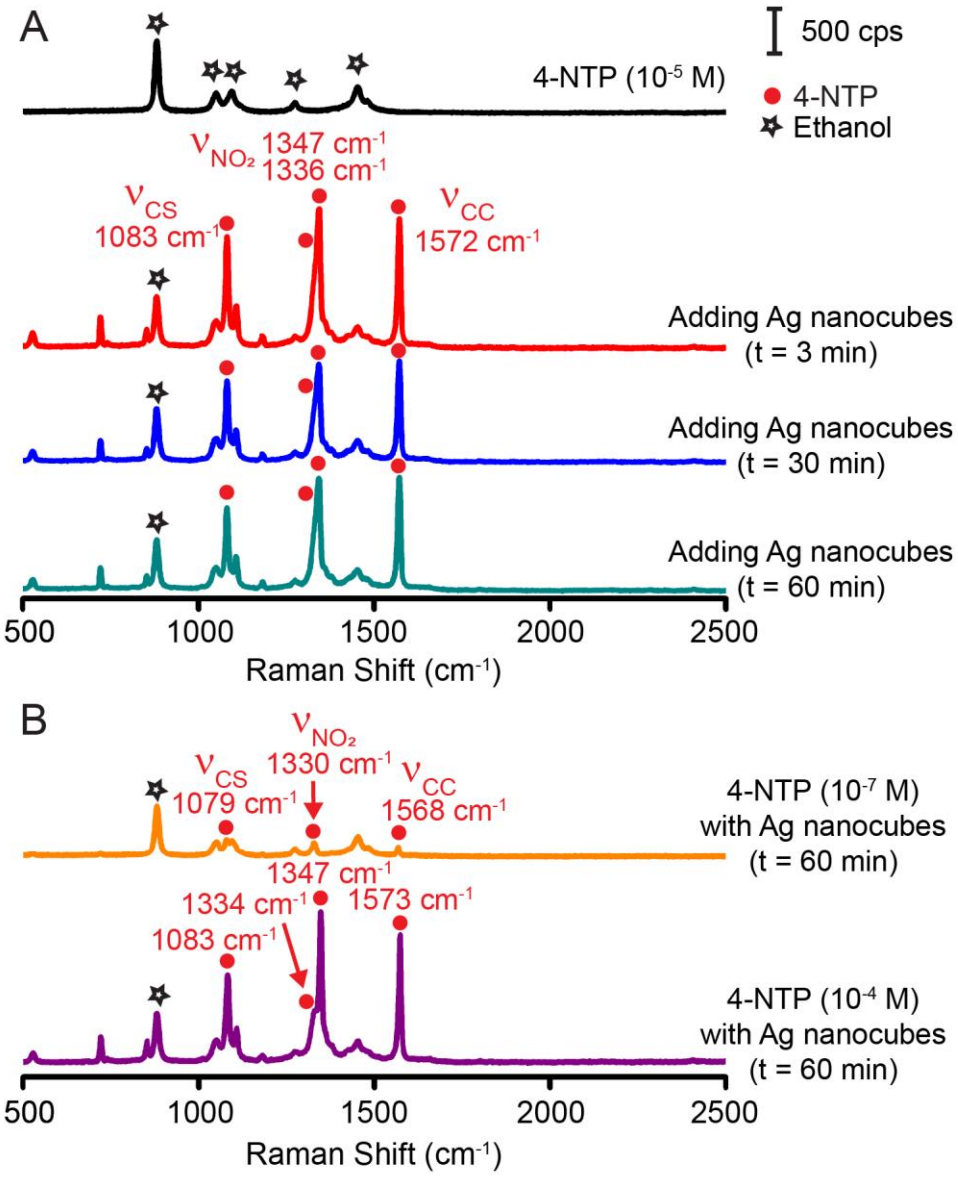

Figure 5.5. (A) Raman spectrum of 4-NTP ethanol solution (10^{-5} M) and the SERS spectra of 4-NTP collected from the same solution at different time points after the introduction of Ag nanocubes. (B) The SERS spectra of 4-NTP collected at t=60 min after introducing Ag nanocubes into the 4-NTP ethanol solutions at concentrations of 10^{-7} M and 10^{-4} M, respectively.

performed the SERS measurements. Based on 20 calibrations, Table 5.1 shows that the spectrometer consistently gives the Raman shift of Si(100) at 520.29 cm^{-1} with a standard deviation of 0.09 cm^{-1}. With regard to the peak intensity, Figure 5.6 shows the

Table 5.1. Raman data of the characteristic peak of Si as periodically measured throughout all the SERS experiments. S. D. refers to the standard deviation of the dataset.

#	Centre	Width	Height	#	Centre	Width	Height
1	520.35	5.11	110652	12	520.44	5.07	117896
2	520.38	4.97	110645	13	520.22	5.42	119255
3	520.35	5.02	115457	14	520.1	5.09	112784
4	520.26	5.02	108978	15	520.32	4.87	122134
5	520.25	5.03	110601	16	520.32	5.48	117520
6	520.2	5.3	108247	17	520.32	5.16	116003
7	520.32	4.87	107954	18	520.31	5.42	113424
8	520.39	5.24	112402	19	520.37	5.11	118993
9	520.29	5.27	108795	20	520.19	5.61	106963
10	520.1	5.09	112784	Mean	**520.29**	**5.19**	**113363**
11	520.34	5.54	115776	S. D.	**0.09**	**0.22**	**4346**

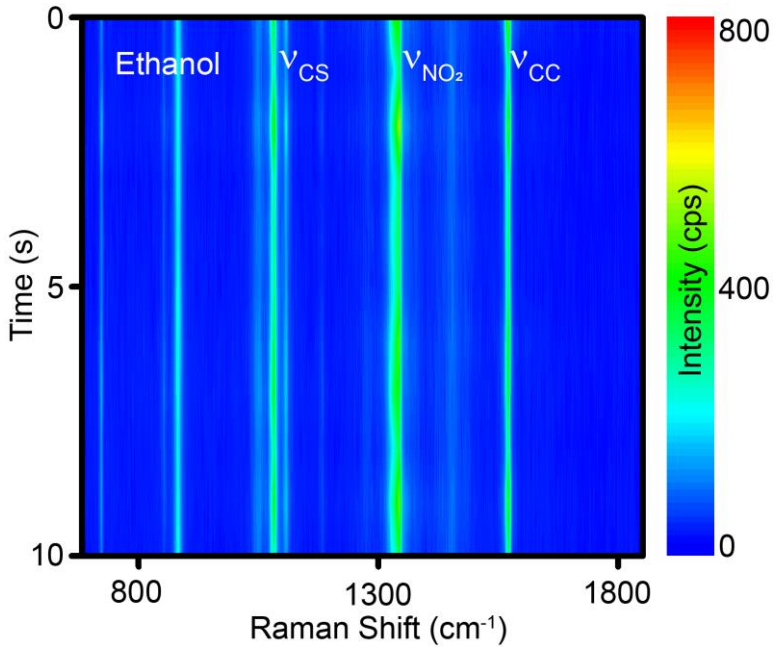

Figure 5.6. Heatmap generated from the time-dependent SERS spectra of 4-NTP (10^{-5} M), successively collected in the *static* mode with a collection time of 1 s each. These data points were collected prior to collecting the SERS spectra at t=3 min.

time-dependent SERS spectra (in the form of a heat map) of 4-NTP collected 3 min after the introduction of Ag. It is interesting to note that the stretching mode of NO_2 (ν_{NO2}) was split into two peaks at 1336 and 1347 cm^{-1}. Although this observation is different from those reported in previous *ex situ* SERS experiments involving 4-NTP,[41,50] it is still difficult to fully elucidate the nature of these two peaks at the moment.

By varying the concentration of 4-NTP while keeping the number of Ag nanocubes unchanged in the ethanol solution, I investigated how the molecules would interact with the Ag surface differently. At t=60 min, Figure 5.5B shows the SERS spectra of 4-NTP adsorbed onto the Ag nanocubes from solutions with concentrations at 10^{-7} M and 10^{-4} M, respectively. At 10^{-7} M, I noticed that the Raman peaks of 4-NTP were noticeably red-shifted to 1079 (ν_{CS}), 1330 (ν_{NO2}), and 1568 cm^{-1} (ν_{CC}), respectively, while the other ν_{NO2} peak at 1346 cm^{-1} was missing. Based on peak areas of ν_{NO2}, the SERS signal became 20-fold weaker relative to that of 10^{-5} M. Conversely, at 10^{-4} M, the peaks of 4-NTP appeared at 1083 (ν_{CS}), 1334, 1347 (ν_{NO2}), and 1573 cm^{-1} (ν_{CC}), consistent with the peak positions at 10^{-5} M. Also, the peak intensities were comparable to those shown in Figure 5.5A.

To further evaluate the concentration-dependent adsorption of 4-NTP on Ag nanocubes, I performed SERS measurements three times at concentration of 10^{-7}, 10^{-5}, or 10^{-4} M, respectively. By fitting the ν_{cc} band (see details in the experimental section), Figure 5.7 shows three plots of the peak area as function of time at three concentrations. My data suggests that the SERS signal reached to the stable state within 3 min regardless the concentration of 4-NTP, suggesting that the adsorption of 4-NTP on the surface of Ag nanocubes could reach equilibrium at a time scale less than 3 min. Because the SERS hot spots are located on the twelve edges of a Ag nanocube while the cube is predominantly

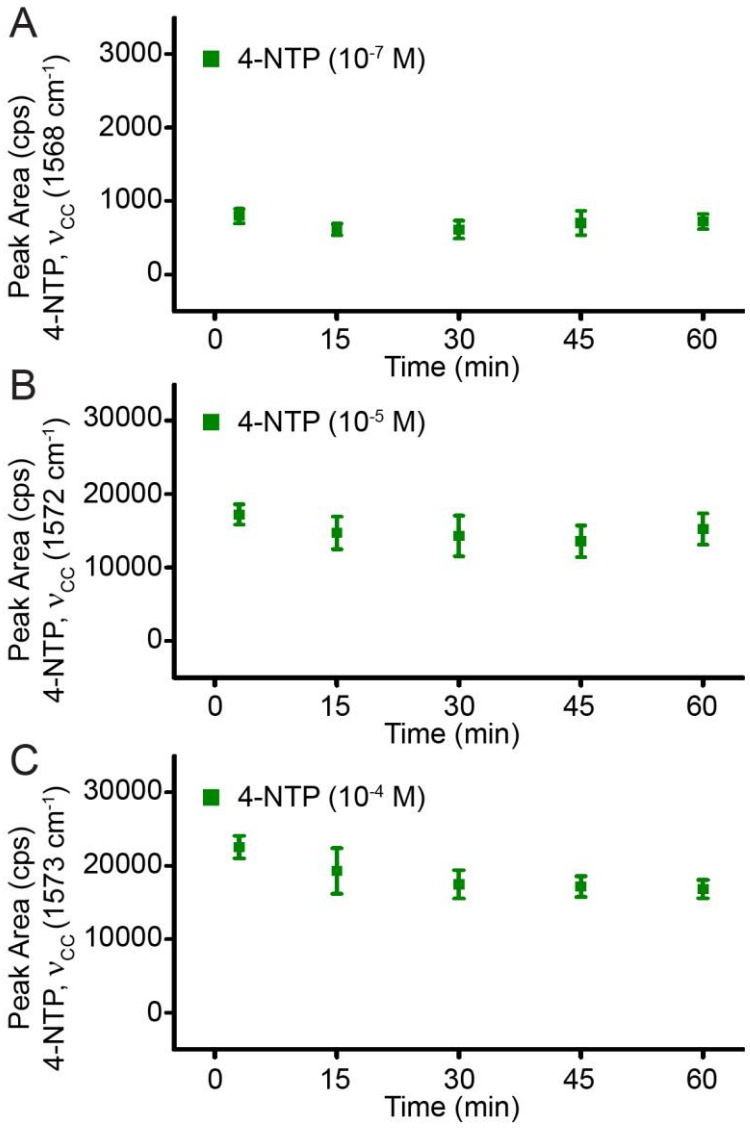

Figure 5.7. Plots of peak areas of the ν_{CC} band of 4-NTP as a function of time at the concentration of (A) 10^{-7} M, (B) 10^{-5} M, and (C) 10^{-4} M, respectively.

enclosed by six side faces, it is not surprising to resolve much weak SERS signal at a concentration of 10^{-7} M when only a limited number of molecules occupied the edges of nanocubes. In comparison, when the concentration was increased to 10^{-5} and then to 10^{-4} M, the SERS signals became stronger and reached saturation, suggesting that the molecules could fully cover the edges of Ag nanocubes where the SERS hot spots were located. On the other hand, the difference in Raman shifts of 4-NTP at various concentrations may

suggest that the 4-NTP molecules could adsorb on the surface of Ag nanocubes in different configurations. It has been established that the orientation of the adsorbed thiols on a metal surface is dependent on the packing density and thus the concentration of the ligand molecules.[2] For example, alkanethiols have been reported to assume an orientation parallel to the metal surface when used at low concentrations, while taking a more or less perpendicular orientation at relatively high concentrations.[51-53] From this perspective, it is possible that the red-shifted SERS peaks observed for 4-NTP at 10^{-7} M reflect those of parallel-lying molecules at a low packing density, whereas the peaks of 4-NTP at 10^{-5} or 10^{-4} M correspond to those perpendicular to the surface in a closely packed monolayer.

We then examined the interaction of 4-ATP with Ag nanocubes. When the electron-withdrawing nitro group is substituted by an electron-donating amine group, one could expect a change to the direction of electron flow between the Ag surface and the molecule, leading to a diminished of chemical enhancement for the SERS.[39] Figure 5.8A shows the SERS data collected from the acid-treated Ag nanocubes after being re-dispersed in the 4-ATP ethanol solution (10^{-5} M). At *t*=3 min, the characteristic peaks of 4-ATP appeared at 1080 (C−S stretching, ν_{CS}) and 1593 cm^{-1} (C−C stretching, ν_{CC}). These two peaks did not change their positions and intensities up to *t*=60 min, consistent with the behavior of 4-NTP. As anticipated, when the ligands were used at the same concentration of 10^{-5} M, the intensities of the 4-ATP signals were much weaker than those from 4-NTP (Figure 5.5A). This trend supports my argument that the signals from 4-ATP should be weaker due to the lack of chemical enhancement. As shown in Figure 5.8B, hardly any peaks associated with 4-ATP could be resolved at 10^{-7} M, while the two peaks located at 1080 (ν_{CS}) and 1594 cm^{-1} (ν_{CC}) returned at 10^{-4} M at the time point of 60 min.

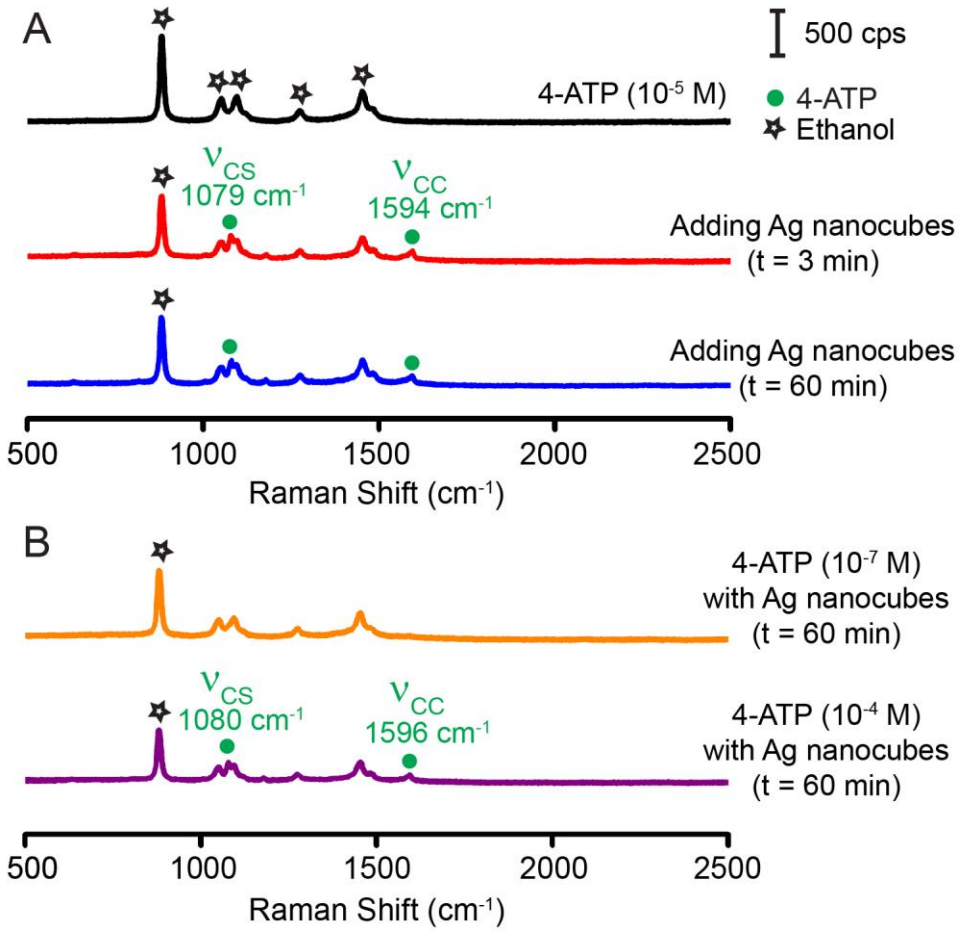

Figure 5.8. (A) Raman spectrum of 4-ATP ethanol solution (10^{-5} M) and the SERS spectra of 4-ATP collected from the same solution at different time points after the introduction of Ag nanocubes. (B) The SERS spectra of 4-ATP collected at *t*=60 min after introducing Ag nanocubes into the 4-ATP ethanol solutions at concentrations of 10^{-7} M and 10^{-4} M, respectively.

5.3.3 Monitoring the Adsorption of 1,4-PDI on the Surface of Ag Nanocubes and Evaluating their Orientation by In Situ SERS

Different from thiols that form a relatively strong Ag-S bond with the Ag surface, 1,4-PDI weakly binds to the surface of Ag nanocubes through σ-donation.[44,46] Figure 5.9A shows Raman spectra collected from a 1,4-PDI solution (10^{-5} M) in ethanol before and after adding the acid-treated Ag nanocubes. At *t*=3 min, the characteristic peaks of 1,4-PDI emerged at 1164 (C−H bending, δ_{CH}), 1204 (C−NC stretching, ν_{C-NC}), and 1597 (C−C

stretching, ν_{CC}), 2125 (N−C stretching, $\nu_{NC(free)}$) and 2177 cm^{-1} (N−C stretching, $\nu_{NC(Ag)}$). At *t*=30 min, there was a slight increase in peak intensity. The SERS spectrum then shows little change up to *t*=60 min. It is interesting to note that the N−C stretching mode appeared at 2177 and 2125 cm^{-1} in the SERS spectrum with their assignments to the $\nu_{NC(Ag)}$ and $\nu_{NC(free)}$, respectively.[46] The presence of the $\nu_{NC(free)}$ peak suggests that the 1,4-PDI molecules would bind to the surface of the Ag nanocubes through one of its two isocyanide groups only, with the benzene ring tilting away from the surface.

We also collected SERS spectra of acid-treated Ag nanocubes after they had been incubated with 1,4-PDI solutions of 10^{-7} M and 10^{-4} M, respectively, at the time point of 60 min. As shown in Figure 5.9B, at 10^{-7} M, the $\nu_{NC(free)}$ peak was not identified while the $\nu_{NC(Ag)}$ peak remained almost unchanged at 2176 cm^{-1}. In comparison, at 10^{-4} M, I resolved both the $\nu_{NC(Ag)}$ and $\nu_{NC(free)}$ peaks. Based on the peak areas of $\nu_{NC(Ag)}$, the overall SERS signal is about two-fold weaker at 10^{-7} M or four-fold stronger at 10^{-4} M compared with that of 10^{-5} M.

To confirm the orientation of 1,4-PDI on Ag surface, I monitored the ν_{CH} band located at 3065 cm^{-1}. According to the surface selection rule, this band can only be identified when the benzene ring is tilting away from the surface.[54] Figure 5.10A shows a small ν_{CH} band when Ag nanocubes were functionalized with 1,4-PDI of 10^{-4} M. Interestingly, Figure 5.10B exhibits the appearance of the ν_{CH} band when I functionalized Ag nanocubes with 1,4-PDI of 10^{-5} M and then doubled the number of functionalized cubes used in the standard protocol for SERS measurements. These results support my previous argument that the1,4-PDI molecules would bind to Ag through a single isocyanide group with the benzene ring tilting away from the surface, giving rise of the $\nu_{NC(free)}$ peak at these two concentrations

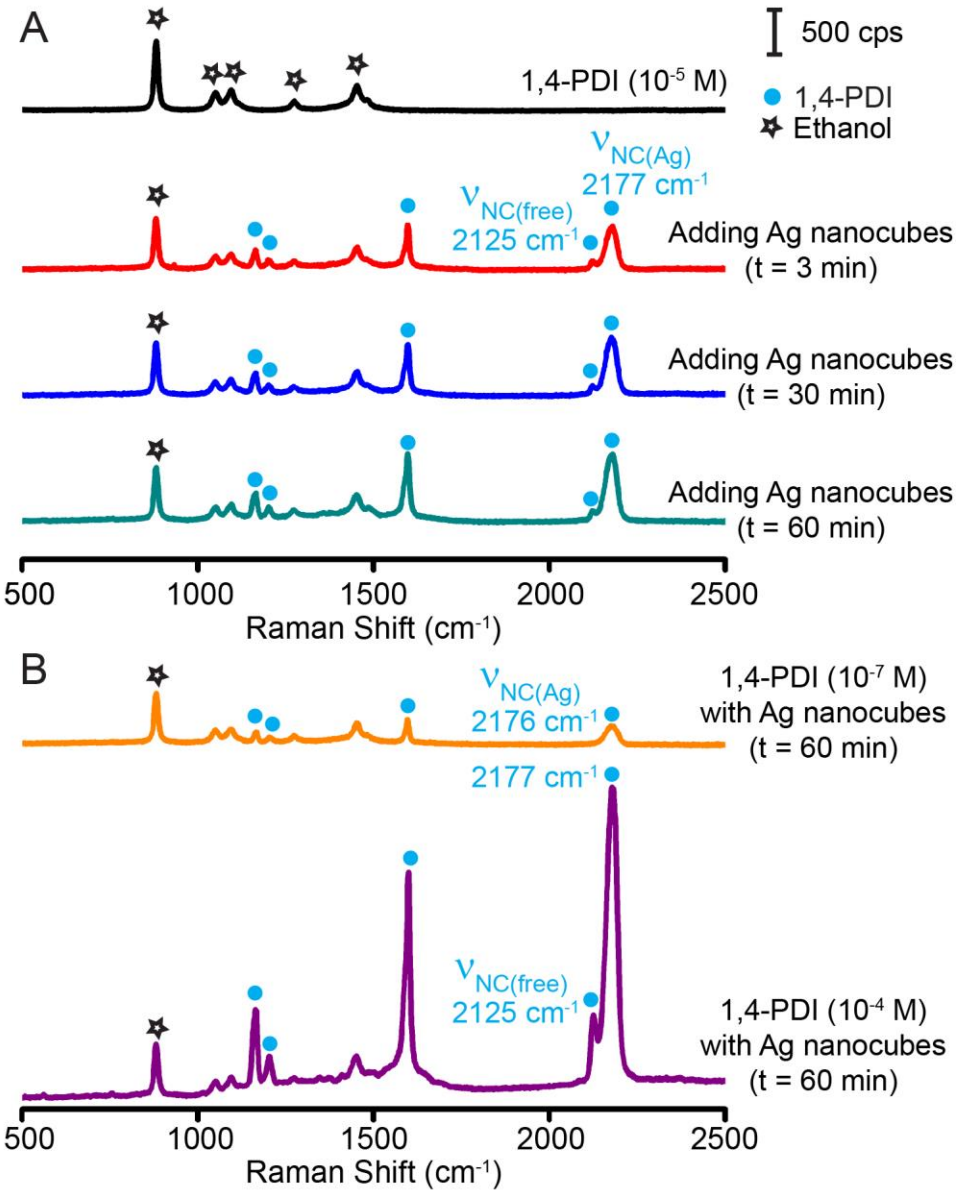

Figure 5.9. (A) Raman spectrum of 1,4-PDI ethanol solution (10^{-5} M) and the SERS spectra of 1,4-PDI collected from the same solution at different time points after the introduction of Ag nanocubes. (B) The SERS spectra of 1,4-PDI collected at *t*=60 min after adding Ag nanocubes into the 1,4-PDI ethanol solutions at 10^{-7} M and 10^{-4} M, respectively.

concentrations (see Figure 5.9, A and B). When I functionalized Ag nanocubes with 1,4-PDI of 10^{-7} M, followed by SERS detection by increasing the number of Ag nanocubes that are four times larger than those used in the standard protocol to improve detection sensitivity, Figure 5.10C shows no observation of the ν_{CH} band even though the increase

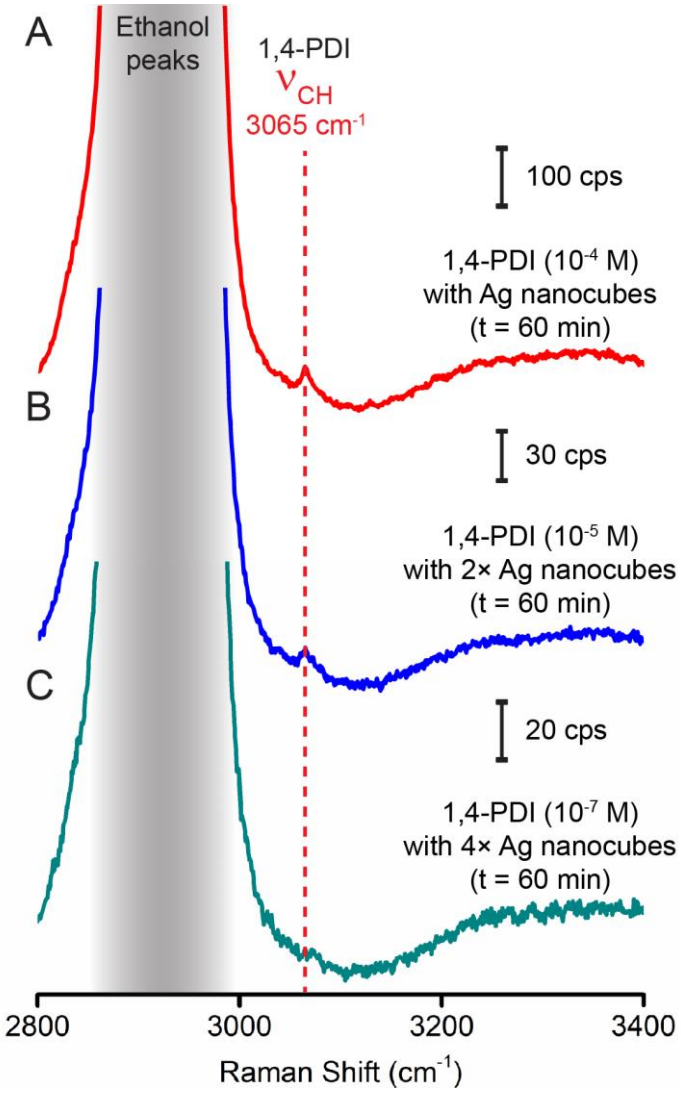

Figure 5.10. The SERS spectra of 1,4-PDI collected at *t*=60 min by using (A) Ag nanocubes prepared with a 1,4-PDI ethanol solution at 10^{-4} M, (B) Ag nanocubes prepared with a 1,4-PDI ethanol solution at 10^{-5} M with the number of particles doubled relative to those in (A), and (C) Ag nanocubes prepared by with a 1,4-PDI ethanol solution at 10^{-7} M with the number of particles quadrupled relative to those in (A).

in the number of nanocubes for this set of SERS measurements was able to increase the peak intensity of $\nu_{NC(Ag)}$ band significantly to the signal level comparable to that of $\nu_{NC(Ag)}$ band collected from Ag nanocubes functionalized with 1,4-PDI of 10^{-5} M. Figure 5.11 shows the direct comparison of the $\nu_{NC(Ag)}$ band, from which one still cannot resolve the $\nu_{NC(free)}$ band. Altogether, I believe that a larger proportion of the 1,4-PDI molecules would

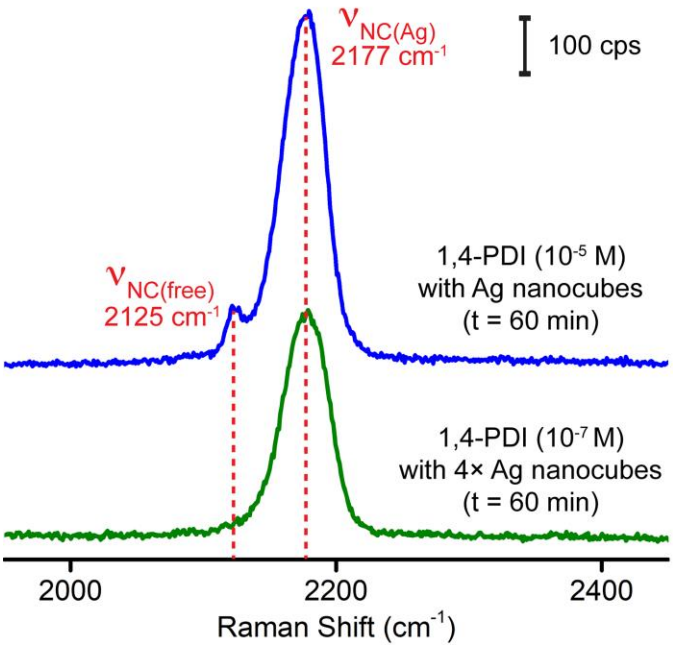

Figure 5.11. The SERS spectra of 1,4-PDI collected at *t*=60 min by using (A) Ag nanocubes prepared by 1,4-PDI ethanol solutions at 10^{-5} M and (B) Ag nanocubes prepared by 1,4-PDI ethanol solutions at 10^{-7} M with the number of particles quadrupled from those in (A).

bind to the edges of Ag nanocubes, the SERS hot spots, through a single isocyanide group, likely in a benzene ring tilting away from the surface, at a high concentration for accommodating closely packed configuration. In the case of 10^{-7} M, it is possible that the molecules might bind to the Ag surface through both isocyanide groups rather than only one of them at such low concentration. We also collected SERS spectra of acid-treated Ag nanocubes after they had been incubated with 1,4-PDI solutions of 10^{-7} M and 10^{-4} M, respectively, at the time point of 60 min. As shown in Figure 5.9B, at 10^{-7} M, the $\nu_{NC(free)}$ peak was not identified while the $\nu_{NC(Ag)}$ peak remained almost unchanged at 2176 cm^{-1}. In comparison, at 10^{-4} M, I resolved both the $\nu_{NC(Ag)}$ and $\nu_{NC(free)}$ peaks. Based on the peak areas of $\nu_{NC(Ag)}$, the overall SERS signal is about two-fold weaker at 10^{-7} M or four-fold stronger at 10^{-4} M compared with that of 10^{-5} M.

5.3.4 Assessing the Competitive Adsorption of Thiols and 1,4-PDI on Ag Nanocubes

Based on the results shown in Figures 5.2-5.11, I argue that 4-NTP, 4-ATP, and 1,4-PDI all can readily adsorb onto the surface of Ag nanocubes dispersed in ethanol. To further examine the difference between thiol and isocyanide, I evaluated their competitive adsorption onto the surface of Ag nanocubes by introducing the acid-treated Ag nanocubes into an ethanol solution containing both types of ligands at specific concentrations. Figure 5.12A shows the Raman spectra collected from an ethanol solution containing 4-NTP and 1,4-PDI (both at 10^{-5} M). At *t*=3 min, the peaks at 1083, 1336, 1347, and 1572 cm^{-1} could be assigned to ν_{CS}, ν_{NO2}, and ν_{CC} of 4-NTP, respectively. However, I could not resolve well-defined peaks associated with 1,4-PDI, except an extremely weak peak located at 2172 cm^{-1}. The SERS spectrum remained essentially the same up to *t*=60 min. This data confirms that thiol would adsorb onto Ag surface more competitively on the edges of Ag nanocubes where the hot spots are located for SERS detection. Interestingly, when I reduced the 4-NTP concentration by 100-fold to 10^{-7} M while keeping the concentration of 1,4-PDI at 10^{-5} M, at *t*=3 min, Figure 5.12B shows the appearance of peaks characteristic of 1,4-PDI at 2123 ($\nu_{NC(free)}$) and 2178 cm^{-1} ($\nu_{NC(Ag)}$), together with characteristic peaks of 4-NTP at 1080 (ν_{CS}), 1330 (ν_{NO2}), and 1568 cm^{-1} (ν_{CC}), I also observed increase in peak intensity for the $\nu_{NC(Ag)}$ band of 1,4-PDI while there was essentially no change to the peaks of 4-NTP by *t*=30 min. From *t*=30 to 60 min, the SERS spectrum remained unaltered. These results infer that 4-NTP and 1,4-PDI could co-exist on the edges of Ag nanocubes.

To further understand the concentration-dependent adsorption of 4-NTP and 1,4-PDI on Ag nanocubes, I repeated the SERS measurements and then analyzed the results. By fitting the ν_{cc} band of 4-NTP, Figure 5.13A shows a plot of the peak area as a function of

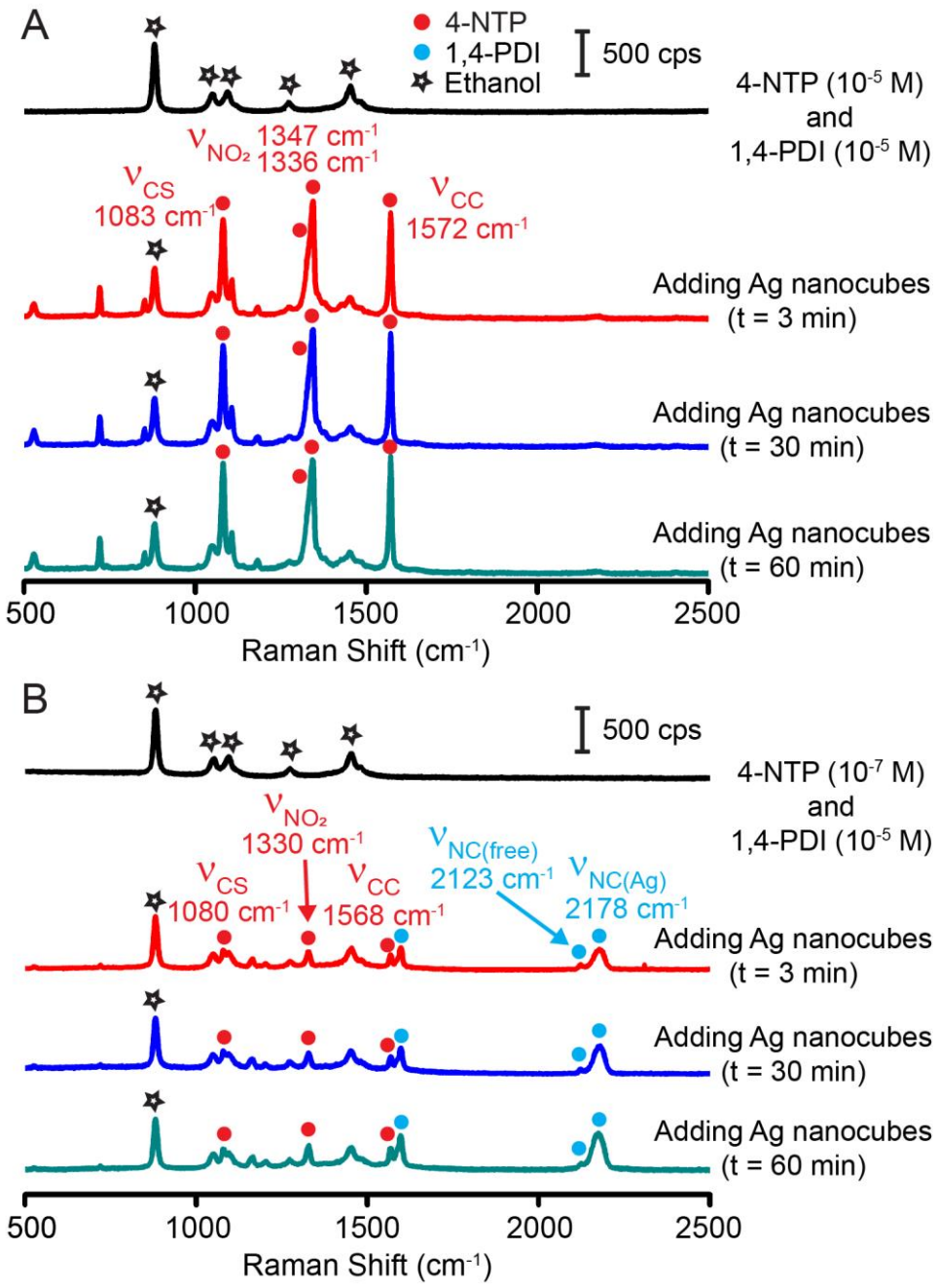

Figure 5.12. (A) Raman spectrum recorded from an ethanol solution containing 4-NTP (10^{-5} M) and 1,4-PDI (10^{-5} M) and the SERS spectra of 4-NTP and 1,4-PDI collected from the same solution at different time points after the introduction of Ag nanocubes. (B) Raman spectrum of an ethanol solution containing 4-NTP (10^{-7} M) and 1,4-PDI (10^{-5} M) and the SERS spectra of 4-NTP and 1,4-PDI collected from the same solution at different time points after adding Ag nanocubes.

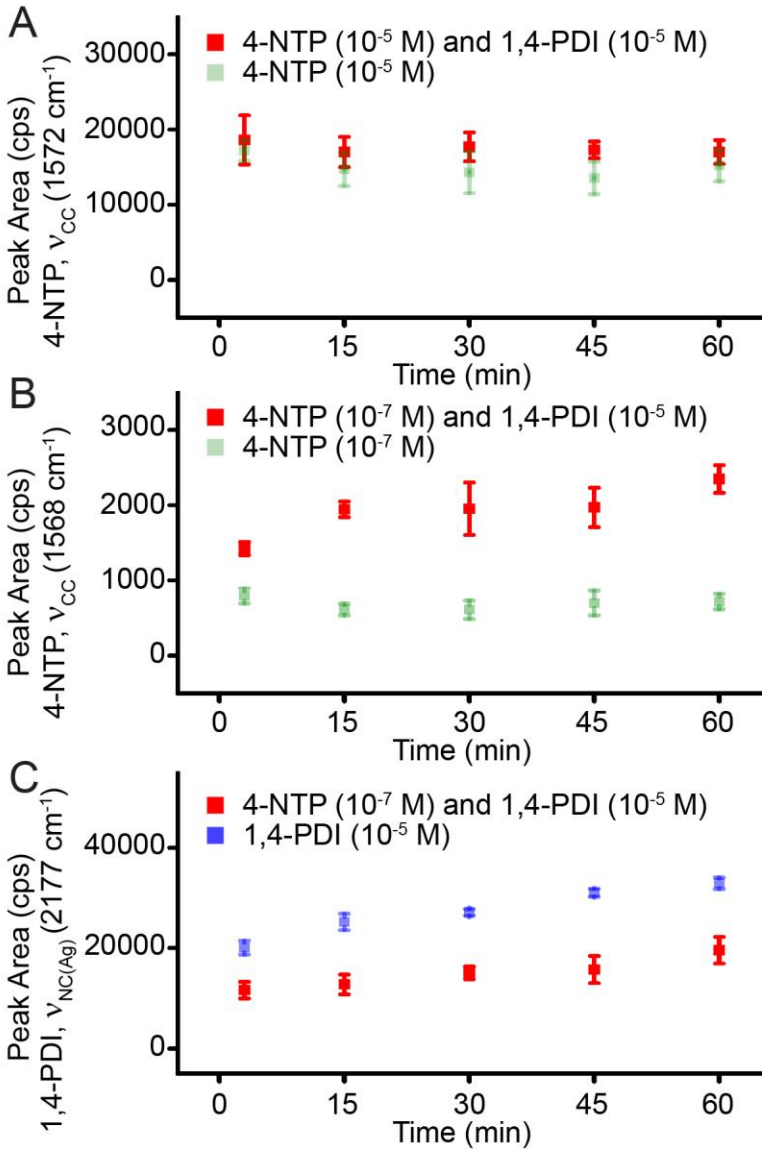

Figure 5.13. (A) Plots of peak area for the ν_{CC} band of 4-NTP as a function of time when the 4-NTP (10^{-5} M) was mixed with 1,4-PDI (10^{-5} M) by benchmarking against 4-NTP (10^{-5} M). (B) Plots of peak area for the ν_{CC} band of 4-NTP as a function of time when 4-NTP (10^{-7} M) was mixed with 1,4-PDI (10^{-5} M) by benchmarking against 4-NTP (10^{-7} M). (C) Plots of peak area for the $\nu_{CN(Ag)}$ band of 1,4-PDI as a function of time when 4-NTP (10^{-7} M) was mixed with 1,4-PDI (10^{-5} M) by benchmarking against 1,4-PDI (10^{-5} M).

time by benchmarking against 4-NTP (10^{-5} M). In this case, I noticed that the SERS signal was comparable to that of 4-NTP, suggesting that the 4-NTP could competitively bind to the edges of Ag nanocubes over 1,4-PDI when they were used at the same concentration.

On the other hand, when I decreased the concentration of 4-NTP to10^{-7} M while keeping the concentration of 1,4-PDI at 10^{-5} M, Figure 5.13B shows a plot of the ν_{CC} band of 4-NTP as a function of time by benchmarking against the plot of 4-NTP (10^{-7} M). Under this condition, I observed an increase in the peak area of 4-NTP when 100-fold more 1,4-PDI molecules were involved in the solution. Because 4-NTP at 10^{-7} M was unable to cover the entire surface of Ag nanocubes, I suspect that the adsorption of 1,4-PDI would occur on the side faces of nanocubes, making it possible to favor the preferential adsorption of 4-NTP molecules on the edges of nanocubes for an increase in the SERS signal. Figure 5.13C shows a plot of the $\nu_{NC(Ag)}$ band of 1,4-PDI as a function of time by benchmarking against the plot of 1,4-PDI (10^{-5} M). Interestingly, I observed a decrease in the SERS signal of 1,4-PDI when a small amount of 4-NTP was involved in the solution. This result indicates that a fewer number of 1,4-PDI molecules were located at the SERS hot spots resulting from the competitive binding of 4-NTP on the edges of nanocubes. Altogether, I argue that it is feasible to use 4-NTP to impede or even inhibit the adsorption of 1,4-PDI molecules on the surface of Ag by tuning the concentration of these two ligands.

We also evaluated the competitive adsorption of 4-ATP and 1,4-PDI on Ag using the same experimental approach. Figure 5.14A shows the Raman spectrum collected from an ethanol solution containing 4-ATP and 1,4-PDI, both at 10^{-5} M. At t=3 min, I observed the peaks of 4-ATP at 1080 (ν_{CS}) and 1595 (ν_{CC}) but not the $\nu_{NC(free)}$ and $\nu_{NC(Ag)}$ bands of 1,4-PDI. Because the ν_{CC} bands of both 1,4-PDI and 4-ATP overlap with each other, I cannot reply on this band for the identification of 1,4-PDI. From t=30 to 60 min, there was essentially no change to the SERS spectrum. These results are similar to the case of 1,4-PDI and 4-NTP, confirming that thiol binds more strongly to Ag surface than isocyanide

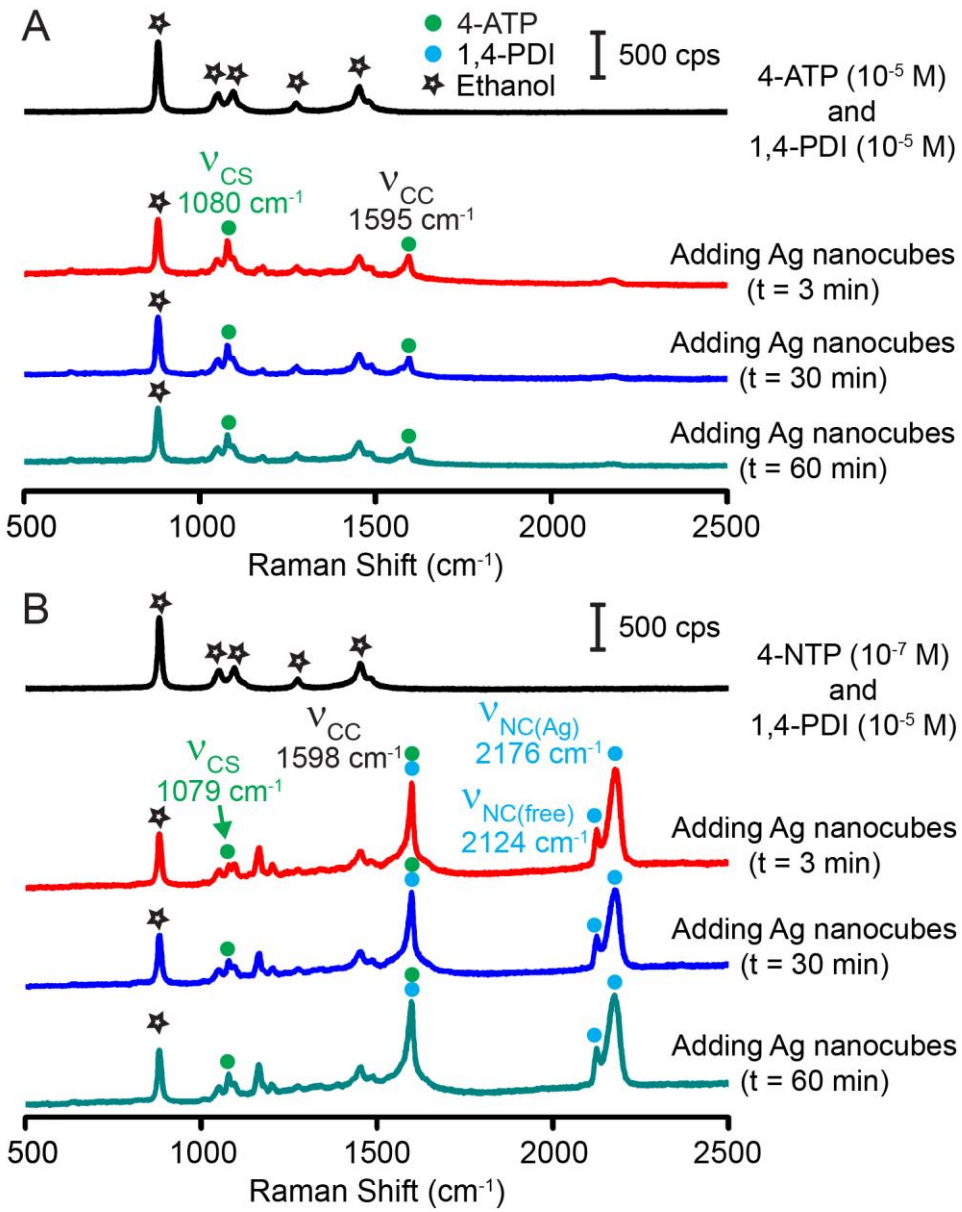

Figure 5.14. (A) Raman spectrum recorded from an ethanol solution containing 4-ATP (10^{-5} M) and 1,4-PDI (10^{-5} M) and the SERS spectra of 4-ATP and 1,4-PDI collected from the same solution at different time points after introducing Ag nanocubes. (B) Raman spectrum of an ethanol solution containing 4-ATP (10^{-5} M) and 1,4-PDI (10^{-3} M) and the SERS spectra of 4-ATP and 1,4-PDI collected from the same solution at different time points after adding Ag nanocubes.

regardless of the difference in the terminal group (NO_2 *vs.* NH_2). Because it was difficult to resolve any SERS signal when decreasing the concentration of 4-ATP from 10^{-5} M to 10^{-7} M (see Figure 5.8B), I increased the concentration of 1,4-PDI to 10^{-3} M while keeping

the 4-ATP concentration at 10^{-5} M to attain a molar ratio of 4-ATP to 1,4-PDI molecules at 1:100. In this case, at *t*=3 min, Figure 5.14B shows the characteristic peaks of 1,4-PDI at 2125 ($\nu_{NC(free)}$) and 2171 cm^{-1} ($\nu_{NC(Ag)}$) in addition to the peaks of 4-ATP. This suggests that both 4-ATP and 1,4-PDI could adsorb on the edges of Ag nanocubes at comparable rates when 1,4-PDI was in excess, consistent with the results of 4-NTP and 1,4-PDI.

5.4 Conclusions

We have explored the use of *in situ* SERS to investigate the adsorption of different ligands on the surface of colloidal Ag nanocubes. In a typical process, I collected SERS spectra at different time points from a mixture of Ag nanocubes and a ligand such as 4-NTP, 4-ATP, or 1,4-PDI at a specific concentration. Time-dependent SERS spectra of 4-NTP indicate that the adsorption could be achieved within 3 min due to the strong binding of thiol to Ag surface. I also recorded the concentration-dependent SERS spectra of 4-NTP, from which I observed a red-shift for all peaks at a concentration of 10^{-7} M relative to the case 10^{-5} M or 10^{-4} M. I argue that such a red-shift could be attributed to the difference in molecular orientation, with the benzene ring oriented parallel to or tilting away from the surface at low and high concentrations, respectively. I confirmed that the adsorption kinetics of 4-ATP on Ag was similar to that of 4-NTP, although the SERS signals from 4-ATP were much weaker due to the absence of chemical enhancement. Different from the case of thiol, 1,4-PDI would bind to a Ag surface through σ-donation, giving slower adsorption kinetics over a time scale of 60 min. At a concentration of 10^{-5} M and above, I observed both $\nu_{NC(free)}$ and $\nu_{NC(Ag)}$ peaks in the SERS spectra, suggesting that the 1,4-PDI molecules could be oriented with the benzene ring tilting away from the surface. I further

evaluated the relative binding strength of the thiol and isocyanide groups toward Ag surface by dispersing Ag nanocubes in an ethanol solution containing both ligands. The SERS signals from 1,4-PDI were not detectable in either case when it was used at the same concentration as 4-NTP or 4-ATP at 10^{-5} M. However, the 1,4-PDI signals became detectable when its concentration was increased by 100 times relative to 4-NTP or 4-ATP. Collectively, my data indicate that the thiols have a much stronger binding to the surface on Ag nanocubes, making it possible to impede or even inhibit the adsorption of isocyanides.

5.5 Notes to Chapter 5

This chapter is adapted from the article "Comparative Study of the Adsorption of Thiol and Isocyanide Molecules on Silver Surface by In Situ Surface-Enhanced Raman Scattering" published in the *Journal of Physical Chemistry C*.[55]

5.6 References

(1) Gast, A. P.; Adamson, A. W. *Physical chemistry of surfaces*, 6th ed.; Wiley-Interscience: New York, 1997.

(2) Love, J. C.; Estroff, L. A.; Kriebel, J. K.; Nuzzo, R. G.; Whitesides, G. M. Self-Assembled Monolayers of Thiolates on Metals as a Form of Nanotechnology. *Chem. Rev.* **2005**, *105*, 1103-1170.

(3) Lévy, R.; Thanh, N. T. K.; Doty, R. C.; Hussain, I.; Nichols, R. J.; Schiffrin, D. J.; Brust, M.; Fernig, D. G. Rational and Combinatorial Design of Peptide Capping Ligands for Gold Nanoparticles. *J. Am. Chem. Soc.* **2004**, *126*, 10076-10084.

(4) Sperling, R. A.; Rivera Gil, P.; Zhang, F.; Zanella, M.; Parak, W. J. Biological Applications of Gold Nanoparticles. *Chem. Soc. Rev.* **2008**, *37*, 1896-1908.

(5) Daniel, M.-C.; Astruc, D. Gold Nanoparticles: Assembly, Supramolecular Chemistry, Quantum-Size-Related Properties, and Applications Toward Biology, Catalysis, and Nanotechnology. *Chem. Rev.* **2004**, *104*, 293-346.

(6) Badia, A.; Singh, S.; Demers, L.; Cuccia, L.; Brown, G. R.; Lennox, R. B. Self-

Assembled Monolayers on Gold Nanoparticles. *Chem. Eur. J.* **1996**, *2*, 359-363.

(7) Templeton, A. C.; Wuelfing, W. P.; Murray, R. W. Monolayer-Protected Cluster Molecules. *Acc. Chem. Res.* **2000**, *33*, 27-36.

(8) Duchesne, L.; Gentili, D.; Comes-Franchini, M.; Fernig, D. G. Robust Ligand Shells for Biological Applications of Gold Nanoparticles. *Langmuir* **2008**, *24*, 13572-13580.

(9) Free, P.; Shaw, C. P.; Lévy, R. PEGylation Modulates the Interfacial Kinetics of Proteases on Peptide-Capped Gold Nanoparticles. *Chem. Comm.* **2009**, 5009-5011.

(10) Nieves, D. J.; Azmi, N. S.; Xu, R.; Lévy, R.; Yates, E. A.; Fernig, D. G. Monovalent Maleimide Functionalization of Gold Nanoparticles via Copper-Free Click Cchemistry. *Chem. Comm.* **2014**, *50*, 13157-13160.

(11) Yang, G.; Liu, G.-Y. New Insights for Self-Assembled Monolayers of Organothiols on Au(111) Revealed by Scanning Tunneling Microscopy. *J. Phys. Chem. B* **2003**, *107*, 8746-8759.

(12) Poirier, G. E. Characterization of Organosulfur Molecular Monolayers on Au(111) using Scanning Tunneling Microscopy. *Chem. Rev.* **1997**, *97*, 1117-1128.

(13) Biscarini, F.; Ong, Q. K.; Albonetti, C.; Liscio, F.; Longobardi, M.; Mali, K. S.; Ciesielski, A.; Reguera, J.; Renner, C.; De Feyter, S.; Samorì, P.; Stellacci, F. Quantitative Analysis of Scanning Tunneling Microscopy Images of Mixed-Ligand-Functionalized Nanoparticles. *Langmuir* **2013**, *29*, 13723-13734.

(14) Ong, Q. K.; Reguera, J.; Silva, P. J.; Moglianetti, M.; Harkness, K.; Longobardi, M.; Mali, K. S.; Renner, C.; De Feyter, S.; Stellacci, F. High-Resolution Scanning Tunneling Microscopy Characterization of Mixed Monolayer Protected Gold Nanoparticles. *ACS Nano* **2013**, *7*, 8529-8539.

(15) Stirling, J.; Lekkas, I.; Sweetman, A.; Djuranovic, P.; Guo, Q.; Pauw, B.; Granwehr, J.; Lévy, R.; Moriarty, P. Critical Assessment of the Evidence for Striped Nanoparticles. *PLOS ONE* **2014**, *9*, e108482.

(16) Schneider, L.; Peukert, W. Second Harmonic Generation Spectroscopy as a Method for In Situ and Online Characterization of Particle Surface Properties. *Part. Part. Syst. Charact.* **2006**, *23*, 351-359.

(17) Eisenthal, K. B. Second Harmonic Spectroscopy of Aqueous Nano- and Microparticle Interfaces. *Chem. Rev.* **2006**, *106*, 1462-1477.

(18) Dinkel, R.; Braunschweig, B.; Peukert, W. Fast and Slow Ligand Exchange at the Surface of Colloidal Gold Nanoparticles. *J. Phys. Chem. C* **2016**, *120*, 1673-1682.

(19) Gan, W.; Gonella, G.; Zhang, M.; Dai, H.-L. Communication: Reactions and Adsorption at the Surface of Silver Nanoparticles Probed by Second Harmonic Generation. *J. Chem. Phys.* **2011**, *134*, 041104.

(20) Campen, R. K.; Zheng, D.-S.; Wang, H.-F.; Borguet, E. Second Harmonic

Generation as a Probe of Multisite Adsorption at Solid−Liquid Interfaces of Aqueous Colloid Suspensions. *J. Phys. Chem. C* **2007**, *111*, 8805-8813.

(21) Hostetler, M. J.; Wingate, J. E.; Zhong, C.-J.; Harris, J. E.; Vachet, R. W.; Clark, M. R.; Londono, J. D.; Green, S. J.; Stokes, J. J.; Wignall, G. D.; Glish, G. L.; Porter, M. D.; Evans, N. D.; Murray R. W. Alkanethiolate Gold Cluster Molecules with Core Diameters from 1.5 to 5.2 nm: Core and Monolayer Properties as a Function of Core Size. *Langmuir* **1998**, *14*, 17-30.

(22) Templeton, A. C.; Hostetler, M. J.; Kraft, C. T.; Murray, R. W. Reactivity of Monolayer-Protected Gold Cluster Molecules: Steric Effects. *J. Am. Chem. Soc.* **1998**, *120*, 1906-1911.

(23) Weaver, M. J. Raman and Infrared Spectroscopies as In Situ probes of Catalytic Adsorbate Chemistry at Electrochemical and Related Metal–Gas Interfaces: Some Perspectives and Prospects. *Top. Catal.* **1999**, *8*, 65-73.

(24) Weaver, M. J. Surface-Enhanced Raman Spectroscopy as a Versatile In Situ Probe of Chemisorption in Catalytic Electrochemical and Gaseous Environments. *J. Raman Spectrosc.* **2002**, *33*, 309-317.

(25) Tian, Z. Q.; Ren, B. Adsorption and Reaction at Electrochemical Interfaces as Probed by Surface-Enhanced Raman Spectroscopy. *Annu. Rev. Phys. Chem.* **2004**, *55*, 197-229.

(26) Fokas, C.; Deckert, V. Towards In Situ Raman Microscopy of Single Catalytic Sites. *Appl. Spectrosc.* **2002**, *56*, 192-199.

(27) Gomez, R.; Solla-Gullon, J.; Perez, J. M.; Aldaz, A. Nanoparticles-on-Electrode Approach for In Situ Surface-Enhanced Raman Spectroscopy Studies with Platinum-Group Metals: Examples and Prospects. *J. Raman Spectrosc.* **2005**, *36*, 613-622.

(28) Zhang, Y.; Wu, Y.; Qin, D. Rational Design and Synthesis of Bifunctional Metal Nanocrystals for Probing Catalytic Reactions by Surface-Enhanced Raman Scattering. *J. Mater. Chem. C* **2018**, *6*, 5353-5362.

(29) Huang, J.; Zhu, Y.; Lin, M.; Wang, Q.; Zhao, L.; Yang, Y.; Yao, K. X.; Han, Y. Site-Specific Growth of Au–Pd Alloy Horns on Au Nanorods: A Platform for Highly Sensitive Monitoring of Catalytic Reactions by Surface Enhancement Raman Spectroscopy. *J. Am. Chem. Soc.* **2013**, *135*, 8552-8561.

(30) Li, J.; Wu, Y.; Sun, X.; Liu, J.; Winget, S. A.; Qin, D. A Dual Catalyst with SERS Activity for Probing Stepwise Reduction and Oxidation Reactions. *ChemNanoMat* **2016**, *2*, 786-790.

(31) Zhang, Y.; Liu, J.; Ahn, J.; Xiao, T.-H.; Li, Z.-Y.; Qin, D. Observing the Overgrowth of a Second Metal on Silver Cubic Seeds in Solution by Surface-Enhanced Raman Scattering. *ACS Nano* **2017**, *11*, 5080-5086.

(32) Wu, Y.; Qin, D. In Situ Atomic-Level Tracking of Heterogeneous Nucleation in Nanocrystal Growth with an Isocyanide Molecular Probe. *J. Am. Chem. Soc.* **2018**,

140, 8340-8349.

(33) Muniz-Miranda, M.; Pagliai, M.; Cardini, G.; Schettino, V. Role of Surface Metal Clusters in SERS Spectra of Ligands Adsorbed on Ag Colloidal Nanoparticles. *J. Phys. Chem. C* **2008**, *112*, 762-767.

(34) Zhang, D.; Ansar, S. M. Ratiometric Surface Enhanced Raman Quantification of Ligand Adsorption onto a Gold Nanoparticle. *Anal. Chem.* **2010**, *82*, 5910-5914.

(35) Darby, B. L.; Le Ru, E. C. Competition between Molecular Adsorption and Diffusion: Dramatic Consequences for SERS in Colloidal Solutions. *J. Am. Chem. Soc.* **2014**, *136*, 10965-10973.

(36) Futamata, M. Surface-Plasmon-Polariton-Enhanced Raman Scattering from Self-Assembled Monolayers of p-Nitrothiophenol and p-Aminothiophenol on Silver. *J. Phys. Chem.* **1995**, *99*, 11901-11908.

(37) Walczak, M. M.; Chung, C.; Stole, S. M.; Widrig, C. A.; Porter, M. D. Structure and Interfacial Properties of Spontaneously Adsorbed n-Alkanethiolate Monolayers on Evaporated Silver Surfaces. *J. Am. Chem. Soc.* **1991**, *113*, 2370-2378.

(38) Kim, K.; Choi, J.-Y.; Shin, K. S. Surface-Enhanced Raman Scattering of 4-Nitrobenzenethiol and 4-Aminobenzenethiol on Silver in Icy Environments at Liquid Nitrogen Temperature. *J. Phys. Chem. C* **2014**, *118*, 11397-11403.

(39) Zhao, L.-B.; Chen, J.-L.; Zhang, M.; Wu, D.-Y.; Tian, Z.-Q. Theoretical Study on Electroreduction of p-Nitrothiophenol on Silver and Gold Electrode Surfaces. *J. Phys. Chem. C* **2015**, *119*, 4949-4958.

(40) Fang, Y.; Li, Y.; Xu, H.; Sun, M. Ascertaining p,p'-Dimercaptoazobenzene Produced from p-Aminothiophenol by Selective Catalytic Coupling Reaction on Silver Nanoparticles. *Langmuir* **2010**, *26*, 7737-7746.

(41) Zhang, J.; Winget, S. A.; Wu, Y.; Su, D.; Sun, X.; Xie, Z.-X.; Qin, D. Ag@Au Concave Cuboctahedra: A Unique Probe for Monitoring Au-Catalyzed Reduction and Oxidation Reactions by Surface-Enhanced Raman Spectroscopy. *ACS Nano* **2016**, *10*, 2607-2616.

(42) Gajdoš, M.; Eichler, A.; Hafner, J. CO Adsorption on Close-packed Transition and Noble Metal Surfaces: Trends From *Ab Initio* Calculations. *J. Phys. Condens. Matter* **2004**, *16*, 1141-1164.

(43) Gruenbaum, S. M.; Henney, M. H.; Kumar, S.; Zou, S. Surface-Enhanced Raman Spectroscopic Study of 1,4-Phenylene Diisocyanide Adsorbed on Gold and Platinum-Group Transition Metal Electrodes. *J. Phys. Chem. B* **2006**, *110*, 4782-4792.

(44) Bae, S. J.; Lee, C.-R.; Choi, I. S.; Hwang, C.-S.; Gong, M.-S.; Kim, K.; Joo, S.-W. Adsorption of 4-Biphenylisocyanide on Gold and Silver Nanoparticle Surfaces: Surface-Enhanced Raman Scattering Study. *J. Phys. Chem. B* **2002**, *106*, 7076-7080.

(45) Hu, J.; Tanabe, M.; Sato, J.; Uosaki, K.; Ikeda, K. Effects of Atomic Geometry and Electronic Structure of Platinum Surfaces on Molecular Adsorbates Studied by Gap-Mode SERS. *J. Am. Chem. Soc.* **2014**, *136*, 10299-10307.

(46) Han, H. S.; Han, S. W.; Joo, S. W.; Kim, K. Adsorption of 1,4-Phenylene Diisocyanide on Silver Investigated by Infrared and Raman Spectroscopy. *Langmuir* **1999**, *15*, 6868-6874.

(47) Angelici, R. J.; Lazar, M. Isocyanide Ligands Adsorbed on Metal Surfaces: Applications in Catalysis, Nanochemistry, and Molecular Electronics. *Inorg. Chem.* **2008**, *47*, 9155-9165.

(48) Sato, S.; Iwase, S.; Namba, K.; Ono, T.; Hara, K.; Fukuoka, A.; Uosaki, K.; Ikeda, K. Electrical Matching at Metal/Molecule Contacts for Efficient Heterogeneous Charge Transfer. *ACS Nano* **2018**, *12*, 1228-1235.

(49) Skrabalak, S. E.; Au, L.; Li, X.; Xia, Y. Facile Synthesis of Ag Nanocubes and Au Nanocages. *Nat. Protoc.* **2007**, *2*, 2182-2190.

(50) Li, J.; Liu, J.; Yang, Y.; Qin, D. Bifunctional Ag@Pd-Ag Nanocubes for Highly Sensitive Monitoring of Catalytic Reactions by Surface-Enhanced Raman Spectroscopy. *J. Am. Chem. Soc.* **2015**, *137*, 7039-7042.

(51) Matsuura, T.; Shimoyama, Y. Growth Kinetics of Self-Assembled Monolayers of Thiophene and Terthiophene on Au(111): An Infrared Spectroscopic Study. *Eur. Phys. J. E* **2002**, *7*, 233-240.

(52) Xu, S.; Cruchon-Dupeyrat, S. J. N.; Garno, J. C.; Liu, G.-Y.; Jennings, G. K.; Yong, T.-H.; Laibinis, P. E. In Situ Studies of Thiol Self-Assembly on Gold from Solution Using Atomic Force Microscopy. *J. Chem. Phys.* **1998**, *108*, 5002-5012.

(53) Jakubowicz, A.; Jia, H.; Wallace, R. M.; Gnade, B. E. Adsorption Kinetics of p-Nitrobenzenethiol Self-Assembled Monolayers on a Gold Surface. *Langmuir* **2005**, *21*, 950-955.

(54) Gao, X.; Davies, J. P.; Weaver, M. J. A Test of Surface Selection Rules for Surface-Enhanced Raman Scattering: The Orientation of Adsorbed Benzene and Monosubstituted Benzenes on Gold. *J. Phys. Chem.* **1990**, *94*, 6858-6864.

(55) Ahn, J.; Shi, S.; Vannatter, B.; Qin, D. Comparative Study of the Adsorption of Thiol and Isocyanide Molecules on a Silver Surface by in Situ Surface-Enhanced Raman Scattering. *J. Phys. Chem. C* **2019**, *123*, 21571-21580.

CHAPTER 6. CONCLUSIONS AND OUTLOOK

6.1 Concluding Remarks

This dissertation documents my contributions to the development of a rational synthesis of multi-metallic nanocrystals with complex shapes and compositions in the solution phase using a Ag nanocrystal template as the starting point. I believe that a rational design plays an essential role to fine-tune the nanocrystal morphology with a specific shape and composition, leading to achieve desired properties based on their structure-property relationship. To this end, I reported two strategies by leveraging both the etching and the deposition for controlling the morphological evolution of a nanocrystal template. Specifically, I focused on the use of galvanic replacement reaction to instigate oxidation (etching) and reduction (growth) on the different facets of Ag nanocrystals in an orthogonal manner. By controlling the relative rates of etching and deposition on selected facets of the nanocrystal template using various ligands, I successfully fabricated bimetallic and trimetallic nanocrystals with specific shapes as well as spatial distribution of elements.

In the first strategy, I coupled the galvanic replacement reaction with a chemical reduction pathway in the presence of cetyltrimethylammonium chloride (CTAC) to demonstrate the transformation of Ag nanocubes into Ag@Ag-Au concave nanocrystals. The mechanism involves the co-deposition of Au and Ag atoms on the edges and corners of the Ag nanocubes while Ag atoms are concomitantly etched away from the side faces. In a typical synthesis, I titrated aqueous $HAuCl_4$ to an aqueous suspension of Ag nanocubes in the presence of ascorbic acid (H_2Asc), NaOH, and CTAC at an initial pH of 11.6 under ambient conditions. The added $HAuCl_4$ remains in the form of $AuCl_4^-$ under an alkaline

condition, facilitating the galvanic replacement reaction with the Ag nanocubes. As the Cl^- ions can selectively bind to the {100} facets of Ag nanocubes. the dissolution of Ag atoms would occur from the side faces. The released Ag^+ ions can be retained in the soluble form of $AgCl_2^-$ by complexing with the Cl^- ions. Both the $AuCl_4^-$ and $AgCl_2^-$ are then reduced by ascorbic monoanion ($HAsc^-$) to generate Au and Ag atoms, followed by their co-deposition preferentially onto the edges and corners of Ag nanocubes. As the reaction progresses, Ag atoms located at the side faces of the nanocubes are continuously carved by the galvanic reaction while Ag and Au atoms are increasingly deposited on the edges and corners, leading to the generation of Ag@Ag-Au core-frame nanocubes with concave side faces. These nanocrystals could also be transformed into Au-Ag nanoframes with controllable ridge thicknesses upon the removal of Ag in the core.

I then demonstrated that the Ag@Ag-Au core-frame nanocubes could be used as a template for the generation of multi-metallic cage cubes by drilling through all the side faces of the template. My success relies on the use of the template with Ag in the core and Ag-Au alloy frames along the corners and edges of a nanocube to confine the drilling of Ag to the center of each side face, and ultimately to align the intersected holes with the center of the nanocube. In a typical protocol, I dispersed Ag@Ag-Au core-frame nanocubes in an aqueous solution containing CTAC, followed by the titration of an aqueous solution of a salt precursor such as H_2PtCl_6, K_2PtCl_4, Na_2PdCl_4, or $HAuCl_4$ under ambient conditions. A simple galvanic replacement reaction between the Ag@Ag-Au nanocubes and the precursor could produce multi-metallic cage cubes with holes of different sizes, which would depend on the stoichiometry and reduction potential of the salt precursor. At the early stage of a synthesis, the Cl^- ions derived from CTAC could bind selectively

toward the Ag(100) surface, making the oxidation of Ag preferentially start from the Ag-dominated regions located at the center of each side face of a nanocube for the creation of a cavity, while the resultant metal atoms are deposited on the edges and corners in an orthogonal manner. As the Ag atoms are removed from the side faces in the form of Ag(I) ions for the generation of other metals followed by their deposition on the edges and corners of nanocubes, I could achieve the continuous carving of Ag atoms from the center of a core-frame nanocube for its ultimate transformation into a cage cube enclosed by a bimetallic or trimetallic alloy, together with three orthogonal, intersected holes.

Because Ag nanocubes have a limited presence of surface facets other than the {100}, I also investigated the facet-selective growth of Au on Ag cuboctahedra templates, which consist of a mix of {100} and {111} facets in a 1.7-to-1 ratio, to support my previous findings. I demonstrated the transformation of Ag cuboctahedra into Ag-Au cuboctahedral nanoboxes with complementary facets by including either poly(vinylpyrrolidone) (PVP) or CTAC to a reaction solution containing Ag cuboctahedra, H_2Asc, and NaOH at the pH around 11, followed by the titration of aqueous $HAuCl_4$. When the PVP was involved, the oxidation of Ag would be initiated on the on the {111} facets for the deposition of Au on the {100} facets in the orthogonal manner, transforming Ag cuboctahedra into $Ag@Au_{\{100\}}$ cuboctahedra and then cuboctahedral nanoboxes enclosed by the {100} facets after the etching of Ag by H_2O_2. In comparison, when the CTAC was added to the reaction solution, the oxidation of Ag would continuously progress on the {100} facets for the generation of concavities. Concomitantly, the dissolved Ag(I) ions and the Au(III) would be co-reduced by chemical reduction for the generation of Ag and Au atoms, followed by their co-deposition on the {111} facets for the generation of $Ag@Au_{\{111\}}$ concave cuboctahedra and

the resultant Ag-$Au_{\{111\}}$ cuboctahedral nanoboxes enclosed by {111} facets after the removal of Ag.

Finally, I explored the use of *in situ* surface-enhanced Raman spectroscopy (SERS) to investigate the adsorption of different ligands on the surface of colloidal Ag nanocubes. In a typical process, I collected SERS spectra at different time points from a mixture of Ag nanocubes and a ligand such as such as 4-nitrothiophenol (4-NTP), 4-aminothiophenol (4-ATP), or 1,4-phenylene diisocyanide (1,4-PDI) at a specific concentration. Time-dependent SERS spectra of 4-NTP indicate that the adsorption could be achieved within 3 min due to the strong binding of thiol to Ag surface. I also recorded the concentration-dependent SERS spectra of 4-NTP, from which I observed a red-shift for all peaks at a concentration of 10^{-7} M relative to the case 10^{-5} M or 10^{-4} M. I argue that such a red-shift could be attributed to the difference in molecular orientation, with the benzene ring oriented parallel to or tilting away from the surface at low and high concentrations, respectively. I confirmed that the adsorption kinetics of 4-ATP on Ag was similar to that of 4-NTP, although the SERS signals from 4-ATP were much weaker due to the absence of chemical enhancement. Different from the case of thiol, 1,4-PDI would bind to a Ag surface through σ-donation, giving slower adsorption kinetics over a time scale of 60 min. At a concentration of 10^{-5} M and above, I observed both $\nu_{NC(free)}$ and $\nu_{NC(Ag)}$ peaks in the SERS spectra, suggesting that the 1,4-PDI molecules could be oriented with the benzene ring tilting away from the surface. I further evaluated the relative binding strength of the thiol and isocyanide groups toward Ag surface by dispersing Ag nanocubes in an ethanol solution containing both ligands. The SERS signals from 1,4-PDI were not detectable in either case when it was used at the same concentration as 4-NTP or 4-ATP at 10^{-5} M. However, the 1,4-PDI signals became

detectable when its concentration was increased by 100 times relative to 4-NTP or 4-ATP. Collectively, my data indicate that the thiols have a much stronger binding to the surface on Ag nanocubes, making it possible to impede or even inhibit the adsorption of isocyanides.

6.2 Future Directions for Research

This research developed several approaches to control the facet-selective etching and deposition of second metal on the surface of Ag nanocrystal templates for their transformation into nanocrystals with complex shapes and spatially well-defined elemental distributions. It is anticipated that these protocols for synthesis can be extended to other metal precursor salts (such as those for Rh or Ir) for the fabrication of core-frame concave nanocubes and nanoscale cage cubes composed of these metals. To this end, I have demonstrated the feasibility through some initial experiments (Chapter 3, Section 3.3.3) that experimental parameters such as reaction stoichiometry or the titration rate could be tuned systematically to further optimize the morphology and composition of the final product. However, as these salts are often insoluble in water, one must consider using another solvent (such as, but not limited to, ethylene glycol) or making other modifications to the protocol, while considering their effects on the reaction pathway to develop a reliable and general approach to the design and production of these unique-morphology nanocrystals.[1-4]

It should be pointed out that there is also active research in progress regarding the synthesis of complex-shape noble metal nanocrystals, in which several additional nanoscale processes such as solid-state diffusion,[5] Kirkendall diffusion,[6,7] and dealloying[8,9]

other than galvanic replacement could kick in to generate nanocrystals with even more complex shapes, morphologies, and compositions. From all these endeavors, one will surely gain further insights into the facet-selective etching and deposition mechanisms while significantly increase the diversity and functionality of metal nanocrystals. Moving forward, it is important to apply these design rules of metal nanocrystals to other systems such as nanostructures consisting of soft-core and hard-shell nanoparticles for the construction of multi-shell hollow nanostructures for potential applications in energy storage and conversion.[10]

Moreover, I argue that the SERS-based platform would embrace much potential in probing the surfaces of colloidal Ag nanocubes and characterizing the interaction between the ligands and the Ag surface atoms. Similar to the case of thiols and isocyanides, I believe that I could characterize the adsorption of other types of ligands, such as PVP and CTAC, that significantly affect the heterogeneous growth of the nanocrystals. In particular, I am investigating the configuration of PVP chains adsorbed on the Ag nanocube surface as a function of the solvent, based on the understanding from polymer sciences that polymer chains would collapse in the presence of an incompatible solvent and expand in the presence of a compatible solvent.[11-13] In addition, the SERS platform could be used to study the effect of replacing the PVP with other ligands, such as CTAC (chloride ions). Although the Ag nanocubes offer several SERS hot spots on its edges with a large enhancement in the local electric field, the anisotropic distribution of these hot spots poses a challenge to characterize the particle surface in general and not just the cubic edges.[14] As such, one should consider the use of an isotropic nanosphere for further investigation.

6.3 Notes for Chapter 6

Parts of this chapter are adapted from the article "Transforming Noble-Metal Nanocrystals into Complex Nanostructures through Facet-Selective Etching and Deposition," a minireview published in *ChemNanoMat*,[15] the article "Site-Selective Carving and Co-Deposition: Transformation of Ag Nanocubes into Concave Nanocrystals Encased by Au–Ag Alloy Frames" published in *ACS* Nano,[16] the article "Fabrication of Nanoscale Cage Cubes by Drilling Orthogonal, Intersected Holes through All Six Side Faces of Ag Nanocubes" under revision for publication in *Chemistry of Materials*,[17] the article "Orthogonal Deposition of Au on Different Facets of Ag Cuboctahedra for the Fabrication of Nanoboxes with Complementary Surfaces" published in *Nanoscale*,[18] and the article "Comparative Study of the Adsorption of Thiol and Isocyanide Molecules on Silver Surface by In Situ Surface-Enhanced Raman Scattering" published in the *Journal of Physical Chemistry C*.[19]

6.4 References

(1) Biacchi, A. J.; Schaak, R. E. The Solvent Matters: Kinetic versus Thermodynamic Shape Control in the Polyol Synthesis of Rhodium Nanoparticles. *ACS Nano* **2011**, *5*, 8089-8099.

(2) Brown, A. L.; Winter, H.; Goforth, A. M.; Sahay, G.; Sun, C. Facile Synthesis of Ligand-Free Iridium Nanoparticles and Their In Vitro Biocompatibility. *Nanoscale Res. Lett.* **2018**, *13*, 208.

(3) Zhang, Y.; Zhu, X.; Guo, J.; Huang, X. Controlling Palladium Nanocrystals by Solvent-Induced Strategy for Efficient Multiple Liquid Fuels Electrooxidation. *ACS Appl. Mater. Interfaces* **2016**, *8*, 20642-20649.

(4) Bonet, F.; Delmas, V.; Grugeon, S.; Herrera Urbina, R.; Silvert, P.-Y.; Tekaia-Elhsissen, K. Synthesis of Monodisperse Au, Pt, Pd, Ru and Ir Nanoparticles in Ethylene Glycol. *Nanostructured Mater.* **1999**, *11*, 1277-1284.

(5) Li, G. G.; Sun, M.; Villarreal, E.; Pandey, S.; Phillpot, S. R.; Wang, H. Galvanic Replacement-Driven Transformations of Atomically Intermixed Bimetallic

Colloidal Nanocrystals: Effects of Compositional Stoichiometry and Structural Ordering. *Langmuir* **2018**, *34*, 4340-4350.

(6) Gonzalez, E.; Arbiol, J.; Puntes, V. F. Carving at the Nanoscale: Sequential Galvanic Exchange and Kirkendall Growth at Room Temperature. *Science* **2011**, *334*, 1377-1380.

(7) Chee, S. W.; Wong, Z. M.; Baraissov, Z.; Tan, S. F.; Tan, T. L.; Mirsaidov, U. Interface-Mediated Kirkendall Effect and Nanoscale Void Migration in Bimetallic Nanoparticles During Interdiffusion. *Nat. Commun.* **2019**, *10*, 2831.

(8) Newman, R. C.; Sieradzki, K. Metallic Corrosion. *Science* **1994**, *263*, 1708-1709.

(9) Erlebacher, J.; Aziz, M. J.; Karma, A.; Dimitrov, N.; Sieradzki, K. Evolution of Nanoporosity in Dealloying. *Nature* **2001**, *410*, 410−453.

(10) Zhou, L.; Zhuang, Z.; Zhao, H.; Lin, M.; Zhao, D.; Mai, L. Intricate Hollow Structures: Controlled Synthesis and Applications in Energy Storage and Conversion. *Adv. Mater.* **2017**, *29*, 1602914.

(11) Flory, P. J. Thermodynamics of High Polymer Solutions. *J. Chem. Phys.* **1942**, *10*, 51-61.

(12) Moran, C. H.; Rycenga, M.; Zhang, Q.; Xia, Y. Replacement of Poly(vinyl pyrrolidone) by Thiols: A Systematic Study of Ag Nanocube Functionalization by Surface-Enhanced Raman Scattering. *J. Phys. Chem. C* **2011**, *115*, 21852-21857.

(13) Balankura, T.; Qi, X.; Fichthorn, K. A. Solvent Effects on Molecular Adsorption on Ag Surfaces: Polyvinylpyrrolidone Oligomers. *J. Phys. Chem. C.* **2018**, *122*, 14566-14573.

(14) McLellan, J. M.; Li, Z.-Y.; Siekkinen, A. R.; Xia, Y. The SERS Activity of a Supported Ag Nanocube Strongly Depends on Its Orientation Relative to Laser Polarization. *Nano Lett.* **2007**, *7*, 1013-1017.

(15) Ahn, J.; Zhang, L.; Qin, D. Transforming Noble-Metal Nanocrystals into Complex Nanostructures through Facet-Selective Etching and Deposition. *ChemNanoMat* **2019**. DOI: 10.1002/cnma.201900378.

(16) Ahn, J.; Wang, D.; Ding, Y.; Zhang, J.; Qin, D. Site-Selective Carving and Co-Deposition: Transformation of Ag Nanocubes into Concave Nanocrystals Encased by Au-Ag Alloy Frames. *ACS Nano* **2018**, *12*, 298–307.

(17) Ahn, J.; Qin, D. Fabrication of Nanoscale Cage Cubes by Drilling Orthogonal, Intersected Holes through All Six Side Faces of Ag Nanocubes. *Chem. Mater.*, in press (under revision).

(18) Ahn, J.*; Kim, J.*; Qin, D. Orthogonal Deposition of Au on Different Facets of Ag Cuboctahedra for the Fabrication of Nanoboxes with Complementary Surfaces. *Nanoscale* **2019**, DOI: 10.1039/C9NR08420G. (*Equal contribution.)

(19) Ahn, J.; Shi, S.; Vannatter, B.; Qin, D. Comparative Study of the Adsorption of

Thiol and Isocyanide Molecules on a Silver Surface by in Situ Surface-Enhanced Raman Scattering. *J. Phys. Chem. C* **2019**, *123*, 21571-21580.